University of Southampton

Faculty of Engineering and Physical Sciences

Optoelectronics Research Centre

Mode Control and Laser Beam Shaping in Multimode and Multicore Fibres

by

Kunhao Ji

ORCID ID: 0000-0002-2300-5942

Supervisors: Dr. Massimiliano Guasoni
Prof. David Richardson
Dr. Lin Xu

Thesis for the degree of Doctor of Philosophy

March 2025

University of Southampton

Abstract

Faculty of Engineering and Physical Sciences

Optoelectronics Research Centre

Doctor of Philosophy

Mode control and laser beam shaping in multimode and multicore fibres

by

Kunhao Ji

Multimode (MM) and multicore fibres (MCFs) have been exploited in numerous important research areas, ranging from fibre lasers and telecommunications to transmission and sensing. However, designing and understanding multimodal nonlinear optical systems present significant technical and conceptual challenges. The ability to control light fields with multiple degrees of freedom is expected to become a key focus for future developments in multimode nonlinear systems. This project aims to investigate the dynamics of multimodal interactions in multimode and multicore fibres. In this thesis, mode control and laser beam shaping in homemade MCFs and commercial MMFs are explored. Firstly, the modal dynamics in multimode counter-propagating systems are investigated, including mode rejection and control when the forward signal and backward control beam (BCB) are both operating in the nonlinear regime (high peak power). Mode rejection of a specific spatial mode was successfully observed in the output forward signal when the input BCB was coupled to the same mode with comparable power, using dual-core fibres (DCFs), tri-core fibres (TCFs), and commercial MMFs with lengths of 0.4-1m, at a total peak power of 4-16 kW for counter-propagating beams with 0.5 ns pulses at a wavelength of 1040 nm. Secondly, the concept of counter-propagating nonlinear gratings is introduced when only the BCB is in the nonlinear regime. The BCB generates a multimode nonlinear grating that can be utilized for all-optical mode switching and power switching for the forward probe beam. Mode switching in 0.4 m MMFs and MCFs was observed with a BCB power of 6-12 kW in 0.5 ns pulses at a wavelength of 1040 nm. Core-to-core power switching in 0.4 m DCF and TCF was measured with a BCB power of 7-10 kW. Thirdly, wavelength and mode conversion in MCFs were investigated by exploring four-wave mixing (FWM) between supermodes in MCFs. Efficient FWM and supermode/wavelength conversion were demonstrated with a pump wavelength of 1040 nm in several homemade MCFs, including DCF, TCF, 4-core, and 7-core fibres. Finally, laser beam shaping in uncoupled MCFs was investigated. The controlled generation of ps-pulsed structured beams was achieved using a coherently combined 6-core Yb-doped MCF amplifier. This method produced linearly polarized Gaussian beams, cylindrical vector mode beams, and orbital angular momentum mode beams with peak powers of 10-14 kW and pulse durations of 92 ps at a wavelength of 1035nm. Overall, these results demonstrate mode control and beam shaping in MMFs and MCFs, highlighting the potential for all-optical light manipulations in various future photonics applications.

Table of Contents

Table of Tables

Table of Figures

Research Thesis: Declaration of Authorship

Print name:

Title of thesis:

I declare that this thesis and the work presented in it are my own and has been generated by me as the result of my own original research.

I confirm that:

1. This work was done wholly or mainly while in candidature for a research degree at this University;
2. Where any part of this thesis has previously been submitted for a degree or any other qualification at this University or any other institution, this has been clearly stated;
3. Where I have consulted the published work of others, this is always clearly attributed;
4. Where I have quoted from the work of others, the source is always given. With the exception of such quotations, this thesis is entirely my own work;
5. I have acknowledged all main sources of help;
6. Where the thesis is based on work done by myself jointly with others, I have made clear exactly what was done by others and what I have contributed myself;
7. Parts of this work have been published as: See List of Publications.

Signature: .... Date:........................

Acknowledgements

Throughout my PhD study at the Optoelectronics Research Centre, I have received enormous amount of support and assistance. First and foremost, I would like to express my sincere gratitude to my supervisors, Prof. David Richardson, Dr. Lin Xu, and especially Dr. Massimiliano Guasoni for their continuous support, guidance, and encouragement throughout my research and the writing of this thesis. Their insight, expertise, and patience have been invaluable, and I am profoundly grateful for the opportunity to learn under their mentorship.

I would like to acknowledge my colleagues and fellow researchers in the Pulsed fibre laser group and Multimode Photonics group for their camaraderie, collaboration, and insightful discussions. Special thanks to Dr. Yongmin Jung, Dr. Di Lin, Dr. Saurabh Jain, Dr. Qiang Fu and Dr. Jack Haines. I would also like to acknowledge Dr. Ian Davidson and Prof. Jayanta Sahu for providing well-performed fibres. I would like to thank Dr. Sijing Liang, Dr. Duanyang Xu, Xin Huang, Panuwat Srisamran, Jikun Yan, and Jing Meng for their support, friendship, and the many inspiring conversations we shared.

I would like to acknowledge the financial support provided by EPSRC, ERC and CSC through “Self-organized light in multicore optical fibers: a route to scalable high-power lasers and all-optical signal processing” and “Multimode light shaping: from optical fibers to nanodevices”, without which this research would not have been possible.

My deepest thanks go to my family, especially my parents, Mr. Lijun Ji and Mrs. Shurong Qiao, for their unwavering love, understanding, and belief in me. Their constant encouragement has been a source of strength throughout this journey.

Definitions and Abbreviations

4CF	4-Core Fibre
7CF	7-Core Fibre
ASE	Amplified Spontaneous Emission
BCB	Backward Control Beam
CBC	Coherent Beam Combination
CCD	Charge-Coupled Device
CCMCF	Coupled-Core Multicore Fibre
CV	Cylindrical Vector
CW	Continuous Wave
DCF	Dual-Core Fibre
DWDM	Dense Wavelength Division Multiplexing
FF	Far-Field
FMF	Few-Mode Fibre
FS	Forward Signal
FWHM	Full Width at Half Maximum
FWM	Four Wave Mixing
GRIN	Graded-Index
HOPS	Higher-Order Poincaré Sphere
HWP	Half Wave Plate
IFA	Interferometric Fibre Analyser
ISO	Isolator
LP	Linearly-Polarized
MCF	Multicore Fibre
MD	Mode Decomposition
MI	Modulation Instability
MLA	Microlens Array
MMF	Multimode Fibre
MMMCF	Multimode Multicore Fibre
MMNLSE	Multimode Nonlinear Schrödinger Equation
MOPA	Master Oscillator Power Amplifier
NA	Numerical Aperture
NF	Near Field
OAM	Orbital Angular Momentum
OFDR	Optical Frequency Domain Reflectometry

OSA	Optical Spectrum Analyser
OSNR	Optical Signal to Noise Ratio
OTDR	Optical Time Domain Reflectometry
PB	Probe Beam
PBS	Polarization Beam Splitter
PER	Polarization Extinction Ratio
PM	Polarization Maintaining
PMF	Polarization Maintaining Fibre
PP	Phase Plate
QWP	Quarter Wave Plate
SBS	Stimulated Brillouin Scattering
SDM	Space-Division Multiplexing
SLM	Spatial Light Modulator
SM	Supermode
SMF	Single Mode Fibre
SNR	Signal to Noise Ratio
SPGD	Stochastic Parallel Gradient Descent
SPM	Self-Phase Modulation
SRS	Stimulated Raman Scattering
STML	Spatiotemporal Mode Locking
TCF	Tri-Core Fibre
THG	Third Harmonic Generation
XPM	Cross Phase Modulation

List of symbols

λ	Wavelength
ω	Angular frequency
c	Velocity of light in vacuum
β	Propagation constant
β_1	First order dispersion
v_g	Group velocity
β_2	Second order dispersion
Δn	Core-cladding refractive index difference
t	Time
ε_0	Vacuum permittivity
$\boldsymbol{E}$	Electric field
$\boldsymbol{P}_L$	Linear part of the induced polarization related to electric field
$\boldsymbol{P}_{NL}$	Nonlinear part of the induced polarization related to electric field
$\widetilde{\boldsymbol{E}}$	Fourier transform of the electric field
$\hat{\boldsymbol{e}}_m$	Polarization state of the *m*-th mode
M_m	Transverse shape of the *m*-th mode
β_m	Propagation constant of the *m*-th mode
c_m^2	Relative mode content (relative power) of the *m*-th mode
θ_m	Relative phase of the *m*-th mode
$\bar{n}_m$	Effective mode refractive index of the *m*-th mode
β_{km}	The *k*-th order dispersion parameter for the *m*-th mode
$\chi_K^{(3)}$	The 3rd order nonlinear susceptibility related to the Kerr nonlinearity
$\chi_R^{(3)}$	The 3rd order nonlinear susceptibility related to the Raman nonlinearity
h_R	Raman response function
γ	Kerr coefficient
A_{eff}	Effective area
f_R	Fractional contribution of the delayed Raman response
$\Delta\beta$	Phase mismatch
f_{mnpq}	Intermodal overlap factor
ω_p	Frequency of pump
ω_i	Frequency of idler
ω_s	Frequency of signal
δ_R	Raman-induced index changes
g_R	Raman gain coefficients

$\tilde{h}_R$	Fourier transform of h_R
Ap_m	Amplitude of pump in the m-th mode
As_m	Amplitude of signal in the m-th mode
Ai_m	Amplitude of idler in the m-th mode
$F_{mx(y)}$	Amplitude of the forward m-th mode in the x/y polarization state
$B_{nx(y)}$	Amplitude of the backward n-th mode in the x/y polarization state
p	Polarization-related coefficient
L	Fibre length
P_f	Total forward powers
P_b	Total backward powers
c_{mn}^2	Mode content of the LP$_{mn}$ mode
θ_{mn}	Mode phase of the LP$_{mn}$ mode
$E_{reconstructed}$	Reconstructed electric field
C_{mn}	Complex modal coefficients of the LP$_{mn}$ mode
P_{BCB}	BCB power
Ω_{pk}	Frequency separation between the FWM gain peaks and pump frequency
Ω_{B}	FWM Gain bandwidth
ℓ	Topological charge
E_{OUT}	Output state of the correlation filter
E_{HOPS}	Polarization state of the HOPS beam
U_{QWP}	Jones matrix of QWP
U_{QP}	Jones matrix of QP
θ_β	Rotation angles of the QWP2 in the correlation filter
θ_γ	Rotation angles of the q-plate in the correlation filter
I_{int}	Intensity distribution of the interference pattern
E_{target}	Electric field of the target wave
E_{ref}	Electric field of the reference wave
E_{rec}	Recovered electric field
$C_{k(j)}$	Complex modal coefficients for the k(j)-th mode
N	Number of modes
I	Intensity profile
T	Transformation matrix

Chapter 1 Introduction

1.1 Multimode and multicore fibres

An optical fibre is a cylindrical dielectric structure designed to guide light between its two ends. It comprises a core, cladding, and coating. When light is launched into the core, it undergoes total internal reflection at the core-cladding interface, enabling it to propagate through the fibre. Optical fibres were first invented for optical communication purposes. The first low-loss practical optical fibre was produced in the 1970s by Corning Incorporated[1, 2]. This breakthrough was soon followed by the instalment of a first optical telephone communication system using several kilometers of optical fibre by General Telephone and Electronics in 1977[3]. Over the past 40 years, optical fibre technologies have seen tremendous development, driven by the growing demand for high-speed, high-bandwidth, and low-attenuation optical fibre networks for data transmission, modern telecommunications, and internet connectivity[4]. Since the 1980s, significant efforts have been devoted to increasing the data-carrying capacity of a single optical fibre. These efforts include improving fibre materials, fibre structures, manufacturing techniques, and transmission systems[5]. Transmission capacity has been significantly enhanced by multiplexing optical signals in time, wavelength, polarization and phase, exploiting the different wavelengths, polarization states and phases of light[4]. Dense Wavelength Division Multiplexing (DWDM) technology, which involves densely packing multiple wavelengths of light, along with modern telecommunication systems, is capable of transmitting Tb/s through a single fibre[6].To further increase transmission capacity, the concept of Space-Division Multiplexing (SDM) was introduced [4, 6, 7]. SDM leverages multiple spatial channels, such as different spatial modes in few-mode fibres (FMFs) and multimode fibres (MMFs) or different cores in multicore fibres (MCFs).

MMFs have large core diameters and support the propagation of multiple spatial modes within the fibre core. The history of MMFs dates back to the early development of optical fibre technology. Figure 1.1(a) shows the annual number of publications on the topic of multimode fibre from 1980 to 2023. Researchers have shown increasing interest in exploring multimode fibres since 2005, driven by advancements in fibre materials, design, and fabrication techniques. Additionally, the simultaneous propagation of multiple modes enables a variety of novel functions and techniques that extend beyond signal processing and communications. The introduction of MCFs also dates back to the same era of MMFs[8]. MCFs have multiple cores within the same fibre, offering variable core numbers, core diameters, and core distributions. This adds several degrees of freedom in optical fibre technology and its applications. The fabrication of the first multicore fibre – a seven core fibre with an average single core loss of 3dB/km – was reported in 1979 by S. Inao[9]. As shown in Figure 1.1(b), researchers continued to explore and investigate multicore fibres from theoretical, fabrication, and application perspectives over the following decades. With the advancements in SDM techniques in the 2010s[4], MCFs have once again attracted researchers' attention due to their capability and potential to meet the increasing demands for transmission capacity and bandwidth. However, compared with MMFs, as illustrated in Figure 1.1(a), MCFs are still in the early stages of development. They need to overcome a series of technical, standardization, and application challenges to realize their large-scale deployment.

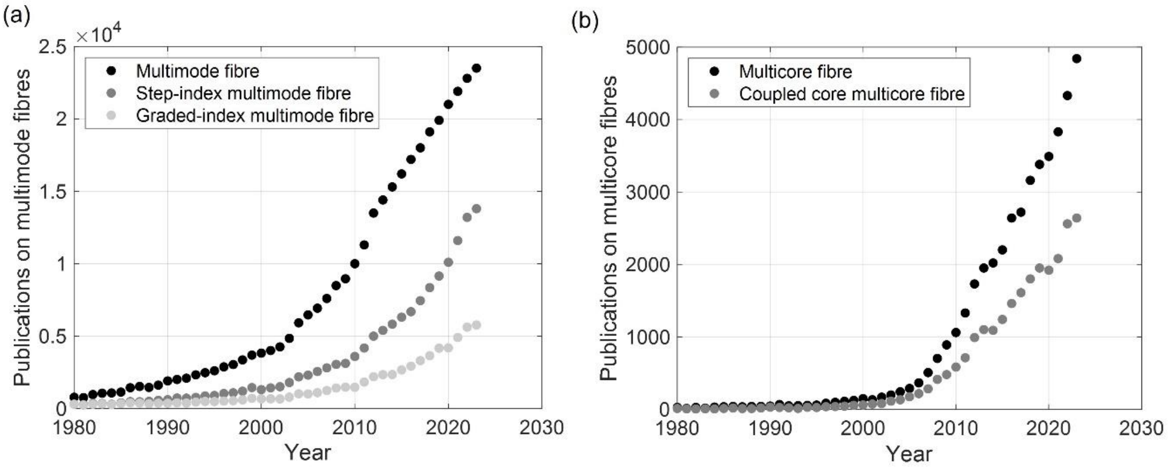

Figure 1.1 Number of publications on the topics of multimode fibres and multicore fibres. (a) Annual publications on multimode fibres, step-index multimode fibres, and graded-index multimode fibres. (b) Annual publications on multicore fibres and coupled-core multicore fibres. Source of data: google scholar.

1.2 Recent progresses on applications of MMFs and MCFs

Optical fibres have become ubiquitous and been utilized in a multitude of applications, including short- and long-distance telecommunications, optical transmissions and sensing, quantum communications, imaging, fibre lasers and amplifiers, light delivery and beam shaping, as well as novel applications based on various nonlinear effects and modal interactions. Over the past few decades, there has been a resurgence of interest in multimode fibres and multicore fibres. This resurgence is primarily driven by the potential and possibilities for rapidly advancing optical fibre techniques and applications. This section will provide a brief introduction to recent progress in the applications of MMFs and MCFs.

1.2.1 Short- and long-distance communications with MMFs and MCFs

Optical fibre communication systems are the backbone of global communication infrastructures. Modern high-capacity communication systems predominantly rely on single-mode fibres (SMFs), which support a transmission capacity limit of around 100 Tb/s within the traditional low-loss spectral window (1530nm to 1610nm) [4, 6]. To further enhance transmission capacity and bandwidth, MMFs and MCFs provide additional spatial channels, but they introduce unique challenges in SDM systems. These challenges include mode coupling, modal dispersion, mode dependent loss, crosstalk between MCF cores, and fibre nonlinearity[10]. To optimize SDM systems, researchers are improving SDM fibres (MMFs and MCFs) with advanced designs to mitigate mode coupling and differential mode delay, developing efficient spatial multiplexers and demultiplexers to ensure minimal loss and crosstalk, and leveraging advanced digital-signal processing techniques to mitigate impairments from mode coupling, modal dispersion, and nonlinear effects[6, 8, 10-12]. Additionally, optimizing multimode and multicore fibre amplifiers to support multiple modes or cores effectively, and conducting extensive modelling and simulation of multimodal, multi-channel information propagation in various types of SDM fibres, are critical steps. SDM fibres include multimode fibres, weakly-coupled multicore fibres, multimode multicore fibres (MMMCFs), and coupled-core multicore fibres (CCMCFs)[10].

Multimode and few-mode fibres have been used in commercial short-reach networks to transport independent signals on multiple modes at the same wavelength. The simultaneous propagation of multiple modes enables high-capacity transmission, with reported capacities ranging from hundreds of Tb/s to 1Pb/s using 3 to 45 fibre modes, as shown in Figure 1.2. To integrate MMFs with modern single-mode fibre communication systems, specialized mode multiplexers are necessary to match the multiple SMFs with the multiple mode patterns of MMFs. Another crucial parameter determining transmission performance is the modal propagation delay, which affects the memory length of the transmission system[8, 10-12]. This is a significant factor limiting current MMFs in long distance transmission. Researchers are working to minimize differential mode delay by optimizing fibre design, using approaches such as graded-index fibres, ring-core fibres, and hollow-core fibres[13]. Additionally, due to the differences in mode-dependent gain and multimode propagation, developing efficient MMF amplifiers remains a challenge for long haul transmission[10].

Weakly coupled MCFs consist of multiple single-mode cores embedded in a common cladding with negligible mode coupling between the cores. The low crosstalk and minimal interference enable a larger transmission capacity and longer transmission distance compared to MMFs. The longest optical fibre transmission to date was achieved using a 12-core fibre, covering a distance of 14350 km at a capacity of 105.1 Tb/s[8].

MMMCFs combine the features of MMFs and weekly coupled MCFs. By incorporating multiple multimode cores, MMMCFs enable denser spatial multiplexing by increasing both the core counts and the mode counts. However, because higher-order modes are not well confined within the fibre core as the fundamental mode, larger core separation is needed to reduce inter-core crosstalk. Reported MMMCFs have cladding diameters larger than SMFs, with the largest exceeding 300 µm[10], potentially limiting their compatibility with modern optical fibre networks. Moreover, utilizing MMMCFs is more complex than using MMFs and MCFs, as both core multiplexing and mode multiplexing must be performed separately. The largest number of spatial channels (core count*mode count) yet reported is 120 with a 12-core 10-mode fibre[14].

CCMCFs feature multiple single-mode cores spaced closely together, resulting in strong crosstalk and coupling between the cores. This strong coupling can beneficially reduce spatial-mode dispersion, consequently shortening the memory length of transmission system[10]. The different coupling conditions between CCMCF cores form mode groups, known as supermodes. Therefore, the light propagation mechanism in CCMCFs is similar to multimode propagation in MMFs, and their transmission performance is also comparable to that of MMFs.

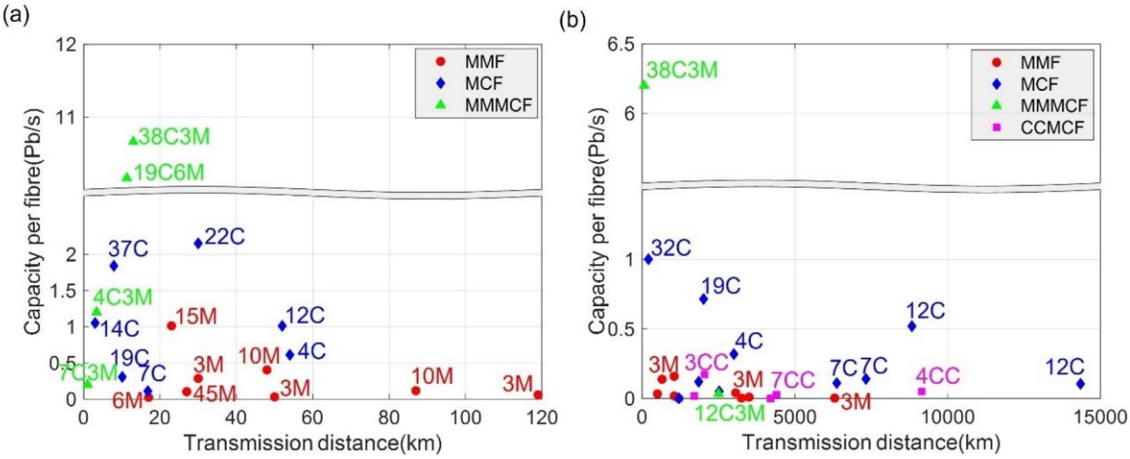

Figure 1.2 Transmission capacity versus transmission distance in MMFs and MCFs[10]. (a) Results for short-distance communications. (b) Results for long-distance communications. Abbreviations: C: core; M: mode; CC: coupled core.

As shown in Figure 1.2, MCFs have the potential to outperform MMFs in high-capacity and long-distance optical transmissions. However, the engineering and commercialization of MCFs for optical communications have not yet been fully realized due to various challenges, including technical complexities, the need for further technological maturity, and high costs[8]. Researchers are focusing on several improvement directions to address these challenges: reducing transmission loss, optimizing MCF structures, developing novel coupling/decoupling devices, and ensuring compatibility and standardization.

1.2.2 Optical sensing with MMFs and MCFs

Fibre optical sensing has undergone tremendous growth in the last few decades due to its unique advantages, including high sensitivity, miniature size, corrosion-resistance, remote sensing capabilities, large scalability, and low maintenance costs. FMFs and MMFs serve as the media for independently and simultaneously measuring multiple sensing parameters in the physical, chemical, and biological fields[15-17]. These parameters include temperature, curvature, refractive index, displacement, and strain. MMF/FMF sensing leverages the differential response of various spatial modes to external environments. For example, the Bragg wavelength of a fibre Bragg grating or Brillouin frequency shift is highly mode-dependent, making it useful for temperature and bending sensing[16]. Additionally, by monitoring the optical attenuation of different modes during propagation in an optical fibre or fibre taper, spatial gas distributions can be measured in environments with extreme temperature and pressure conditions[17]. Multimodal interference in fibre interferometers has also been demonstrated for sensing various physical parameters such as temperature, curvature, and distance[18, 19].

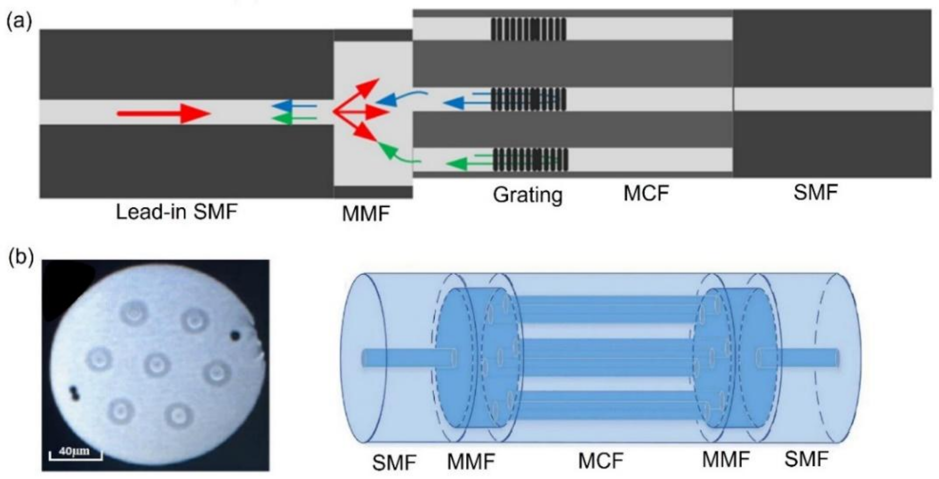

Figure 1.3 Examples of optical fibre sensor structures using MMFs and MCFs[20, 21].

MCFs are ideal platforms for optical sensing due to their unique features, including multi-channel transmission, high integration, spatial flexibility and multifunctionality[8]. They can be used for both point sensing and distributed sensing applications. In MCF point sensing, various interferometers implemented with weakly-coupled MCFs or coupled-core MCFs have been demonstrated for sensing temperature, bending, vibration, and distance[20, 21]. Additionally, MCF distributed sensing utilizes Optical Time Domain Reflectometry (OTDR) or Optical Frequency Domain Reflectometry (OFDR) techniques to achieve efficient sensing at multiple points or along the entire fibre length[8]. By incorporating SMFs, MMFs, MCFs, and fibre gratings, several sensors have been demonstrated for a wide range of applications. Figure 1.3 illustrates two examples of integrated optical fibre sensor structures. In Figure 1.3(a)[20], the structure is designed for bending sensing, featuring an MCF with six identical outer cores and a central core with a lower refractive index. The reflection peak of the Bragg grating inscribed in the central core is separated from the reflection peaks of the other cores, which can be measured by a segment of MMF between the MCF and the lead-in SMF. In Figure 1.3(b)[21], a SMF-MMF-MCF-MMF-SMF structure is designed to form a Mach-Zehnder interferometer for temperature sensing. The MMF serves as a coupler between the SMF and the MCF. The MCF has seven cores with slight refractive index differences between the central core and the surrounding cores, inducing interference between the cores. The change in the interference spectrum is measured to monitor external temperature changes.

1.2.3 Image transmission and imaging through MMFs and MCFs

When an image pattern is projected onto the proximal (input) side of a multimode or multicore fibre, the resulting image at the distal (output) side appears as a speckle pattern. This occurs because the input light couples into multiple fibre modes in MMFs or into multiple fibre cores in MCFs, each travelling with different propagation constants and phases along the fibre length. Highly multimode fibres and densely multicore fibres are typical media for image transmission and imaging[6], necessitating an understanding of the relationship between the optical fields at the proximal and distal sides of the fibre[22, 23].

The principle of image transmission and imaging through MMFs and MCFs involves achieving high-fidelity image transmission or reconstruction at the fibre output by analysing the transmission matrix of the fibres[22-26] or by utilizing speckle correlations[27, 28]. This is illustrated in Figure 1.4. Once a transmission matrix or conversion matrix is determined for a specific transmission fibre, the fibre is calibrated and must remain static. This transmission matrix can then be employed to reconstruct the input image, facilitating image transmission. Additionally, the transmission matrix can be used to control the input wavefront to achieve diffraction-limited imaging, such as in MMF/MCF endoscopy. Various methods have been demonstrated to obtain the transmission matrix of a transmission fibre, including phase conjugation[24], iterative methods, measuring the complex amplitudes corresponding to several input patterns, deep learning approaches[23, 25, 26], and numerical modelling[22].

Conversely, it is also possible to reconstruct the input image from the output speckle pattern using the angular memory effect in MMFs and MCFs[27, 28]. This effect preserves the phase gradients at the fibre input to some extent. For instance, the inherent preservation of phase information during propagation through a multicore fibre[28] allows for widefield imaging of planar objects across a large range of working distances. This can be achieved by computationally analysing a single image of the output speckled intensity pattern.

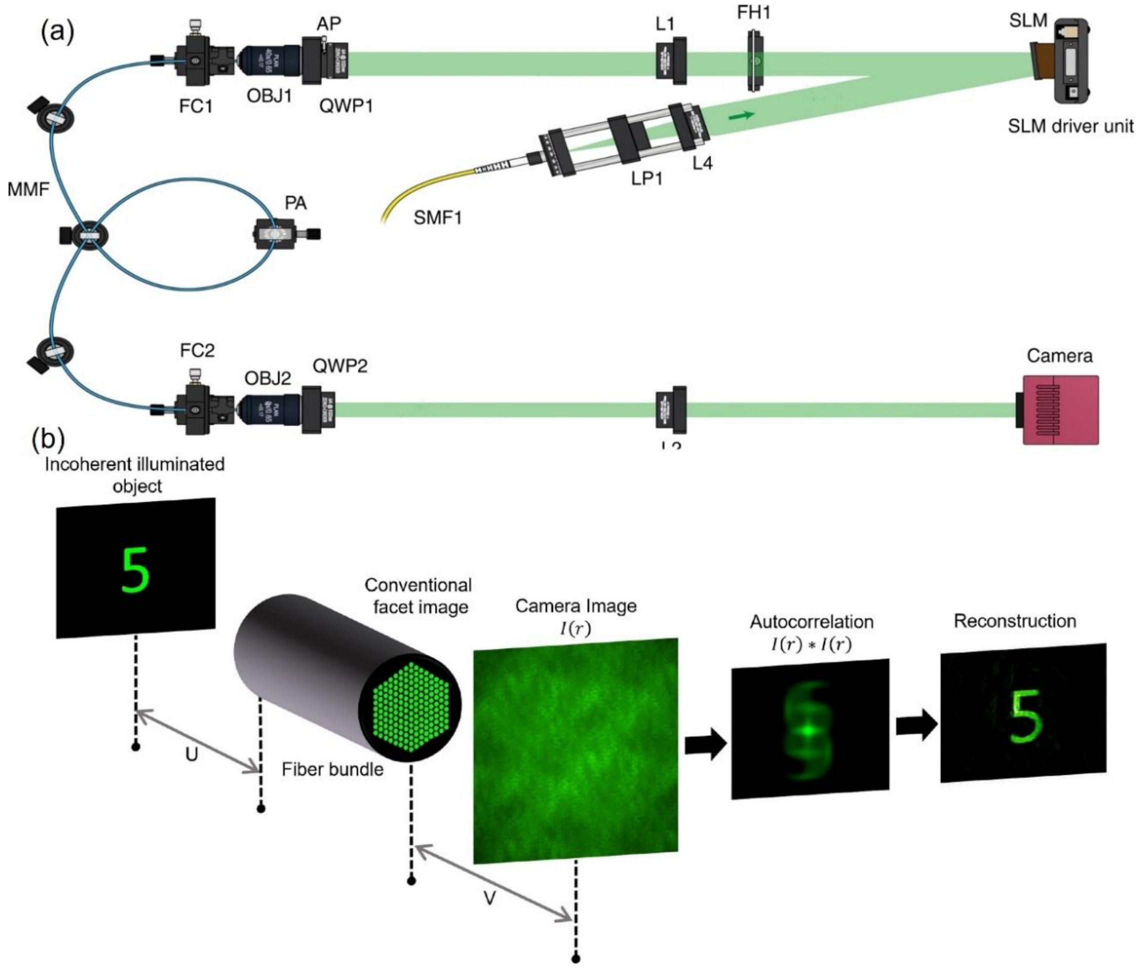

Figure 1.4 Schematics of the experimental setup for (a) image transmission with a MMF[25] and (b) speckle-correlation imaging with an MCF[28].

Despite these successes, the fragility of the measured transmission matrix or the matrix trained by neural networks remains a significant challenge, preventing full optical control of light transmission through MMFs and MCFs[6]. Developing new methods to control light and continuously image through flexible fibres will not only benefit image transmission but also enhance other areas, including optical communications and information processing.

1.2.4 Multimode/Multicore fibre lasers and amplifiers

Fibre lasers have been experiencing significant growth and present a substantial share of the global laser market, thanks to their unique advantages such as power scalability, compact size, high efficiency, and versatility in applications. The large effective modal areas of MMFs and MCFs enable power scaling of fibre lasers[6, 29, 30], enhancing their performance and capacity. Additionally, multimodal and multi-channel properties of these fibres offer diversities in spatial and temporal shapes[31-34], directions, and wavelengths[35, 36] for fibre lasers and amplifiers, broadening their range of applications and functionality.

The optical signal can be amplified in rare earth-doped fibres (also called active fibres), with different emission wavelengths achievable using various dopants[36]. For instance, Yb^{3+}-doped fibre lasers have an emission window of 1050-1120nm, Er^{3+}-doped fibre lasers emit from 1530nm to 1600nm, and Tm^{3+}-doped and Tm^{3+}- Ho^{3+} co-doped fibre lasers have an emission range of 1900-2100nm. The past decade has seen tremendous enhancements in the power scaling of continuous-wave (CW) and pulsed lasers. These advancements are attributed to the rapid development of active fibres, pump diodes, and the power handling capabilities of fibre components such as isolators, combiners, gratings, and coatings[29, 30, 36, 37]. Figure 1.5[36] illustrates the power evolution over the past several years of CW all-fibre lasers and amplifiers operating at wavelengths of ~1μm, ~1.5μm, and ~2μm. The spectrum windows not covered by rare earth-doped fibres can be generated using various nonlinear effects, including Raman Scattering, Four-Wave Mixing (FWM), Self-Phase Modulation (SPM), and supercontinuum generation[33, 35-37].

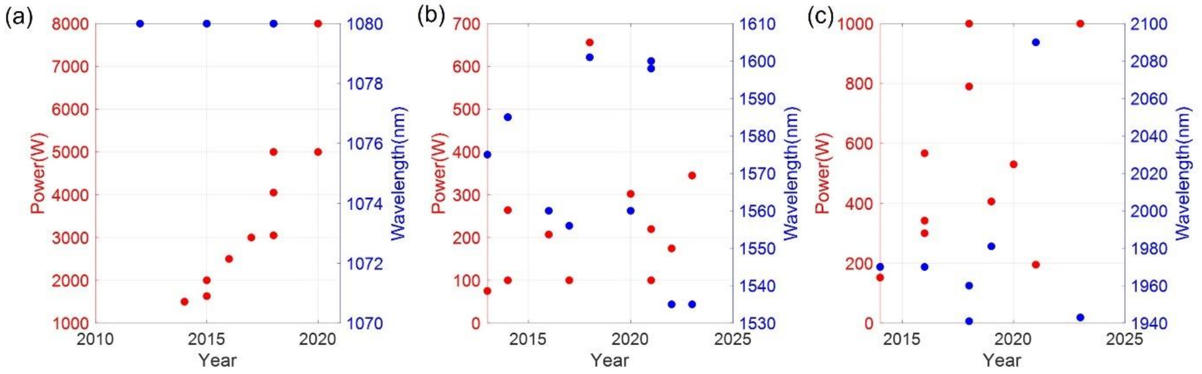

Figure 1.5 Power evolution of CW all-fibre lasers with different rare earth dopants operating at wavelengths of (a) ~1μm, (b) ~1.5μm, and (c) ~2μm[36].

In addition to power scaling through master oscillator power amplifiers (MOPA) and high-power fiber amplifiers, pulsed fibre lasers have seen advancements in pulse energy, operation duration, and pulse generation mechanisms[33, 37]. Recently, MMFs have been introduced into mode-locked fibre lasers, where the multiple spatial (transverse) modes play a crucial role in mode-locking. For instance, using a short segment of MMF as a novel saturable absorber, various ultrafast fibre lasers operating at 1μm, ~1.5μm, and ~2μm have been demonstrated[37]. Another promising method is to achieve spatiotemporal mode-locking (STML) in a fully multimode cavity, where the mode locking of multiple longitudinal and transverse modes is possible[33, 37]. The realization of STML relies on delicate balances between intracavity linear and nonlinear effects, including chromatic and modal dispersion, inter- and intra-modal nonlinearities, spectral and spatial filtering, and cavity gain and loss.

With the advancements in MMF lasers and amplifiers, MCF laser cavities and MCF amplifiers have also been investigated and demonstrated in recent years, utilizing either uncoupled MCFs or coupled-core MCFs[38-40]. Significant progress has been made in power scaling, spectrum extension, and spatiotemporal control of fibre lasers. However, challenges remain in mitigating quantum defects[36], managing heat power generation, and studying the limits of gain media[37]. Once single-aperture power limits are reached, the primary option for further power scaling is beam combination. Parallel fibre laser arrays and uncoupled multicore fibres have been employed to achieve diffraction-limited combination with high power or high energy in both CW and pulsed regimes[41-43]. Researchers have also demonstrated the reconfigurable and controlled generation of structured light beams by exploiting tilted-aperture coherent beam combination[44-46]. By incorporating various technical approaches, including coherent or incoherent combination, linear or nonlinear methods, active or passive techniques, as well as adaptive or deep learning strategies, significant improvements can be expected towards intelligent fibre lasers in both CW and pulsed regimes.

1.2.5 Beam shaping of multimode and multicore fibre lasers

Precisely controlling the distribution of light is crucial for various applications in optics, ranging from microscopy and optical manipulation to spectroscopy and telecommunications[47, 48]. In recent years, beam shaping of multimode and multicore lasers has been demonstrated across various degrees of freedom, including spatial beam shaping and temporal/frequency shaping at different propagation planes. Structured lights with controllable amplitude, phase, and polarization distributions have been successfully generated from multimode and multicore fibre lasers using internal or external methods with laser cavities[45-47, 49-53]. Numerous techniques have been explored to optimize the generated spatial shapes or modes with minimal loss and high distinction. These include traditional diffractive optical elements, modern liquid crystal and metasurface elements, adaptive wavefront shaping methods[54], reconfigurable solutions employing beam-steering devices like digital micro-mirror devices and spatial light modulators[49, 51], coherent combinations of parallel laser arrays or multicore fibre amplifiers[46, 50], and more recently, deep learning-assisted beam shaping solutions[53].

In addition to spatial beam shaping, efforts have been directed towards achieving time or frequency shaping of light, and more recently, the simultaneous manipulation of spatial and temporal properties of light has emerged. By dispersing optical pulses into different frequency components and modulating the amplitude and phase in the frequency domain, temporally shaped output can be obtained through the combination of multiple shaped frequency components[48]. Concepts such as supercontinuum and optical frequency combs generation have emerged in fibre lasers for the extensive spectrum broadening. However, several challenges need to be addressed, including mode instability, nonlinear coupling and dispersion management, multimodal nonlinear effects, as well as specialty fibre design and fabrications[48, 55, 56]. Overall, advancements in fibre lasers and fibre optic technologies are steering laser beam shaping towards real-time, self-organized, spatiotemporal shaping techniques.

1.2.6 Multimodal nonlinear effects in MMFs and MCFs

As previously mentioned, with the power scaling of fibre lasers and advancements in fibre design and fabrication technologies, numerous applications relying on nonlinear optical effects have emerged. Compared to single-mode fibres, multimode and multicore fibres offer diverse phase matching possibilities and mode choices due to their multi-mode and multi-supermode nature. Excitingly, multimodal nonlinear interactions can lead to several new nonlinear effects and phenomena in multimode systems. These include forward Brillouin scattering[57], Kerr beam self-cleaning[58-63], modal selection for Raman scattering[64, 65], broadband parametric amplification[6], optical gratings generated from periodic intermodal beating[66], and the combination of Raman and Kerr effects[6].

Multimode nonlinear systems are evolving along two primary pathways[6]. One approach aims to maximize nonlinear multimode interactions by exploiting the distinct dispersions and mode areas of different spatial modes. The other involves combining linear and nonlinear mode mixing. Despite progress in understanding the complexities of multimode nonlinear dynamics and advancements in specialty fibres and fibre lasers, significant challenges remain. These include achieving low-loss, high-purity, and on-demand excitation of desired spatial modes for various multimode and multicore fibres, as well as developing real-time, broadband mode decomposition approaches[67].

1.3 Motivation and key achievements

As we have reviewed, multimode and multicore fibres present attractive platforms for exploiting complex multimodal interaction dynamics, beneficial across a variety of applications such as telecommunications, transmission, fibre lasers, and sensing. However, understanding and designing multimodal nonlinear optical systems pose significant technical and conceptual challenges. The ability to control light fields with many degrees of freedom is anticipated to be a prominent direction for future advancements in multimode nonlinear systems. With the development of fibre fabrication techniques and power scaling of pulsed fibre lasers, numerous approaches have been demonstrated to achieve mode control and mode conversion in multimode and multicore fibre systems. Incorporated with tremendous advancements in wavefront shaping elements and devices, several methods for arbitrary spatial beam shaping with MMFs and MCFs have been investigated.

The work presented in this thesis contributes to mode control and beam shaping in multimode and multicore fibres by exploring multimode nonlinear dynamics in homemade coupled-core multicore fibres and commercial multimode fibres. The key achievements are listed below:

- Demonstrated mode rejection and control in nonlinear multimode systems. Developed concepts for mode rejection and control by injecting an intense backward control beam into a multimode/multicore fibre. This method effectively rejects specific spatial mode contents (resulting in null content for the rejected mode) and allows precise mode control, driven by multimodal interactions between counter-propagating beams. Efficient rejection and control of linearly-polarized (LP) modes and supermodes in MMFs and MCFs were successfully achieved.
- Provided the demonstration of counter-propagating nonlinear gratings in multimode systems. By adjusting the counter-propagating beams with a substantial power difference, an intense backward multimode beam can generate counter-propagating nonlinear gratings that lead to the mode conversion of a forward low-power signal. Controllable conversion between the LP modes or supermodes in MMFs and MCFs was achieved. Additionally, ultrafast power switching among cores in MCFs was also demonstrated owing to supermode conversion and mixing.
- Investigated parametric amplification dynamics and wavelength conversion in coupled-core multicore fibres. The four-wave mixing between multiple supermodes was numerically estimated and experimentally measured. The Raman scattering in multi-supermode systems was also explored.
- Demonstrated reconfigurable spatial beam shaping with a pulsed multicore fibre amplifier. In parallel with exploring mode control and conversion in a nonlinear manner, arbitrary spatial beam shaping was achieved by coherently combining beamlets from a Yb-doped 6-core MCF amplifier. This includes the reconfigurable generation of the LP modes, cylindrical vector modes, and orbital angular momentum modes.

1.4 Thesis outline

The thesis is organized as follows. Chapter 2 provides a comprehensive review of essential concepts in optical fibres and fibre modes, alongside an exploration of nonlinear processes in multimode light propagation. It begins with an overview of optical fibre parameters and characteristics, followed by introductions of fibre modes and techniques for fibre mode decomposition. Subsequently, the chapter delves into the formulation of coupled multimode nonlinear Schrödinger equations, discussing both intramodal and intermodal nonlinear effects. Finally, it reviews various processes involved in nonlinear spatial control within multimode systems, covering the topics that are highly relevant to this thesis, such as dissipative spatial beam clean-up, Kerr beam self-cleaning, self-organization in multimode gain media, polarization and mode attractors, and the generation of optically induced long period gratings.

Chapter 3 investigates the first proposed concept - mode rejection and control within counter-propagating nonlinear multimode systems. Firstly, the theory and simulations are presented to estimate and validate the mode rejection phenomenon. Secondly, experimental demonstrations elucidate the rejection of the LP modes in various commercially available few-mode fibres, including both polarization-maintaining (PM) fibres such as PM1550-xp, PMHN1, and PM2000, and non-PM isotropic fibres like SMF28. Thirdly, the rejection of supermodes is demonstrated by experiments conducted with homemade coupled-core multicore fibres, specifically a dual-core fibre (DCF) and a tri-core fibre (TCF). To accurately gauge the extent of mode content rejection, quantitative assessments employing intensity-based mode decomposition methods are introduced and implemented.

Chapter 4 delves into the intricacies of counter-propagating nonlinear gratings in multimode and multicore fibres. Initially, the chapter elucidates the dynamics of counter-propagating nonlinear gratings, underpinned by the interaction between a forward probe beam and a backward control beam in multimode systems. However, a substantial power difference exists between the forward probe beam and the backward control beam, thus necessitating a thorough examination of their dynamics through theoretical frameworks and simulations. Subsequently, the chapter explores mode conversion phenomena driven by the counter-propagating nonlinear gratings, specifically focusing on the conversion between the LP modes within PM-FMFs and between supermodes within MCFs, supported by experimental validations. Leveraging the coupled-core architecture of the MCFs, the chapter also elucidates how supermode conversion and mixing facilitate power switching between cores, ultimately demonstrating ultrafast core-to-core power switching in MCFs.

Chapter 5 studies four-wave mixing and wavelength conversion in coupled-core MCFs. The chapter starts with an introduction of the mechanisms of four-wave mixing and Raman scattering in MCFs. Then the estimations of four-wave mixing in several homemade MCFs are presented, accompanied by discussions on fibre design considerations, customized phase-matching conditions, and the impact of Raman scattering. In the end, experimentally measured wavelength and supermode conversions are demonstrated by using DCF, TCF, and fibres with 4 and 7 cores.

Chapter 6 demonstrates reconfigurable spatial beam shaping through coherent beam combination utilizing a 6-core Yb-doped MCF amplifier. The chapter commences by outlining the principle behind coherent beam combination and introduces the active 6-core fibre. By adaptively adjusting the amplitudes and phases injected into the individual MCF cores, the controlled generation of various spatial mode beams is presented in a picosecond pulsed regime, including the LP modes and higher-order Poincaré sphere modes.

Chapter 7 concludes the mode control and beam shaping work presented in this thesis and discusses potential pathways for future work.

Chapter 2 Theory and review of nonlinear spatial control processes in multimode systems

2.1 Introduction

In this chapter, the background knowledge of multimode light propagation in optical fibres is reviewed. Initially, the structure of optical fibres, their characteristics, fibre modes, and laser beam propagation are introduced. Then, the propagation of multimode laser beams in optical fibres is explored using the multimode nonlinear Schrödinger equation (MM-NLSEs). Intramodal and intermodal nonlinear processes are discussed, including single-/multi-mode modulation instability, self- and cross-phase modulation, four-wave mixing, Raman scattering, and the interaction between different nonlinear effects. The corresponding derivations of analytical solutions to the MM-NLSEs are demonstrated. Finally, a review of nonlinear spatial control processes in multimode systems, highly relevant to the topic of this thesis, is presented. These nonlinear processes include dissipative spatial beam clean-up, Kerr beam self-cleaning, beam self-organization in multimode gain media, polarization and mode attractors in counter-propagating beams, and optically induced long period gratings.

2.2 Optical fibres and fibre modes

2.2.1 Optical fibres

Optical fibres have high refractive index cores and lower refractive index claddings, which confine light propagation within the cores through total internal refraction at the core-cladding interface. An additional coating layer with a refractive index lower than the cladding provides mechanical protection. Figure 2.1(a) shows a cross-section image of a step-index single-mode fibre. The core and cladding are typically made of silica glass, and their refractive indices can be increased or decreased by using different dopants, such as germania and fluorine. The coating material is usually a polymer, such as acrylate or silicone. Several parameters that can be adjusted when designing optical fibres, including core diameter, core shape, refractive index profile, multiple layers, and multiple cores. Figure 2.1(b) illustrates the structures of single-mode, multimode, and multicore fibres. SMFs have core diameters of a few micrometres. Even SMFs are not truly single mode, as they can support two degenerate polarization modes with orthogonal polarizations. When polarized light is launched into a conventional SMF, the polarization state is quickly lost after a few metres due to inevitable variations of fibre geometry or external stress. By changing the core shape from circular to asymmetrical, such as elliptical, or by adding additional stress rods, birefringence can be introduced to help maintain the polarization state during propagation.

MMFs (including FMFs) have larger cores that support the simultaneous propagation of multiple spatial modes. These modes propagate at different velocities and travel along different paths due to variations in their effective refractive indices. MCFs have multiple single-mode or multimode cores embedded within a single cladding. When the cores are sufficiently separated, coupling between them is minimized, resulting in weakly-coupled or uncoupled MCFs, which can be treated as a bundle of SMFs. However, as the cores are brought closer together, crosstalk between them increases, leading to coupled-core MCFs. In this configuration, light transfers between cores during propagation, and supermodes are formed with specific amplitude and phase distributions among the cores.

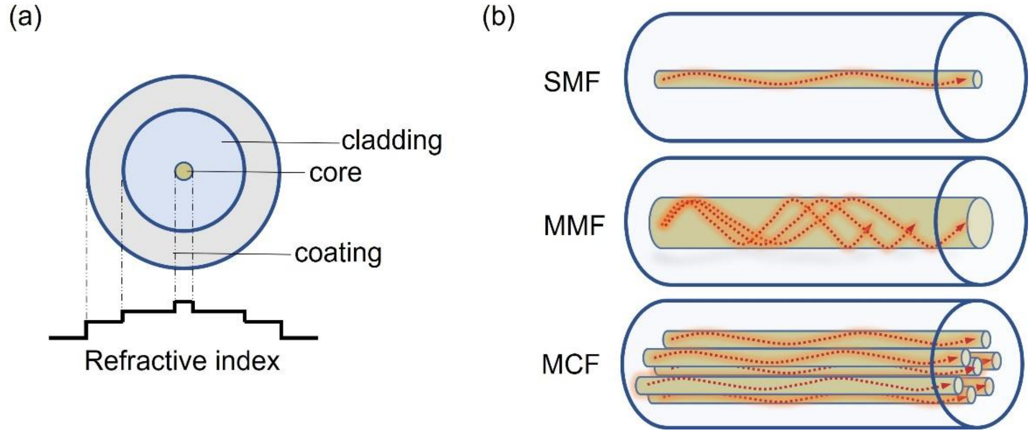

Figure 2.1 (a) Cross section of a single-mode fibre and the refractive index distribution. (b) Structures of single-mode, multimode, and multicore fibres.

One important parameter of optical fibre is the transmission loss of optical signals within the fibre. Fibre loss depends on the wavelength (λ) of light and is influenced by several factors, such as material absorption and Rayleigh scattering[68]. Silica glass has minimal light absorption in the wavelength region of 0.5 to 2 μm, with a minimum loss of ~ 0.2 dB/km at the λ=1.55 μm wavelength. The impurity-induced absorption can also affect fibre loss, such as the OH-absorption peak around λ=1.4 μm. Losses are considerably higher at shorter wavelengths, reaching ~1 dB/km at λ=1 μm and a few dB/km in the visible region, which is due to the intrinsic Rayleigh scattering of fused silica[69]. Rayleigh scattering loss is inversely proportional to wavelength and is dominant at short wavelengths.

Another important parameter of optical fibre is dispersion, which includes chromatic dispersion and mode dispersion. Chromatic dispersion can be further classified into material dispersion and waveguide dispersion[68]. Material dispersion is related to the wavelength or frequency (ω) dependence of the refractive index and can be well approximated by the Sellmeier equation[68]:

$$n^2(\omega) = 1 + \sum_{j=1}^{m} \frac{B_j \omega_j^2}{\omega_j^2 - \omega^2} \tag{2.2.1}$$

where ω=2πc/λ is the angular frequency (with c being the velocity of light in vacuum), ω_j is the resonance frequency and B_j is the strength of the j-th resonance. In optical fibres, the parameters ω_j and B_j are obtained experimentally with m=3 by fitting the measured dispersion curves to Eq.(2.2.1). Material dispersion plays a critical role in the propagation of short optical pulses. Its effects can be understood by expanding the mode propagation constant (β) in a Taylor series around the frequency ω_0, where the pulse spectrum is centred:

$$\beta(\omega) = n(\omega)\frac{\omega}{c} = \sum_{k=0}^{K} \frac{1}{k!}\beta_k(\omega - \omega_0)^k \tag{2.2.2}$$

where $\beta_k = \left(\frac{d^k\beta}{d\omega^k}\right)_{\omega=\omega_0}$ and k=0,1,2,3,..., which is often referred to as the k-th order dispersion parameter. The first order dispersion (β_1) is the inverse of the group velocity (v_g), which is the speed at which the envelope of an optical pulse travels:

$$\beta_1 = \frac{1}{c}\left(n + \omega\frac{dn}{d\omega}\right) = \frac{n_g}{c} = \frac{1}{v_g} \tag{2.2.3}$$

where n_g is the group index. The second order dispersion (β_2) is the group velocity dispersion, which represents the frequency derivative of β_1 and is related to pulse distortion and reshaping during propagation.

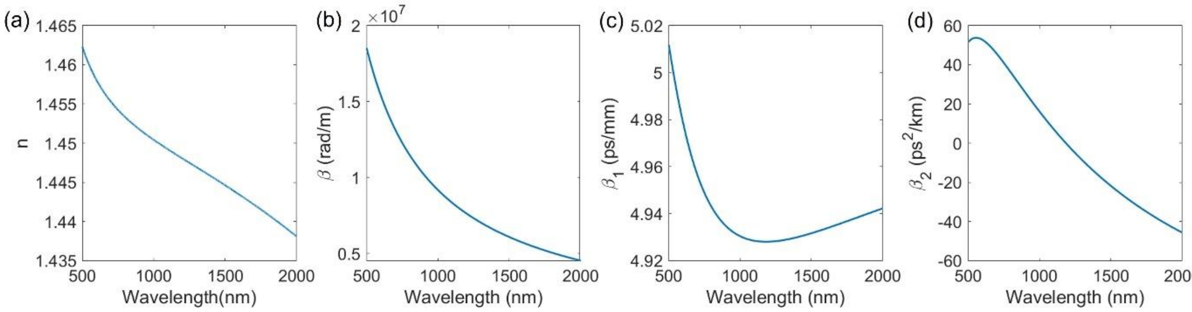

Figure 2.2 (a) Variation of refractive index n with wavelength for silica glass. And the (b) propagation constant of fundamental mode, (c) β_1, (d) β_2, as a function of wavelength for a silica fibre (a=4.1 μm, Δn=0.0052).

Differently from plane waves, light experiences core confinement in an optical fibre, resulting in waveguide dispersion that must be added to the material dispersion to determine the total chromatic dispersion. Waveguide dispersion is influenced by fibre geometry, such as core radius (a) and core-cladding index difference (Δn). Figure 2.2 illustrates the variation of dispersion parameters with wavelength for a step-index silica fibre. Figure 2.2(a) depicts the refractive index variation of fused silica as described by Eq. (2.2.1). Figure 2.2(b)-(d) show the parameters β, β_1, and β_2 for the fundamental mode (LP$_{01}$ mode) that can propagate in this fibre, which can be computed using a finite-element-method software, such as Comsol Multiphysics. As Figure 2.2(d) demonstrates, a notable feature for β_2 is its vanishing at λ=~1.3 μm, known as the zero-dispersion wavelength. In the region shorter than this wavelength, $\beta_2>0$, indicating normal dispersion in the fibre, whereas in the longer wavelength region, the fibre exhibits anomalous dispersion. This implies that longer-wavelength pulses travel slower in anomalous dispersion region, contrasting with the behaviour in the normal dispersion.

In addition to chromatic dispersion, mode dispersion also needs to be considered in multimode fibres. This encompasses polarization-mode dispersion and intermodal dispersion. Because the propagation constants of various polarization modes or spatial modes differ, different modes travel at different velocities, resulting in pulse broadening. By combining chromatic dispersion, mode dispersion, and fibre nonlinearity, a range of nonlinear effects can be observed, which will be discussed in the subsequent sections.

2.2.2 Fibre modes and mode decomposition

Light propagates in optical fibres as a combination of fibre modes. To understand light propagation and fibre modes, it is necessary to consider the theory of the electromagnetic wave equation in dispersive nonlinear media. Starting from Maxwell's equations, the wave equation can be derived[68]:

$$\nabla^2 \boldsymbol{E}(\boldsymbol{r},t) - \frac{1}{c^2}\frac{\partial^2 \boldsymbol{E}(\boldsymbol{r},t)}{\partial t^2} = \frac{1}{\varepsilon_0 c^2}\frac{\partial^2 \boldsymbol{P_L}(\boldsymbol{r},t)}{\partial t^2} + \frac{1}{\varepsilon_0 c^2}\frac{\partial^2 \boldsymbol{P_{NL}}(\boldsymbol{r},t)}{\partial t^2} \tag{2.2.4}$$

where $\boldsymbol{r}$ and t denote the spatial coordinates and time, respectively, ε_0 is the vacuum permittivity, $\boldsymbol{E}$ is the electric field, and $\boldsymbol{P_L}$ and $\boldsymbol{P_{NL}}$ are the linear and nonlinear parts of the induced polarization related to $\boldsymbol{E}$. After taking the Fourier transform of Eq. (2.2.4), it takes the form[70]:

$$\nabla^2 \widetilde{\boldsymbol{E}}(\boldsymbol{r},\omega) + n^2(\boldsymbol{r},\omega)\frac{\omega^2}{c^2}\widetilde{\boldsymbol{E}}(\boldsymbol{r},\omega) = -\frac{\omega^2}{\varepsilon_0 c^2}\widetilde{\boldsymbol{P}}_{\boldsymbol{NL}}(\boldsymbol{r},\omega) \tag{2.2.5}$$

where n is the linear part of the refractive index and $\widetilde{\boldsymbol{E}}$ represents the Fourier transform of the electric field. $\widetilde{\boldsymbol{E}}$ can be expressed as the summation of all the electric field components, assuming that the polarization state is maintained inside the fibre:

$$\widetilde{\boldsymbol{E}}(\boldsymbol{r},\omega) = \sum\nolimits_m \hat{\boldsymbol{e}}_m M_m(x,y,\omega)\tilde{B}_m(z,\omega)exp[i\beta_m(\omega)z] \tag{2.2.6}$$

where $\hat{\boldsymbol{e}}_m$ is the polarization state of a specific mode m, M_m governs its transverse shape, $\tilde{B}_m$ represents the amplitude of this mode, and β_m is the corresponding propagation constant. The summation typically includes only the guided modes in multimode fibres. This expression describes how each mode m contributes to the overall electric field in the fibre, considering its amplitude, polarization, transverse shape, and propagation constant.

By neglecting the nonlinear contribution ($\boldsymbol{P_{NL}}$=0), the remaining part of Eq. (2.2.5) reduces to the Helmholtz equation, whose solution $\widetilde{\boldsymbol{E}}$ represents the guided modes (eigenmodes) of the fibre. The Helmholtz equation can be solved using various numerical methods or analytical techniques, such as the finite element method, finite difference method, and approximate analytical methods. For standard single-core step-index fibres, the spatial distributions $M_m(x,y,\omega)$ can be obtained by rewriting the Helmholtz equation in cylindrical coordinates[68]. The solutions can be classified into four types of fibre vector modes: HE_{nm}, EH_{nm}, TE_{0m}, and TM_{0m} modes. An alternative classification known as the LP modes can be constructed by combining different vector modes. For instance, the LP_{01} mode corresponds to the HE_{11} mode, and the LP_{11} mode is the combination of TE_{01}, TM_{01}, and HE_{21} modes. Calculating guided modes is more convenient using finite-element-method software, such as the aforementioned Comsol Multiphysics, especially for fibres with higher mode counts, complex index distributions, or complex geometries like multicore fibres.

In a MMF or a coupled-core MCF, multiple spatial modes propagate with random amplitudes and phases due to mode coupling, mode competition, and differential modal gain. Assuming that all the spatial modes are in the same polarization state and have a single frequency, Eq. (2.2.6) suggests that the transverse distribution of the electric field in a fibre can be represented by a linear combination of eigenmodes due to modal orthogonality[67]:

$$M(x,y) = \sum\nolimits_{m} c_m exp(i\theta_m) M_m(x,y) \tag{2.2.7}$$

where the c_m^2 and θ_m represent the relative mode content (relative power in the mode) and relative phase for the m-th eigenmode, respectively. M and M_m denote the transverse mode distribution of the total electric field and the m-th mode, respectively. In a multimode system, M tends to change randomly when perturbation exists or the system is under instable state (for example, the transverse mode instability in high power multimode fibre systems[71]). Analysing the power and phase of different modes is useful and necessary for a complete description of multimode beam shapes, a process known as mode decomposition (MD). MD aims to obtain the parameters c_m and θ_m given the knowledge of M_m for a specific fibre at the output. Numerous methods for mode decomposition have been demonstrated, including interference methods that measure the complex amplitude M[72, 73], numerical methods based on intensity measurements($|M|^2$)[67, 74, 75], and machine learning methods[76]. In the later chapters, demonstrations of mode decomposition based on intensity measurements are introduced for MMFs and MCFs.

2.3 Nonlinear processes in multimode laser beam propagation

2.3.1 Multimode nonlinear Schrödinger equations

To study the nonlinear processes in multimode fibres, the nonlinear contribution $\boldsymbol{P_{NL}}$ needs to be considered in the wave equation Eq. (2.2.5). By substituting the electric field from Eq. (2.2.6) into the wave equation, and under the assumption of slowly varying amplitude with respect to *z* while neglecting the second derivative with respect to *z*, the following equations can be obtained:

$$\nabla_T^2 M_m(x,y,\omega) + n^2(x,y,\omega)\frac{\omega^2}{c^2} M_m(x,y,\omega) = \beta_m^2 M_m^2(x,y,\omega) \tag{2.3.1}$$

where ∇_T^2 denotes the transverse part of the Laplace operator. Eq. (2.3.1) determines the transverse mode shape and the propagation constant β_m of each mode.

$$\sum\nolimits_m 2i\beta_m \hat{\boldsymbol{e}}_m \frac{\partial \tilde{B}_m}{\partial z} M_m(x,y,\omega) e^{i\beta_m z} = -\frac{\omega^2}{\epsilon_0 c^2}\tilde{\boldsymbol{P}}_{NL}(\boldsymbol{r},\omega) \tag{2.3.2}$$

Eq. (2.3.2) describes the evolution of the amplitude $\tilde{B}_m$ of the *m*-th mode as it propagates along the *z* direction. By multiplying Eq. (2.3.2) with M_m* and integrating over the transverse plane, the amplitude of the *m*-th mode satisfies the following equation:

$$\frac{\partial \tilde{B}_m}{\partial z} = \frac{i\omega e^{-i\beta_m z}}{2\epsilon_0 c\bar{n}_m}\iint \hat{\boldsymbol{e}}_m M_m^*(x,y,\omega)\tilde{\boldsymbol{P}}_{NL}(\boldsymbol{r},\omega)\,dxdy \tag{2.3.3}$$

where the orthogonality relation between modes ($\iint M_m^* M_n\,dxdy = \delta_{mn}$, $\delta_{mn} = 0$ when $m \neq n$, $\delta_{mn} = 1$ when $m=n$) is applied and $\beta_m = \bar{n}_m\omega/c$ with the effective mode refractive index $\bar{n}_m$. By defining a slowly varying function[68],

$$A_m(z,t) = \int_{-\infty}^{\infty}\tilde{B}_m(z,\omega)e^{i[(\beta_m-\beta_{0m})z-(\omega-\omega_0)t]}d(\omega-\omega_0) \tag{2.3.4}$$

where β_m is the propagation constant of the *m*-th mode, β_{0m} is its value at the carrier frequency ω_0(see Eq. (2.2.2)). By calculating the partial derivative of $A_m(z,t)$ and expanding β_m in a Taylor series around the frequency ω_0, after some algebra, one can obtain the following time-domain amplitude evolution equation[77]:

$$\frac{\partial A_m}{\partial z} - i\sum_{k=1}^{\infty}\frac{i^k\beta_{km}}{k!}\frac{\partial^k A_m}{\partial t^k} = \frac{i\omega_0 e^{-i(\beta_{0m}z-\omega_0 t)}}{2\epsilon_0 c\bar{n}_m}\iint \hat{\boldsymbol{e}}_m M_m^*(x,y)\boldsymbol{P}_{NL}(\boldsymbol{r},t)\,dxdy \tag{2.3.5}$$

where $\beta_{km}=(\partial^k\beta_m/\partial\omega^k)_{\omega=\omega_0}$, is the *k*-th order dispersion parameter for the *m*-th mode of the fibre at frequency ω_0. The right-hand side of this equation includes all the nonlinear effects.

To specify the nonlinear polarization $\boldsymbol{P_{NL}}$ on the right-hand side of Eq. (2.3.5), the Kerr and Raman contributions are considered. The nonlinear polarization can be written in the form[68]:

$$\begin{aligned}\boldsymbol{P_{NL}}(\boldsymbol{r},t) = \frac{3\epsilon_0}{4}\chi_K^{(3)} \vdots\, \boldsymbol{E}(\boldsymbol{r},t)\boldsymbol{E}(\boldsymbol{r},t)\boldsymbol{E}(\boldsymbol{r},t) + \frac{3\epsilon_0}{4}\chi_R^{(3)} \\ \vdots\, \boldsymbol{E}(\boldsymbol{r},t)\int_{-\infty}^{t} h_R(t-\tau)\,\boldsymbol{E}(\boldsymbol{r},\tau)\boldsymbol{E}(\boldsymbol{r},\tau)d\tau\end{aligned} \tag{2.3.6}$$

where $\chi_K^{(3)}$ and $\chi_R^{(3)}$ represent the 3rd order nonlinear susceptibility related to the Kerr and Raman nonlinearities, respectively. The nonlinear polarization $\boldsymbol{P_{NL}}$ is a tensor product of the electric fields, and h_R is the Raman response function. In a simple case without the Raman contribution, the last term involving h_R can be neglected. Since the mode profile F_m does not change significantly over the spectral bandwidth of the electric field, $M_m(x,y,\omega)$ can be approximated by its value at the carrier frequency ω_0, denoted as $M_m(x,y,\omega_0)$. By substituting the ansatz:

$$\boldsymbol{E}(\boldsymbol{r},t) = \sum\nolimits_m \hat{\boldsymbol{e}}_m M_m(x,y,\omega_0)A_m(z,t)\mathrm{e}^{i(\beta_{0m}z-\omega_0 t)} \tag{2.3.7}$$

through the Eq. (2.3.6) into the Eq. (2.3.5), and retaining only the terms that oscillate at the carrier frequency ω_0, the multimode nonlinear Schrödinger equations (MM-NLSEs) for the m-th mode can be derived[68]:

$$\begin{aligned}&\frac{\partial A_m}{\partial z} - i\sum_{k=1}^{\infty}\frac{i^k\beta_{km}}{k!}\frac{\partial^k A_m}{\partial t^k} \\ &\quad = i\gamma(1-f_R)\sum_n\sum_p\sum_q\left[f_{mnpq}\,A_nA_p^*A_q e^{i\Delta\beta_{mnpq}z}\right] \\ &\quad + i\gamma f_R A_m\int_{-\infty}^{t} h_R(t-\tau)\left[f_{mmmm}|A_m(z,\tau)|^2 + \sum_{k\neq m} f_{mmkk}|A_k(z,\tau)|^2\right]d\tau \\ &\quad + \sum_{k\neq m} j\gamma f_R A_k\int_{-\infty}^{t} f_{mmkk}h_R(t-\tau)A_m(z,\tau)A_k^*(z,\tau)\,d\tau\end{aligned} \tag{2.3.8}$$

where the nonlinear parameter $\gamma = \frac{3\omega_0\chi^{(3)}}{8c\bar{n}_m A_{eff}}$ is defined using the effective area $A_{eff} = \frac{\left(\iint|M_1(x,y)|^2dxdy\right)^2}{\iint|M_1(x,y)|^4dxdy}$ of the fundamental mode m=1, The term f_R represents the fractional contribution of the delayed Raman response to the nonlinear polarization and typically has a value of ~0.18. The triple sum extends over the number of modes supported by the fibre. The phase mismatch $\Delta\beta$ is defined as:

$$\Delta\beta_{mnpq} = \beta_{0n} - \beta_{0m} + \beta_{0q} - \beta_{0p} \tag{2.3.9}$$

The time-dependent terms on the left-hand side of Eq. (2.3.8) represent the dispersion effects. The right-hand side of Eq. (2.3.8) includes all the intramodal and intermodal nonlinear effects that are related to the Kerr nonlinearity and Raman scattering. The intermodal overlap factor, determining the relative strength of various intermodal processes, is defined as[68]:

$$f_{mnpq} = A_{eff}\frac{\iint M_m^* M_n M_p^* M_q\, dxdy}{\sqrt{\left(\iint M_m^* M_m\, dxdy\right)\left(\iint M_n^* M_n\, dxdy\right)\left(\iint M_p^* M_p\, dxdy\right)\left(\iint M_q^* M_q\, dxdy\right)}} \tag{2.3.10}$$

For instance, in the simple case of a co-polarized bimodal beam, where only two modes (*m*=1 and *m*=2) are considered, the MM-NLSE can be written as:

$$\begin{aligned}
&\frac{\partial A_1}{\partial z} - i\sum_{k=1}^{\infty}\frac{i^k\beta_{k1}}{k!}\frac{\partial^k A_1}{\partial t^k} \\
&\qquad = i\gamma(1-f_R)\left[f_{11}A_1A_1^*A_1 + 2f_{12}A_2A_2^*A_1 + f_{12}A_2A_1^*A_2e^{i\Delta\beta_{12}z}\right] \\
&\qquad + i\gamma f_R A_1\int_{-\infty}^{t} h_R(t-\tau)\,[f_{11}|A_1(z,\tau)|^2 + f_{12}|A_2(z,\tau)|^2]d\tau \\
&\qquad + j\gamma f_R A_2\int_{-\infty}^{t} f_{12}h_R(t-\tau)A_1(z,\tau)A_2^*(z,\tau)\,d\tau
\end{aligned} \tag{2.3.11}$$

$$\begin{aligned}
&\frac{\partial A_2}{\partial z} - i\sum_{k=1}^{\infty}\frac{i^k\beta_{k2}}{k!}\frac{\partial^k A_2}{\partial t^k} \\
&\qquad = i\gamma(1-f_R)\left[f_{22}A_2A_2^*A_2 + 2f_{21}A_1A_1^*A_2 + f_{21}A_1A_2^*A_1e^{-i\Delta\beta_{12}z}\right] \\
&\qquad + i\gamma f_R A_2\int_{-\infty}^{t} h_R(t-\tau)\,[f_{22}|A_2(z,\tau)|^2 + f_{21}|A_1(z,\tau)|^2]d\tau \\
&\qquad + j\gamma f_R A_1\int_{-\infty}^{t} f_{21}h_R(t-\tau)A_2(z,\tau)A_1^*(z,\tau)\,d\tau
\end{aligned} \tag{2.3.12}$$

where $f_{11}=f_{1111}$, $f_{22}=f_{2222}$, $f_{12}= f_{21}=f_{1122}=f_{2211}=f_{1212}=f_{2121}$, and $\Delta\beta_{12}=2(\beta_{02}-\beta_{01})$ is the difference between the propagation constants of modes 1 and 2. The right-hand side of these two equations includes various intramodal and intermodal nonlinear effects. The first term accounts for the self-phase modulation (SPM), cross-phase modulation (XPM), and four-wave mixing (FWM). These effects arise from the Kerr nonlinearity, leading to changes in the phase and amplitude of the modes due to the intensity-dependent refractive index. The second term describes contributions to the SPM and XPM induced by Raman scattering, where molecular vibrations in the fibre medium generate additional phase modulation and coupling between the modes. The last term represents Raman amplification, where energy exchange occurs within the modes. These nonlinear interaction processes are fundamental in understanding the complex dynamics of multimode optical fibres and will be further elucidated in subsequent sections.

2.3.2 Intramodal and intermodal nonlinear effects

The response of optical fibres to light becomes nonlinear under intense electromagnetic fields. This nonlinear response arises from the anharmonic motion of bound electrons when exposed to an optical field. In silica (SiO_2) fibres, which are symmetric molecules, the 2nd-order nonlinear effects are absent. Thus, the lowest order nonlinear effects present in optical fibres are the 3rd-order nonlinearities, which includes two types of nonlinear processes. One is the non-dissipative processes, where no energy is exchanged between the electric field and the optical fibre, including SPM, XPM, third-harmonic generation (THG), and FWM. On the contrary, the other type of nonlinear responses is dissipative, where some of the energy from the electric field is transferred to the optical fibre, including the stimulated Raman scattering (SRS) and stimulated Brillouin scattering (SBS).

SPM is an intramodal process where an electric field experiences a self-induced phase shift as it propagates along optical fibres. This nonlinear phase shift is proportional to the intensity of the electric field. In a multimode fibre, SPM occurs due to interactions between electric fields of the same mode and frequency. A direct consequence of SPM is the spectral broadening of optical pulses. In contrast, XPM is an intermodal nonlinear phase shift process. Here, an electric field undergoes a nonlinear phase shift induced by another electric field with a different frequency, direction, polarization state, or spatial mode. The phase shift due to XPM is proportional to the intensity of the participating electric fields. XPM can result in an asymmetric spectral broadening of optical pulses[68].

THG and FWM involve the generation of new frequencies and require specific phase-matching conditions, determined by the propagation constant differences between the electric fields. THG refers to the process where three photons at frequency ω transfer their energy to a single photon at frequency 3ω. For efficient THG, the phase-matching condition must be satisfied, which typically is challenging in optical fibres. Consequently, THG is often neglected in practical applications such as those described in Eq. (2.3.8). FWM is a parametric process where two photons at frequencies ω_{p1} and ω_{p2} interact to generate two new photons at frequencies ω_s and ω_i. The relationship between these frequencies is given by:

$$\omega_{p1} + \omega_{p2} = \omega_s + \omega_i \tag{2.3.13}$$

The donating frequencies ω_{p1} and ω_{p2} in FWM are typically called pumps. The new frequency fields generated by this process are referred to as the low-frequency Stokes wave (ω_s) and the high-frequency anti-Stokes wave (ω_i), often referred to as the signal and idler waves, respectively. Another phenomenon related to FWM is modulation instability (MI), which manifests as the exponential growth of weak perturbations imposed on a CW state during propagation[68, 78]. This growth can be understood through FWM processes involving the perturbation waves and the pump CW wave. As the perturbation waves interact with the pump wave, energy exchange occurs, leading to the amplification of these perturbations. This interaction results in the exponential growth characteristic of MI.

SBS and SRS are related to vibrational excitation modes of silica. Acoustic phonons participate in SBS, whereas optical phonons are involved in SRS. Fundamentally, these processes involve the annihilation of a photon, which creates a photon at a lower frequency (Stokes wave) and a phonon with the appropriate energy and momentum[68]. In optical fibres, SBS typically occurs in the backward direction relative to the incident wave, with a frequency shift of ~10 GHz and a bandwidth of ~100 MHz, whereas SRS occurs along the propagation of the incident wave and spans a wide bandwidth of ~ 40THz, with peak conversion occurring at ~ 13.1 THz from the incident wave[68]. It is important to note that SBS and SRS are temporally delayed processes, unlike instantaneous processes such as SPM, XPM, THG, and FWM. The delayed nature of SBS and SRS stems from the time required for the phonon population to build up and participate in the scattering process.

This thesis focuses on the nonlinear interactions in multimode systems, thus both intramodal and intermodal nonlinear processes need to be considered simultaneously. Since SBS can be neglected when using optical pulses with durations of hundreds of picoseconds, this section introduces FWM and Raman scattering (which has a response time of ~0.1 ps) by solving the MM-NLSEs (see Eq. (2.3.8)). There are no direct general analytical solutions to the MM-NLSEs; however, they can be solved via several numerical methods, with the split-step Fourier method [68] being extensively used. This method is based on the assumption that dispersion and nonlinear effects act independently over a short propagation distance *dz* in fibres. To describe light propagation along fibres, the fibre length is divided into multiple *dz* segments, within which the dispersive and nonlinear steps are implemented separately. Additionally, analytical solutions of the MM-NLSEs can also be derived under certain conditions, as demonstrated by Eqs. (2.3.21) to (2.3.31). Considering a multimode beam oscillating at frequencies ω_p, ω_s, and ω_i, where the two pumps are at the same frequency ($\omega_{p1}= \omega_{p2}= \omega_p$), known as degenerate FWM, the electric field is in a fixed polarization state and can be defined as:

$$\begin{aligned} E(r,t) = \sum\nolimits_m & M_m(x,y,\omega_p)Ap_m(z,t)exp\left[j\left(\beta^{(m,\omega_p)}z - \omega_p t\right)\right] \\ & + M_m(x,y,\omega_s)As_m(z,t)exp\left[j\left(\beta^{(m,\omega_s)}z - \omega_s t\right)\right] \\ & + M_m(x,y,\omega_i)Ai_m(z,t)exp\left[j\left(\beta^{(m,\omega_i)}z - \omega_i t\right)\right] \end{aligned} \qquad (2.3.14)$$

where $\beta^{(m,\omega_n)}$ denotes the propagation constant of the m-th mode at the frequency ω_n(n=p, s, i), M_m is the modal distribution of the m-th mode, and An_m(n=p, s, i) represents the amplitude of the pump, signal and idler in the m-th mode. By substituting Eq. (2.3.14) into the wave equation Eq. (2.2.4) and then following the same approach introduced in section 2.3.1, the following coupled-amplitude equations are obtained, which include both the Kerr (SPM, XPM, and FWM) and Raman nonlinearities:

$$\begin{aligned}\frac{\partial Ap_m}{\partial z} &= j\gamma(1-f_R)\left[f_{mm}Ap_m|Ap_m|^2 + \sum_{k\neq m} 2f_{mk}Ap_m|Ap_k|^2\right] \\ &\quad + j\gamma f_R Ap_m \int_{-\infty}^{t} h_R(t-\tau)\left[f_{mm}|Ap_m(z,\tau)|^2 + \sum_{k\neq m} f_{mk}|Ap_k(z,\tau)|^2\right]d\tau \\ &\quad + \sum_{k\neq m} j\gamma f_R Ap_k \int_{-\infty}^{t} f_{mk}h_R(t-\tau)Ap_m(z,\tau)Ap_k^*(z,\tau)\,d\tau\end{aligned} \tag{2.3.15}$$

$$\frac{\partial As_m}{\partial z} = j\gamma(1-f_R)K + j\gamma f_R R \tag{2.3.16}$$

$$\begin{aligned}K = \Bigg[& 2f_{mm}As_m|Ap_m|^2 + \sum_{k\neq m} 2f_{mk}As_m|Ap_k|^2 + \sum_{k\neq m} 2f_{mk}Ap_m Ai_k^* Ap_k e^{-j\left(\Delta\beta_m^{(s,p)}+\Delta\beta_k^{(i,p)}\right)z} \\ & + f_{mm}Ap_m Ai_m^* Ap_m e^{-j\left(\Delta\beta_m^{(s,p)}+\Delta\beta_m^{(i,p)}\right)z} + \sum_{k\neq m} 2f_{mk}Ap_m Ap_k^* As_k e^{-j\left(\Delta\beta_m^{(s,p)}-\Delta\beta_k^{(s,p)}\right)z}\Bigg]\end{aligned} \tag{2.3.17}$$

$$\begin{aligned}R = As_m &\int_{-\infty}^{t} h_R(t-\tau)\left[f_{mm}|Ap_m(z,\tau)|^2 + \sum_{m\neq k} f_{mk}|Ap_k(z,\tau)|^2\right]d\tau \\ & + Ap_m \int_{-\infty}^{t} h_R(t-\tau)f_{mm}As_m(z,\tau)Ap_m^*(z,\tau)\,exp\left[j\left(\omega_p-\omega_s\right)(\tau-t)\right]d\tau \\ & + \sum_{k\neq m} Ap_k \int_{-\infty}^{t} h_R(t-\tau)f_{mk}As_m(z,\tau)Ap_k^*(z,\tau)\,exp\left[j\left(\omega_p-\omega_s\right)(\tau-t)\right]d\tau \\ & + \sum_{k\neq m} Ap_m \int_{-\infty}^{t} f_{mk}h_R(t-\tau)Ap_k(z,\tau)Ai_k^*(z,\tau)\,e^{-j\left(\Delta\beta_m^{(s,p)}+\Delta\beta_k^{(i,p)}\right)z} exp\left[j\left(\omega_i-\omega_p\right)(\tau-t)\right]d\tau \\ & + \sum_{k\neq m} Ap_k \int_{-\infty}^{t} f_{mk}h_R(t-\tau)Ap_m(z,\tau)Ai_k^*(z,\tau)\,e^{-j\left(\Delta\beta_m^{(s,p)}+\Delta\beta_k^{(i,p)}\right)z} exp\left[j\left(\omega_i-\omega_p\right)(\tau-t)\right]d\tau \\ & + Ap_m \int_{-\infty}^{t} f_{mm}h_R(t-\tau)Ap_m(z,\tau)Ai_m^*(z,\tau)\,e^{-j\left(\Delta\beta_m^{(s,p)}+\Delta\beta_m^{(i,p)}\right)z} exp\left[j\left(\omega_i-\omega_p\right)(\tau-t)\right]d\tau \\ & + \sum_{k\neq m} Ap_m \int_{-\infty}^{t} f_{mk}h_R(t-\tau)Ap_k^*(z,\tau)As_k(z,\tau)e^{-j\left(\Delta\beta_m^{(s,p)}-\Delta\beta_k^{(s,p)}\right)z}\,exp\left[j\left(\omega_p-\omega_s\right)(\tau-t)\right]d\tau \\ & + \sum_{k\neq m} As_k \int_{-\infty}^{t} f_{mk}h_R(t-\tau)Ap_k^*(z,\tau)Ap_m(z,\tau)e^{-j\left(\Delta\beta_m^{(s,p)}-\Delta\beta_k^{(s,p)}\right)z}\,d\tau\end{aligned} \tag{2.3.18}$$

where rapidly oscillating terms are neglected (they average out to 0), and the signal and idler amplitudes are much weaker than the pump amplitude (|*Ap*| >> |*As*|, |*Ai*|). Consequently, the terms that contain more than one weak-field amplitude, such as Ap_1AsAs^*, are reduced. The letter *K* and *R* refer to the Kerr and Raman nonlinearities, respectively. Eq. (2.3.16) describes the amplitude evolution of the signal in the *m*-th mode with the contributions of intramodal and intermodal interactions between the pump, signal, and idler waves. An equation for the idler of the *m*-th mode can be obtained by exchanging the label *s* with *i* in Eqs. (2.3.16) - (2.3.18). The wave vector mismatch is defined as:

$$\Delta\beta_m^{(s,p)} = \beta^{(m,\omega_s)} - \beta^{(m,\omega_p)} \tag{2.3.19}$$

$$\Delta\beta_m^{(i,p)} = \beta^{(m,\omega_i)} - \beta^{(m,\omega_p)} \tag{2.3.20}$$

When the pulse width exceeds 1 ps, the amplitude variations over the time scale of the Raman response function h_R can be considered negligible. This simplification allows to introduce the Raman-induced index changes (δ_R) and gain coefficients (g_R) as follows[68]:

$$\delta_R = f_R \mathrm{Re}[\tilde{h}_R(\Omega)] \tag{2.3.21}$$

$$g_R = 2\gamma f_R \mathrm{Im}[\tilde{h}_R(\Omega)] \tag{2.3.22}$$

where $\tilde{h}_R$ denotes the Fourier transform of h_R, and $\Omega = \omega_p - \omega_s = \omega_i - \omega_p$ is the Stokes shift, then Eqs. (2.3.15) and (2.3.16) can be rewritten as follows:

$$\frac{\partial Ap_m}{\partial z} = j\gamma \left[f_{mm}|Ap_m|^2 + \sum_{k\neq m} 2f_{mk}|Ap_k|^2 \right] Ap_m \tag{2.3.23}$$

$$\begin{aligned}
\frac{\partial As_m}{\partial z} = {} & j\gamma \left[(2 - f_R + \delta_R) f_{mm}|Ap_m|^2 + \sum_{k\neq m} (2 - f_R + \delta_R) f_{mk}|Ap_k|^2 \right] As_m \\
& + \sum_{k\neq m} j2\gamma(1 - f_R + \delta_R) f_{mk} Ap_m Ai_k^* Ap_k e^{-j\left(\Delta\beta_m^{(s,p)} + \Delta\beta_k^{(i,p)}\right)z} \\
& + j\gamma(1 - f_R + \delta_R) f_{mm} Ap_m Ai_m^* Ap_m e^{-j\left(\Delta\beta_m^{(s,p)} + \Delta\beta_m^{(i,p)}\right)z} \\
& + \sum_{k\neq m} j\gamma(2 - f_R + \delta_R) f_{mk} Ap_m Ap_k^* As_k e^{-j\left(\Delta\beta_m^{(s,p)} - \Delta\beta_k^{(s,p)}\right)z} + \frac{g_R}{2} f_{mm}|Ap_m|^2 As_m \\
& + \sum_{k\neq m} \frac{g_R}{2} f_{mk}|Ap_k|^2 As_m + \sum_{k\neq m} g_R f_{mk} Ap_m Ap_k Ai_k^* e^{-j\left(\Delta\beta_m^{(s,p)} + \Delta\beta_k^{(i,p)}\right)z} \\
& + \frac{g_R}{2} f_{mm} Ap_m Ap_m Ai_m^* e^{-j\left(\Delta\beta_m^{(s,p)} + \Delta\beta_m^{(i,p)}\right)z} + \sum_{k\neq m} \frac{g_R}{2} f_{mk} Ap_m Ap_k^* As_k e^{-j\left(\Delta\beta_m^{(s,p)} - \Delta\beta_k^{(s,p)}\right)z}
\end{aligned} \tag{2.3.24}$$

$$\begin{aligned}
\frac{\partial Ai_m}{\partial z} = {} & j\gamma \left[(2 - f_R + \delta_R) f_{mm}|Ap_m|^2 + \sum_{k\neq m} (2 - f_R + \delta_R) f_{mk}|Ap_k|^2 \right] Ai_m \\
& + \sum_{k\neq m} j2\gamma(1 - f_R + \delta_R) f_{mk} Ap_k Ap_m As_k^* e^{-j\left(\Delta\beta_k^{(s,p)} + \Delta\beta_m^{(i,p)}\right)z} \\
& + j\gamma(1 - f_R + \delta_R) f_{mm} Ap_m Ap_m As_m^* e^{-j\left(\Delta\beta_m^{(s,p)} + \Delta\beta_m^{(i,p)}\right)z} \\
& + \sum_{k\neq m} j\gamma(2 - f_R + \delta_R) f_{mk} Ap_m Ap_k^* Ai_k e^{j\left(\Delta\beta_k^{(i,p)} - \Delta\beta_m^{(i,p)}\right)z} - \frac{g_R}{2} f_{mm}|Ap_m|^2 Ai_m \\
& - \sum_{k\neq m} \frac{g_R}{2} f_{mk}|Ap_k|^2 Ai_m - \sum_{k\neq m} g_R f_{mk} Ap_k Ap_m As_k^* e^{-j\left(\Delta\beta_k^{(s,p)} + \Delta\beta_m^{(i,p)}\right)z} \\
& - \frac{g_R}{2} f_{mm} Ap_m Ap_m As_m^* e^{-j\left(\Delta\beta_m^{(s,p)} + \Delta\beta_m^{(i,p)}\right)z} - \sum_{k\neq m} \frac{g_R}{2} f_{mk} Ap_m Ap_k^* Ai_k e^{j\left(\Delta\beta_k^{(i,p)} - \Delta\beta_m^{(i,p)}\right)z}
\end{aligned} \tag{2.3.25}$$

Under the un-depleted pump assumption, Eq. (2.3.23) describes the propagation of the pump and yields the solutions:

$$Ap_m = \sqrt{P_m} e^{j\gamma\left(f_{mm}P_m + \sum_{k\neq m} 2f_{mk}P_k\right)z}, P_m = |Ap_m|^2, P_k = |Ap_k|^2 \tag{2.3.26}$$

The pump experiences different intensity-dependent phase shifts for different modes. After substituting this solution into Eqs. (2.3.24) and (2.3.25), one can obtain the following equations determining the evolution of the signal and idler amplitudes:

$$\begin{aligned}
\frac{\partial \bar{A}s_m}{\partial z} = {} & \left\{ j\left[\Delta\beta_m^{(s,p)} + \gamma(1 - f_R + \delta_R) f_{mm}P_m + \sum_{k\neq m} \gamma(-f_R + \delta_R) f_{mk}P_k \right] + \frac{g_R}{2}\left(f_{mm}P_m + \sum_{k\neq m} f_{mk}P_k \right) \right\} \bar{A}s_m \\
& + \sum_{k\neq m} [j2\gamma(1 - f_R + \delta_R) + g_R] f_{mk}\sqrt{P_m P_k}\bar{A}i_k^* + \left[j\gamma(1 - f_R + \delta_R) + \frac{g_R}{2} \right] f_{mm}P_m \bar{A}i_m^* \\
& + \sum_{k\neq m} \left[j\gamma(2 - f_R + \delta_R) + \frac{g_R}{2} \right] f_{mk}\sqrt{P_m P_k}\bar{A}s_k
\end{aligned}$$

(2.3.27)

$$\begin{aligned}\frac{\partial \bar{A}i_m^*}{\partial z} = &-\left\{j\left[\Delta\beta_m^{(i,p)} + \gamma(1-f_R+\delta_R)f_{mm}P_m + \sum_{k\neq m}\gamma(-f_R+\delta_R)f_{mk}P_k\right] + \frac{g_R}{2}\left(f_{mm}P_m + \sum_{k\neq m} f_{mk}P_k\right)\right\}\bar{A}i_m^* \\ &- \sum_{k\neq m}[j2\gamma(1-f_R+\delta_R)+g_R]f_{mk}\sqrt{P_mP_k}\bar{A}s_k - \left[j\gamma(1-f_R+\delta_R)+\frac{g_R}{2}\right]f_{mm}P_m\bar{A}s_m \\ &- \sum_{k\neq m}\left[j\gamma(2-f_R+\delta_R)+\frac{g_R}{2}\right]f_{mk}\sqrt{P_mP_k}\bar{A}i_k^*\end{aligned}$$

(2.3.28)

where $\bar{A}s_m = As_m \exp\left[j\phi_m z - j\Delta\beta_m^{(s,p)}z\right]$, $\bar{A}i_m^* = Ai_m^* \exp\left[-j\phi_m z + j\Delta\beta_m^{(i,p)}z\right]$ with $\phi_m = \gamma(f_{mm}P_m + \sum_{k\neq m} 2f_{mk}P_k)$. At this step, Eqs. (2.3.27) and (2.3.28) can be analytically solved in a matrix formalism by rewriting them in the form of:

$$\partial_z \mathbf{v} = \mathbf{M}\mathbf{v}, \mathbf{v} = [\bar{A}s\ \bar{A}i^*]^T, \mathbf{M} = \begin{bmatrix} \mathbf{M}_{s,s} & \mathbf{M}_{s,i} \\ -\mathbf{M}_{i,s} & -\mathbf{M}_{i,i}\end{bmatrix} \tag{2.3.29}$$

where **v** is a 2*N* x 1 vector with *N* as the number of modes, $\bar{A}s$ and $\bar{A}i^*$ are *N* x 1 vectors ($\bar{A}s = [\bar{A}s_1, \bar{A}s_2, \ldots, \bar{A}s_N]$, $\bar{A}i^* = [\bar{A}i_1^*, \bar{A}i_2^*, \ldots, \bar{A}i_N^*]$), and **M** is a 2*N* x 2*N* matrix:

$$\begin{aligned}&\mathbf{M}_{s,s}[m,m] = \left\{j\left[\Delta\beta_m^{(s,p)} + \gamma(1-f_R+\delta_R)f_{mm}P_m + \textstyle\sum_{k\neq m}\gamma(-f_R+\delta_R)f_{mk}P_k\right] + \right.\\ &\left.\tfrac{g_R}{2}(f_{mm}P_m + \textstyle\sum_{k\neq m} f_{mk}P_k)\right\}, \\ &\mathbf{M}_{s,s}[m,k] = \left[j\gamma(2-f_R+\delta_R)+\tfrac{g_R}{2}\right]f_{mk}\sqrt{P_mP_k}, \\ &\mathbf{M}_{s,i}[m,m] = \left[j\gamma(1-f_R+\delta_R)+\tfrac{g_R}{2}\right]f_{mm}P_m, \\ &\mathbf{M}_{s,i}[m,k] = [j2\gamma(1-f_R+\delta_R)+g_R]f_{mk}\sqrt{P_mP_k}, \\ &\mathbf{M}_{i,i}[m,m] = \left\{j\left[\Delta\beta_m^{(i,p)} + \gamma(1-f_R+\delta_R)f_{mm}P_m + \textstyle\sum_{k\neq m}\gamma(-f_R+\delta_R)f_{mk}P_k\right] + \tfrac{g_R}{2}(f_{mm}P_m + \right.\\ &\left.\textstyle\sum_{k\neq m} f_{mk}P_k)\right\}, \\ &\mathbf{M}_{i,i}[m,k] = \left[j\gamma(2-f_R+\delta_R)+\tfrac{g_R}{2}\right]f_{mk}\sqrt{P_mP_k}, \\ &\mathbf{M}_{i,s}[m,m] = \left[j\gamma(1-f_R+\delta_R)+\tfrac{g_R}{2}\right]f_{mm}P_m, \\ &\mathbf{M}_{i,s}[m,k] = [j2\gamma(1-f_R+\delta_R)+g_R]f_{mk}\sqrt{P_mP_k}.\end{aligned}$$

(2.3.30)

The solution of Eq. (2.3.29) can be written as:

$$\mathbf{v}[j](z) = \sum_{k=1}^{2N} c_k w_k[j]\exp(\lambda_k z) \tag{2.3.31}$$

where λ_k and w_k are the eigenvalues and eigenvectors of **M**, the label *j* denotes the *j*-th element of **v**, and the coefficients $c_k = \frac{\mathrm{v}(z=0)\cdot\mathrm{diag}(\mathrm{ones}_N, -\mathrm{ones}_N)\cdot w_k}{w_k\cdot\mathrm{diag}(\mathrm{ones}_N, -\mathrm{ones}_N)\cdot w_k}$ with ones$_N$ denoting an *N* x 1 vector of ones.

In order to verify the accuracy of the analytical solution Eq. (2.3.31) and to demonstrate Kerr and Raman effects in multimodal systems, the split-step Fourier method was implemented to numerically solve the MM-NLSEs Eq. (2.3.8). Initially, the Raman contribution is neglected ($f_R = \delta_R = g_R = 0$), and three different modes with the same polarization states are considered, which are maintained during propagation. The fibre dispersion parameters and nonlinear coefficients are listed in Table 2.1.

Table 2.1 Fibre dispersion parameters and nonlinear coefficients for the 3-mode fibre

@ λ=1040 nm	Mode 1	Mode 2	Mode 3
β_1 (ps/mm)	4.902	4.904	4.906
β_2 (ps^2/km)	30.362	27.101	22.639
β_3 (x0.01 ps^3/km)	2.227	2.405	3.006
γ (W^{-1}km^{-1})	3	Overlap factor (f_{11}, f_{22}, f_{33}, f_{12}, f_{13}, f_{23})	(1, 1.44, 1.18, 0.70, 1.08, 0.74)

Figure 2.3 illustrates the comparison between the numerical and analytical solutions for the evolution of the three modes over a fibre propagation length of 1m. Figure 2.3(a) shows the spectral envelopes for the input and output three modes. The input modes are continuous waves oscillating at the same frequency 288.5 THz (wavelength=1040 nm), each with an average power of 2 kW. Background noise added to the input serves as a probe that can be amplified by the gain provided by the modulation instability, resulting from phase-matched four-wave mixing. Consequently, new frequencies emerge in distinct spectral regions centred at ±8.5 THz, ±12 THz, and ±22 THz, arising from MI between different pairs of modes. Mode-dependent gain, depicted as red lines in Figure 2.3(b), can be readily calculated. The analytical gains calculated from Eq.(2.3.31) via $20\log_{10}(v(z=1m)/v(z=0))$, perfectly align with the numerical results. The slight discrepancy in gain around the pump frequency is attributable to the Lorentzian shape of the input spectra in the simulations, while the analytical model assumes a single-frequency input.

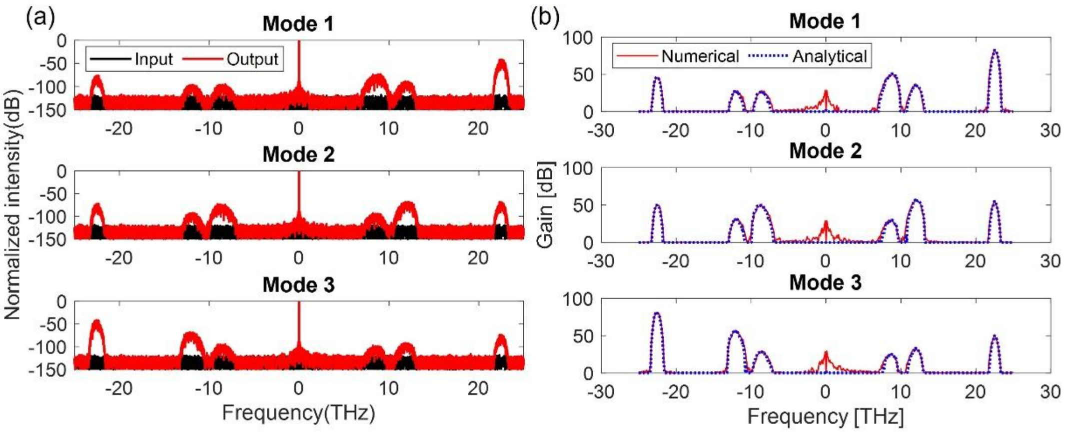

Figure 2.3 Comparison between the numerical and analytical solutions to the MM-NLSEs for a 3-mode fibre when only considering Kerr nonlinearity. (a) Input and output spectra for each mode (centred around the pump frequency) obtained by numerical simulation. (b) Gain spectra obtained from numerical (red) and analytical (blue) methods.

Another simulation instance is conducted, incorporating Raman contributions. Analytical solutions (Eq.(2.3.31)) are computed, considering both Kerr and Raman nonlinearity (f_R=0.18), within the same 3-mode fibre and utilizing identical parameters, including modes, powers, and fibre length. Figure 2.4(a) illustrates the input and output spectra envelopes when considering the complex intramodal and intermodal processes. Notably, the gain spectra in Figure 2.4(b) diverge from those depicted in Figure 2.3(b) within the frequency range from -25 THz to 0 THz, attributed to Raman scattering. Figure 2.3 and Figure 2.4 validate the accuracy of the analytical methods presented in this section. Moreover, while numerical methods entail time-consuming processes due to various inherent challenges such as step size and resolution, analytical method offers rapidity through matrix calculations. Hence, it serves as efficient precursor to the implementation of time-consuming numerical methods. Leveraging these methods facilitates the study and prediction of the complex interaction dynamics within multimode nonlinear systems.

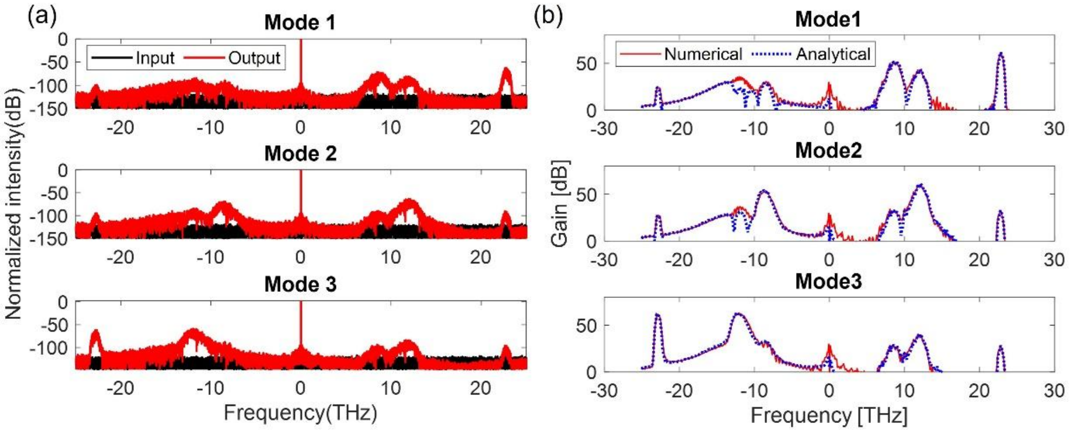

Figure 2.4 Comparison between the numerical and analytical solutions to the MM-NLSEs for the same 3-mode fibre as Figure 2.3, when taking into account both Kerr and Raman nonlinearity. (a) Input and output spectra obtained by numerical simulation. (b) Gain spectra obtained from numerical (red) and analytical (blue) methods.

2.4 Review of nonlinear spatial control processes in multimode systems

The multimode interaction in nonlinear multimode systems brings a plethora of novel effects and phenomena. Controlling the output beam pattern in these systems is pivotal and has been achieved by complex mode control devices and signal-processing algorithms. This section reviews various all-optical nonlinear spatial control processes in multimode systems, which are highly relevant to the objective of this thesis – mode control and beam shaping in multimode systems. The following nonlinear spatial control processes are introduced: dissipative spatial beam clean-up, Kerr beam self-cleaning, beam self-organization in multimode gain media, polarization and mode attractors, and optical long period gratings.

2.4.1 Spatial beam clean-up through dissipative nonlinear process

Spatial beam clean-up refers to the process by which a spatial beam profile is cleaned to a single mode condition, typically evolving towards the fundamental mode with a Gaussian-shaped profile. In multimode graded-index (MM-GRIN) fibres, dissipative nonlinear processes such as SBS and SRS cause the generated Stokes waves to evolve into one of the lower-order modes [79-83]. In this process, the pump is coupled to multiple modes, and the beam clean-up in Stokes waves is predominantly observed in MM-GRIN fibres. The output Stokes mode can be selectively controlled to propagate lower-order modes by adjusting the launching conditions of pump wave[82]. This is due to the significant overlap between the lower-order Stokes modes and the multimode pump modes [81, 82], resulting in mode-dependent gain that favours the lower-order modes. The output Stokes mode can be selectively controlled to propagate lower-order modes by adjusting the launching conditions of the pump wave[82]. However, step-index MMFs are not suitable for exploring Brillouin- or Raman-induced beam clean-up. In these fibres, the overlap between the multimode pump modes and different orders of Stokes modes is similar, and no mode-selective gain is achieved[83].

In recent years, the Brillouin and Raman beam clean-up effects have been developed to achieve high-power, high brightness Stokes light with high fundamental mode purity. Raman fibre lasers based on MM-GRIN fibres, pumped with high-power multimode laser diodes, have been studied, resulting in an output power of 50 W with high brightness[84]. Another significant application of dissipative nonlinear beam clean-up is in amplifier configurations[82, 84, 85], where the Brillouin- or Raman-induced Stokes beam maintain the same mode as the externally excited seed beams. In such amplifiers, the amplification of low-order modes is possible by selectively exciting seed modes. The dependence of the Raman clean-up effect on the seed beam quality has been demonstrated at the 2-kW level with MM-GRIN fibres[86].

2.4.2 Kerr beam self-cleaning in highly multimode fibres

Kerr beam self-cleaning involves the transformation of the transverse intensity profiles at the MMF output from a speckled pattern to a bell-shaped beam sitting on a low intensity background. Unlike dissipative beam clean-up, Kerr beam self-cleaning is observed at the pump wavelength rather than the Stokes wavelength. This effect has been experimentally observed in MM-GRIN fibres with pulse durations ranging from nanosecond down to femtoseconds, and at wavelengths ranging from visible to near-infrared region. Table 2.2 provides a review of experiments reported on Kerr beam self-cleaning. Kerr beam self-cleaning primarily occurs with ps pulses having tens of kW peak power over a few meters of MM-GRIN fibres. Most experiments have used 1 μm lasers, with one notable exception at 532 nm using a frequency-doubling technique[87]. Typically, the self-cleaned output beam resembles the fundamental fibre mode (LP_{01} mode), as indicated in the last column of Table 2.2. However, by adjusting the input launching conditions - such as using tilted injection[88], a deformable mirror[89], or dual beams[63] - self-cleaning to higher order fibre modes has also been observed. More recently, the concept of cascaded Kerr beam self-cleaning has been numerically investigated to further improve laser beam quality by using multiple MM-GRIN fibres[90].

Table 2.2 Review of experiments on Kerr beam self-cleaning

Year	Name of researcher	Pulse duration	Peak power (kW)	Wavelength (nm)	Fibre	Output resembling
2016	Krupa[91]	900 ps	50	1064	6m GRIN	LP_{01}
2016	Liu[92]	80 fs	600	1030	20cm GRIN	LP_{01}
2016	Wright[87]	1 ns	0.5-3	532	100m GRIN	LP_{01}
2017	Guenard[59]	500 ps	200	1064	3m Yb-MMF	LP_{01}
2017	Krupa[60]	900 ps	44	1064	12m GRIN	LP_{01}
2018	Deliancourt[93]	750 ps	50	1064	8.3m GRIN	LP_{01}
2019	Deliancourt[89]	7 ps	30-45	1064	5m GRIN	LP_{01}, LP_{11}, LP_{02}, LP_{21}, LP_{12}, LP_{22}
2019	Niang[94]	500 ps	130	1064	9.5m Yb-GRIN taper	LP_{01}
2020	Fabret[95]	60 ps	55	1064	12m GRIN	LP_{01}
2022	Mangini[96]	174 fs-0.5ns	30	1030, 1064	3m GRIN	LP_{01}
2023	Ferraro[63]	65 ps	100	1064	2m GRIN	LP_{01}
2023	Ferraro[63]	174 fs-7.8 ps	23.4	1030	2m GRIN	LP_{01}

There are some appealing features of the Kerr beam self-cleaning process. Firstly, it requires a peak power level lower than the threshold required for self-focusing, which needs megawatt peak power. Moreover, Kerr beam self-cleaning is observed well before Raman amplification, indicating that beam self-cleaning occurs without significant spectral broadening, frequency conversion, or dissipative processes. Secondly, the efficiency of self-cleaning is highly dependent on the refractive index profile of the fibre core and the number of modes involved. This dependency explains why beam self-cleaning is typically observed in MM-GRIN fibres. Thirdly, a cut-back study[60] shows that the Kerr self-cleaning is an accumulated nonlinear phase shift process, proportional to the product of fibre length and power. This is distinct from self-focusing or scattering processes, which require a fixed power threshold. Fourthly, the self-cleaned output beam typically resembles the fundamental fibre mode whereas the higher-order modes remain significant in the output. Lastly, the self-cleaned output beam can preserve the spatial coherence of the input laser source. This has been demonstrated by the coherent combination of two self-cleaned beams from two independent GRIN fibres pumped by the same laser[95].

The several features of Kerr beam self-cleaning suggest that this effect is associated with a beam's evolution towards a well-defined mode power distribution in a MM-GRIN fibre, rather than merely converting power from higher-order modes to the fundamental mode. Since the first observation of this effect, researchers have been working to elucidate the physical mechanisms behind it. Several hypotheses and models have been presented to explain the complex multimode dynamics[83], including nonreciprocal intermodal coupling driven by a dynamic optical grating, quasi-phase-matching conditions favouring gain in the fundamental mode, hydrodynamic 2D turbulence, wave condensation, mode-dependent losses, the transfer of entropy from the spatial shape to the temporal pulse shape[92], and so forth. Among these studies, two prevailing theories have emerged to explain the Kerr beam self-cleaning effect, both supported by experimental results. One is the purely Kerr-induced transfer of disorder from the spatial to temporal/spectral domain[97]. Driven by a complex multimode intermodal four-wave mixing process, the output spectrum of each fibre mode will be deformed in a different manner. As a result, the fundamental mode emerges with dominant weight in the pump wavelength after the propagation through the MM-GRIN fibre. This increased spectral disorder also results in temporal reshaping, causing pulse break-up and compression[83, 92]. The other theory is based on a statistical mechanics model of wave thermalization[61, 62, 96, 98]. In this framework, a multimode beam is described as a gas of photons obeying an equation of state at thermal equilibrium. The occupation probability of the fibre modes can be reproduced by the Rayleigh-Jeans law[62]. At thermal equilibrium, the fundamental mode achieves macroscopic occupation in MM-GRIN fibres, leading to beam self-cleaning to the fundamental mode.

2.4.3 Beam self-organization in multimode gain media

Kerr beam self-cleaning occurs in passive MMFs in an energy-conservative manner. However, it is also crucial to investigate this phenomenon in multimode gain media. A similar effect, known as beam self-organization, has been observed in active fibres. In an initial experiment, Kerr self-cleaning effect was demonstrated in an amplifying MMF using a 3-metre double-clad ytterbium-doped MMF with non-parabolic refractive index profile [59]. This experiment compared the self-cleaning effect in both passive and active configurations using the same fibre. It was found that spatial self-cleaning could be achieved with a significantly lower power threshold in the active configuration. In the passive setup, self-cleaning required input peak powers above 40 kW with 500 ps pulses. Conversely, when the fibre was pumped (active configuration) and with a gain of 20 dB, only a peak power of 500 W was needed to initiate the beam self-cleaning process. Another experiment used a 9.5m-long Yb-doped MM-GRIN fibre taper, with the fibre's cross-section diameter gradually decreasing from 122 μm to 37 μm[94]. This setup further explores the beam self-cleaning phenomenon in multimode gain media, highlighting the potential for lower power thresholds and enhanced control over beam profiles in active fibre systems.

In addition to the beam shaping with doped MMFs, fibre laser arrays and multicore fibres offer alternative platforms for achieving beam self-organization. Mutually injected fibre laser arrays have been investigated both theoretically and experimentally to achieve different phase-locked states of the laser arrays[99-101]. In one configuration involving two laser arrays, each array uses an individual Erbium doped single mode fibre as the gain medium, and the two arrays are mutually injected through fibre splitters. Experiments demonstrated that these two fibre lasers could output coherent light at the same wavelength with a stable phase relationship between the arrays[99]. This stable phase condition, which can be either in-phase or out-of-phase, is induced by virtual longitudinal mode competition within the entire laser array cavity. This setup showcases the potential for controlled and coherent beam output from multiple laser sources.

The self-organization of fibre laser arrays holds significant importance for achieving coherent beam combination, leading to the generation of high power, high-brightness, and diffraction-limited light. As multicore fibres have been proposed for power scaling and beam combination, researchers have explored their potential for obtaining self-organized supermode outputs, where multiple beamlets from MCF cores exhibit fixed intensity and phase relations.

In one early experiment, a hexagonal 7 coupled-core Yb-doped fibre, with a length of 15 m, served as the gain media within a laser cavity[102]. The output exhibited a high-brightness beam in the far field, indicating that the dominant modes in the MCF were in-phase supermode (the fundamental supermode) in the near-field. A subsequent theoretical explanation proposed the nonlinear refraction mechanism[103] as the basis for this self-organization effect in active MCFs. It suggested that either in-phase or out-of-phase supermode could be selected by controlling the pump intensity. Further experiments demonstrated the fundamental supermode operation of a 5.8m-long 19-coupled-core Yb-doped MCF amplifier, achieving high pulse energies up to 0.65 mJ with ~100 ns pulses[104].

More recently, coupled-core MCFs have attracted attention for exploring a broader range of effects involving both spatial and temporal dynamics[105-108]. These include phenomena such as spatiotemporal optical bullets, simultaneous beam combining and pulse compression[105, 106, 108], multicore beam self-focusing[107], and multicore supercontinuum generation. For instance, an 11-mm 7-core MCF has been shown to function as a saturable absorber, inducing pulse compression from ~ 370 fs to ~200 fs in the central core, while spatially trapping pulse energy in the central core[106]. Such studies highlight the versatility and potential applications of coupled-core MCFs in advanced optical systems.

2.4.4 Polarization and mode attractors in counter-propagating beams

The Kerr beam self-cleaning and self-organization processes typically take place in a co-propagating multimode system, where spatial redistribution arises from the one-directional multimode interactions. However, researchers have also explored the interaction between two counter-propagating beams in optical fibres over the last two decades. In this context, the concept of polarization and mode attraction has been demonstrated.

Polarization attraction is a Kerr effect where the polarization state of an intense optical signal beam can be transformed from arbitrary to a desired state[109]. This transformation in nonlinear fibres is driven by the intermodal FWM process between the signal beam and a strong counter-propagating control beam. This phenomenon is observable in single-mode ultralow-birefringence fibres, where the counter-propagating beams can be treated as two polarization modes, such as left- and right-circular polarization states. Through specific boundary conditions applied to the counter-propagating system, the output forward beam adopts the polarization state of the backward input beam, given that the two beams have sufficiently high power or the interaction medium (fibre) has significant nonlinearity.

In the first experiment reported in 2001[110], 22 ns pulses with a peak power of ~200 W were launched at the two ends of a 1.45m-long step-index ultralow birefringence fibre, operating at a wavelength of 532 nm. Nonlinear polarization switching occurred in the forward beams when selectively adjusting the bidirectional beams with the same or opposite linear or circular polarization states. Subsequently, in 2005, a similar effect known as mode attraction was proposed using bimodal high-birefringence fibres. In mode attraction, the forward beam is attracted to the opposite mode of the backward control mode. An initial experimental investigation demonstrated this effect in a 2 m-long bimodal fibre using 6.5 ns pulses with 175 W peak power at a wavelength of 532 nm[109].

With a growing interest in controlling polarization states in telecommunication fibres, polarization attraction was extensively explored from various perspectives[111, 112], including wavelength extension to C-band[113-116], reduction in power requirement[114], variation in pulse duration[114, 116], performance in kilometres long telecommunication fibres, and high data rate and bandwidth[116]. Additionally, conceptual devices such as the omnipolarizer[117, 118], four-wave mixing polarizer[119], and mode attractor[118, 120] have been demonstrated. However, the mode attraction process remains incompletely explored, particularly concerning the complex dynamics when extending from a bimodal system to a multimode counter-propagating system.

The investigation of mode control dynamics in nonlinear multimode counter-propagating systems is addressed in subsequent chapters.

The theory behind polarization and mode attraction has been explored using the nonlinear Schrödinger equations in a bimodal context. To generalize this to counter-propagating multimode systems, the co-propagating MM-NLSEs (see Eq.(2.3.8)) can be modified accordingly. In an isotropic multimode fibre, where forward and backward beams are coupled across *N* spatial modes at the same frequency, and can be decomposed into *x*/*y* linear polarization states, the Fourier transform of the electric field can be expressed as:

$$\begin{aligned}\tilde{\boldsymbol{E}}(r,\omega) = \sum\nolimits_{m} \Big\{ & \hat{\boldsymbol{e}}_{xm} M_m(x,y,\omega)\tilde{F}_{mx}(z,\omega) exp\left[i\beta_x^{(m)}(\omega)z\right] \\ & + \hat{\boldsymbol{e}}_{ym} M_m(x,y,\omega)\tilde{F}_{my}(z,\omega) exp\left[i\beta_y^{(m)}(\omega)z\right] \\ & + \hat{\boldsymbol{e}}_{xm} M_m(x,y,\omega)\tilde{B}_{mx}(z,\omega) exp\left[-i\beta_x^{(m)}(\omega)z\right] \\ & + \hat{\boldsymbol{e}}_{ym} M_m(x,y,\omega)\tilde{B}_{my}(z,\omega) exp\left[-i\beta_y^{(m)}(\omega)z\right]\Big\}\end{aligned} \qquad (2.4.1)$$

where the spatial distributions of the orthogonally polarized modes are assumed to be the same (the transverse mode distribution of the *m*-th mode denoted as M_m). ${\beta_x}^{(m)}$ and ${\beta_y}^{(m)}$ are the propagation constants of the *x* and *y* polarization components for the *m*-th mode, $\tilde{F}_{mx}$, $\tilde{F}_{my}$, $\tilde{B}_{mx}$, and $\tilde{B}_{my}$ represent the amplitudes of the forward(*F*) and backward(*B*) modes.

By substituting Eq. (2.4.1) into the wave equation Eq. (2.2.4), and following the same procedures introduced in section 2.3.1, one can derive the coupled-amplitude equations that govern the interaction between the counter-propagating beams[109, 110]:

$$\begin{aligned}\frac{\partial F_{mx}}{\partial z} - i\sum_{k=1}^{\infty}\frac{i^k\beta_{kmx}}{k!}\frac{\partial^k F_{mx}}{\partial t^k} \\ = i\gamma f_{mm}\left[F_{mx}F_{mx}^*F_{mx} + \frac{2}{3}F_{mx}F_{my}^*F_{my} + 2F_{mx}B_{mx}^*B_{mx} + \frac{2}{3}F_{mx}B_{my}^*B_{my}\right] \\ + i\gamma\sum\nolimits_{n\neq m} f_{mn}\left[2F_{mx}F_{nx}^*F_{nx} + \frac{2}{3}F_{mx}F_{ny}^*F_{ny} + 2F_{mx}B_{nx}^*B_{nx} + \frac{2}{3}F_{mx}B_{ny}^*B_{ny}\right. \\ \left. + 2F_{nx}B_{mx}^*B_{nx} + \frac{2}{3}F_{nx}B_{my}^*B_{ny}\right]\end{aligned} \qquad (2.4.2)$$

$$\begin{aligned}\frac{\partial B_{my}}{\partial z} + i\sum_{k=1}^{\infty}\frac{i^k\beta_{kmy}}{k!}\frac{\partial^k B_{my}}{\partial t^k} \\ = -i\gamma f_{mm}\left[B_{my}B_{my}^*B_{my} + \frac{2}{3}B_{my}B_{mx}^*B_{mx} + 2B_{my}F_{my}^*F_{my} + \frac{2}{3}B_{my}F_{mx}^*F_{mx}\right] \\ - i\gamma\sum\nolimits_{n\neq m} f_{mn}\left[2B_{my}B_{ny}^*B_{ny} + \frac{2}{3}B_{mx}B_{ny}^*B_{ny} + 2B_{my}F_{ny}^*F_{ny} + \frac{2}{3}B_{my}F_{nx}^*F_{nx}\right. \\ \left. + 2B_{ny}F_{my}^*F_{ny} + \frac{2}{3}B_{ny}F_{mx}^*F_{nx}\right]\end{aligned} \qquad (2.4.3)$$

where the Raman interaction is neglected, $F_{mx(y)}(z,t)$ and $B_{nx(y)}(z,t)$ denote the amplitude of the forward m-th mode in the x/y polarization state and the amplitude of the backward n-th mode in the x/y polarization state, respectively. The last two terms on the right-hand side of these equations are automatically phase-matched, representing the energy exchange among the forward beams with different polarization states and mode distributions driven by the counter-propagating beams. These inherently phase-matched terms are unique to a counter-propagating configuration because similar intermodal phase matching conditions would require specific fibre designs in a co-propagating system. The coupling strength between the orthogonally polarized modes is one third of the coupling strength between the parallelly polarized modes, as indicated with the coefficients 2 and 2/3. The equations for the mode F_{my} and B_{mx} can be obtained by replacing the label $x(y)$ with $y(x)$ in these two equations.

2.4.5 Optically induced long period gratings in multimode fibres

Spatial control over the transverse mode distribution in optical fibres can also be achieved through the introduction of periodic perturbations to the light propagation[121]. Beyond permanent optical gratings and acousto-optic mode converters, the concept of optically induced long period gratings has been proposed and experimentally investigated using nanosecond and femtosecond pulses with kilowatt peak powers[66, 122-125]. When a high-power beam (writing beam) is coupled with two modes into the fibre, the mode beating between these modes generates an instantaneous and temporal grating via the Kerr effect. Another low-power beam (probe beam) can be diffracted by this optical grating, leading to a periodic mode conversion for the probe beam.

Initial experiments were conducted with step-index few-mode fibres, spanning lengths from a few metres to centimetres[66, 123]. In these experiments, the writing beam and probe beam were orthogonally polarized to separate them at the same wavelength. Efficient mode conversion of probe beam requires phase matching between the writing and probe beams. By using graded-index fibres, which feature flat dispersion and phase-matching curves, the wavelength of the probe beam can be extended from a single frequency to a large bandwidth[122, 125]. For instance, in an experiment using a 19.5 cm MM-GRIN fibre, 400-fs pulses with 250 kW peak power at a wavelength of 1030 nm were used as the writing beam. An energy conversion of 18% between the LP_{01} mode and the LP_{11} mode was observed in a probe beam at a wavelength of 1250 nm with 2 ps pulses at 500 W peak power[125].

Meanwhile, theoretical and simulation approaches have been developed to understand the transverse mode conversion controlled by optical long period gratings. These approaches include the development of coupled mode equations[122], the beam propagation method[66], solutions to the MM-NLSEs[124], material representations[121], four-wave mixing representations[121], and the intermodal Bragg-scattering four-wave mixing effect[126, 127]. However, state-of-the-art theories and models typically consider up to only two modes. It is crucial to generalize these theories to account for any number of modes. Furthermore, the optical long period grating effect in counter-propagating systems remains unexplored both theoretically and experimentally. These aspects are investigated in Chapter 4, where counter-propagating optical nonlinear gratings in multimode and multicore fibres are demonstrated theoretically and experimentally.

2.5 Conclusions

In this chapter, the propagation of multimode laser beams in optical fibres has been introduced using the MM-NLSEs. The intramodal and intermodal nonlinear interaction processes have been discussed based on the derivation of analytical solutions to the MM NLSEs, including self- and cross-phase modulation, four-wave mixing, and Raman scattering. The multimode interaction in multimode systems brings several novel effects and phenomena. As the main objective of this thesis is spatial mode control and laser beam shaping, several nonlinear spatial control processes in multimode systems have been reviewed, including dissipative spatial beam clean-up, Kerr beam self-cleaning, beam self-organization in multimode gain media, polarization and mode attractors in counter propagating beams, and optically induced long period gratings. The work introduced in Chapters 3 and 4 is based on the nonlinear interaction between counter-propagating beams, which shares a similar mechanism with polarization and mode attractors. However, the number of involved modes has been extended from two to multiple modes, and the mode control/shaping dynamics for the counter-propagating beams has been further investigated. Chapter 5 introduces spectrally beam shaping (wavelength conversion) in multicore fibres, and the corresponding background theory is reviewed in Section 2.3. Chapter 6 also investigates spatial beam shaping in multicore fibres; however, it focuses on a linear coherent beam combination approach. The corresponding state-of-the art and underlying mechanism are introduced at the beginning of Chapter 6.

Chapter 3 Mode rejection and control in multimode and multicore fibres

3.1 Introduction

In this chapter, the concept of "mode rejection in nonlinear optical fibres" is introduced and validated through experiments conducted with various few-mode fibres and homemade coupled multicore fibres. The phenomenon observed involves a forward-propagating beam autonomously rejecting a specific spatial mode when influenced by a backward-propagating beam of comparable power. Initially, the theoretical framework of mode rejection within counter-propagating beams is outlined, supported by simulation results. Subsequently, experimental investigations are conducted to demonstrate the rejection of different LP modes or supermodes using a range of fibres, including 2-mode fibres (PM1550-xp, PMHN1, SMF28, and dual-core fibre), a 3-mode fibre (tri-core fibre), and a 6-mode fibre (PM2000), all operating at a wavelength of 1.04 μm. The chapter explores the impact of various parameters on the mode rejection effect through experimentation and simulations, including factors such as the input conditions of the counter-propagating beams (launch power, polarization state, and mode composition), fibre design, and fibre nonlinearity. Lastly, the concept of mode control within counter-propagating multimode beams is demonstrated, expanding upon the initial observations of mode rejection to further elucidate the dynamics of multimode nonlinear interactions.

3.2 Mode rejection dynamics

3.2.1 Theory

The coupled nonlinear Schrödinger equations (see Eqs. (2.4.2) and (2.4.3)) introduced in Chapter 2 describe the conservative nonlinear interactions among electric fields in a counter-propagating system with varying properties, including different polarization states, propagation directions, and spatial modes. These equations suggest a range of nonlinear effects commonly explored in counter-propagating multimode systems, such as four-wave mixing. However, a novel nonlinear effect – mode rejection – has not been thoroughly investigated. Mode rejection occurs when two laser beams are injected into opposite ends of a Kerr nonlinear medium (optical fibres, in this thesis), enabling a forward signal (FS) beam to self-organize its spatial mode distribution to eliminate a specific mode from the output signal. This process is driven by a backward propagating beam, termed the backward control beam (BCB). For simplicity, the following theory is introduced in a scalar regime, considering the FS and BCB as either co-polarized or orthogonally polarized. This allows the simplification of Eqs. (2.4.2) and (2.4.3) to:

$$\frac{\partial F_m}{\partial z} + \beta_1^{(m)}\frac{\partial F_m}{\partial t} = -i\gamma_{mm}|F_m|^2F_m + iF_m\sum\nolimits_n \gamma_{mn}(p|B_n|^2 + 2|F_m|^2) + iB_m^*\sum\nolimits_{n\neq m} p\gamma_{mn}B_nF_n \tag{3.2.1}$$

$$-\frac{\partial B_m}{\partial z} + \beta_1^{(m)}\frac{\partial B_m}{\partial t} = -i\gamma_{mm}|B_m|^2B_m + iB_m\sum\nolimits_n \gamma_{mn}(p|F_n|^2 + 2|B_n|^2) + iF_m^*\sum\nolimits_{n\neq m} p\gamma_{mn}B_nF_n \tag{3.2.2}$$

where the second and higher order derivatives with respect to *t* are neglected, meaning that the dispersion length is much larger than the fibre length. These simplified equations hold true for experiments involving picosecond pulses, kilowatt peak power, and fibre lengths on the order of metres. γ_{mn} is the nonlinear Kerr coefficient related to the *m*-th and the *n*-th modes and it is defined by $\gamma_{mn}=\gamma f_{mn}$ (see Eq.(2.3.10) for f_{mn}). The polarization-related coefficient p=2 when the FS and the BCB are co-polarized, whereas p=2/3 when they are orthogonally polarized. On the right-hand side of Eqs. (3.2.1) and (3.2.2), the first two terms describe the self-phase modulation and cross-phase modulation, which result in phase evolutions of the *m*-th mode. The last term gives rise to the energy exchange between the *m*-th and *n*-th modes of the FS and BCB.

Stationary solutions can be found such that $F_m(z,t)=F_m(z)$ and $B_m(z,t)=B_m(z)$. By focusing on a stationary problem and considering the case where $\gamma_{mm}=2\gamma_{mn}=\gamma$, the equations without time-dependent terms simplify as follows:

$$\frac{\partial F_m}{\partial z} = i\gamma F_m\sum\nolimits_n(\rho|B_n|^2 + |F_m|^2) + i\rho\gamma B_m^*\sum\nolimits_n B_nF_n \tag{3.2.3}$$

$$-\frac{\partial B_m}{\partial z} = i\gamma B_m\sum\nolimits_n(\rho|F_n|^2 + |B_n|^2) + i\rho\gamma F_m^*\sum\nolimits_n B_nF_n \tag{3.2.4}$$

where $\rho=p/2$, the equations simplify and the boundary conditions fix the input FS at z=0 and the input BCB at z=L (L is the fibre length), i.e., $F_m(0)$ and $B_m(\mathrm{L})$. To further analyse the system, the following change of variables is introduced:

$$F_m = P_f^{1/2}\,\hat{f}_m e^{i\gamma(P_f+\rho P_b)z} \tag{3.2.5}$$

$$B_m = P_b^{1/2}\,\hat{b}_m e^{-i\gamma(P_b+\rho P_f)z} \tag{3.2.6}$$

where $P_f = \sum_m|F_m|^2$ and $P_b = \sum_m|B_m|^2$ are the total forward and backward powers and they are conserved during propagation (with losses neglected). According to Eqs. (3.2.5) and (3.2.6), $\sum_m|\hat{f}_m|^2 = \sum_m|\hat{b}_m|^2 = 1$. In the following derivations, the focus is on a defined correlation coefficient $D_R = (\sum_m F_m B_m|)/(P_f P_b)^{1/2}$. Note that D_R and $\hat{D}_R = \sum_m \hat{f}_m \hat{b}_m$ are identical except for a phase term

$e^{i\gamma\Delta P(\rho-1)z}$ with $\Delta P = P_b - P_f$, and consequently $|D_R| = |\widehat{D}_R|$. Inserting Eqs. (3.2.5) and (3.2.6) into Eqs. (3.2.3) and (3.2.4) yields the following relations:

$$\partial_z \hat{f}_m = \quad i\gamma\rho P_b \widehat{D}_R \hat{b}_m^* \tag{3.2.7}$$

$$\partial_z \hat{b}_m^* = \quad i\gamma\rho P_f \widehat{D}_R^* \hat{f}_m \tag{3.2.8}$$

By calculating the derivative of $\widehat{D}_R$ with respect to z, one can find a simple equation by substituting Eqs. (3.2.7) and (3.2.8) into $\partial_z \widehat{D}_R$:

$$\partial_z \widehat{D}_R = i\gamma\rho\, \widehat{D}_R \cdot \Delta P \tag{3.2.9}$$

Eq. (3.2.9) can be solved analytically and the solution reads $\widehat{D}_R(z) = \widehat{D}_R(0) \cdot e^{i\gamma\rho\Delta P z}$. Note that at this point $\widehat{D}_R(z)$ is still undetermined. Indeed, due to the counter-propagating nature of the system, $\widehat{D}_R(0)$ is unknown since it depends on $b_n(0)$. However, by inserting the solution of Eq. (3.2.9) into Eqs. (3.2.7) and (3.2.8), the solution for $\hat{f}_m(\mathrm{L})$ can be obtained. After some algebra, this leads to the following equality:

$$\hat{f}_m(\mathrm{L}) = \frac{i\hat{f}_m(0) h e^{\frac{1}{2} i\gamma\,\rho\,\Delta P\,\mathrm{L}} - \hat{b}_m^*(\mathrm{L})\widehat{D}_R(\mathrm{L})\, sin(T\,h)\,(v+w)}{ih\,cos(T\,h) - v\,sin(T\,h)} \tag{3.2.10}$$

where $v = \Delta P/(2Q)$, $w = \mathrm{P}_{\mathrm{tot}}/(2Q)$, $h^2 = v^2 + |\widehat{D}_R(\mathrm{L})|^2$, $T = \rho\gamma Q\mathrm{L}$, $Q^2 = P_f P_b$, $\mathrm{P}_{\mathrm{tot}} = \mathrm{P}_\mathrm{f} + \mathrm{P}_\mathrm{b}$. After multiplying the left- and right-hand sides of Eq. (3.2.10) by $\hat{b}_m(\mathrm{L})$, one can take the summation over the spatial modes to obtain the following implicit equation for $\widehat{D}_R(\mathrm{L})$:

$$\widehat{D}_R(\mathrm{L}) = \frac{i\widehat{D}_R^{(in)} h e^{\frac{1}{2} i\gamma\,\rho\,\Delta P\,\mathrm{L}} - \widehat{D}_R(\mathrm{L})\, sin(T\,h)\,(v+w)}{ih\,cos(T\,h) - v\,sin(T\,h)} \tag{3.2.11}$$

where $\widehat{D}_R^{(in)} = \sum_m \hat{f}_m(0)\hat{b}_m(\mathrm{L})$ represents the correlation among the input FS ($\hat{f}_m(0)$) and the input BCB ($\hat{b}_m(\mathrm{L})$), and it is fixed by the boundary conditions. Note that $\widehat{D}_R^{(in)}$ and $D_R^{(in)} = \left(\sum_m f_m(0) b_m(\mathrm{L})\right)/\left(P_f P_b\right)^{1/2}$ are identical up to a phase term and therefore they share the same magnitude. Eq. (3.2.11) can be solved numerically for determining $\widehat{D}_R(\mathrm{L})$ in the complex domain. It is however useful to derive an equation for the magnitude $\left|\widehat{D}_R(\mathrm{L})\right| \equiv |D_R(\mathrm{L})|$. For the sake of simplicity, an example case where the powers of the FS and the BCB are identical (ΔP=0) is analysed, then Eq. (3.2.11) can be further simplified with v=0, w=1, and h=$|\widehat{D}_R(\mathrm{L})|$:

$$\widehat{D}_R(\mathrm{L}) = \frac{i\widehat{D}_R^{(in)} h - \widehat{D}_R(\mathrm{L})\, sin(T\,h)}{ih\,cos(T\,h)} \tag{3.2.12}$$

By multiplying Eq. (3.2.12) with $ih\,cos(T\,h)$, the following condition can be obtained:

$$\widehat{D}_R(\mathrm{L})[ih\,cos(T\,h) + sin(T\,h)] = i\widehat{D}_R^{(in)} h \tag{3.2.13}$$

Finally, by computing the magnitude of the left- and right-hand sides of Eq. (3.2.13), one can obtain the relation determining the mode rejection:

$$\sin^2(Th) = \frac{h^2 - |D_R^{(in)}|^2}{h^2 - 1} \tag{3.2.14}$$

In order to obtain an estimate for $|\widehat{D}_R(\mathrm{L})|$, it proves useful to graphically represent Eq. (3.2.14). Figure 3.1 shows an example of the solutions (h), which indicate the correlation coefficients at the fibre output ($|\widehat{D}_R(\mathrm{L})|$). It is worth noting that, despite the existence of multiple solutions (green points of intersection), the system always relaxes towards the one corresponding to the smallest value of h, namely h_1. Figure 3.1 compares the solutions with different fibre lengths (L), suggesting that in a highly nonlinear regime (T>>1 with sufficiently high L or Q), the solution h_1 will approach 0. With a further approximation by eliminating h, Eq. (3.2.14) can be recast as $|\widehat{D}_R(\mathrm{L})| = |D_R(\mathrm{L})| = asin(\,|D_R^{(in)}|\,)/T$, which indicates that $D_R(\mathrm{L})$ will decrease to 1/(QL). Under this estimation, if the input BCB is coupled into a specific mode, for instance, the m-th mode, such that $b_m(\mathrm{L}) = \sqrt{P_b}$ and $b_{n\neq m}(\mathrm{L}) = 0$, then $|D_R(\mathrm{L})| = (\sum_m f_m(\mathrm{L}) b_m(\mathrm{L}))/(P_f P_b)^{1/2}$ reduces to $f_m(\mathrm{L})/\sqrt{P_f}$. The condition $|D_R(\mathrm{L})| \to 0$ implies that $|f_m(\mathrm{L})| \to 0$, suggesting that the output FS carries no energy in the m-th mode irrespective of the input conditions of the FS, meaning the m-th mode is rejected at the fibre output.

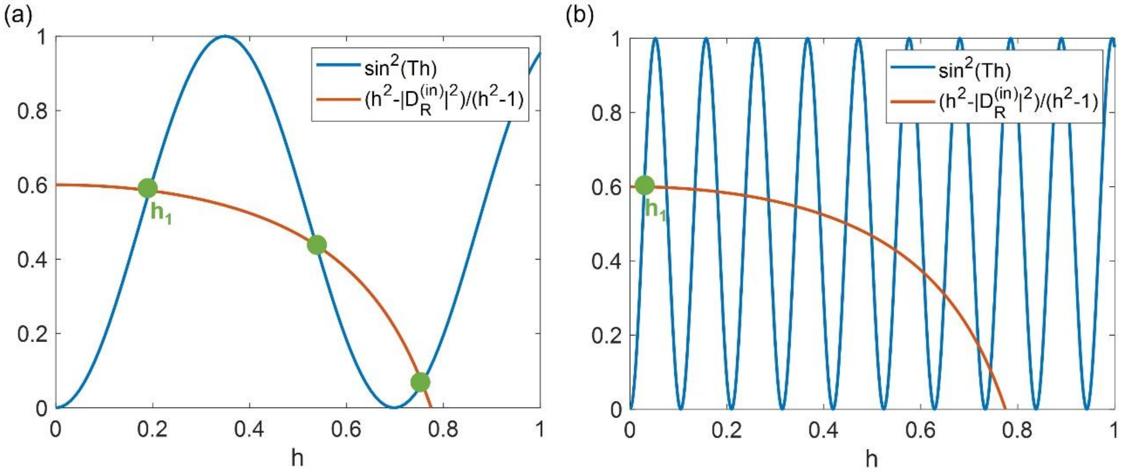

Figure 3.1 Graphical representation of Eq. (3.2.14) when ΔP=0. The parameters are set as: (a) ρ=1, γ=0.003 $\mathrm{W^{-1}m^{-1}}$, L=0.2 m, Q=10 kW, $|D_R^{(in)}|^2$=0.6; (b) ρ=1, γ=0.003 $\mathrm{W^{-1}m^{-1}}$, L=1 m, Q=10 kW, $|D_R^{(in)}|^2$=0.6.

3.2.2 Simulations

A striking feature of Eqs. (3.2.1) and (3.2.2) is that they exhibit the same mode rejection dynamics even in the general case where the Kerr coefficients γ_{mn} are arbitrary. Indeed, one could still observe a relaxation towards a stationary state and again the nonlinear interaction among the counter-propagating modes performs as an underpinning "driving force" that leads to mode rejection. To illustrate and confirm the validity of the theoretical estimation shown in Figure 3.1, a simulation tool is used to numerically solve the coupled nonlinear Schrödinger equations (Eqs. (3.2.1) and (3.2.2)) via a standard finite-difference method[110]. The evolution of the counter-propagating beams $F_m(z)$ and $B_m(z)$ can be numerically solved with the defined boundary conditions. The validity of the simulation tool was tested against a different numerical tool (the shooting method[128]) and compared with the experimental results of mode rejection, which are demonstrated in the following sections of this chapter.

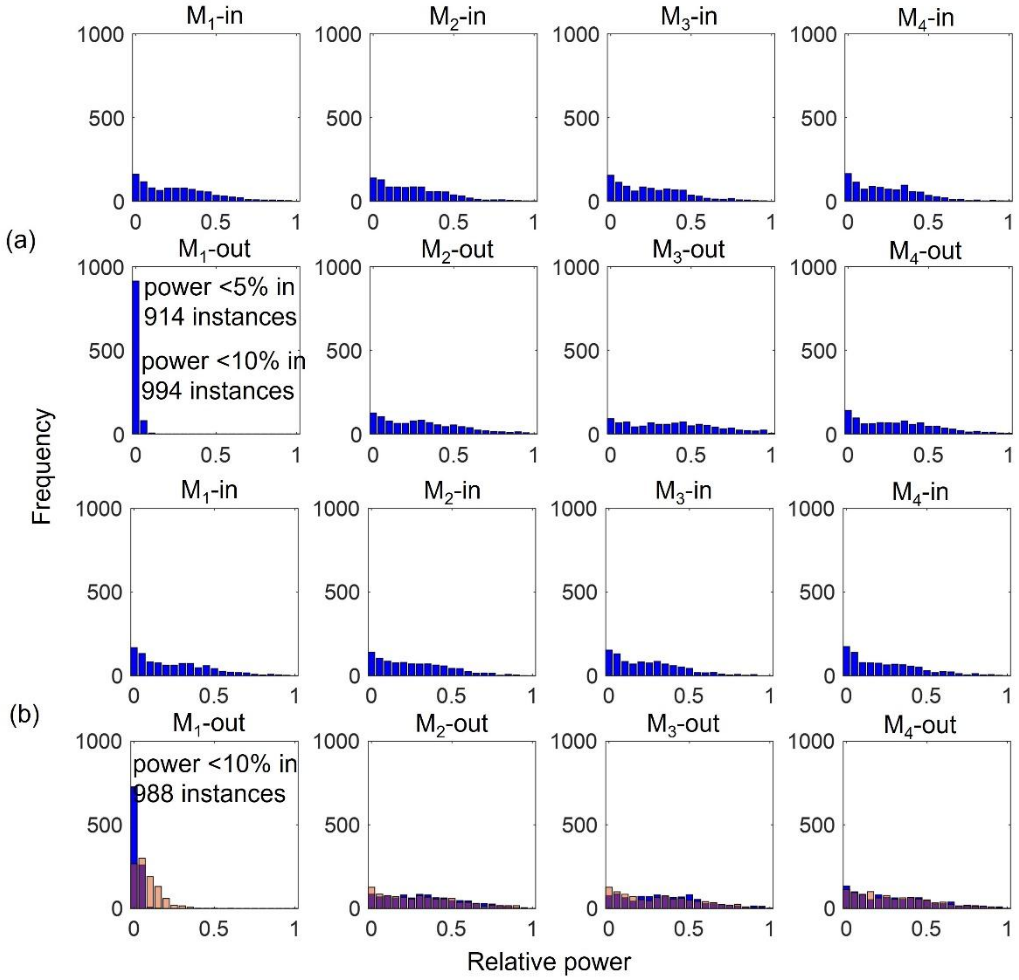

Figure 3.2 Distribution function of the input relative powers $|F_m(t,0)|^2/P_f$ and of the output relative powers $|F_m(t,0)|^2/P_f$ of the FS when simulating 1000 instances of Eqs. (3.2.1) and (3.2.2). The FS and the BCB are continuous waves in (a), whereas they are pulsed waves in (b). The following set of Kerr coefficients is used in each simulation: γ_{11}=1 W^{-1}km^{-1}; γ_{22}=1.5 W^{-1}km^{-1}; γ_{33}=1.6 W^{-1}km^{-1}; γ_{44}=1.2 W^{-1}km^{-1}; γ_{12}= γ_{21}=0.7 W^{-1}km^{-1}; γ_{13}= γ_{31}=1.1 W^{-1}km^{-1}; γ_{14}= γ_{41}=0.8 W^{-1}km^{-1}; γ_{23}= γ_{32}=0.7 W^{-1}km^{-1}; γ_{24}= γ_{42}=1 W^{-1}km^{-1}; γ_{34}= γ_{43}=0.9 W^{-1}km^{-1}.

Figure 3.2 shows the simulation of Eqs. (3.2.1) and (3.2.2) when using a 0.4m-long 4-mode fibre with arbitrary Kerr coefficients as listed in the caption. In Figure 3.2(a) the FS and the BCB are co-polarized continuous waves, both with average powers of $P_f = P_b$ = 2.5 kW. By running 1000 simulations where the 4 modes are randomly coupled into the input FS while the input BCB only coupled to the M_1 mode, the power distribution among the modes in the output FS is redistributed. The dispersed power distribution function of the input and output FS is shown in Figure 3.2(a). The top row represents the power distribution for the modes in the input FS, and the bottom row represents the power distribution for the modes in the output FS. The result clearly illustrates an effective rejection of the M_1 mode from the output FS. In almost all 1000 instances, the power of the output FS coupled to the M_1 mode is lower than 10% and is less than 5% in 914 instances.

In comparison to the CW regime, 1000 simulations were also implemented considering the co-polarized FS and BCB with pulse widths of 1 ns and peak powers of 2.5kW (semi-transparent red bars in Figure 3.2(b)) and 40 kW(blue bars in Figure 3.2(b)), respectively. Figure 3.2(b) displays the power distribution functions over the 4 modes for the input FS and output FS. In this case, the input BCB is also coupled to the M_1 mode while the input FS is randomly coupled with the 4 modes. A comparison between Figure 3.2(a) and (b) reveals that the efficiency of rejecting the M_1 mode is lower in Figure 3.2(b). In 988 out of 1000 simulations, the power of the output FS coupled to the M_1 mode is less than 10% when using much higher peak powers. However, when the peak power is not high enough (for instance, 2.5kW in Figure 3.2(b)), the rejection of a specific mode is inefficient. This inefficiency arises because the pulse length of a 1 ns pulse in fibres is ~0.2 m, meaning that the maximum interaction length of the FS and the BCB is also 0.2m, provided the two pulses encounter inside the fibre. Despite using the same fibre length and same peak/average power for the pulsed/CW simulation, the nonlinearity (effective fibre length times coupled power) is lower in the pulsed case. However, the nonlinearity can be increased by using pulses with longer pulse widths or with higher peak powers.

Indeed, the simulations align closely with the theoretical predictions in both CW and pulsed regimes. They illustrate that a specific mode can be selectively rejected from the output FS regardless of its input launching mode composition, as long as a backward-injected intense BCB is coupled to the rejected mode with similar power as the input FS.

3.3 Rejection of LP modes in multimode fibres

3.3.1 Experimental setup and mode decomposition of multimode fibres

In this section, the mode rejection effect is experimentally investigated using several few-mode fibres. The selective rejection of different LP modes is demonstrated to validate the theoretical and simulation predictions. The experiments were conducted in commercial PM fibres (PM1550-xp, PMHN1, and PM2000) and non-PM isotropic fibres (SMF28).

3.3.1.1 Experimental setup

To experimentally illustrate the mode rejection process, few-mode fibres were first utilized to explore the mode conversion of the FS controlled by the BCB. A schematic of the experimental setup is depicted in Figure 3.3. The output from an in-house built linearly polarized laser source (a YDF MOPA system operating at a wavelength of 1040 nm and emitting ~0.5 ns Gaussian-shaped pulses with maximum peak power of ~40 kW) is passed through a free-space isolator (ISO, Coherent PAVOS) to prevent damage from the backward beams. Then the input beam was split into two beams to work as the FS and BCB using a combination of a half-wave plate (HWP) and a polarization beam splitter (PBS). The FS and BCB were injected at opposite ends of test fibres, including bimodal fibres (PM1550-xp, PMHN1, SMF28) supporting the LP_{01} and LP_{11} mode, and a 6-mode fibre (PM2000) supporting the propagation of LP_{01}, LP_{11e}, LP_{11o}, LP_{21e}, LP_{21o}, and LP_{02} modes. Both ends of the test fibres were perpendicularly cleaved for high-quality mode excitation. A phase plate (PP) and a spatial light modulator (SLM, Holoeye PLUTO) were employed to excite different combinations of the spatial modes propagating in the fibre. The combination of HWP, PBS and another HWP was used to control the power and polarization states of the input FS and BCB beams. The output FS and BCB were sampled with optical wedges and observed at different polarization orientations on a camera by using a rotatable linear polarizer. The wedges were placed with the incident beam angle of ~10 degrees ensuring that the sampled beam maintains a similar polarization state to the output beam. The far-field (FF) and near-field (NF) beam profiles were collected with cameras placed after a beam splitter (BS) and a lens. The coupling efficiency of the FS and BCB into the test fibres was characterized by measuring both the input power (with unused power from the FS(BCB) recorded by the power meters (PWM), as shown in Figure 3.3) and output power from the test fibres.

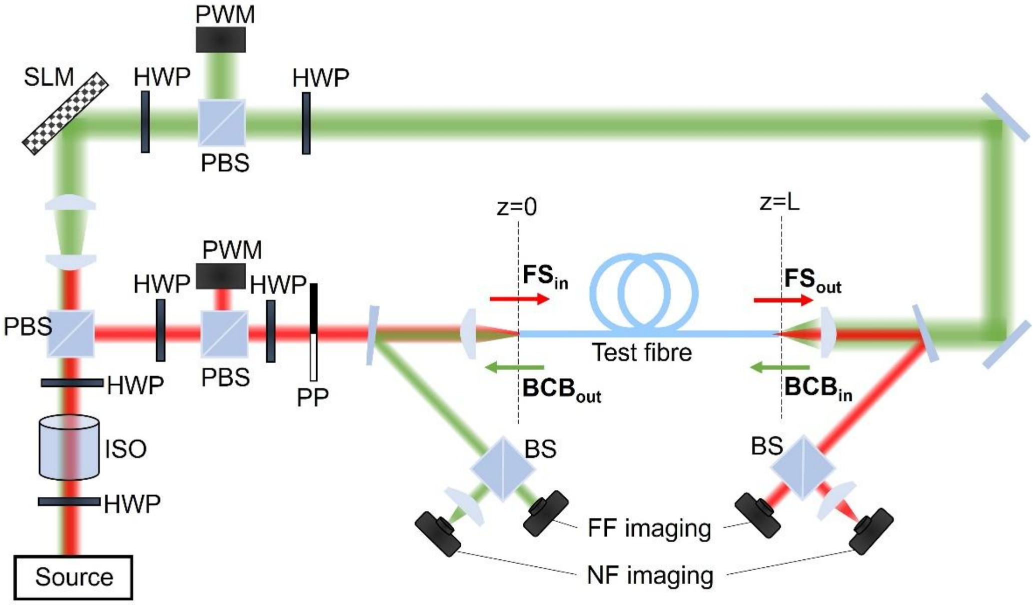

Figure 3.3 Schematic experimental setup for the investigation of mode rejection.

The pulse length is ~0.1 m in the fibre, and the nonlinear interaction length for the counter-propagating pulses is ~0.2m. Considering the limitations imposed by the size of optics and multi-axis stages, as well as the need to mitigate Raman amplification, the test fibres was chosen to be between 0.4m and 2m in length. With a coupled peak power of ~10 kW and a Kerr coefficient γ=3 $W^{-1}km^{-1}$, the nonlinear length is ~0.03 m, which is significantly smaller than the dispersion length. The group velocity dispersion parameter β_2 is ~20 ps^2/km for the test fibres at a wavelength of 1040 nm, allowing the dispersion to be neglected in the experiments with 0.5ns pulses. This was confirmed by measuring the output pulse shape and spectrum, which showed no significant changes compared to the input pulse shape and spectrum.

In addition to qualitatively monitoring the mode conversion on the camera, mode decomposition is implemented by numerically analysing the near-field beam profiles. The camera, placed on an optical rail, captures the beam profiles around the focal plane of the lens positioned before the NF imaging camera (see Figure 3.3). The focal length of the lens used to collimate the output signal is 20 mm. Another lens with a focal length of 500 mm is placed ~520 mm away from the collimating lens, forming a 4-*f* system that images the fibre end facet with a magnification factor of 25x. The camera (Beamage-3.0, Gentec) has a pixel size of 5.5 μm, providing sufficient resolution for the near-field beam profiles (filling ~2000 pixels) of a fibre with a mode field diameter of ~10 μm. The complex amplitude (intensity and phase) of the output beams in the near-field is retrieved using an iterative phase retrieval method[43, 74]. The retrieved field is then decomposed over the fibre eigenmodes to obtain the relative mode content and relative phase, as introduced in section 2.2.2. An optimization method, the stochastic parallel gradient descent algorithm (SPGD)[75], is used to compensate for mode decomposition errors induced by noise and aberrations.

3.3.1.2 Mode decomposition of LP modes

The mode decomposition method for few-mode fibres used in this thesis consists of two procedures: data acquisition and post-processing. After aligning the experimental setup (see Figure 3.3), beam profiles are measured at three different positions (before, on, and after the focal plane) by translating the camera along an optical rail. The complex amplitude can then be retrieved iteratively by virtually propagating the beam from one position to another in a sequential order. As shown in Figure 3.4, the intensity profiles (I_1, I_2, I_3) are measured at three different positions (z_1, z_2, z_3). Intensity profiles are typically collected near a magnified near-field using a 4-*f* system, with the resulting image size on the order of a few hundred micrometres. These profiles are used to retrieve the phases (P_1, P_2, P_3) and complex amplitudes (E_1, E_2, E_3). Starting from an initial guessed phase ($P_{initial}$), the complex amplitude E_1 is constructed. E_1 is then virtually propagated to position z_2 by using the angular spectrum theory [43], yielding E_2. At this stage, E_2

is updated by replacing its amplitude with the square root of the measured intensity I₂ while retaining the phase information (P₂). This procedure is repeated, iteratively updating the complex amplitudes between the three positions until the phase and complex amplitude are accurately retrieved after sufficient rounds of iteration.

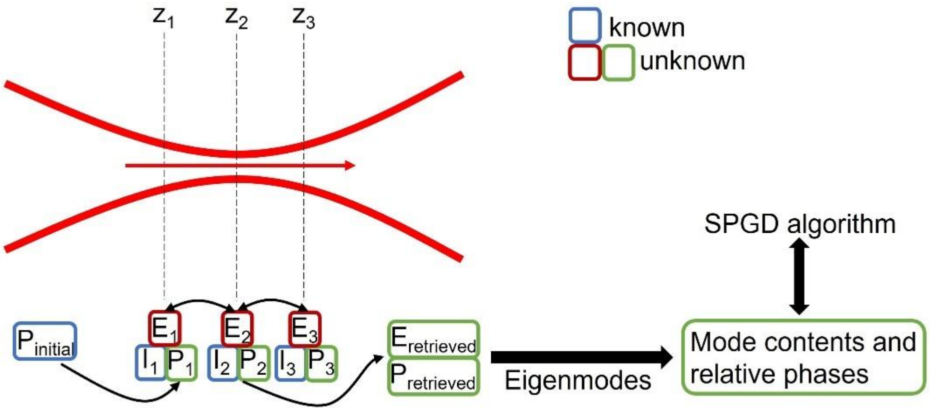

Figure 3.4 Schematic of the mode decomposition method used for FMFs.

Once the complex amplitude at the focal plane (z_2) is retrieved, the complex modal coefficients C_{mn} can be calculated by applying the correlation calculation between the retrieved complex amplitude and the fibre eigenmodes[72]:

$$C_{mn} = \frac{\iint E_{retrieved}(x,y)\cdot E_{LPmn}^{*}(x,y)\,dxdy}{\sqrt{(\iint |E_{retrieved}(x,y)|^2\,dxdy)(\iint |E_{LPmn}(x,y)|^2\,dxdy)}} = c_{mn}\exp(i\theta_{mn}) \quad (3.3.1)$$

where E_{LPmn} is the complex amplitude of the LP_{mn} mode, c_{mn}^2 and θ_{mn} are the mode content and phase of this mode. To evaluate the mode decomposition results, the multimode electric fields are typically reconstructed by superposing all the supported LP modes:

$$E_{reconstructed}(x,y) = \sum C_{mn}E_{LPmn}(x,y) \quad (3.3.2)$$

The reconstructed field $E_{reconstructed}$ is theoretically equal to the retrieved field and should have the same intensity distribution as the measured beam profiles. However, in practice, they can differ due to noise and aberrations in the measuring system. Additionally, the theoretically defined LP modes might deviate from the actual LP modes supported by the fibre, as the magnified complex amplitude of LP modes is used in mode composition methods to ensure sufficient spatial resolution. This discrepancy in E_{LPmn} can introduce errors in mode decomposition. To achieve more accurate results, the modal coefficients are further optimized by using the SPGD algorithm, which minimizes the difference between the reconstructed field and the measured beam profile.

3.3.2 Mode rejection in polarization-maintaining fibres

3.3.2.1 Mode rejection in PM1550-xp

To simplify the analysis, the initial investigation of mode rejection focuses on the scalar regime, where the counter-propagating beams are in the same polarization state. This configuration is facilitated by employing polarization-maintaining fibres and polarized input beams. Initially, a bimodal PM fibre (PM1550-xp, Thorlabs) is utilized in the experiment. The refractive index profile and core geometry of the fibre are measured using an Interferometric Fibre Analyser (Rayphotonics IFA-100). The measured refractive index profiles are depicted in Figure 3.5, indicating a core-to-cladding index difference (Δn) of ~0.0054, corresponding to a core numerical aperture (NA) of 0.125. Additionally, the stress rod exhibits a lower refractive index than the cladding, with a difference of 0.012.

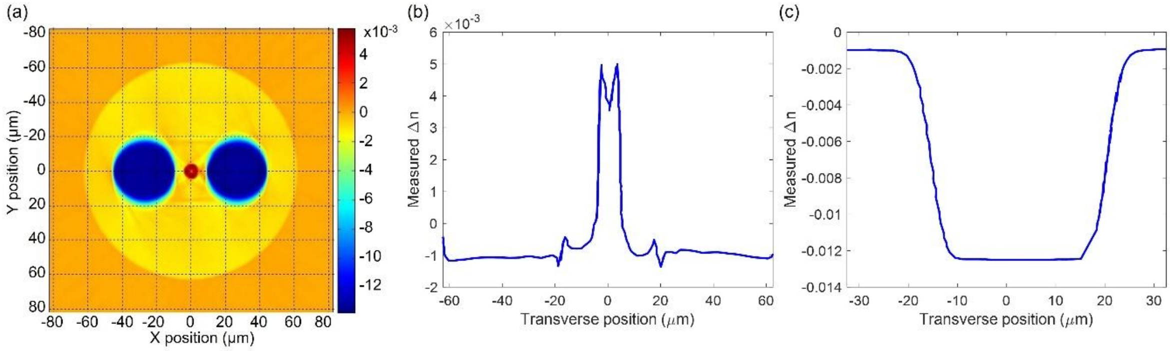

Figure 3.5 Refractive index profile measurement for PM1550-xp. (a) 2D refractive index profile. (b) Refractive index profile along the fast axis. (c) Refractive index profile of the stress rod.

Table 3.1 The dispersion and nonlinear coefficients for PM1550-xp

Dispersion	β (μm^{-1})	β_1 (ps/mm)	β_2 (ps^2/km)
LP_{01}	8.7857	4.8987	14.6301
LP_{11}	8.7714	4.8986	26.4917
Kerr coefficient	γ=3 $W^{-1}km^{-1}$		
Overlap factor f_{m1_m2}	m1=LP_{01}	m1=LP_{11e}	m1=LP_{11o}
m2=LP_{01}	1	0.5770	0.5567
m2=LP_{11e}	0.5770	0.8617	0.2796
m2=LP_{11o}	0.5567	0.2796	0.8144

Next, the propagation constants, dispersion, and nonlinear coefficients of this fibre at a wavelength of 1μm were computed based on the measured index profile using Comsol software.

The PM1550-xp fibre supports the propagation of LP_{01} and LP_{11} modes, with their corresponding coefficients listed in Table 3.1. For simplicity in the subsequent analysis, the degenerate LP_{11} mode (LP_{11e}, LP_{11o}) is considered as a single mode. Therefore, the mode rejection of the LP_{01} mode leads to mode conversion towards these two quasi-degenerate LP_{11} modes.

Prior to the mode rejection experiments, a 1m length of the PM1550-xp fibre was placed in the experimental setup (see Figure 3.3), where the polarization extinction ratio (PER) of the output signal beam was evaluated. When solely launching signal beams with either the LP_{01} mode or the LP_{11} mode at different power levels, the PER of the output signal beam ranged from 13 to 28 dB, as illustrated in Figure 3.6. Notably, the input beam exhibited a good PER of ~28 dB. The observed variation in the output beam's PER can be attributed to slight polarization fluctuations in the laser source and the sensitivity of the HWP angles (see Figure 3.3), which are utilized to align the input linear polarization state with the fast/slow axis of the PM1550-xp. With the PER of the output beams from the 1-m PM1550-xp consistently surpassing 12dB, the scalar regime approximation is satisfactorily met.

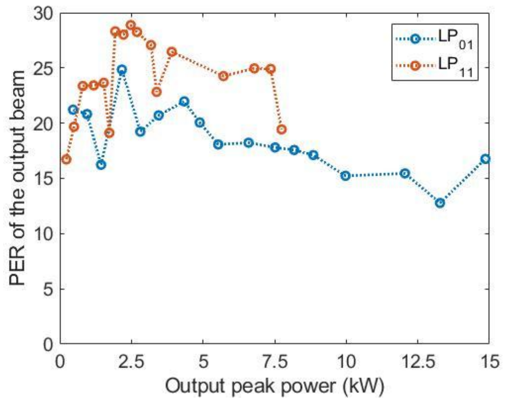

Figure 3.6 PER of the output beams from a 1m-long PM1550-xp fibre

The mode rejection experiments began with rejecting the LP_{01} mode in the FS. In this scenario, the BCB was only coupled into the LP_{01} mode, while the FS was coupled into a combination of the LP_{01} and LP_{11} modes. To ensure the nonlinear interaction involved counter-propagating modes with the same polarization states, the polarization state of the input FS and BCB was orientated along the slow or fast axis by optimizing the rotation angles of the two HWPs before the fibre ends. Figure 3.7 shows the evolution of the modal distribution in the output FS as the BCB power varied, while the total input FS power was kept constant at ~15 kW. The coupling loss was ~1 dB for the LP_{01} mode and ~4 dB for the LP_{11} mode, resulting in the FS being coupled with a peak power of 6 to 12 kW when coupled with the combination of the two LP modes. The maximum peak power of the BCB was ~8 kW. Figure 3.7(a) displays the result when the input FS was primarily coupled to the LP_{01} mode, holding ~83 % of the FS power (point A). As the BCB power increased, the FS spontaneously converted towards the LP_{11} mode, effectively rejecting the LP_{01} mode. Figure 3.7(b) provides the corresponding output beam profiles of the FS. The conversion efficiency was ~34 %, limited by system insertion loss and the available laser power. Alternatively, the mode rejection of the LP_{01} mode was further investigated with an input FS coupled with a combination of modes, with ~46% of the power coupled to the LP_{01} mode (point D), as shown in Figure 3.7(d) and (e). The output FS rejected the LP_{01} mode and efficiently self-organized into the two-lobe LP_{11} mode (point F in Figure 3.7(e)), which contained ~90 % LP_{11} mode. The MD method introduced in section 3.3.1.2 was implemented at each BCB power, and the mode contents in Figure 3.7(a) and (d) were obtained from MD. Additionally, the beam quality factor M^2 was calculated from the retrieved complex amplitude by virtually propagating the electric field within several Rayleigh lengths[43]. Figure 3.7(c) and (f) show the calculated M^2 of the FS output at different BCB powers, indicating that the beam quality worsened (M^2 increased with more LP_{11} mode content) as the BCB power increased, corresponding to a decrease in LP_{01} mode content. It is worth noting that the curves in Figure 3.7 are not smooth, which could be attributed to mode decomposition error (deviation along y-axis direction in (a) and (d) and the corresponding M^2 value deviation in (c) and (f)) as well as BCB power variation (along x-axis direction, resulting from variation in coupling efficiency).

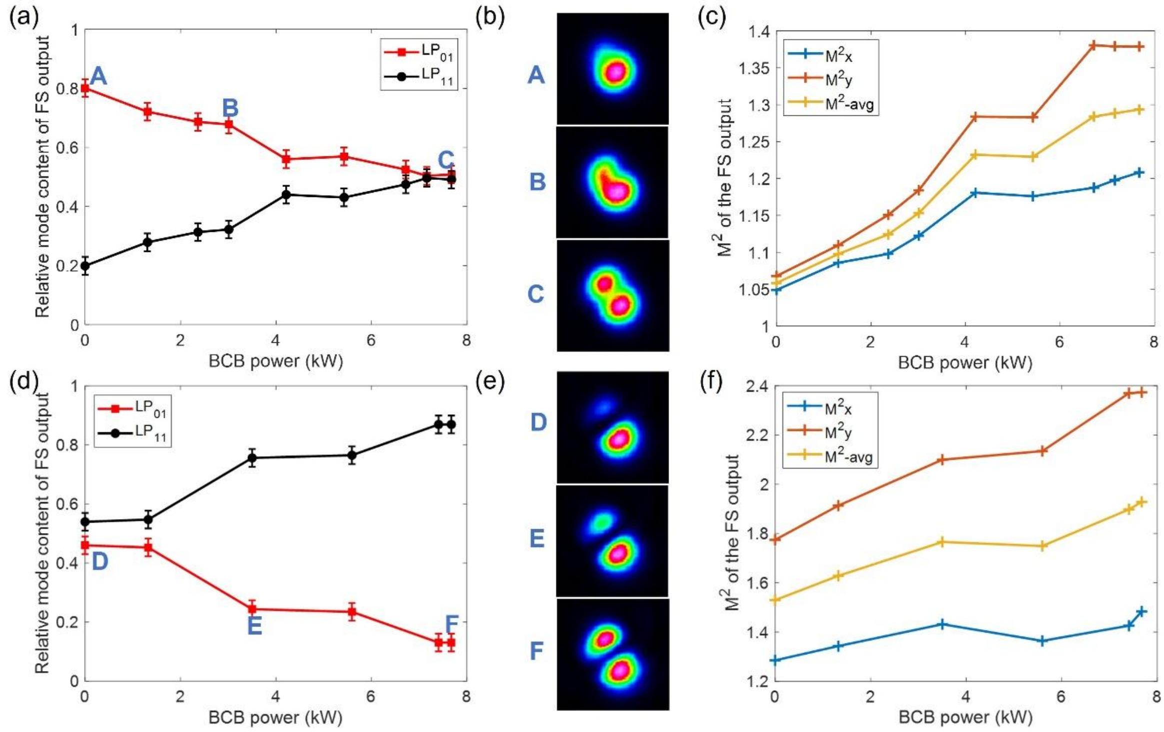

Figure 3.7 Mode rejection of the LP_{01} mode in the PM1550-xp with the input FS coupled into different combinations of modes and the BCB coupled into the LP_{01} mode. (a), (d) Relative mode content of the output FS as a function of the BCB power. Error bars of ±2% are added in the experimental results to represent the estimated uncertainty of the MD algorithm (see Section 3.3.1.2). (b), (e) Output FS beam profiles corresponding to different BCB powers (labelled A - F). (c), (f) The calculated M^2 factor for the output FS versus the BCB powers.

To illustrate the MD accuracy in the measurements, two examples of MD results are provided in Figure 3.8, corresponding to results at point A (BCB=0 kW) and point C (BCB=7.7 kW) as labelled in Figure 3.7(a). Figure 3.8(a) shows the FS consists of ~4.8 % LP_{11e} and ~12.3 % LP_{11o} modes when the BCB is switched off, while Figure 3.8(c) shows the content of the LP_{11e} and LP_{11o} modes increases to ~17.1 % and ~34.1 % respectively when the BCB is switched on, resulting in ~34 % power reduction in the LP_{01} mode. Figure 3.8(b) and (d) display the intensity and phase distribution reconstructed from the MD results. The two-dimensional correlation coefficients [74] of the reconstructed intensity profiles with respect to the measured ones are higher than 99%, which is the typical value for MD accuracy based on the intensity measurements[67].

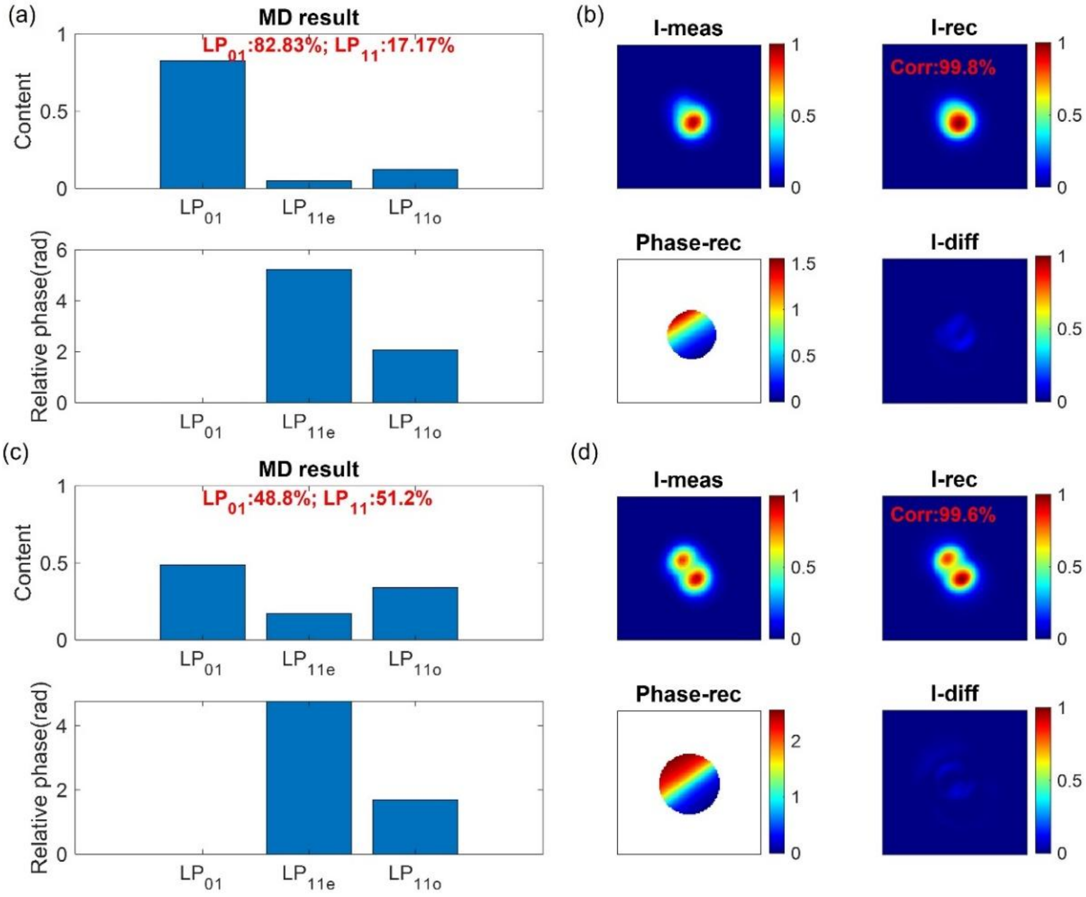

Figure 3.8 Mode decomposition results at points A and C shown in Figure 3.7(a). (a), (c) MD results: normalized mode contents of LP_{01}, LP_{11e}, and LP_{11o} modes and the relative phase between them. (b), (d) Reconstructed intensity and phase based on the MD results in comparison with the measured intensity. I-meas: measured intensity, I-rec: reconstructed intensity, Phase-rec: reconstructed phase, I-diff: discrepancy between I-meas and I-rec, Corr: two-dimensional correlation coefficient.

In contrast, the mode rejection of the LP_{11} mode in the FS is investigated next, with the input FS coupled with a combination of the LP_{01} and LP_{11} modes while the BCB is coupled into the LP_{11} mode. Figure 3.9(a) shows the evolution of the output FS modal distribution as the BCB power varies. The input FS is kept constant at a peak power of ~6.5 kW (~10 kW incident at the fibre end), and the BCB is coupled into the LP_{11} mode with a maximum power of ~3 kW (~11.5 kW launched at the fibre end, noting that the low coupling efficiency due to exciting the LP_{11} mode with a phase plate). The output FS gradually evolves towards the LP_{01} mode, with the LP_{11} mode content decreasing by ~28%. Figure 3.9(b) demonstrates that the output FS is converted to a single lobe with more LP_{01} mode output. The rejection of the LP_{11} mode is further confirmed by the improvement in the M^2 factor, as shown in Figure 3.9(c).

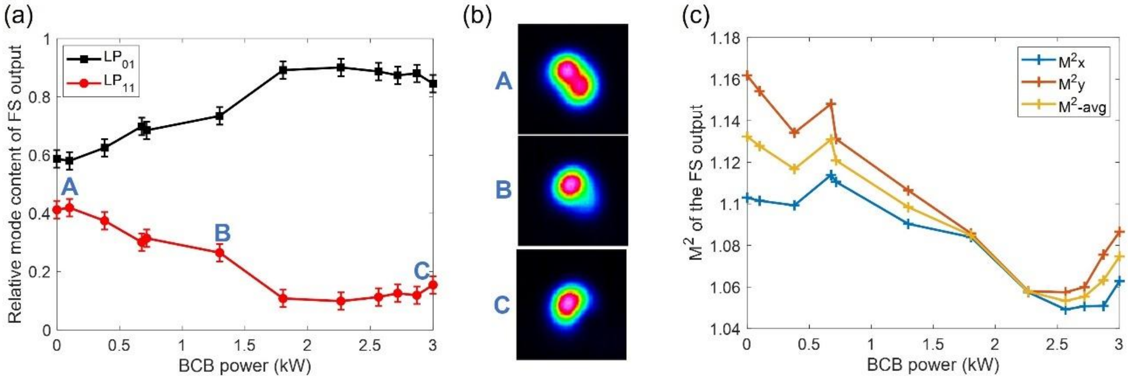

Figure 3.9 Mode rejection of the LP_{11} mode in the PM1550-xp with the BCB coupled into the LP_{11} mode. (a) Relative mode content of the output FS as a function of the BCB power. (b) Output FS beam profiles corresponding to different BCB powers (labelled with A - C). (c) Calculated M^2 factor for the output FS versus the BCB powers.

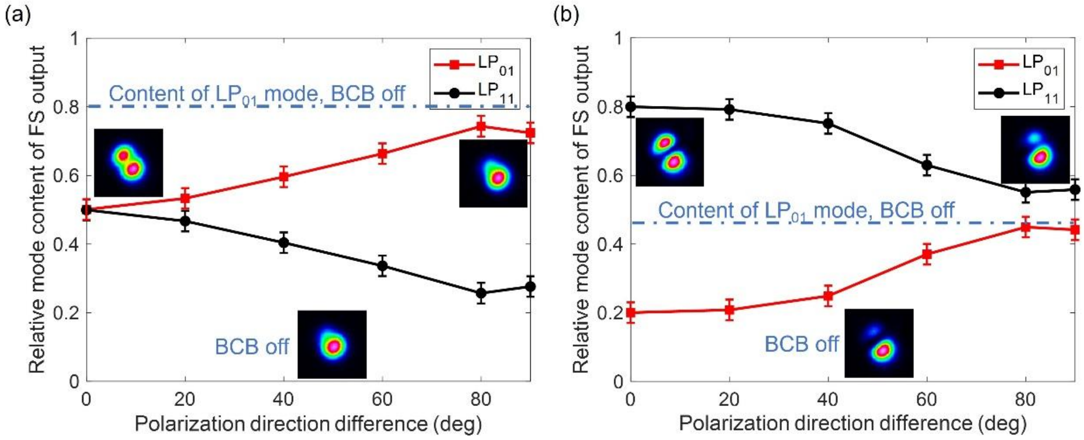

Figure 3.10 Efficiency of mode rejection versus the polarization direction difference between the FS and BCB. The input FS and BCB in (a) and (b) have the same mode compositions as those in Figure 3.7 (a) and (d), respectively.

To gain a more comprehensive understanding of this nonlinear process, two factors affecting the efficiency of mode rejection were experimentally investigated. One factor is the relative polarization states of the counter-propagating beams. Using a PMF ensures the polarization state is well maintained. By continuously adjusting the relative polarization between the FS and the BCB while keeping their powers constant, the efficiency of mode rejection is compared in Figure 3.10. Figure 3.10(a) shows the case having the same mode composition and polarization state as the input FS in Figure 3.7(a), but the input BCB is in the LP_{01} mode with varying polarization states with respect to Figure 3.7(a). Figure 3.10(b) corresponds to Figure 3.7(d) but also features a varying polarization state for the input BCB. The results illustrate that maximized rejection is achieved when the FS and BCB are co-polarized (0-deg polarization direction difference, with both beams being linearly polarized). The efficiency of mode rejection decreases as the polarization difference increases. The reduction in the LP_{01} mode content is ~30 % at a 0-deg polarization difference and ~10 % at a 90-deg difference. This variation in mode rejection efficiency aligns with the predicted coupling coefficient p (see Eqs. (3.2.1) and (3.2.2)), where the p=2 corresponds to the co-polarized condition and p=2/3 to the orthogonally polarized condition. A conversion efficiency comparable to the co-polarized case can be achieved under orthogonal polarization if the power of the input FS and BCB is increased threefold. Figure 3.10 also illustrates that when the FS and BCB are orthogonally polarized, the output FS beam profile remains similar whether the BCB is switched on or off, as shown by the dashed lines and inset pictures.

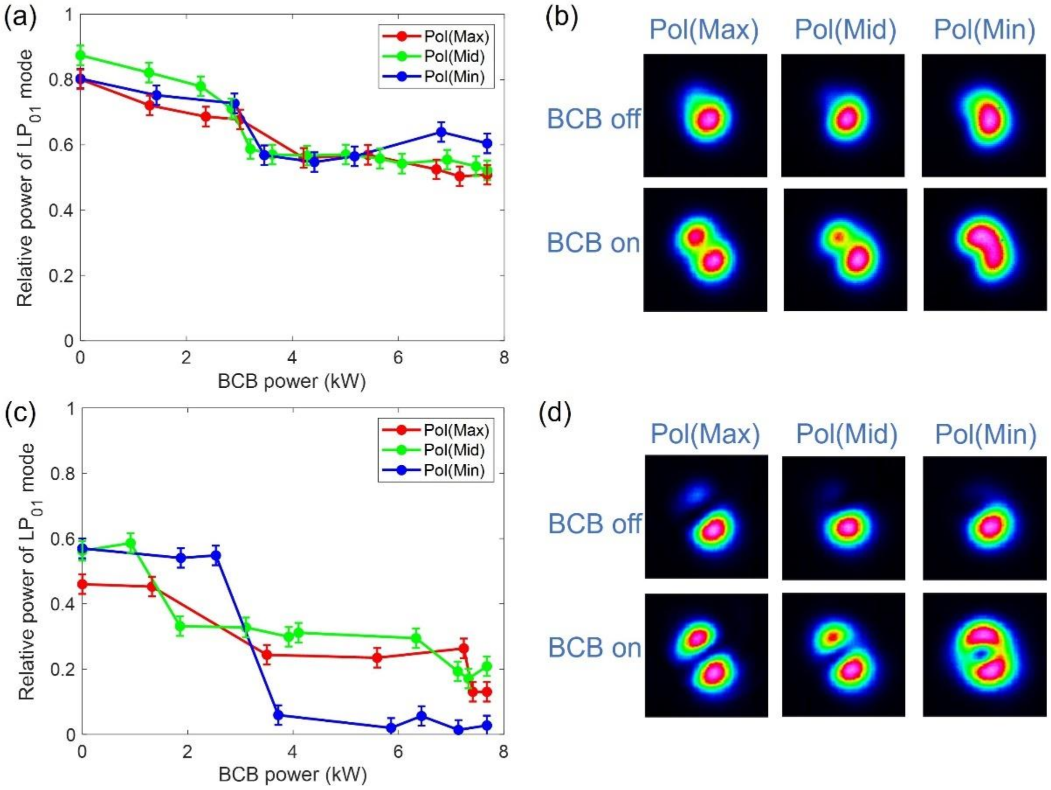

Figure 3.11 Mode rejection observed in different polarization orientations with the BCB coupled into the LP_{01} mode. (a), (c) Mode content of the LP_{01} mode versus the BCB power when observed in different polarization directions. (b), (d) Comparison of the FS output beam profiles at different polarization directions when the BCB is switched on/off. Pol(Max/Mid/Min): polarization direction containing the maximum/medium/minimum power of output FS.

Another factor to consider is the relationship between the polarization states of the output FS and the orientation of polarization where mode rejection is observed using camera (assuming the FS and the BCB are linearly polarized, and a rotatable linear polarizer is positioned before the camera). In Figure 3.7 and Figure 3.9, mode conversion was observed in the polarization orientation aligned with the axis containing the maximum power, as the sampled FS output (see Figure 3.3) is linearly polarized with a PER of ~11 dB. However, it is worth measuring mode conversion in other polarization orientations. For instance, Figure 3.11 illustrates the evolution of the LP_{01} mode content with respect to the BCB power when measuring at three polarization directions by rotating the polarizer before the camera. In these measurements, the input BCB is coupled to the LP_{01} mode, and the counter-propagating beams are co-polarized. The curves and FS output beam profiles indicate that the rejection of the LP_{01} mode exhibits similar efficiency across different polarization orientations.

In conclusion, this section demonstrates the mode rejection of the LP_{01} and LP_{11} modes in PM1550-xp by injecting counter-propagating beams into the fibre. The experimental findings align well with the theoretical predictions: when two counter-propagating beams with comparable powers propagate in a multimode fibre, the forward signal organizes itself to reject the mode matching that of the backward control beam. Maximal mode rejection efficiency occurs when the two beams are co-polarized, with mode conversion efficiency gradually dropping as the polarization states of the counter-propagating beams diverge. Utilizing a 1m-long PM1550-xp and a total peak power of ~16kW, rejection of the LP_{01} or LP_{11} modes is achieved with a conversion efficiency of ~30%.

3.3.2.2 Mode rejection in PMHN1

The PM1550-xp fibre exhibits standard nonlinearity due to its regular fibre core diameter. To further explore the mode rejection effect and its applicability to other fibres, a highly nonlinear PMHN1 (Thorlabs) was used. The PMHN1 features an elliptical core with a mode field area of ~12.4 μm^2 and a mode field diameter of ~4 μm, resulting in higher nonlinearity compared to the PM1550-xp. The PMHN1 supports two-mode propagation at a wavelength of 1 μm, specifically the LP_{01} mode and LP_{11} mode. Figure 3.12 shows the cross-section image of the PMHN1 and the supported LP mode distributions at 1 μm. The dispersion and nonlinear coefficients of the LP modes for this fibre are listed in Table 3.2.

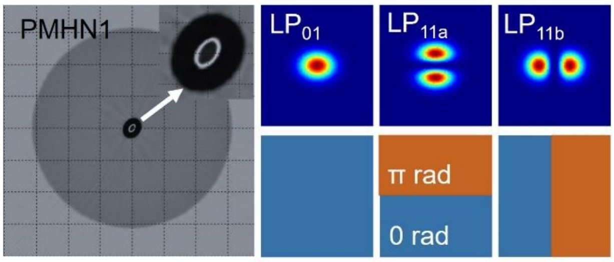

Figure 3.12 Cross section of the PMHN1 and the supported LP modes at 1 μm

Table 3.2 The dispersion and nonlinear coefficients for PMHN1

Dispersion	β (μm^{-1})	β_1 (ps/mm)	β_2 (ps^2/km)
LP$_{01}$	8.8737	4.9782	15.5632
LP$_{11e}$	8.8267	4.9901	22.4802
LP$_{11o}$	8.7947	4.9789	57.2380
Kerr coefficient	γ=13.2 W^{-1}km^{-1}		
Overlap factor f_{m1_m2}	m1=LP$_{01}$	m1=LP$_{11e}$	m1=LP$_{11o}$
m2=LP$_{01}$	1	0.6372	0.5544
m2=LP$_{11e}$	0.6372	0.9467	0.2911
m2=LP$_{11o}$	0.5544	0.2911	0.8112

Following similar procedures to those used in the PM1550-xp experiments, a ~0.4 m long PMHN1 fibre was placed in the counter-propagating setup (see Figure 3.3). Prior to the high-power experiments, a series of preliminary optimizations were conducted at a low power level. These optimizations included adjusting the rotation angles of the waveplates, the phase patterns loaded onto the SLM, the position of the phase plate, and the choice of lenses. The BCB was selectively coupled into either the LP$_{01}$ or LP$_{11}$ mode by changing the phase pattern displayed on the SLM (the phase pattern for the LP01 mode is a flat phase profile, whereas the phase pattern for the LP11 mode is split into two regions with π phase difference), while the FS was coupled into a combination of the LP$_{01}$ and LP$_{11}$ modes by adjusting the position of the phase-plate with respect to the incident beam. The polarization state of the input FS and BCB was aligned along the slow or fast axis to ensure that the nonlinear interaction involved the counter-propagating modes with the same polarization states.

Figure 3.13 illustrates the rejection of the LP$_{01}$ and LP$_{11}$ modes in the FS in the PMHN1. In Figure 3.13(a), the input BCB is coupled into the LP$_{01}$ mode, and the FS shows a gradual rejection of the LP$_{01}$ mode as the BCB power increases. Initially, 79% of the power is in the LP$_{01}$ mode, this decreases to 50% when the BCB power reaches ~2 kW. Compared to the results with PM1550-xp (see Figure 3.7), achieving a reduction of the LP$_{01}$ mode content from 80% to 50% in PM1550-xp requires counter-propagating beams with a total power of ~16kW (2*8 kW). However, in PMHN1, a similar conversion efficiency is achieved with a total power of ~4 kW (2*2 kW). This discrepancy arises from the difference in nonlinear coupling coefficients between the two fibres, with PMHN1's intra- and inter-modal nonlinear coefficients being ~4 times larger than those of PM1550-xp (see Table 3.1 and Table 3.2).

Figure 3.13(b) demonstrates the mode rejection when the input BCB is coupled into the LP_{11} mode. As the BCB power increases, the output FS shows a gradual rejection of the LP_{11} mode, with its relative power decreasing from 76% to 40% as the BCB power rises from 0 kW to ~2 kW. Figure 3.13(c) illustrates efficiency of LP_{11} mode rejection when varying the relative polarization states between the FS and the BCB, while maintaining the input mode distributions. A significant rejection (26% conversion of LP_{11} mode content) is observed when the BCB is co-polarized (0 deg) with the FS. Conversely, when the BCB is orthogonally polarized relative to the FS, the LP_{11} mode rejection is negligible. These experimental results align well with the simulations (discussed in section 3.2.2) that use the experimental parameters, including pulse duration, peak power, fibre length, mode composition, and the relative polarization state of the counter-propagating beams.

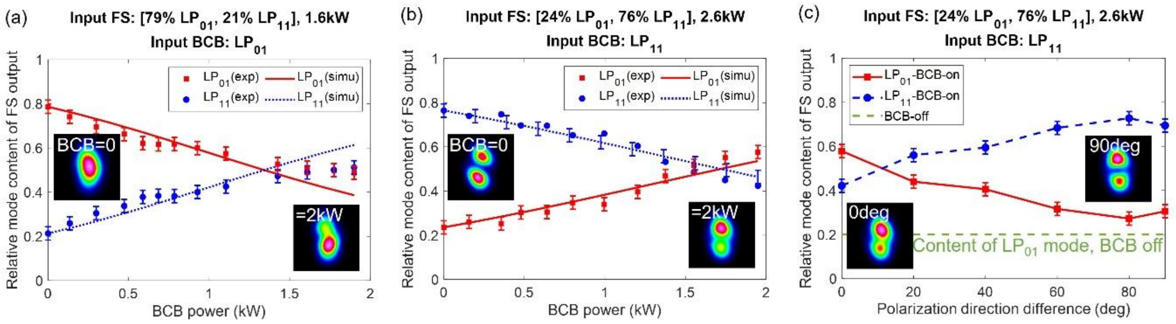

Figure 3.13 Mode rejection of different LP modes in PMHN1 with experimental results (markers) compared to simulations (lines). Abbreviations: exp – experiment, simu - simulation. (a) Rejection of the LP_{01} mode when the input FS is a combination of 79% LP_{01} mode and 21% LP_{11} mode with a total peak power of ~1.6 kW. (b) Rejection of the LP_{11} mode when the input FS is a combination of 24% LP_{01} mode and 76% LP_{11} mode with a total power of ~2.6 kW. (c) Relative power of the FS modes as a function of the polarization difference between the FS and the BCB when the BCB is coupled into the LP_{11} mode.

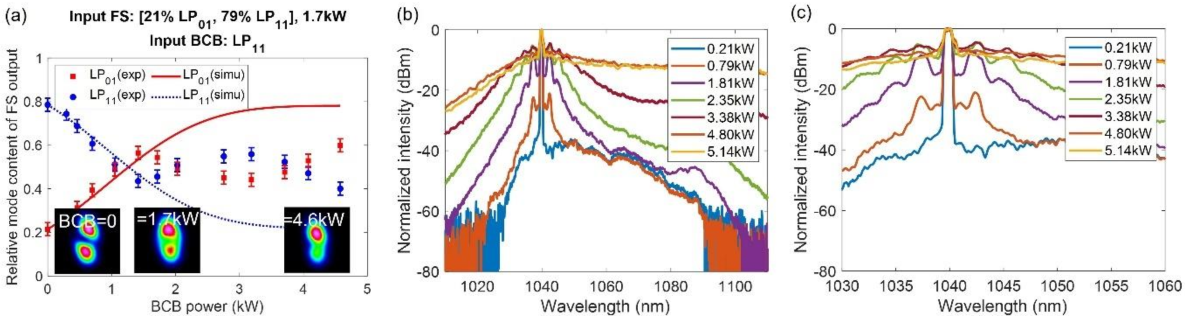

Figure 3.14 Mode rejection of the LP_{11} mode in PMHN1 when further increasing the counter-propagating beam powers. (a) Relative power of the output FS modes versus the launched BCB power, along with the beam profiles at different BCB powers. (b) Measured spectra of the output BCB at different powers when the FS is switched off. (c) A zoomed-in view of the spectra shown in (b).

Given that similar mode rejection efficiency can be achieved in the PMHN1 with ~4 times lower power than in the PM1550-xp, further investigations involved increasing the input power. Figure 3.14 presents results when the counter-propagating beam powers were increased from 2kW to 5kW. The input BCB was coupled into the LP_{11} mode, and the input FS was coupled with a combination of 21% LP_{01} mode and 79% LP_{11} mode. However, instead of observing continued rejection of a specific mode when the BCB power exceeded ~1.8 kW, the relative power of the LP_{11} mode stabilized at 40% – 50%. In Figure 3.14(a), the experimental results diverge from the simulation predictions beyond ~1.8 kW BCB power. This discrepancy can be explained by analysing the output spectra of the BCB at different coupled powers. Figure 3.14(b) and (c) show significant generation of new frequencies when the BCB power exceeds ~1.8 kW, with a supercontinuum observed at ~3.38 kW peak power. Consequently, the effective BCB power at 1040 nm (the central wavelength) constitutes only a portion of the launched power, meaning that the BCB power at 1040 nm does not increase beyond ~1.8 kW. These new frequency components degrade the observation of mode rejection, as the process relies on transverse mode control at the same wavelength within a narrow bandwidth.

To conclude, the mode rejection of the LP_{01} and LP_{11} modes in a 0.4m long highly nonlinear PMHN1 fibre has been experimentally demonstrated. A mode rejection efficiency of ~30% was achieved using a total power of ~4 kW (2*2kW) for the counter-propagating beams, which is ~4 times lower than the power requirement for achieving a 30% mode rejection in the PM1550-xp. The rejection of different LP modes was measured, and the experimental results align well with theoretical predictions and simulations.

3.3.2.3 Mode rejection in PM2000

The PM1550-xp and PMHN1 fibres serve as 2-mode platforms for the experimental implementation of mode rejection. To increase the number of modes and investigate the mode rejection process in a multimode medium, another PMF (PM2000, Thorlabs) is used. The PM2000 fibre supports the propagation of six LP modes at a 1 μm wavelength, including the LP_{01}, LP_{11e}, LP_{11o}, LP_{21e}, LP_{21o}, and LP_{02} modes. The PM2000 has a core diameter of ~7 μm and a numerical aperture of ~0.2. The dispersion and nonlinear coefficients of the LP modes for this fibre are listed in Table 3.3 and Table 3.4.

Following procedures similar to those used for the experiments with PM1550-xp and PMHN1, a ~0.4m long PM2000 was placed in the counter-propagating setup. Preliminary optimizations at low power levels, such as adjusting the waveplate angles and SLM phase patterns, were conducted. The BCB was selectively coupled into either the LP_{01} or the LP_{11} mode by adjusting the position of the phase plate, while the FS was coupled with a combination of LP modes with varying relative powers and phases by modifying the phase pattern loaded on the SLM. The polarization state of the input FS and BCB was orientated along the slow or fast axis of the fibre to ensure that the nonlinear interaction involved counter-propagating modes with the same polarization states.

Table 3.3 The dispersion coefficients for PM2000

Dispersion	β (μm^{-1})	β_1 (ps/mm)	β_2 (ps^2/km)
LP_{01}	8.8290	4.9298	15.2879
LP_{11e}	8.8039	4.9363	16.0593
LP_{11o}	8.8035	4.9363	16.1967
LP_{21e}	8.7730	4.9381	43.0024
LP_{21o}	8.7728	4.9382	43.4914
LP_{02}	8.7667	4.9228	131.0580

Table 3.4 Nonlinear coefficients for PM2000

Overlap factor f_{m1_m2}	m1=LP_{01}	m1=LP_{11e}	m1=LP_{11o}	m1=LP_{21e}	m1=LP_{21o}	m1=LP_{02}
m2=LP_{01}	1	0.6432	0.6430	0.4046	0.4008	0.5207
m2=LP_{11e}	0.6432	0.9419	0.3978	0.5436	0.5412	0.2531
m2=LP_{11o}	0.6430	0.3978	0.9411	0.5296	0.5285	0.2664
m2=LP_{21e}	0.4046	0.5436	0.5296	0.5125	0.5110	0.2312
m2=LP_{21o}	0.4008	0.5412	0.5285	0.5110	0.5111	0.2306
m2=LP_{02}	0.5207	0.2531	0.2664	0.2312	0.2306	0.5148
Kerr coefficient	$\gamma=5.3\ W^{-1}km^{-1}$					

Figure 3.15 and Figure 3.16 provide examples of the rejection of LP_{01} and LP_{11o} modes in the output FS from the PM2000. Figure 3.15 illustrates a scenario where the input BCB is coupled into the LP_{01} mode, resulting in a gradual rejection of the LP_{01} mode in the output FS as the launched BCB power increases. Initially, nearly 95% of the power is in the LP_{01} mode, decreasing to ~13 % with a BCB power of ~4.6 kW. It is worth noting that, despite the transition to a 6-mode platform from a 2-mode one, the experimental results align well with simulations. Figure 3.15(b) demonstrates the close match between the theoretical predictions and experimental results, considering the experimental parameters such as pulse duration, peak power, fibre length, and input mode compositions.

Figure 3.16 presents two additional instances of mode rejection in PM2000, where the input BCB is coupled to the LP_{01} mode (Figure 3.16(a)) and the LP_{11} mode (Figure 3.16(b)). In Figure 3.16(a), a reduction in the LP_{01} mode content from ~35 % down to ~16 % is observed with a BCB power of

~4.5 kW. However, the mode conversion efficiency is not as pronounced as seen in Figure 3.15 due to different conditions of the input FS. The relative power and phase of each LP mode in the FS can affect mode rejection performance, meaning that while rejection of a specific mode matching the input BCB mode may occur, the increase in other mode contents will vary depending on the input FS condition. In this instance, rejection of the LP_{01} mode in FS results in increased content of the LP_{11o}, LP_{21e}, and LP_{211o} modes by ~15 %, ~25 %, and ~23 %, respectively. In Figure 3.16(b), the input FS comprises ~46 % LP_{11o}, ~25 % LP_{11e}, ~21 % LP_{02}, and ~8 % LP_{21o} modes. With a launched BCB power of ~2.6 kW, the output FS demonstrates rejection of the LP_{11o} mode, with its mode content reduced by ~35 %.

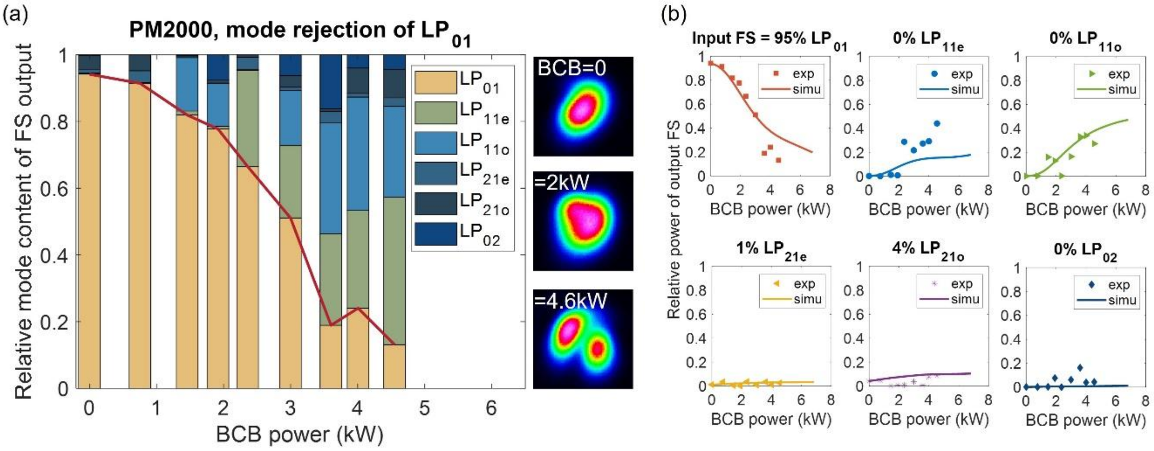

Figure 3.15 Mode rejection of the LP_{01} mode in PM2000. (a) Relative power of the output FS modes versus the launched BCB power, along with the output FS beam profiles at different BCB powers. (b) Relative power of individual LP modes versus the BCB power, in comparison with simulations (lines).

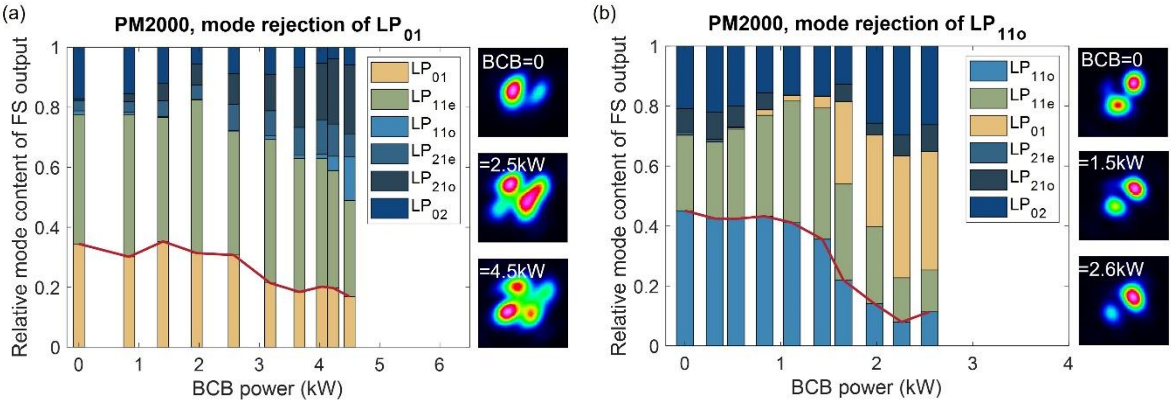

Figure 3.16 Relative power of the output FS modes versus the launched BCB power, along with beam profiles at different BCB powers, illustrating the rejection of (a) the LP_{01} mode and (b) the LP_{11o} mode in PM2000.

3.3.3 Mode rejection in isotropic fibres

To explore the mode rejection process in a more general medium, such as an isotropic fibre where polarization maintenance is not feasible like in PMFs, a bimodal fibre, SMF28, is employed. The refractive index profile of SMF28 is shown in Figure 3.17, revealing an average core to cladding refractive index difference of ~0.0053 (corresponding to NA~0.124 @1.04 μm) and a core diameter of ~8.3 μm. Through simulation in Comsol using the measured index profile, the dispersion and nonlinear coefficients are obtained and listed in Table 3.5. Despite similarities in core size, NA, modal dispersion parameters between SMF28 and PM1550-xp, the intermodal nonlinear coefficients (f_{m1_m2}) in SMF28 are ~50% smaller (compared to PM1550-xp coefficients in Table 3.1). This reduction stems from a lower intermodal overlap between the LP_{01} and the LP_{11} modes in SMF28, potentially affecting mode rejection efficiency.

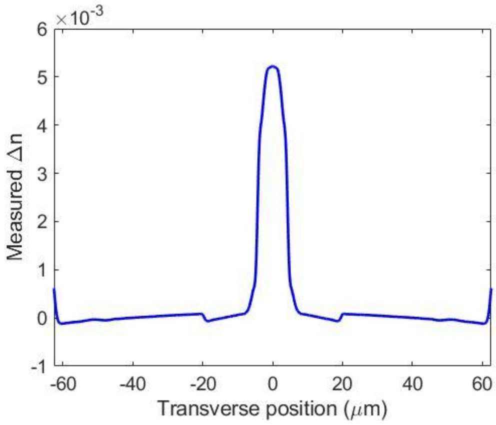

Figure 3.17 Measured refractive index profile for SMF28

Table 3.5 The dispersion and nonlinear coefficients for SMF28

Dispersion	β (μm^{-1})	β_1 (ps/mm)	β_2 (ps^2/km)
LP_{01}	8.7820	4.8965	16.0203
LP_{11}	8.7684	4.8925	26.6194
Kerr coefficient	$\gamma=3.1\ W^{-1}km^{-1}$		
Overlap factor f_{m1_m2}	m1=LP_{01}	m1=LP_{11e}	m1=LP_{11o}
m2=LP_{01}	1	0.2967	0.2563
m2=LP_{11e}	0.2967	0.4290	0.1968
m2=LP_{11o}	0.2563	0.1968	0.4341

Prior to implementing the mode rejection experiments with SMF28 fibre, preliminary measurements were conducted to understand polarization and modal coupling in a co-propagating configuration. A 1m-long piece of SMF28 was placed in the experimental setup (see

Figure 3.3), with the BCB blocked. The FS was coupled into either the LP_{01} or LP_{11} mode at various power levels. Intermodal coupling between the LP_{01} and LP_{11} modes was quantified using the MD method introduced in section3.3.1.2, revealing coupling variations between ~5 to 10% at different powers. The input FS exhibited a high PER of ~25 dB, and the output PER was measured using a combination of a quarter wave plate (QWP), a HWP and a PBS. The results, shown in Figure 3.18, indicate that the output PER as a function of the coupled powers, with wave plate angles optimized for each measurement to achieve maximum PER. The LP_{01} mode maintained a good PER (>10 dB) at low powers, but experienced decreased PER at high peak powers due to strong polarization coupling. Conversely, the LP_{11} mode exhibited significant scrambling even at low power levels, and PER measurements showed randomness and variability over time, indicating substantial random polarization coupling. These observations suggest that while the LP_{01} mode can maintain its polarization state to some extent at low powers, the LP_{11} mode faces considerable polarization scrambling, leading to unpredictable polarization states within the fibre. Despite these challenges, investigating the mode rejection process in SMF28 remains valuable for understanding mode control in more complex environments.

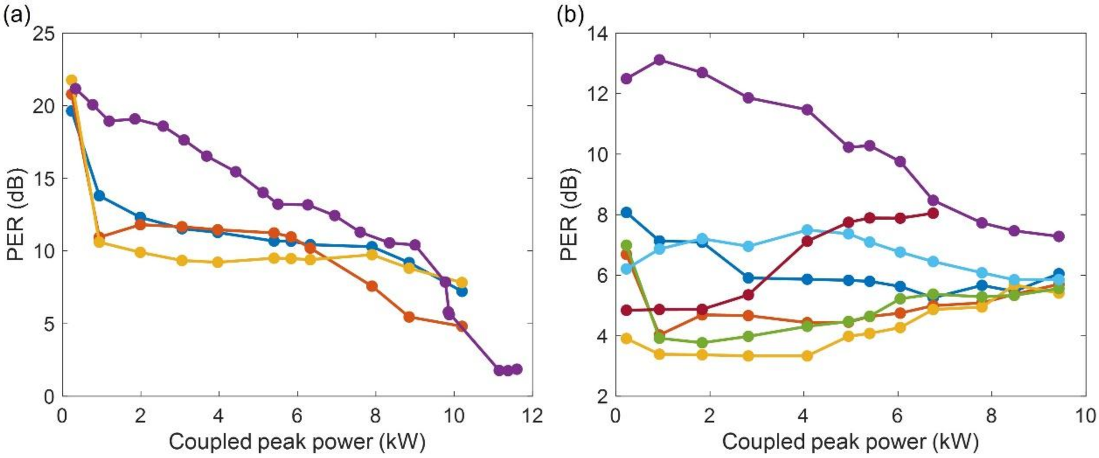

Figure 3.18 PER of the output beams from a 1m-long SMF28 versus the coupled peak power, measured at different times (represented by different colours) and in different mode coupling conditions: (a) LP_{01} mode and (b) LP_{11} mode.

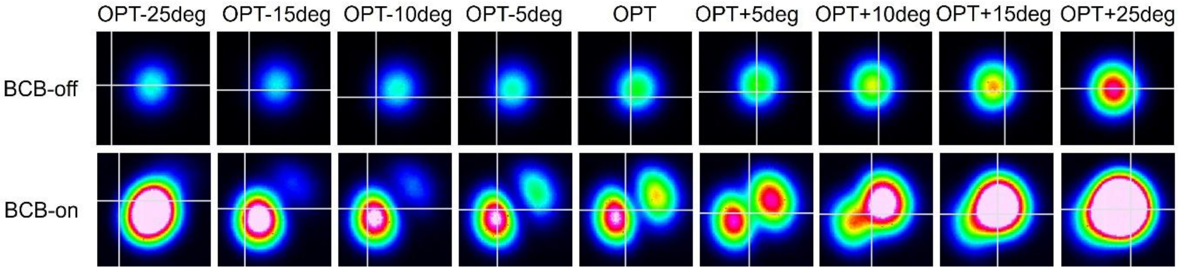

Figure 3.19 Mode conversion in SMF28 when observing in different polarization directions with the BCB (LP_{01} mode) switched on and off.

The initial investigation focused on the rejection of the LP_{01} mode, with the input BCB coupled into the LP_{01} mode and the input FS coupled with a combination of the LP_{01} and LP_{11} modes. Initially, both the input BCB and FS were polarized along the same axis. Figure 3.19 illustrates the mode conversion for the output FS, observed at various polarization orientations by rotating the linear polarizer before the camera, with fixed camera exposure time to demonstrate relative powers. With the FS and BCB coupled at ~6.5 kW and ~7.5 kW, respectively, optimal rejection of the LP_{01} mode occurred at a specific angle (OPT angle), close to the polarization orthogonal to the input polarization. For instance, if the input FS is x-polarized, the OPT angle aligns with the y-polarization direction. This OPT angle is influenced by factors such as the relative polarization between the FS and BCB, FS mode composition, and random polarization coupling, as well as mode coupling related to the launched power. In Figure 3.19, the OPT angle deviates ~15 deg from the minimum power orientation (OPT-15 deg), with efficient mode rejection observed within orientations ranging from OPT-10 deg to OPT+10 deg. When observed in the direction orthogonal to the OPT angle, mode rejection is negligible, and the output FS beam shape is similar when the BCB is switched on and off. This behaviour contrasts with observations using the PM1550-xp, where mode rejection occurs across all polarization directions (see Figure 3.11).

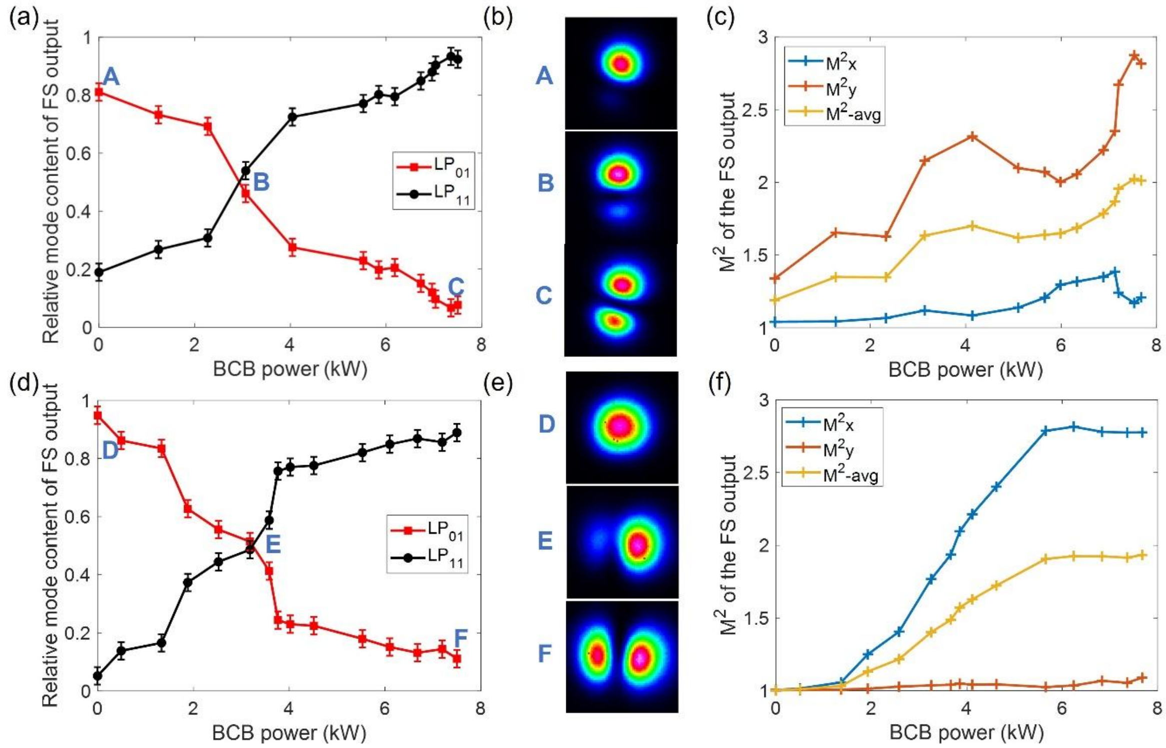

Figure 3.20 Mode rejection of the LP_{01} mode in SMF28 with mode conversion towards the LP_{11} degenerate modes when observing at the OPT angle. (a), (d) Mode content in the output FS versus the BCB power. (b), (e) Output FS beam profiles at different BCB powers. (c), (f) Calculated M^2 factor for the output FS versus the BCB power.

The mode conversion at the OPT angle was measured to analyse mode rejection in the SMF28, as depicted in Figure 3.20 and Figure 3.21. In Figure 3.20, two measurements showcase the input FS predominantly coupled to the LP$_{01}$ mode at the OPT angle (point A: ~81% LP$_{01}$ mode power, point D: ~95% LP$_{01}$ mode power), while the input BCB is coupled with the LP$_{01}$ mode. As the BCB power increases, a conspicuous conversion towards the LP$_{11}$ mode is observed in the output FS. Figure 3.20(a)-(c) demonstrate that the rejection of the LP$_{01}$ mode leads to a conversion to the LP$_{11}$ mode with two lobes oriented vertically, with the mode composition at point C being ~7.6% LP$_{01}$ mode, ~5.4% LP$_{11e}$ mode, and ~87% LP$_{11o}$ mode. Figure 3.20(c) shows that the increase in the M^2 factor is more pronounced in the vertical(y) direction with increasing BCB power (M^2 increment is ~0.34/~1.53 in the x/y direction), emphasizing the dominance of conversion from the LP$_{01}$ mode to the LP$_{11o}$ mode in this measurement. In contrast, Figure 3.20(d)-(f) illustrate that the FS mode is primarily converted to the LP$_{11e}$ mode, with the output FS at point F containing ~11% LP$_{01}$ mode, ~87% LP$_{11e}$ mode, and ~2% LP$_{11o}$ mode. As a consequence, the M^2 factor increases ~1.77 and ~0.09 in the x and y directions, respectively. It is worth noting that the curves in Figure 3.20 are not smooth, which could be attributed to mode decomposition error (deviation along y-axis direction in (a) and (d), and the corresponding M^2 value deviation in (c) and (f)) as well as BCB power variation (along x-axis direction, resulting from variation in coupling efficiency).

Likewise, the rejection of the LP$_{11}$ mode in SMF28 was measured at the OPT angle. Figure 3.21 shows the mode content evolution in the output FS as a function of the BCB power, with the input FS at ~8.75 kW and the input BCB coupled into the LP$_{11}$ mode with a maximum power of ~5 kW. Notably, the output FS exhibits a rejection of the LP$_{11}$ mode, with a reduction of ~22 % in mode content, accompanied by a transformation of the output FS shape towards a single lobe.

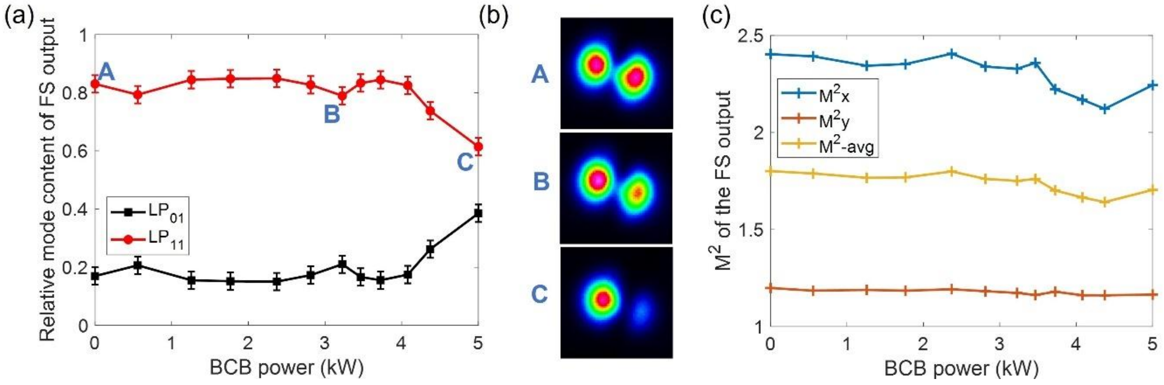

Figure 3.21 Mode rejection of the LP$_{11}$ mode in SMF28 when observing at the OPT angle. (a) Mode content in the output FS versus the BCB power. (b) Output FS beam profiles at different BCB powers. (c) Calculated M^2 factor for the output FS versus the BCB power.

To understand the influence of the relative polarization states between the counter-propagating beams in the SMF28, the random polarization coupling shown in Figure 3.18 should be considered as well. By adjusting the FS and BCB with different polarization differences (Pol-diff), the mode rejection efficiency at the OPT angle is compared in Figure 3.22, where the LP$_{01}$ mode is rejected. The maximized rejection is achieved when the input FS and BCB are co-polarized (Pol-diff=0 deg), and the mode rejection efficiency gradually degrades as the polarization difference increases. It is noteworthy that when the polarization state of the BCB differs from that of the FS, the mode conversion can follow an uncertain direction. For example, with Pol-diff=20 deg in Figure 3.22(a), the content of the LP_{01} mode decreases from ~100% to ~40% at ~4 kW BCB power, then unexpectedly increases to 80% at ~6 kW, before decreasing again. Another notable difference in the mode rejection behaviour in SMF28 compared to PM1550-xp (see Figure 3.10) is the conversion efficiency. The increment in the LP_{11} mode content is ~70% when the Pol-diff is 0 deg and ~10% when Pol-diff is 90 deg, with a difference larger than the theoretical prediction (the mode conversion efficiency is ~3x lower when the Pol-diff changes from 0 deg to 90 deg).

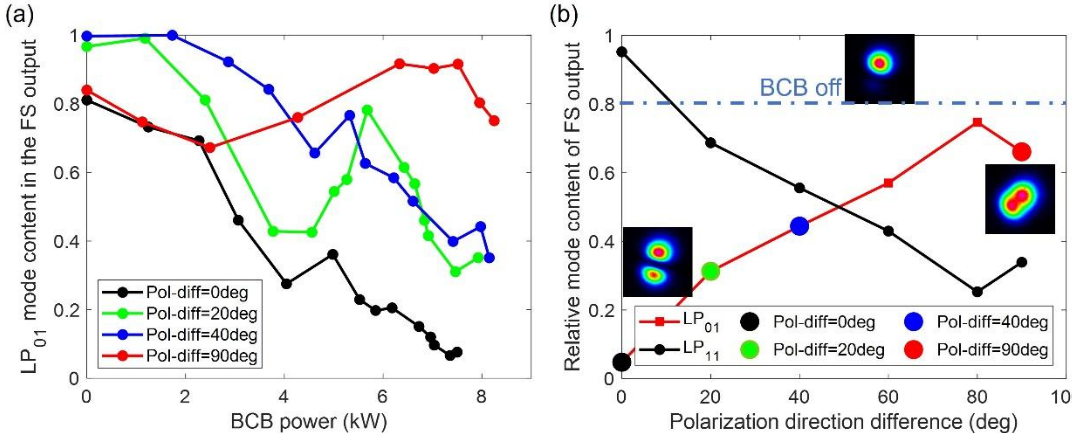

Figure 3.22 Mode rejection efficiency at the OPT angle with different relative polarizations between the FS and the BCB. (a) Content of the LP_{01} mode in the output FS versus the BCB power when the polarization difference between the FS and the BCB is 0 deg to 90 deg. (b) Mode conversion results for the output FS at different Pol-diff values in comparison with the case when the BCB is switched off.

To conclude, the measurement of the mode rejection in SMF28 provides an example of beam self-organization in a random multimode medium where strong polarization coupling influences the complex nonlinear processes. Despite these complexities, mode rejection still occurs at an optimal polarization direction (OPT angle), and the rejection is observed in the mode that is the same as the input BCB mode. The mode rejection efficiency is maximized at the OPT angle when the input FS and BCB are co-polarized. However, when the input beams are not co-polarized, the mode conversion may follow an uncertain direction into different mode states.

3.3.4 Conclusion on the rejection of LP modes in multimode fibres

In section 3.3, the mode rejection of different LP modes is demonstrated using various FMFs in a setup with few-kW, 0.5ns-pulsed counter-propagating laser beams. Using a 1m long PM1550-xp fibre with a total peak power of 16 kW, selective rejection of the LP_{01} and LP_{11} mode in the FS is achieved with ~30% mode conversion efficiency. In comparison, a 0.4m long, highly nonlinear PMHN1 fibre requires only ~4 kW total power to achieve similar selective rejection of the LP_{01} and LP_{11} modes with ~30% mode conversion efficiency. Extending beyond the 2-mode case, a 0.4m long, 6-mode PM2000 fibre with 9 kW total power achieves rejection of the LP_{01} and LP_{11o} mode with 20% - 80% conversion efficiency. Finally, the mode rejection effect is explored in an isotropic fibre, SMF28, where rejection of the LP_{01} and LP_{11} modes is observed around the OPT angle with 22% - 80% mode conversion efficiency. It is worth noting that these fibres are placed in a relaxed state (0.4 m long fibres are kept straight, while 1 m long fibres are bent with a curvature radius greater than 20 cm), ensuring that higher-order modes are well-maintained during propagation.

Several parameters affecting mode rejection efficiency have been investigated theoretically and experimentally. These include input mode composition (see $|B_n|^2$ in Eqs.(3.2.1) and (3.2.2)), input polarization (see p in Eqs.(3.2.1) and (3.2.2)), polarization coupling (changes in p), and spectrum broadening during propagation (changes in $|B_n|^2$ within a specific linewidth). Maximized mode rejection occurs when the input FS and BCB are co-polarized with equivalent powers. However, polarization coupling and spectrum broadening can degrade mode rejection efficiency.

3.4 Rejection of supermodes in multicore fibres

3.4.1 Homemade multicore fibres and experimental setup

In this section, the investigation focuses on the mode rejection effect within two homemade multicore fibres with strongly coupled cores, utilizing the concept of supermode (SM) to represent specific field distributions (relative power and phase between cores) in MCFs. A dual-core fibre (DCF) and a tri-core fibre (TCF) are meticulously designed and fabricated via the stack-and-draw technique[13]. The rejection of supermodes in MCFs is explained through the same theoretical framework as mode rejection in MMFs.

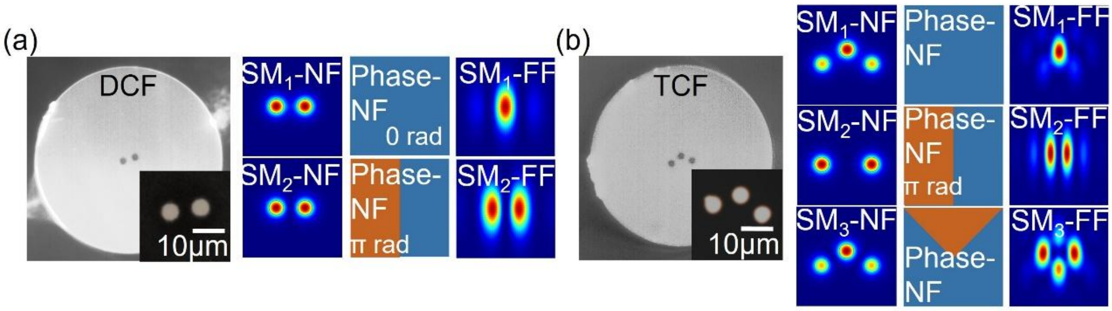

Figure 3.23 Cross-section images of the homemade DCF and TCF, along with the corresponding supermode ($SM_{1(2,3)}$) distributions in the near-field and far-field.

Table 3.6 Information of the fabricated DCF and TCF

		Core diameter (μm)	Core spacing (μm)	Core NA	Cladding diameter (μm)	Outer diameter (μm)	Length (m)
DCF	A1664	5.0±0.1	9.4	0.15	140.2	175	2004
	A1665	5.2±0.1	9.8	0.15	145.8	185	2005
TCF	S01	5±0.15	9.4	0.15	137.9	-	105
	S02	4.8±0.14	9.8	0.15	146.5	-	65
	S1	4.6±0.14	7.4	0.15	110.5	-	420

Table 3.7 The dispersion and nonlinear coefficients for the DCF and TCF

		β (μm^{-1})	β_1 (ps/mm)	β_2 (ps^2/km)
DCF	SM_1	8.7820	4.9061	23.5772
	SM_2	8.7817	4.9070	20.6093
TCF	SM_1	8.7855	4.9057	24.4249
	SM_2	8.7853	4.9066	22.1396
	SM_3	8.7850	4.9074	19.5544
DCF		Kerr coefficient	$\gamma=3\ W^{-1}km^{-1}$	
		Overlap factor	$f_{SM1\_SM1}=1$ $f_{SM1\_SM2}=1.04$ $f_{SM2\_SM2}=1.02$	
TCF		Kerr coefficient	$\gamma=2.3\ W^{-1}km^{-1}$	
		Overlap factor	$f_{SM1\_SM1}=1$ $f_{SM1\_SM2}=0.68$ $f_{SM1\_SM3}=1.03$	$f_{SM2\_SM2}=1.38$ $f_{SM2\_SM3}=0.70$ $f_{SM3\_SM3}=1.07$

Prior to fabricating the MCFs, fibre design was conducted using Comsol software, starting with a step-index dual-core geometry. Through comparisons of designs with varying core diameters, spacings, positions, and core-to-cladding refractive index differences, considering both feasibility and fabrication accuracy, the designs for the DCF and TCF with Germanium-doped cores were finalized. The geometries as shown in Figure 3.23, and the information of the fabricated fibres is summarized in Table 3.6. The DCF features two identical cores symmetrically positioned within a silica cladding, while the TCF comprises one central core and two side cores equidistant from the central core. The nonsymmetric core positions induce large birefringence, making these two fibres function as polarization-maintaining fibres. The DCF and TCF have single-mode cores and support the propagation of 2 and 3 supermodes, respectively. The SM_1 mode represents the fundamental mode, where the electric fields from all cores are in phase, resulting in a mainly single lobe distribution in the far-field. Higher-order supermodes (SM_X, $X>1$) exhibit specific relative powers and phases among the cores, leading to various NF and FF beam profiles, as depicted in Figure 3.23. These MCFs were simulated in Comsol using the measured core geometry, and the resulting dispersion and nonlinear coefficients are summarized in Table 3.7.

The supermodes represent the electric field distribution across the cores, and their distribution may vary with changes in core geometry, such as alterations in core diameter, core spacing, or core refractive index. Additionally, bending can also influence the supermode distributions. These variations in supermode distribution can, in turn, result in changes to modal dispersion and nonlinear coefficients. Here, an example analysis of core size discrepancies and macro-bending effects on the DCF is presented. Figure 3.24 compares the 3 DCFs with changes in core size or bending condition. DCF1 supports the supermodes with similar amplitudes in the two cores. It can represent straight fibre with identical cores, also represents bent fibres with non-identical cores, as illustrated in the first row of Figure 3.24. DCF2 and DCF3 represent straight fibres with non-identical cores or bent fibres with identical cores, and there is a significant difference between the amplitudes of the corresponding supermodes in the two cores, as shown in the second and third rows of Figure 3.24. For example, if a DCF with two identical cores is bent (along the line connecting the two core centres) with a decreasing curvature radius, the supermode distribution changes from DCF1 to DCF2 and then to DCF3. Conversely, when a DCF with non-identical cores is bent at a certain radius of curvature, the supermode distribution evolves from DCF3/DCF2 to DCF1. In addition, the changes in supermode distributions are negligible when the bending direction is orthogonal to the line connecting the two cores.

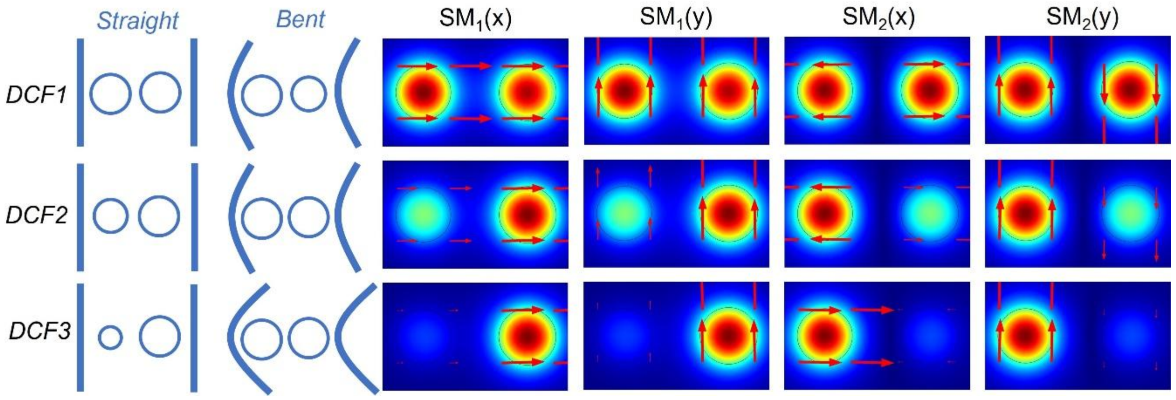

Figure 3.24 Simulated electric field distributions for the DCFs with core spacings twice the core diameter (diameter~5 μm). DCF1: straight fibres with identical cores or bent fibres with non-identical cores. DCF2: bent fibres (16 – 30 cm bending radius) with either identical cores or straight fibres with non-identical cores. DCF3: bent fibres (bending radius.

Changes in supermode distributions can significantly affect nonlinear coupling efficiency. Figure 3.25 illustrates the calculated nonlinear coefficients for two DCFs under different bending conditions based on Comsol simulations. While the propagation constants and dispersion parameters for different supermodes remain similar across different scenarios, the nonlinear coefficients, particularly the intermodal overlap factor ($f_{SM1\text{-}SM2x(y)}$), exhibit substantial variations. In Figure 3.25(a), for a DCF with identical cores, the intermodal coupling strength is comparable to the intramodal coupling strength when the fibre is nearly straight (bending radius>100 cm). However, the intermodal coupling strength decreases drastically with an decreasing bending radius. The Kerr coefficient (γ) doubles from 3.1 $W^{-1}km^{-1}$ to 5.7 $W^{-1}km^{-1}$ as the fibre bending radius decreases from 100 cm down to 4 cm, attributed to the reduced effective mode area as amplitude redistributing from two cores to one core. Conversely, Figure 3.25(b) shows that for fibre cores with non-identical cores, the intermodal coupling strength increases as the bending radius decreases. Overall, the intermodal overlap factor could decrease by ~85% from a symmetrical to an asymmetrical supermode distribution. This suggests that in experiments involving coupled MCFs, it is crucial to consider core geometry and fibre bending conditions to ensure optimal nonlinear coupling efficiency.

One of the advantages of using MCFs for mode rejection experiments is the higher intermodal overlap between supermodes compared to LP modes, leading to stronger intermodal coupling in MCFs. For example, the coupling coefficient between the SM_1 and SM_2 modes in a DCF is similar to the intermodal Kerr coefficients ($\gamma_{11}= \gamma_{22}= \gamma_{12}$). In contrast, in the PM1550-xp fibre, the intermodal Kerr coefficients are lower, with $\gamma_{11}=1.2\gamma_{22}=1.8\gamma_{12}$ (see Table 3.1).

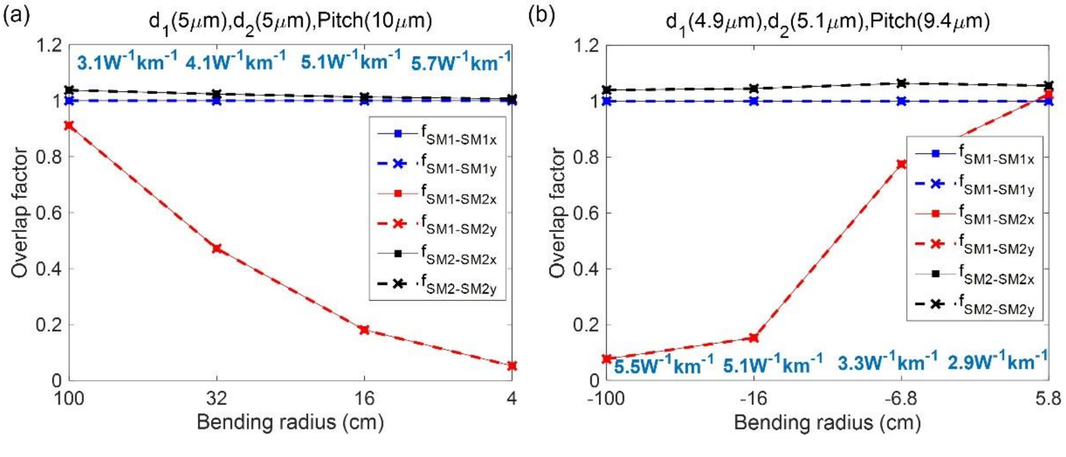

Figure 3.25 Calculated nonlinear coupling coefficients of two DCFs with (a) identical cores and (b) non-identical cores at different bending radii. The inset numbers are the Kerr coefficients (γ) and the lines are overlap factors.

To experimentally explore mode rejection in DCF and TCF, the same setup shown in Figure 3.3 is used. The input BCB is shaped with an SLM to effectively excite different supermodes in the DCF and TCF. The phase pattern for coupling into the DCF is a superposition of 2 two-dimensional blazed gratings with a grating period determined by the core spacing and the focal length of the lens used for coupling. For TCF coupling, the phase pattern is a superposition of 3 two-dimensional blazed gratings with specific grating periods. When a Gaussian shaped beam is incident on the SLM, multiple beamlets are reflected from the SLM screen. The angle, phase, and amplitude of each beamlet can be controlled by adjusting each blazed grating in the phase pattern. The corresponding beam spots in the Fourier plane of the focusing lens are then coupled into the MCF cores. The insertion loss of the SLM is ~1 dB, and the coupling loss into the MCF ranges from 3 to 3.5 dB depending on the supermode excitations. On the input FS side, the coupling over supermodes is adjusted by changing the position of the phase plate and the incident beam angle. A more straightforward method to excite a combination of supermodes with lower loss is by selectively coupling the light into one of the MCF cores.

3.4.2 Characterization and mode decomposition of MCFs

Prior to conducting the mode rejection experiments with MCFs, the fabricated MCFs are characterized, and a mode decomposition method for coupled MCFs is proposed and demonstrated. A 0.4m-long DCF/TCF (see Table 3.6) is placed straight in the counter-propagating setup (see Figure 3.3), and the supermode excitation results are shown in Figure 3.26. The supermode (SM_x) excitation is controlled by the SLM, and the output beam profiles resemble the theoretical NF and FF shapes (see Figure 3.23). Notably, the excited supermodes remain stable at various power levels in this short piece of fibre. Figure 3.26 demonstrates that when the relative content and phase for the SM_1 and SM_2 modes are different in the DCF, the NF profile may retain the same distribution, whereas the FF shape differs. This observation is evident when comparing Mix1(Mix3) and Mix2(Mix4). This finding indicates that mode decomposition for the supermodes is more effectively implemented with the FF beam profiles.

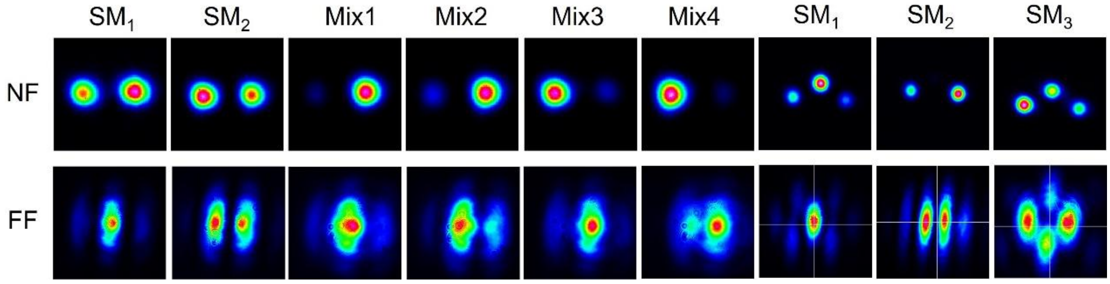

Figure 3.26 Output beam profiles from the DCF and TCF measured in both the near-field and far-field under different supermode coupling conditions.

As shown in the simulation in Figure 3.27, the NF and FF distributions are compared when the DCF is coupled with different mode contents and phases between the supermodes. Figure 3.27(a) illustrates the NF distribution characterized by the intensity ratio between the two cores. Different combinations of supermodes can result in the same power ratio between the cores, leading to identical NF distributions. Examples in Figure 3.27(b) and (c) show combinations of SM_1 and SM_2 modes with varying relative powers. Despite the different mode compositions, the NF distributions appear the same, as indicated in the first columns of these figures. However, the FF distributions vary significantly with different supermode combinations, providing a basis for mode decomposition to determine the relative supermode content.

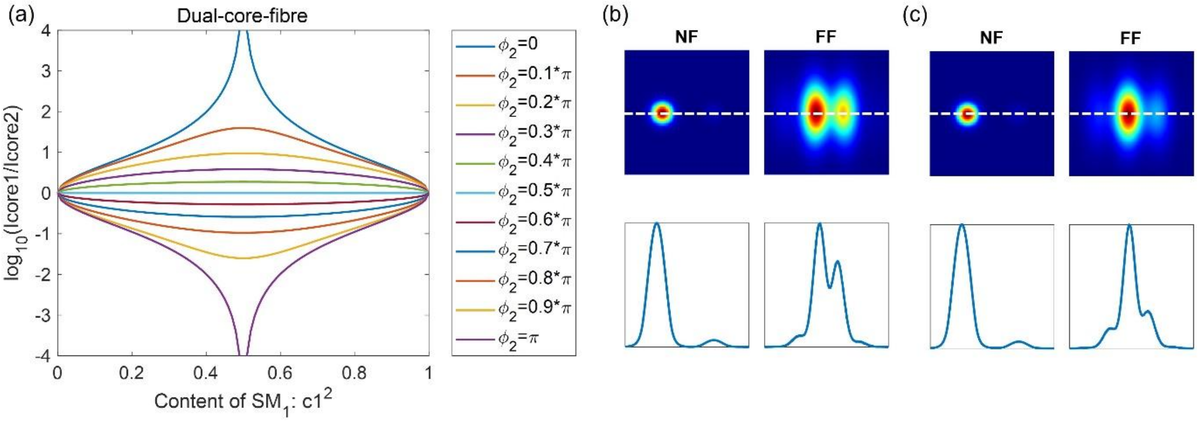

Figure 3.27 Comparison of the near-field and far-field distributions for the DCF with different mode contents and relative phases. (a) The ratio of the intensities in two cores as a function of the SM_1 mode content (c_1^2) with a relative phase (ϕ_2) between the two modes. (b) The NF and FF beam profiles when c_1^2=1/3, ϕ_2=0.1*π. (c) The NF and FF beam profiles when c_1^2=2/3, ϕ_2=0.1*π.

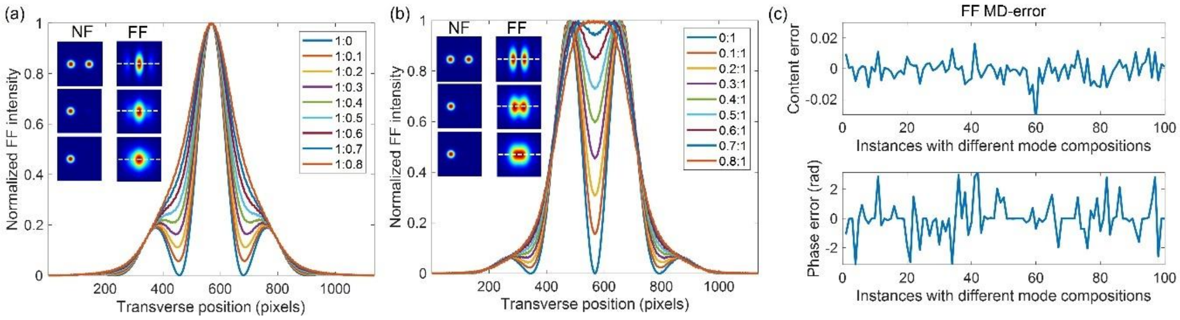

Figure 3.28 Comparison of FF beam profiles for the DCF with different mode compositions when (a) the content of the SM_1 mode is larger than the SM_2 mode, with the legend indicating the relative powers between the two modes. (b) the content of the SM_2 mode is larger than the SM_1 mode. (c) Theoretical accuracy for mode decomposition based on FF beam profiles.

To illustrate the distinguishable differences in the FF beam profiles, the FF beam profiles for the DCF with different mode compositions are compared in Figure 3.28(a) and (b). Figure 3.28(a) shows that the FF features a main lobe in the centre when the SM_1 mode is dominant, whereas the FF exhibits two identical lobes when the SM_2 mode is dominant, as shown in Figure 3.28(b). Note that these results represent the case when the relative phase between the two modes is 0. However, the change in the FF profiles remains distinguishable if the relative phase changes. These results illustrate that implementing mode decomposition in the far-field is feasible and reliable by comparing the measured FF beam profiles with the reconstructed intensity profiles that can be obtained with the SPGD algorithm. The theoretical mode decomposition accuracy exceeds 98%, as shown in Figure 3.28(c), where the FF mode decomposition for the DCF is implemented in 100 instances with different supermode compositions (random mode content and phase). It is worth mentioning that mode decomposition methods based on off-axis holography method [129] and matrix formalism method [67] have also been implemented for the DCF and TCF, details of which are provided in Appendix A. The proposed MD method, based on FF beam profiles and the SPGD algorithm, is primarily used in the following experiments due to its easy implementation, high accuracy, and robustness to noise and fibre perturbations.

3.4.3 Mode rejection in dual-core fibres

In this section, mode rejection is experimentally demonstrated using the DCF. A 1 m long DCF was used, and the preliminary optimization of the experimental setup (see Figure 3.3) followed similar procedures introduced for the few-mode fibres. The input BCB was selectively coupled into the SM_1 or SM_2 mode by optimizing the phase pattern displayed on the SLM, while the input FS was randomly coupled into a combination of the two supermodes. Since the DCF is a high birefringent fibre, the input FS and BCB were co-polarized along the fast or slow axis (parallel to the line connecting the two core centres) to ensure that the nonlinear interaction involves the counter-propagating modes with the same polarization states. The output FS/BCB maintained the input polarization with a PER > 20 dB at different powers.

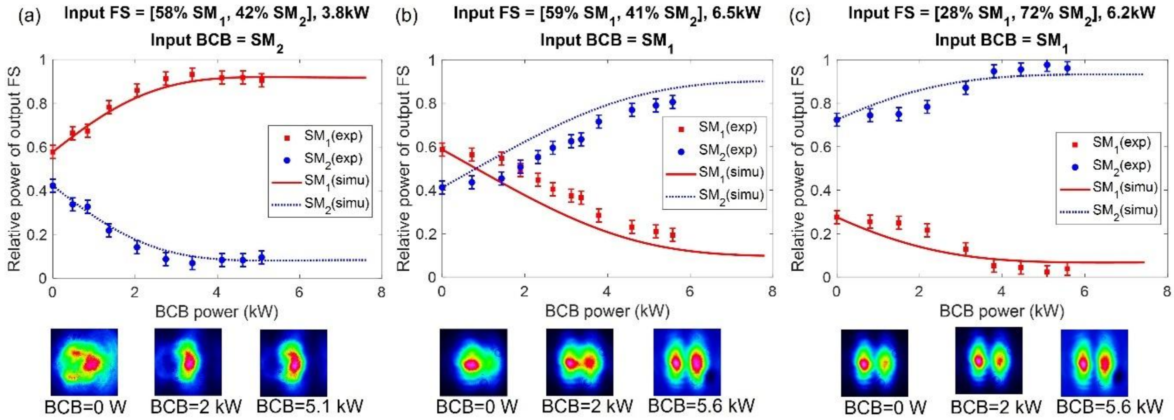

Figure 3.29 Mode rejection results in the DCF. Mode decomposition of the output FS versus the BCB power under different launching conditions (experiments: markers; simulations: lines). The bottom images are the FF beam profiles of the output FS for 3 distinct values of BCB power. The input power and mode composition of the FS and BCB are listed on the top of each panel. Error bars of ±3% are added to the experimental results, which represents the estimated uncertainty of the MD algorithm.

Figure 3.29 illustrates three examples of supermode rejection in the output FS. In Figure 3.29(a), the input BCB is coupled into the SM_2 mode, resulting in a gradual rejection of the SM_2 mode in the output FS as the BCB power increases. Initially, with ~40% of the power in the SM$_2$ mode, the output FS contains less than 10% of the power in the SM$_2$ mode at a BCB power of ~5.1 kW. As a result, ~90 % of the output FS power is coupled to the SM$_1$ mode. Consequently, the output FS exhibits a single lobe in the far-field and resembles the SM$_1$ mode, corresponding to the in-phase combination of the two cores. On the contrary, when the input BCB is coupled to the SM$_1$ mode, as shown in Figure 3.29(b) and (c), the output FS undergoes rejection of the SM$_1$ mode and is therefore mainly coupled to the SM$_2$ mode. When the input BCB power is ~5.6 kW, ~81% and ~98% of the output FS power is coupled to the SM$_2$ mode in Figure 3.29(b) and (c), respectively. Consequently, the output FS exhibits two distinct symmetric lobes and resembles the SM$_2$ mode in the far-field, corresponding to the out-of-phase combination of the two cores. It is worth mentioning that these experimental results align well with simulations using the experimental parameters, such as pulse duration, peak power, fibre length, mode composition, and polarization state of the counter-propagating beams.

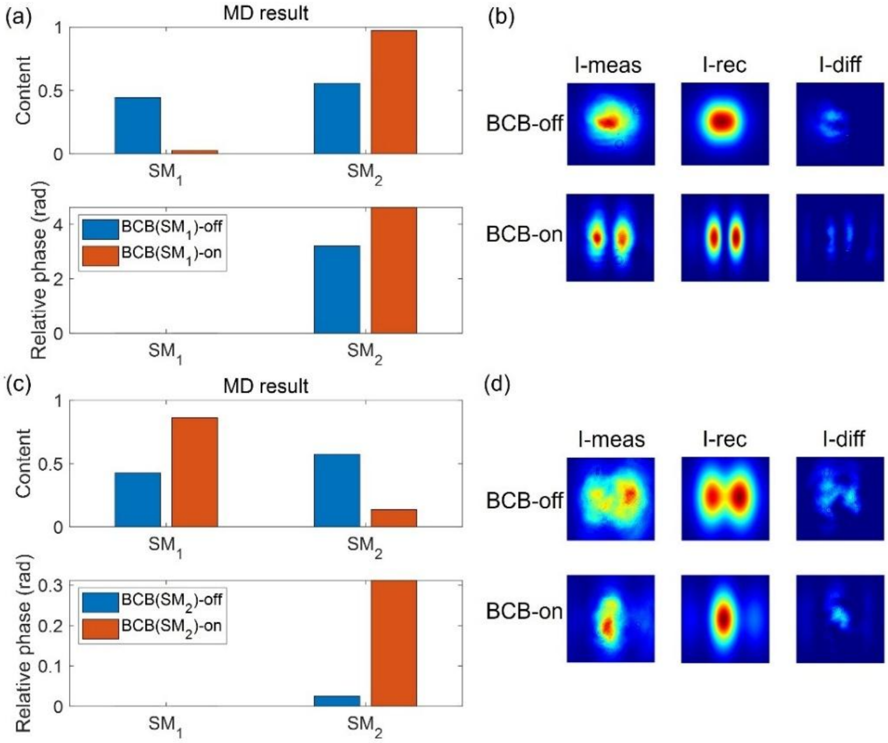

Figure 3.30 Mode decomposition results for the DCF in the far-field. (a), (b) MD results and the comparison between the measured and reconstructed FF beam profiles when the input BCB is the SM$_1$ mode. (c), (d) MD results and beam profile comparisons when the input BCB is the SM$_2$ mode.

In Figure 3.29, the MD of the output FS is implemented at each measurement at different BCB powers. Two examples of MD results for the FF beam profiles are illustrated in Figure 3.30, demonstrating the rejection of the SM$_1$ mode and the SM$_2$ mode. Figure 3.30(a) shows that the output FS consists of ~44.4% SM$_1$ mode when the BCB (coupled into the SM$_1$ mode) is switched off, whereas the content of the SM_1 mode drastically decreases to just 2.6% when the BCB is switched on with the maximum power. The measured and reconstructed FF beam profiles with the BCB off/on are shown in Figure 3.30(b), exhibiting an intensity correlation coefficients [74] of ~ 98% and confirming that the SM_1 mode is effectively rejected at maximum BCB power. Conversely, Figure 3.30(c) shows that the SM_2 mode content in the output FS decreases from ~57.4% to ~13.7% when the BCB (coupled into the SM_2 mode) is switched from off to on. The correlation coefficient for the measured and reconstructed FF beam profiles in this case is also ~98%, confirming effective rejection of the SM_2 mode. The correlation coefficients for the FF MD results in DCF are slightly lower than those for the FMFs in the near field, which is primarily due to aberrations and noise in the imaging system. NF profiles fill ~2k pixels on camera, whereas FF profiles could occupy ~750k pixels, making the FF profiles more susceptible to deformation from system aberrations. Therefore, aberration-free lenses should be used, and careful attention should be paid to FF beam profile measurements. Several parameters that could influence mode rejection efficiency are experimentally analysed in the following sections, including the impact of the input BCB, variations in the FS, and the influence of perturbations applied to the fibre.

3.4.3.1 Impact of control beams

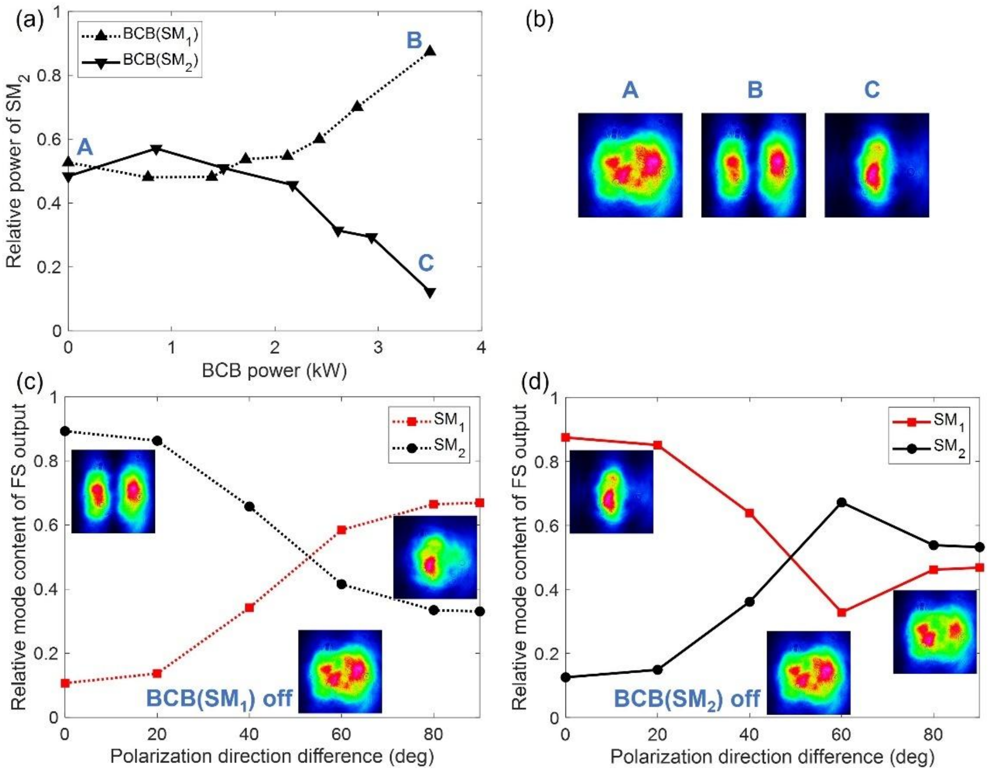

Figure 3.31 Mode rejection results for a specific input FS in the DCF but with different input BCBs. (a) The SM_2 mode content versus the BCB power with different input BCB modes, and the output FS beam profiles at points A-C are given in (b). (c), (d) The mode rejection results with different BCB polarization directions relative to the FS.

Previous experiments with the FMFs have demonstrated that the mode composition and the polarization state of the BCB could significantly influence mode rejection in the output FS. Figure 3.31(a) shows the mode rejection results for the output FS when the input FS is coupled with ~50% SM_1 mode and ~50% SM_2 mode (point A). By switching the input BCB from the SM_1 mode to the SM_2 mode, selective rejection of the SM_1 mode and SM_2 mode is observed, respectively. With a BCB power of ~3.5 kW, the output FS (~2.5 kW) is selectively coupled to the SM_2 mode (point B) and the SM_1 mode (point C), as depicted in the FF beam profiles in Figure 3.31(b).

Additionally, the mode rejection efficiency is analysed by varying the polarization direction of the input BCB while maintaining the same input FS conditions. Figure 3.31(c) and (d) illustrate that the efficiency of rejecting the SM_1(SM_2) mode gradually decreases as the polarization direction difference between the FS and the BCB increases from 0 degrees to 90 degrees. This trend aligns with theoretical predictions and previous experimental observations in FMFs. These results highlight the importance of controlling both mode composition and polarization states to optimize mode rejection efficiency in DCFs.

3.4.3.2 Variation of forward signals

Following the discussion of the mode rejection effect under different BCB launching conditions, the mode rejection efficiency is further investigated when the FS is randomly coupled with a combination of two supermodes, while the input BCB is fixed at either the single SM_1 or SM_2 mode. Figure 3.32 illustrates the efficient mode rejection of the SM_1 or SM_2 mode, regardless of the FS initial state, with the FS and BCB being co-polarized in all instances. Specifically, the content of the SM_1 mode is reduced from an initial range of 20% to 60% down to 3% to 20%, as shown in Figure 3.32(a). Similarly, the content of the SM_2 mode decreases from an initial range of 40% to 100% down to 0% to 30%, as depicted in Figure 3.32(b). These results demonstrate the consistent efficiency of mode rejection even when the FS is randomly coupled, provided that the input BCB maintains the coupling to a fixed single supermode.

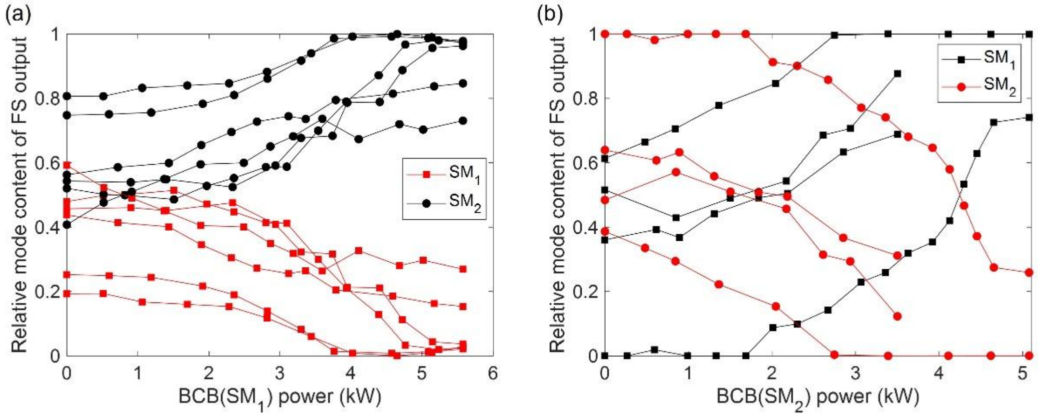

Figure 3.32 Mode rejection results for the DCF with different input FSs and a fixed input BCB in the (a) SM_1 mode and (b) SM_2 mode.

3.4.3.3 Robustness of mode rejection

The robustness of the mode rejection effect in the counter-propagating setup is investigated using the DCF. Figure 3.33 shows the variation of the SM_1 and SM_2 mode content in the output FS under different fibre perturbations when the BCB is coupled to a single mode. Each perturbation involves moving or bending the fibre with varying intensities and at different positions, leading to random coupling among the fibre modes and potentially altering the FS launching conditions. For each perturbation, the MD of the output FS is computed, and the output FS beam profile is imaged with the BCB either switched off or on.

When the BCB is switched off, the output FS varies randomly, as indicated by the black lines and FF beam profiles in Figure 3.33. However, when the BCB is switched on and coupled to a single mode, mode rejection occurs irrespective of the FS launching conditions. As a result, effective rejection of the SM_1 mode is observed in the output FS, with the relative power of the SM_1 mode dropping below 10%, as shown in Figure 3.33(a). Consequently, the output FS is locked into the SM_2 mode with a total counter-propagating beam power of ~12kW (2*6 kW). Similarly, Figure 3.33(b) demonstrates robust rejection of the SM_2 mode when the input BCB is in the SM_2 mode, and the FS is perturbed to different mode states with varied SM_2 mode content. The output FS far-field consistently exhibits a distribution similar to the SM_1 mode when the BCB is switched on, with the relative power of the SM_2 mode falling below 40%. Although the mode rejection efficiency is lower due to the high relative power of the SM_2 mode in the output FS (up to 85%) when the BCB is switched off, the SM_2 mode is still robustly rejected using ~12 kW counter-propagating beam power. The robustness analysis suggests that mode rejection is a useful method for achieving stable spatial mode locking in a bimodal system.

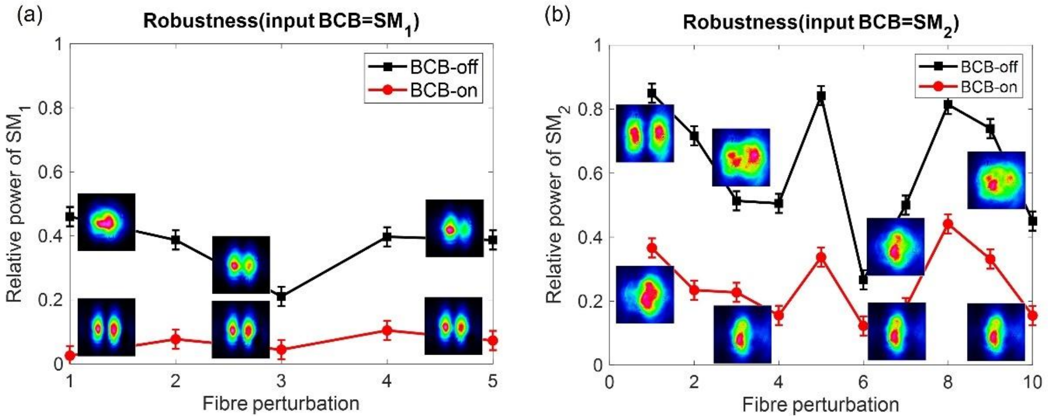

Figure 3.33 Robustness of the mode rejection effect (red lines) in the DCF with comparisons to the output FS when the BCB is switched off (black lines). 5 and 10 different perturbations are included in (a) and (b).

To conclude, mode rejection of each supermode in a 1m long DCF is observed using 5-6 kW peak powers for the FS and the BCB. By adjusting the mode composition and polarization state of the input BCB, the mode rejection effect can provide stable and robust spatial mode locking to a specific mode in the output FS from the DCF, irrespective of the initial launching conditions.

3.4.4 Mode rejection in tri-core fibres

In this section, mode rejection is further explored using the TCF. As shown in Figure 3.23, the three supermodes in the TCF are: the SM_1 mode, where all three cores are in-phase with the intensity in the centre core being twice that of the side cores; the SM_2 mode, where the centre core has zero intensity, and the two side cores are out of phase with identical intensities; and the SM_3 mode, where the intensity distribution among the cores is the same as the SM_1 mode, but the centre core has a π rad phase difference with the two side cores. Following a similar procedure to the experiments with the DCF, a ~0.4m long TCF was placed in the experimental setup (see Figure 3.3) to explore the selective rejection of the supermodes. The input BCB is selectively coupled into the SM_1, SM_2, or SM_3 mode by adjusting the phase pattern loaded on the SLM, while the input FS is coupled into a combination of supermodes with different relative powers and phases. The TCF is a birefringent fibre due to the nonsymmetric design. The polarization state of the input FS and BCB is orientated along the fast or slow axis (parallel to the line connecting the centres of the two side cores), ensuring that the nonlinear interaction involves the counter-propagating modes with the same polarization states.

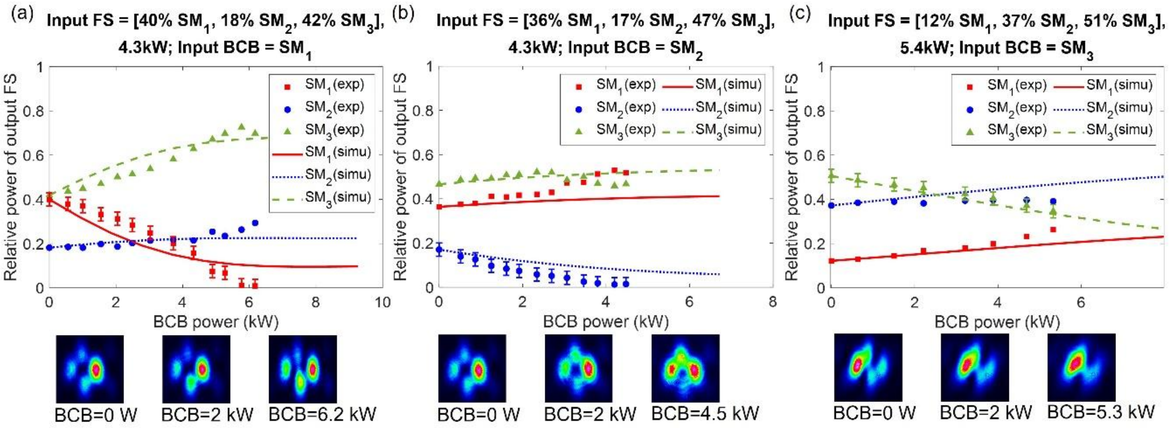

Figure 3.34 Mode rejection of the (a) SM_1, (b) SM_2, (c) SM_3 mode in the TCF. Mode decomposition of the output FS in the TCF versus the BCB power under different launching conditions (experiments: markers, simulations: lines). The bottom images are the FF beam profiles of the output FS for three distinct BCB powers. The input power and mode composition of the input FS and BCB are listed on the top of each panel.

Figure 3.34 illustrates the experimental observations of mode rejection in the TCF, in comparison with simulation results. Figure 3.34(a) shows an example when the input BCB is coupled to the SM_1 mode, so that the output FS gradually rejects the SM_1 mode as BCB power increases. Initially, with ~40% of the power in the SM_1 mode, the output FS ultimately contains nearly 0% SM_1 mode content at a BCB power of ~6.2 kW. Consequently, the output FS power is redistributed, with ~70% coupling to the SM$_3$ mode and ~30% coupling to the SM$_2$ mode. Starting with a similar initial FS condition, but with the input BCB coupled to the SM$_2$ mode, the output FS undergoes a different conversion process, as shown in Figure 3.34(b). The SM$_2$ mode content is almost completely rejected with a BCB power of ~4.5 kW. Finally, when the input BCB is coupled to the SM$_3$ mode, as shown in Figure 3.34(c), the output FS experiences a rejection of the SM$_3$ mode, with ~16% reduction of the SM$_3$ mode content at a BCB power of ~5.3 kW. These observations demonstrate the effective mode rejection in the TCF for different supermodes. The experimental results align closely with the simulations, confirming the reliability of numerical simulations.

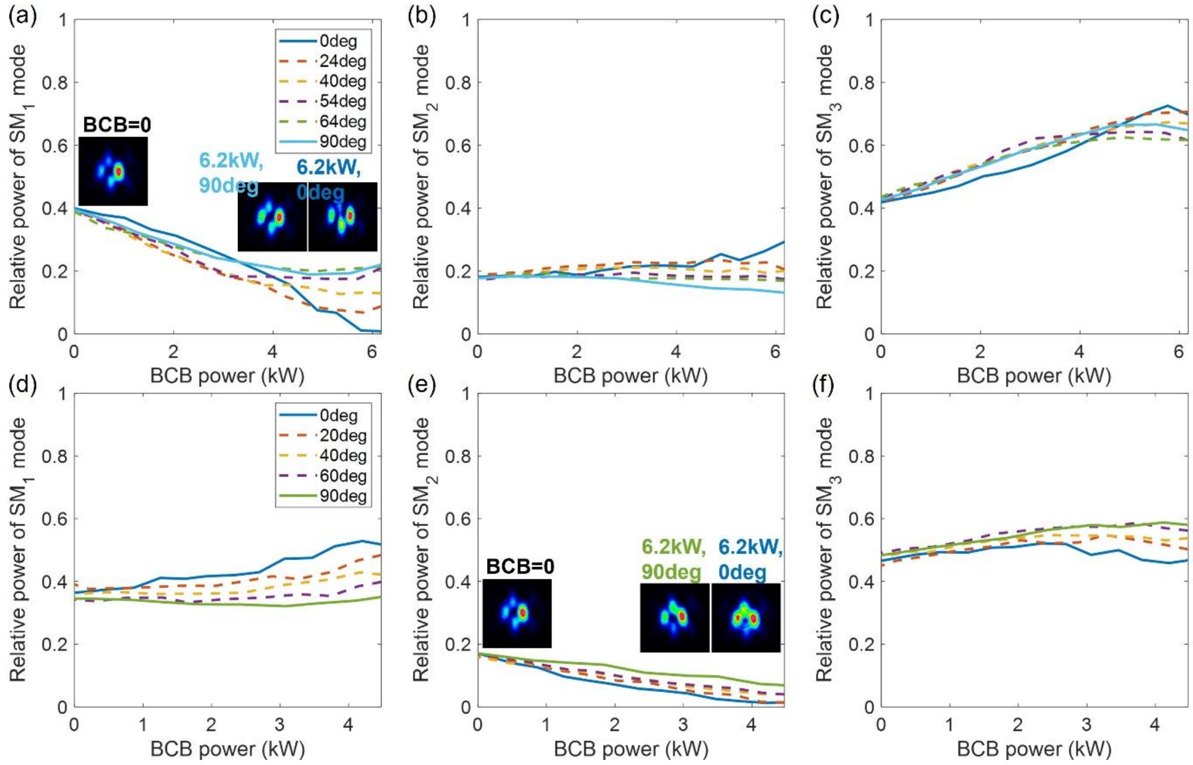

Figure 3.35 Mode rejection effect in the TCF with varying polarization states between the BCB and the FS. (a)-(c) Mode conversion of the three supermodes when the input BCB is coupled to the SM$_1$ mode with different polarization directions relative to the FS. (d)-(f) Mode conversion of the three supermodes when the input BCB is coupled to the SM$_2$ mode with varying polarization directions relative to the FS.

Furthermore, Figure 3.35 illustrates the impact of relative BCB polarization on mode rejection efficiency in the TCF. In Figure 3.35(a)-(c), the input BCB is coupled into the SM$_1$ mode, while it is coupled to the SM$_2$ mode in Figure 3.35(d)-(f). At ~6 kW BCB power, the SM$_1$ mode is absent in the output FS when the FS and BCB are co-polarized (0deg, dark blue line in Figure 3.35(a)). However, with orthogonal polarization (0deg, light blue line in Figure 3.35(a)), ~20% of FS power remains in the SM$_1$ mode at the output. At ~4.5 kW BCB power, complete rejection of the SM$_2$ mode from the output FS is achieved with co-polarization (0deg, dark blue line in Figure 3.35(e)). Nonetheless, there is still ~7% power coupled to the SM_2 mode with orthogonal polarization (90deg, green line in Figure 3.35(e)). Additionally, Figure 3.35 shows that mode rejection occurs with intermediate efficiency as relative polarization between the counter-propagating beams varies from 0 deg and 90 deg.

3.4.5 Mode conversion dynamics of the BCB

Eqs. (3.2.1) and (3.2.2) are invariant with respect to the exchange between FS and BCB modes. However, different boundary conditions apply to the input FS and to the input BCB, which reflect their different roles. Because the input BCB plays the role of control beam, its mode content is fixed and coupled to one single mode. For this reason, the output FS systematically undergoes rejection irrespectively of the input FS mode content. On the other hand, the input FS plays the role of a probe beam with arbitrary mode content. Exploring the mode conversion in the output BCB offers valuable insights into the interaction dynamics of counter-propagating multimode systems.

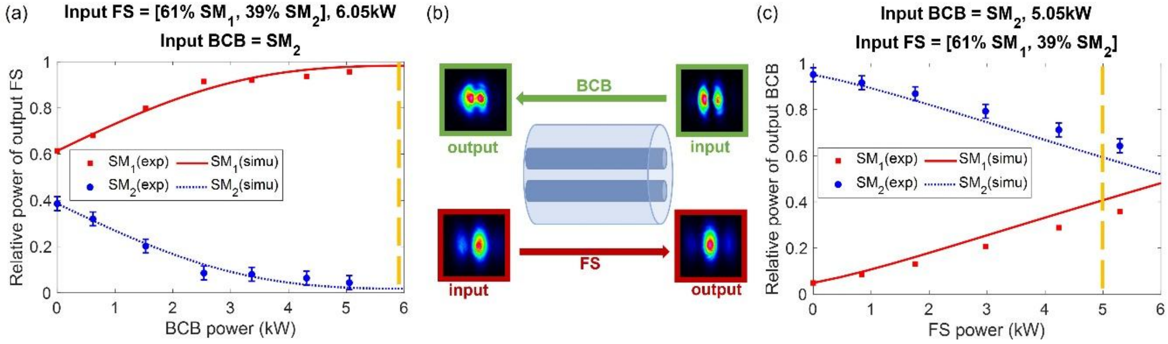

Figure 3.36 Comparison between the dynamics of the output FS and output BCB in the DCF. The MD of the output FS(BCB) versus the launched BCB(FS) powers during the rejection of the SM_2 mode in the output FS. The input and output FS(BCB) far-field beam profiles are shown in (b). The input power and mode composition of the input FS and BCB are listed on the top of each panel.

Figure 3.36 illustrates the mode decomposition of the output BCB(FS) from the DCF as a function of the launched FS(BCB) power when the BCB is primarily coupled to a single mode. Similar to earlier findings, increasing the BCB power results in the output FS rejecting the same mode as the input BCB mode, as depicted in Figure 3.36(a). In contrast, the output BCB does not exhibit any rejection dynamics, since different input FSs with arbitrary mode content can lead to different output BCB mode compositions.

It is worth noting that in the special case of a two-mode fibre with identical Kerr coefficients (γ_{11}= γ_{22}= γ_{12}), the mode content of the output BCB is organized towards the orthogonal modal state of the input FS when they have equal power[130]. This phenomenon is observed in the DCF experiments, where the condition for the Kerr coefficients is approximately met (see Table 3.7). In Figure 3.36(c), the input BCB is mainly coupled to the SM_2 mode, whereas the input FS is a combination of 61% SM_1 mode and 39% SM_2 mode. As expected, the output BCB achieves a mode content of ~40% SM_1 mode and ~60% SM_2 mode when the two beams have equal power (indicated by the yellow dashed vertical lines). This observation is remarkable, particularly when the input FS exhibits a random mode content over time. In such a scenario, the amount of disorder of the input FS is transferred to the output BCB, whose mode content becomes therefore randomly distributed. This dynamic is similar to that of polarization attraction phenomena in single-mode fibres[109, 112, 113], where a mutual exchange in the degree of polarization is achieved between FS and BCB, that is to say, the polarization attraction undergone by the output FS takes place at the expense of a depolarization of the output BCB.

3.5 From mode rejection to mode control

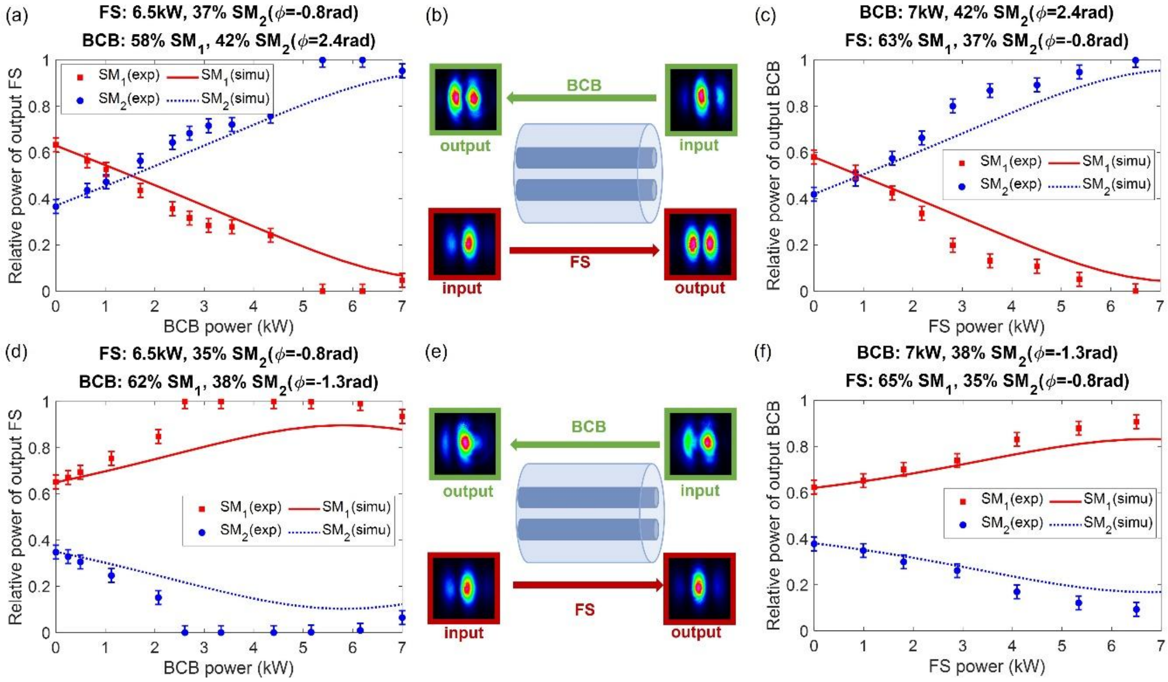

Figure 3.37 Comparison between the dynamics of the counter-propagating beams in the DCF. The mode decomposition of the output FS(BCB) in the DCF versus the launched BCB(FS) powers when the BCB is not coupled to a single mode. (a)-(c) Both the output FS and output BCB are in the SM_2 mode. (d)-(f) Both output counter-propagating beams are mainly in the SM_1 mode.

Mode rejection occurs when the input BCB is coupled to a single mode. In more complex scenarios, the input BCB can be coupled to a set of modes. Within this framework, it becomes pertinent to explore whether a specific output FS mode distribution can be achieved by appropriately setting the input BCB for a given input FS. Figure 3.37 presents two experimental results (dots) alongside their corresponding simulations (lines) where both the input BCB and input FS are coupled to a mixture of modes, as depicted at the top of each panel. In Figure 3.37, the input FS is coupled with ~60% SM$_1$ mode and ~40% SM$_2$ mode, with a relative phase of -0.8 rad. Similarly, the input BCB is coupled with ~60% SM$_1$ mode and ~40% SM$_2$ mode. However, in Figure 3.37(a)-(c), the input BCB has a relative mode phase of 2.4 rad, whereas in Figure 3.37(d)-(f), the relative mode phase for the input BCB is -1.3 rad. With ~7kW peak power for each counter-propagating beam, the mode content for both output FS and output BCB evolves similarly in both experiments and simulations. Consequently, the output FS and output BCB exhibit similar far-field profiles, as shown in Figure 3.37(b) and (e). This demonstrates that the output FS can be converted to a specific mode distribution from a given input FS by properly adjusting the input BCB, even when the input BCB is not single mode (not mode rejection). Additionally, it is possible to achieve identical output beam profiles from both ends of the fibre (similar output FS and output BCB) despite differing launching conditions at the input ends.

Similarly, the interaction dynamics of the counter-propagating beams in the TCF is also investigated. The theoretical framework developed for the special case where $\gamma_{mm}=2\gamma_{mn}=\gamma$ provides insight into possible scenarios (see section 3.2.1). For instance, it is possible to focus all the output FS power into a single mode, say the *k*-th mode, provided that the input BCB has the following configuration: $\left|\hat{b}_k(\mathrm{L})\right| \approx 0,\ \hat{b}_{n\neq k}(\mathrm{L}) \approx -i\left|\hat{f}_n(0)\right|e^{i\emptyset_{kn}}/\sqrt{1-\left|\hat{f}_k(0)\right|^2}$, where $\emptyset_{kn}$ is the relative phase between the input FS *k*-th mode and *n*-th mode. Figure 3.38 shows two preliminary experiments in TCF where the input BCB is coupled to a combination of modes. For the same input FS, different input BCBs result in substantially different output FS mode distributions.

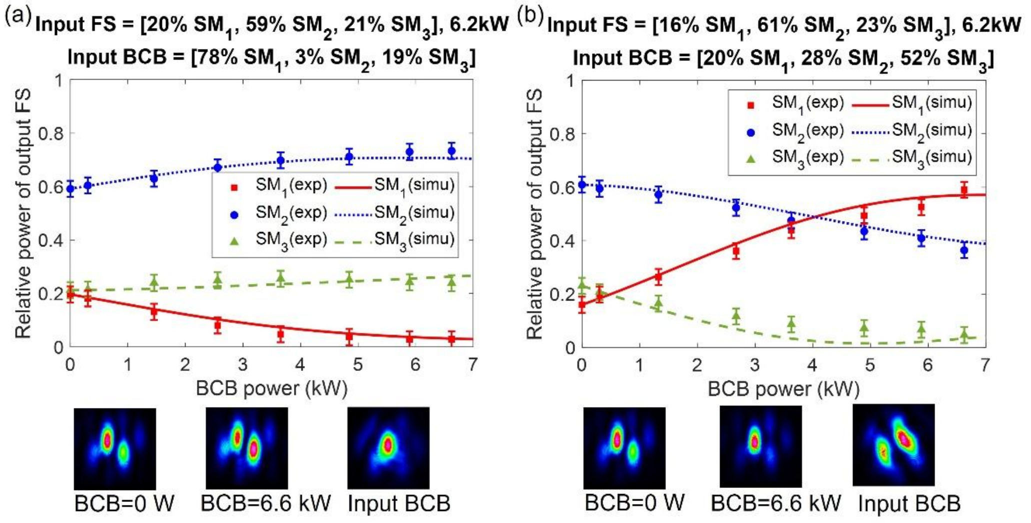
(a) Input FS = [20% SM$_1$, 59% SM$_2$, 21% SM$_3$], 6.2kW
Input BCB = [78% SM$_1$, 3% SM$_2$, 19% SM$_3$]
(b) Input FS = [16% SM$_1$, 61% SM$_2$, 23% SM$_3$], 6.2kW
Input BCB = [20% SM$_1$, 28% SM$_2$, 52% SM$_3$]

Figure 3.38 Preliminary experiments of all-optical mode control in the TCF, where the input BCB is coupled to a combination of supermodes (see the mode composition on the top of each panel), while the input FS remains almost identical. The bottom images display the FF beam profiles of the output FS at different BCB powers.

These preliminary results pave the way towards a more general idea of mode control in multimode systems, that is to say, the ability to control the mode content of the output FS on demand and all-optically via the BCB, or to efficiently manage the mode content of two counter-propagating beams. The BCB can also be generated through back-reflection or amplification of the FS, eliminating the need for an independent and additional optical source. This leads to the idea of light self-organization, where the output counter-propagating beams can be shaped in time and space. This approach opens new opportunities such as all-optical spatiotemporal beam shaping or highly scalable coherent combination in multimode and multicore fibres and waveguides.

3.6 Conclusions

In this chapter, the concepts of mode rejection and mode control are proposed and investigated in multimode counter-propagating systems using several few-mode fibres and two homemade multicore fibres. Mode rejection refers to the reduction of a specific mode content in the output FS when the input BCB is coupled to the same mode with intense power. By appropriately adjusting the input BCB, the selectivity and robustness of the mode rejection effect are demonstrated, leading to an all-optical method for achieving spatial mode locking. By tuning the temporal behaviour, all-optical spatiotemporal beam shaping can be obtained. In addition to the mode rejection effect observed in the output FS, the evolution dynamics of the output BCB are also investigated using the DCF and the TCF. The general idea of mode control is explored, showing that the output counter-propagating beams can potentially be spatiotemporally controlled in an all-optical manner.

Notes: The results reported in this chapter have been selectively published (see LoP1, LoP4, LoP5, LoP11, LoP12 in the List of Publications). LoP1 includes the mode decomposition method for multicore fibres, where also includes some results reported in the Appendix A.2. This is a single-authored paper published in Optics Letters. LoP5 includes the main results of mode rejection and control that were demonstrated in this chapter. This is a co-authored paper published together with Ian Davidson, Jayanta Sahu, David J. Richardson, Stefan Wabnitz, and Massimiliano Guasoni in Nature Communications. The experiments, simulations, co-development of derivations and code were my work; the 3-core fibre was fabricated by Ian Davidson from the Optoelectronics Research Centre; the dual-core fibres used in the experiments were fabricated by Jayanta Sahu from the Optoelectronics Research Centre; the idea of mode rejection and light self-organization was originally conceived by Massimiliano Guasoni from the Optoelectronics Research Centre; this project was supervised by Massimiliano

Guasoni and David J. Richardson from the Optoelectronics Research Centre. I also sincerely acknowledge Saurabh Jain for his assistance with the preliminary experiments. LoP4, LoP11, and LoP12 are conference papers where we reported on the observation of mode rejection and light self-organization in optical fibres.

Table 3.8 summarizes the mode rejection results for the LP modes and supermodes in the MMFs and MCFs introduced in this chapter. By using 0.4m-1m long fibres and a total peak power of ~4-16 kW (0.5 ns pulses), selective rejection of individual LP modes and supermodes is achieved with a conversion efficiency ~20-80%. The maximum mode rejection efficiency is obtained when using co-polarized FS and BCB in polarization maintaining fibres. Other factors that can affect the efficiency of mode rejection, such as launched power, fibre nonlinearity, polarization coupling, and spectrum broadening, have also been investigated.

By appropriately adjusting the input BCB, the selectivity and robustness of the mode rejection effect are demonstrated, leading to an all-optical method for achieving spatial mode locking. By tuning the temporal behaviour, all-optical spatiotemporal beam shaping can be obtained. In addition to the mode rejection effect observed in the output FS, the evolution dynamics of the output BCB are also investigated using the DCF and the TCF. The general idea of mode control is explored, showing that the output counter-propagating beams can potentially be spatiotemporally controlled in an all-optical manner.

Notes: The results reported in this chapter have been selectively published (see LoP1, LoP4, LoP5, LoP11, LoP12 in the List of Publications). LoP1 includes the mode decomposition method for multicore fibres, where also includes some results reported in the Appendix A.2. This is a single-authored paper published in Optics Letters. LoP5 includes the main results of mode rejection and control that were demonstrated in this chapter. This is a co-authored paper published together with Ian Davidson, Jayanta Sahu, David J. Richardson, Stefan Wabnitz, and Massimiliano Guasoni in Nature Communications. The experiments, simulations, co-development of derivations and code were my work; the 3-core fibre was fabricated by Ian Davidson from the Optoelectronics Research Centre; the dual-core fibres used in the experiments were fabricated by Jayanta Sahu from the Optoelectronics Research Centre; the idea of mode rejection and light self-organization was originally conceived by Massimiliano Guasoni from the Optoelectronics Research Centre; this project was supervised by Massimiliano Guasoni and David J. Richardson from the Optoelectronics Research Centre. I also sincerely acknowledge Saurabh Jain for his assistance with the preliminary experiments. LoP4, LoP11, and LoP12 are conference papers where we reported on the observation of mode rejection and light self-organization in optical fibres.

Table 3.8 Summary of the mode rejection results for MMFs and MCFs

Fibre	Length (m)	Total peak power of FS and BCB (kW)	Rejected modes	Efficiency
PM1550-xp	1	16	LP_{01}, LP_{11}	30%
PMHN1	0.4	4	LP_{01}, LP_{11}	30%
PM2000	0.4	9	LP_{01}, LP_{11e}, LP_{11o}, LP_{21e}, LP_{21o}, LP_{02}	20% - 80%
SMF28	1	16	LP_{01}, LP_{11}	22% - 80%
DCF	0.4 - 1	12	SM_1, SM_2	20%-50%
TCF	0.4	12	SM_1, SM_2, SM_3	20%-40%

Chapter 4 Counter-propagating nonlinear gratings in multimode and multicore fibres

4.1 Introduction

In this chapter, the concept of “all-optical counter-propagating nonlinear gratings” in multimode systems is proposed. These gratings are generated by a backward-propagating multimodal beam with intense power, the mode beating between these modes generates an instantaneous grating via the Kerr effect. This optical nonlinear grating could lead to all-optical ultrafast switching of a low-power forward-propagating beam, while in Chapter 3 both forward and backward beams are in a high nonlinear regime. All-optical mode switching between fibre modes (in MMFs and MCFs) and power switching between fibre cores (in MCFs) are validated through experiments conducted with various FMFs and homemade MCFs. Initially, the theoretical framework of counter-propagating nonlinear gratings is introduced, supported by theoretical estimations of mode switching and power switching in MMFs and MCFs. Subsequently, experimental investigations demonstrate the all-optical switching of LP modes or supermodes using a range of fibres, including PM1550-xp, PMHN1, DCF, and TCF. Lastly, ultrafast all-optical power switching between MCF cores is demonstrated using counter-propagating beams with 500 ps pulses in DCF and TCF. The dynamics of counter-propagating nonlinear gratings are discussed by comparing the experimental results from different fibres and by direct comparison with the theory and simulations. Several conceptual devices are introduced based on the dynamics of counter-propagating nonlinear gratings, including all-optically tuneable mode converters, all-optically tuneable power splitters, combiners, and power switches, as well as all-optical phase detection at terminal ends.

4.2 Dynamics of counter-propagating nonlinear gratings

4.2.1 Theory

The counter-propagating nonlinear grating is generated by a high-power backward control beam (BCB) in a multimode system, and it can influence the propagation of a low-power forward probe beam (PB) in an all-optical manner. However, unlike the governing equations of mode rejection introduced in Chapter 3, here the coupled nonlinear Schrödinger equations are modified due to the substantial power difference between the counter-propagating beams. Assuming that the PB fields F_m are much weaker than the BCB fields B_m, Eqs. (3.2.1) and (3.2.2) are simplified as follows:

$$\frac{\partial F_m}{\partial z} + \beta_1^{(m)}\frac{\partial F_m}{\partial t} = iF_m\sum\nolimits_n \gamma_{mn}p|B_n|^2 + iB_m^*\sum\nolimits_{n\neq m} p\gamma_{mn}B_nF_n \tag{4.2.1}$$

$$-\frac{\partial B_m}{\partial z} + \beta_1^{(m)}\frac{\partial B_m}{\partial t} = -i\gamma_{mm}|B_m|^2B_m + iB_m\sum\nolimits_n 2\gamma_{mn}|B_n|^2 \tag{4.2.2}$$

where F_m (B_m) denotes the amplitude of the m-th mode in the *PB* (*BCB*). As a result, the right-hand side of Eq. (4.2.1) is left with the cross-phase modulation terms induced by the BCB modes, and the energy exchange term describing the interaction between the m-th and n-th modes. In contrast, the right-hand side of Eq. (4.2.2) is left with only the self-phase and cross-phase modulation terms induced by the BCB modes.

The evolution of the BCB amplitude B_m can be readily found from Eq. (4.2.2) in the CW limit,

$$B_m = |B_m|exp\left[-i\left(\gamma_{mm}|B_m|^2 + \sum\nolimits_{n\neq m} 2\gamma_{mn}|B_n|^2\right)z\right] \tag{4.2.3}$$

By substituting this solution into Eq. (4.2.1) and applying the transformation $F_m = f_m exp[i(\gamma_{mm}|B_m|^2 + \sum_{n\neq m} 2\gamma_{mn}|B_n|^2)z]$, the following equations describing the evolution of the m-th mode in the PB along the propagation direction z can be obtained (again, in the CW limit),

$$\begin{aligned}\frac{\partial f_m}{\partial z} = i\left[(p-1)\gamma_{mm}|B_m|^2 + \sum\nolimits_{n\neq m}(p-2)\gamma_{mn}|B_n|^2\right]f_m \\ + i\sum\nolimits_{n\neq m} p\,\gamma_{mn}|B_m||B_n|f_n\end{aligned} \tag{4.2.4}$$

The amplitude f_m can be analytically solved from these equations by rewriting them as,

$$\frac{\partial}{\partial z}\begin{bmatrix} f_1 \\ \vdots \\ f_N \end{bmatrix} = iM\begin{bmatrix} f_1 \\ \vdots \\ f_N \end{bmatrix} \tag{4.2.5}$$

$$M = \begin{bmatrix} \begin{bmatrix} (p-1)\gamma_{11}|B_1|^2 \\ +\sum_{n\neq 1}(p-2)\gamma_{1n}|B_n|^2 \end{bmatrix} & p\gamma_{12}|B_1||B_2| & \cdots & p\gamma_{1N}|B_1||B_N| \\ p\gamma_{21}|B_2||B_1| & \begin{bmatrix} (p-1)\gamma_{22}|B_2|^2 \\ +\sum_{n\neq 2}(p-2)\gamma_{2n}|B_n|^2 \end{bmatrix} & \cdots & p\gamma_{2N}|B_2||B_N| \\ \vdots & \vdots & \ddots & \vdots \\ p\gamma_{N1}|B_N||B_1| & p\gamma_{N2}|B_N||B_2| & \cdots & \begin{bmatrix} (p-1)\gamma_{NN}|B_N|^2 \\ +\sum_{n\neq N}(p-2)\gamma_{Nn}|B_n|^2 \end{bmatrix} \end{bmatrix} \tag{4.2.6}$$

where M is a $N*N$ matrix representing the interactions between the PB modes influenced by the BCB, with N as the total mode count. By calculating the eigenvalues and eigenvectors of M, the analytical evolution of the PB amplitude can be obtained,

$$\begin{bmatrix} f_1(z) \\ \vdots \\ f_N(z) \end{bmatrix} = w\begin{bmatrix} e^{i\lambda_1 z} & 0 & 0 \\ 0 & \cdots & 0 \\ 0 & 0 & e^{i\lambda_N z} \end{bmatrix}w^{-1}\begin{bmatrix} f_1(z=0) \\ \vdots \\ f_N(z=0) \end{bmatrix} \tag{4.2.7}$$

where w is the matrix of eigenvectors, λ_k are eigenvalues obtained through eigenvalue decomposition of M, and $f_m(z=0)$ represents the initial PB launching condition. In the simplest instance of a 2-mode and co-polarization (p=2) scenario, the solutions describing the PB evolutions can be derived as follows,

$$f_1(z) = \left[A_1 e^{i\frac{g}{2}z} + A_2 e^{-i\frac{g}{2}z}\right] e^{i\frac{\Delta\emptyset_{12}}{2}z} \tag{4.2.8}$$

$$f_2(z) = \left[\frac{A_1 g}{2C} e^{i\frac{g}{2}z} - \frac{A_2 g}{2C} e^{-i\frac{g}{2}z}\right] e^{-i\frac{\Delta\emptyset_{12}}{2}z} + \left[\frac{A_1}{C} e^{i\frac{g}{2}z} + \frac{A_2}{C} e^{-i\frac{g}{2}z}\right] \frac{\Delta\emptyset_{12}}{2} e^{-i\frac{\Delta\emptyset_{12}}{2}z} \tag{4.2.9}$$

where $A_1 = \frac{-\Delta\emptyset_{12}+g}{2g} f_1(z=0) + \frac{C}{g} f_2(z=0)$, $A_2 = \frac{\Delta\emptyset_{12}+g}{2g} f_1(z=0) - \frac{C}{g} f_2(z=0)$, $C = 2\gamma_{12}|B_1||B_2|$, $g = \sqrt{\Delta\emptyset_{12}{}^2 + 4C^2}$, $\Delta\emptyset_{12} = -\gamma_{11}|B_1|^2 + \gamma_{22}|B_2|^2$. Therefore, the BCB acts as a tuneable optical grating that can be used for all-optical switching among the modes of the output PB. The switching of the PB modes depends on the launched power $|B_m|^2$, mode composition $|B_m|^2/\sum_n|B_n|^2$, and the polarization state p of the BCB, as well as the initial PB conditions f_m(z=0).

4.2.2 Simulations

4.2.2.1 Mode switching driven by counter-propagating nonlinear gratings

In this section, the theoretical mode switching of the PB (Eq. (4.2.7)) is demonstrated for several fibres used in Chapter 3, including PM1550-xp, PMHN1, DCF, and TCF. The mode switching results are discussed by varying the power, mode composition, and polarization state of the BCB, along with different initial PB mode compositions.

The first type of fibre under consideration is the traditional single-core multimode fibre, demonstrated using PM1550-xp and PMHN1. The dispersion parameters and Kerr coefficients of different modes in these fibres are provided in Table 3.1 and Table 3.2. For these fibres, a 2-mode scenario (LP_{01} and LP_{11} modes) is considered, with the counter-propagating beams in either co-polarization or orthogonal polarization states. The counter-propagating beams are continuous waves and have the same frequency in the calculations.

Considering a 10cm-long PM1550-xp fibre, a BCB with 10 kW power and a forward PB with a substantially weaker power of 0.1 kW are launched from its opposite ends, both in the same polarization state. The initial PB condition (input into the left end of the fibre, z=0 in Figure 4.1) is set as 100% LP_{01} mode, whereas the input BCB is set as 50% LP_{01} mode and 50% LP_{11} mode with 0 rad phase difference between them. After applying the PM1550-xp parameters (nonlinear coefficients and fibre length) and boundary conditions (mode composition, power, and polarization) to Eqs. (4.2.3)-(4.2.7), the amplitudes (F_m and B_m) of different modes for PB and BCB can be obtained at specific positions. These amplitudes are the modal coefficients of different modes (see Eq.(3.3.2)). By superposing the transverse mode profiles with the corresponding amplitudes, one can obtain the evolution of spatial shapes for PB (propagating from left to right) and BCB (propagating from right to left). Figure 4.1 illustrates the side views (along y-axis) of the spatial shape of PB(BCB) as a function of the longitudinal position (along z-axis) inside the fibre. The propagation distance is converted to the numbers of nonlinear length L_{NL}. In this case, L_{NL} is 3.3 cm (10kW peak power and $\gamma=3kW^{-1}m^{-1}$), consequently, this 10cm-long fibre supports a propagation of $3*L_{NL}$.A complete mode switching of the PB from the LP_{01} mode to the LP_{11} mode is achieved in this fibre, as shown in the inset mode profiles. On the contrary, the BCB mode distribution remains unchanged during propagation. It is worth noting that increasing the number of propagated nonlinear lengths can be achieved by either using a longer fibre or increasing the launched BCB power while maintaining the fibre length. The theoretical mode switching remains the same using either approach, as Eqs. (4.2.6) and (4.2.7) include the tuneable parameters z (fibre length) and $|B_m|^2$ (BCB powers). Notably, the latter approach indicates an all-optical method to achieve mode switching in fixed optical fibres.

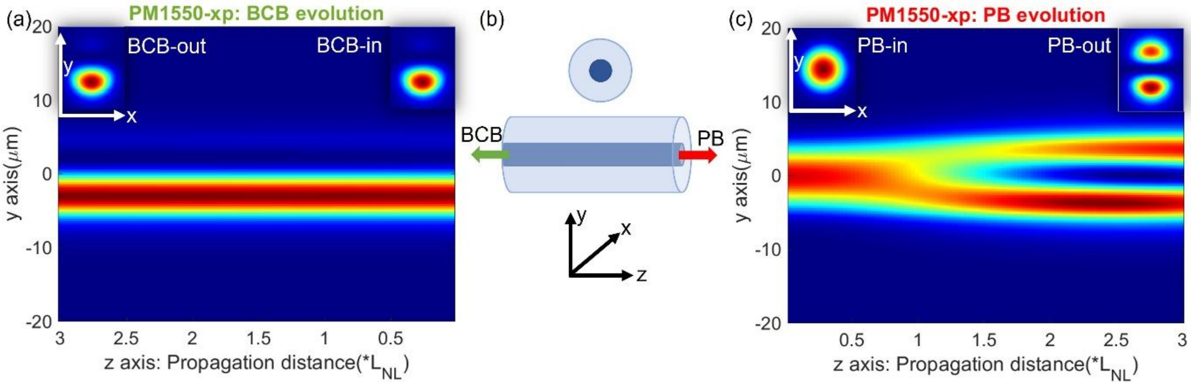

Figure 4.1 Theoretical mode switching of the PB in PM1550-xp calculated from Eq. (4.2.7), with the evolution of the counter-propagating BCB calculated from Eq. (4.2.3). The boundary conditions: PB (z=0, 100% LP_{01} mode, total power=0.1 kW), BCB (z=$3*L_{NL}$ (10 cm), 50% LP_{01} mode and 50% LP_{11} mode, total power=10 kW).

Similarly, by applying the PMHN1 parameters to Eqs. (4.2.3) and (4.2.7), theoretical mode switching results can be obtained for a 10cm-long PMHN1 fibre, as depicted in Figure 4.2. The boundary conditions are the same as those for the PM1550-xp as shown in Figure 4.1. However, due to an approximately fourfold increase in the nonlinearity for elliptical-core PMHN1 (see Table 3.1 and Table 3.2), the 10cm-long PMHN1 fibre supports a propagation of $13.2*L_{NL}$. In comparison with Figure 4.1, Figure 4.2 clearly highlights that the PB mode distribution at the fibre output can be all-optically and periodically tuned by increasing BCB power or using fibres with higher nonlinearity. In the specific case of switching between the LP_{01} and LP_{11} modes, where $\gamma_{12} \sim 0.6\ \gamma_{11}$ (see Table 3.1 and Table 3.2), complete mode switching from one mode to another requires propagation of approximately 3*L$_{NL}$ (3*L$_{NL}$ needed for PM1550-xp, ~2.7*L$_{NL}$ needed for PMHN1, obtained from Figure 4.1(c) and Figure 4.2(c)). This suggests that an all-optical mode switching for a fixed fibre can be achieved by adjusting the BCB powers to satisfy the requirements of the nonlinear length.

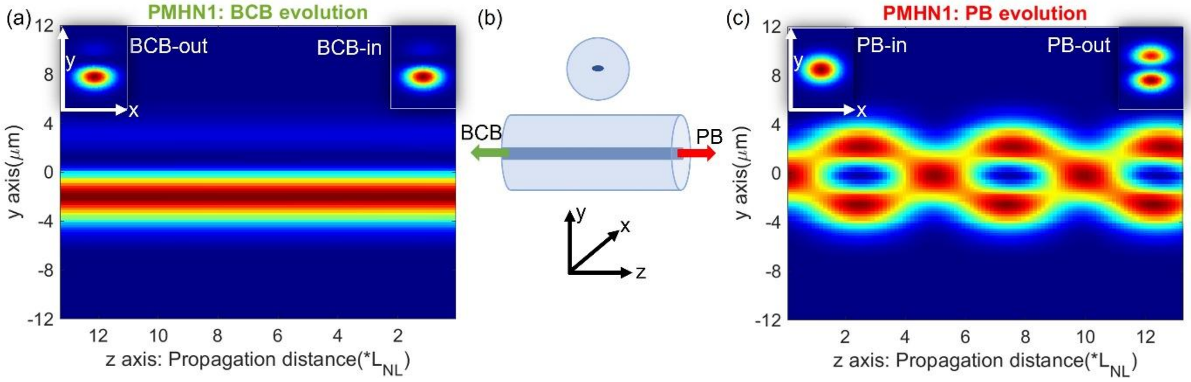

Figure 4.2 Theoretical mode switching of the PB in PMHN1, with the boundary conditions: PB (z=0, 100% LP$_{01}$ mode, total power=0.1 kW), BCB (z=13.2*L$_{NL}$ (10 cm), 50% LP$_{01}$ mode and 50% LP$_{11}$ mode, total power=10 kW).

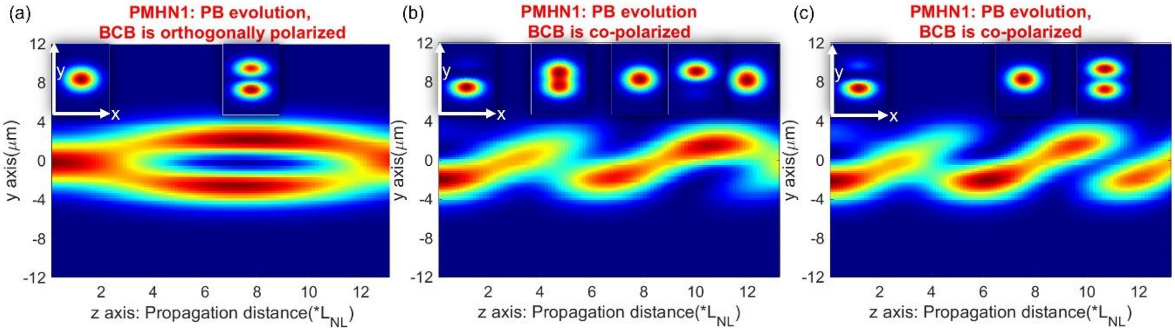

Figure 4.3 Theoretical mode switching in PMHN1 with different boundary conditions. (a) PB (z=0, 100% LP$_{01}$ mode, total power=0.1 kW), BCB (z=13.2*L$_{NL}$ (10 cm), 50% LP$_{01}$ mode and 50% LP$_{11}$ mode, total power=10 kW, orthogonally polarized with the PB). (b) PB (z=0, 50% LP$_{01}$ mode and 50% LP$_{11}$ mode, total power=0.1 kW), BCB (z=13.2*L$_{NL}$, 90% LP$_{01}$ mode and 10% LP$_{11}$ mode, total power=10 kW, co-polarized with the PB). (c) PB (z=0, 30% LP$_{01}$ mode and 70% LP$_{11}$ mode, total power=0.1 kW), BCB (z=13.2*L$_{NL}$, 80% LP$_{01}$ mode and 20% LP$_{11}$ mode, total power=10 kW, co-polarized with the PB).

Additionally, mode switching can also be controlled by adjusting the polarization state and mode composition of the BCB. Figure 4.3 presents three examples using the PMHN1 fibre, with boundary conditions different from those in Figure 4.2. In Figure 4.3(a), the mode switching period (the numbers of nonlinear lengths needed for complete conversion from one mode to another) is stretched by three times when the BCB polarization is converted from the co-polarized state to the orthogonally polarized state with respect to the PB polarization. This variation is determined by the polarization-dependent coefficient p (p=2 and 2/3 respectively for the co-polarized and orthogonally polarized cases). Figure 4.3(b) and (c) depict cases where the initial PB condition is not in single-mode and the BCB is not evenly coupled into the two LP modes (see caption for details). These results indicate that the mode switching behaviour varies when either the PB or the BCB changes. However, all-optical mode switching for a PB with a random mode composition is still achievable by properly adjusting the BCB launching conditions.

To validate the theoretical outcomes, analytical solutions from Eq. (4.2.7) are computed against the numerical simulations of the coupled nonlinear Schrödinger equations, Eqs. (3.2.1) and (3.2.2), using the standard finite-difference method introduced in Section 3.2.2. Figure 4.4 presents the comparisons of PB mode switching from the same initial state containing 100% LP_{01} mode, under different BCB conditions: (a) launched total powers, (b) mode compositions, (c) polarization states. Importantly, the analytical solutions (lines) agree well with the numerical simulations (dots) in all the different cases under test. In Figure 4.4(a), three BCB powers are compared to illustrate the tuneable mode switching period within a fixed fibre length. In Figure 4.4(b), three BCB mode compositions are compared to illustrate the tuneable maximum mode conversion. Finally, in Figure 4.4(c), the comparison between the co-polarized and orthogonally polarized BCB demonstrates the polarization dependence of mode switching.

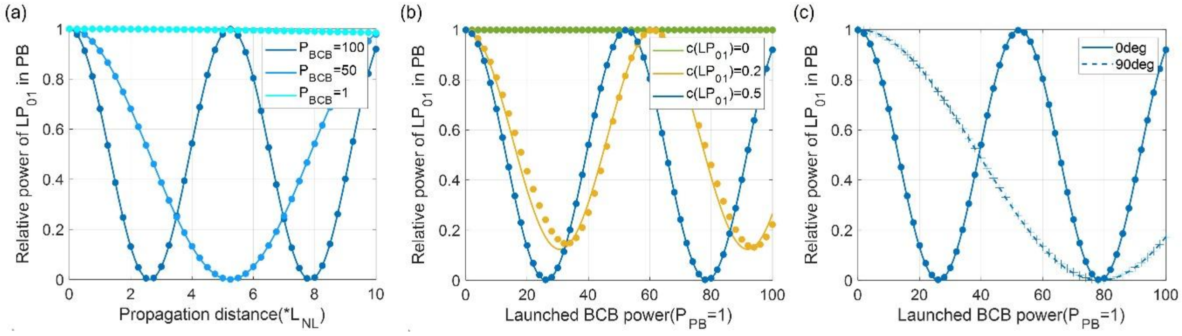

Figure 4.4 Analytical solutions (lines) from Eq. (4.2.7) and numerical simulations (dots) of Eqs. (3.2.1) and (3.2.2) in a 2-mode counter-propagating scenario, with the PMHN1 fibre parameters applied. (a) Mode switching of the PB (normalized power P_{PB}=1) versus the propagation distance when the BCB is evenly coupled to the LP_{01} mode and the LP_{11} mode under different total launched powers (P_{CB}=1, 50, 100). (b) Mode switching of the PB versus the launched BCB power under different BCB mode compositions, with c(LP_{01}) of the total launched BCB power coupled to the LP_{01} mode. (c) Mode switching of the PB versus the launched BCB power under different BCB polarization states, with 0 deg denoting the co-polarization and 90 deg denoting the orthogonal polarization.

Followingly, DCF and TCF are also analysed by applying their parameters (see Table 3.7) into Eqs. (4.2.3) and (4.2.7). Figure 4.5 demonstrates the theoretical mode switching between the supermodes in a 10cm-long DCF. A forward PB with 0.1 kW power and a co-polarized BCB with 10 kW power are launched at opposite fibre ends. Initially, the PB is coupled into 100% SM_1 mode, while the BCB is evenly coupled to the SM_1 and SM_2 modes with a 0 rad phase difference between them. In DCF, periodic mode switching of the PB from the SM_1 mode to the SM_2 mode is achieved, as depicted in Figure 4.5(c) with inset mode and phase distributions. In contrast, Figure 4.5(a) shows that the BCB mode composition remains constant during propagation. Unlike the case for the PM1550-xp illustrated in Figure 4.1, here, a complete switching from one mode to another requires a shorter propagation distance of just $1.5*L_{NL}$. This increased efficiency is due to the larger intermodal Kerr coefficient γ_{12} in DCF, which is approximately twice as large as those in PM1550-xp (see Table 3.1 and Table 3.7), leading to a more efficient energy exchange between the modes (indicated by the last term in Eq. (4.2.1)).

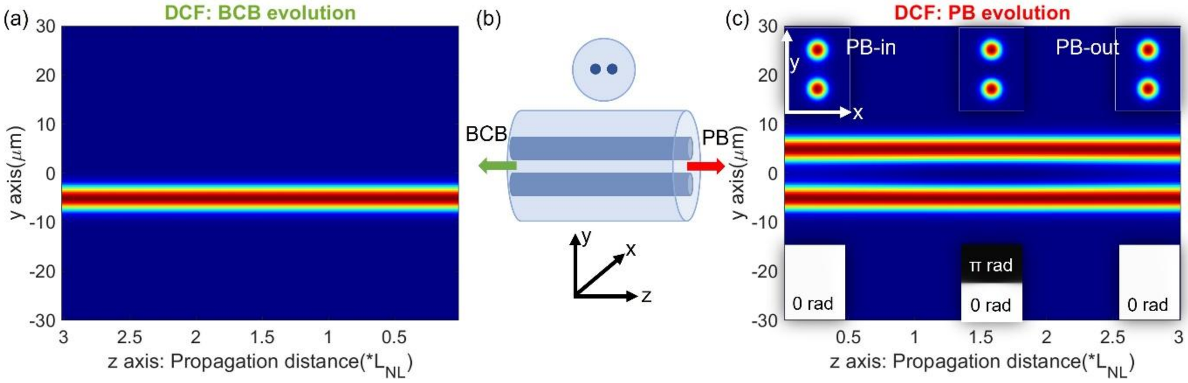

Figure 4.5 Theoretical mode switching of the PB in DCF, with the boundary conditions: PB (z=0, 100% SM_1 mode, total power=0.1 kW), BCB ($z=3*L_{NL}$ (10 cm), 50% SM_1 mode and 50% SM_2 mode, total power=10 kW).

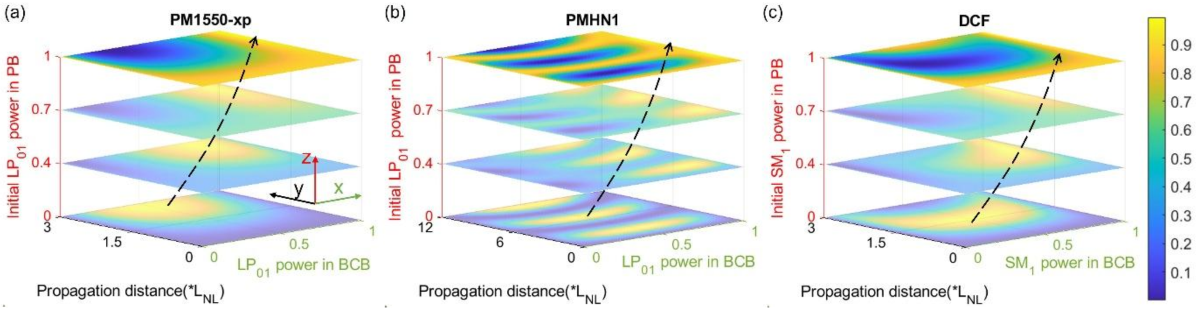

Figure 4.6 Theoretical mode switching in bimodal platforms: (a) PM1550-xp, (b) PMHN1, (c) DCF. For each fibre, the relative power of the LP_{01}(or SM_1) mode in PB is plotted as a function of the LP_{01} mode power in BCB (x-axis), the propagation distance (y-axis), and the initial LP_{01} mode power in PB (z-axis). The slices are the LP_{01} mode power evolutions in PB with the same initial LP_{01} mode power but under different BCB mode compositions and at different propagation distances.

Until now, specific instances of mode switching under defined boundary conditions have been demonstrated using bimodal fibres (PM1550-xp, PMHN1, and DCF). To delve deeper into the mode switching process and the dynamics of counter-propagating nonlinear gratings, the PB evolution over propagation distance is computed while varying the boundary conditions. Specifically, the input mode compositions of the BCB and PB are independently varied, resulting in the 3D plots depicted in Figure 4.6. In each figure, assuming the BCB and PB co-polarized, the relative power of the fundamental mode (LP_{01} mode or SM_1 mode) in PB is depicted as a function of three parameters: (1) BCB mode composition (x-axis), (2) propagation distance (either real fibre length or substituted with variable BCB powers, y-axis), and (3) initial PB condition (z-axis). By comparing the slices along the z-axis, it is observed that the power distribution shifts along the x-axis as the initial power of the fundamental mode increases from 0 to 1 in the PB, as indicated with the dashed arrows. Figure 4.6 provides comprehensive predictions for the all-optically tuneable mode switching of the PB in these bimodal fibres, even with random initial PB conditions. The mode switching capability can be adjusted in several ways, including varying launched power, mode composition, and polarization state of the BCB, as well as altering fibre length and nonlinearity.

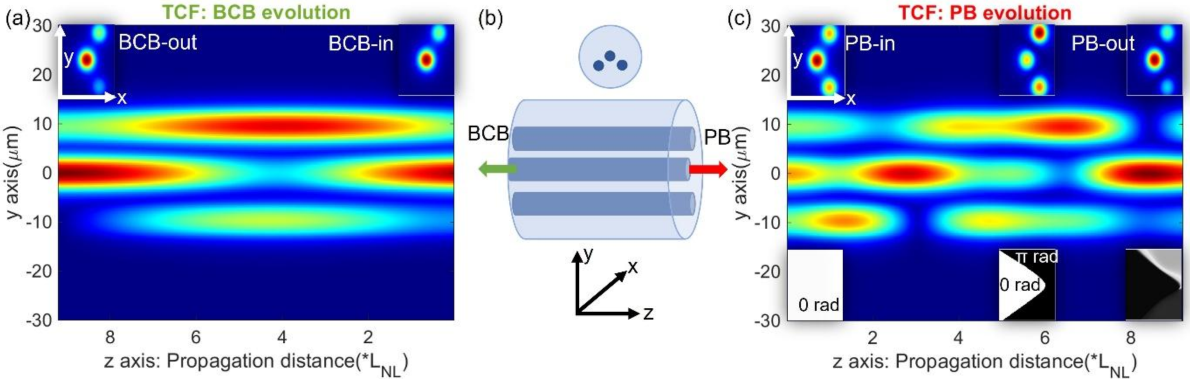

Figure 4.7 Theoretical mode switching of the PB in TCF, with the boundary conditions: PB (z=0, 100% SM_1 mode, total power=0.1 kW), BCB (z=9.2*L_{NL} (40 cm), 73% SM_1 mode, 10% SM_2 mode, and 17% SM_3 mode, total power=10 kW).

In contrast to previous analyses focusing on bimodal scenarios, the exploration now extends to the general case using a fibre supporting more than two spatial modes, with TCF serving as an example. Nonetheless, the generalisation to an arbitrary number of modes (and cores) follows a similar approach. Leveraging Eqs. (4.2.3) and (4.2.7), the evolution of the PB and BCB can be derived as a function of propagation distance. Figure 4.7 illustrates an instance of mode switching where the PB is initially coupled solely into the SM_1 mode, while the BCB is coupled with 73% SM_1 mode, 10% SM_2 mode, and 17% SM_3 mode. The fibre length is set at 40 cm, corresponding to a propagation of 9.2*L_{NL}. Other parameters, such as counter-propagating beam power and polarization state, remain consistent with the DCF analysis. A switching from the SM_1 mode to the SM_3 mode in the PB occurs during propagation from 0 to ~6*L_{NL}, as indicated by the inset near-field intensity profiles and phase distributions in Figure 4.7(c). In contrast, the relative power of each BCB mode remains constant throughout propagation. However, the varying relative phases between the BCB modes result in a fluctuating transverse mode distribution, as depicted in Figure 4.7(a). It is essential to note that in a fibre supporting more than two modes, mode switching between the modes may not occur in a periodic manner as the propagation length or BCB power increases. This variation arises from a much higher degree of freedom in the system, including the relative power and phase between multiple modes in the PB and BCB.

4.2.2.2 All-optical power switching in multicore fibres

Due to the multi-channel architecture in multicore fibres, switching between the supermodes gives rise to another intriguing phenomenon: all-optical core-to-core power switching. As demonstrated in the TCF mode switching results depicted in Figure 4.7, the capabilities of power combining and splitting have already been showcased. Here, a detailed elucidation is provided. Through the coherent combination of supermodes with varying relative power and phase, the power distribution among the MCF cores can be modified. This relationship between core fields and mode fields (as obtained in Eq. (4.2.7)) can be expressed as:

$$\begin{bmatrix} E_{c1}(z) \\ \vdots \\ E_{cN}(z) \end{bmatrix} = \mathrm{T} \begin{bmatrix} f_1(z) \\ \vdots \\ f_N(z) \end{bmatrix} \tag{4.2.10}$$

where E_{cN} is the electric field in the N-th core, and T is a transformation matrix. T is contingent upon the supermode distributions specific to a given MCF. For instance, in the case of a DCF, $\mathrm{T} = \frac{1}{\sqrt{2}}\begin{bmatrix} 1 & 1 \\ 1 & -1 \end{bmatrix}$, while for a TCF, $\mathrm{T} = \frac{1}{2}\begin{bmatrix} \sqrt{2} & 0 & \sqrt{2} \\ 1 & \sqrt{2} & -1 \\ 1 & -\sqrt{2} & -1 \end{bmatrix}$.

Based on Eq. (4.2.10), the distribution of PB power across each core of the fibre can be determined. Figure 4.8 illustrates the theoretical power switching in a 20cm-long DCF, where a total BCB power of 10 kW and a total PB power of 0.1 kW are applied. Similar to Figure 4.6, Figure 4.8(a) presents a 3D plot showcasing the PB power distributions within the right DCF core, as a function of (1) BCB mode composition (x-axis), (2) propagation distance (either real fibre length or substituted with variable BCB powers, y-axis), and (3) initial PB condition (z-axis). Compared with Figure 4.6(c), it is obvious that power switching requires different PB and BCB conditions compared to mode switching.

A clear power switching between the DCF cores can be obtained when the PB is initially evenly coupled into the SM_1 and SM_2 modes with a 0 rad phase difference between them. Under this condition, the corresponding power distribution slice is depicted in Figure 4.8(b), where all the PB power is focused on the right core before propagation (resulting from the in-phase combination of the SM_1 and SM_2 modes leading to destructive interference within one core). Figure 4.8(b) demonstrates that a complete power switching from the right core to the left core can be achieved when the relative SM_1 mode power in the BCB is approximately 88% or 12%. As an illustration, Figure 4.8(c) depicts the power distribution within the two DCF cores when the BCB is coupled with 88% SM$_1$ mode and 12% SM$_2$ mode, showcasing complete power switching from the right core to the left core achieved at a propagation distance of 3.5*L_{NL} – 4.7*L_{NL}. Notably, Figure 4.8(c) also illustrates an effective power splitting with a tuneable ratio between the cores. By adjusting the nonlinear length through varying the launched BCB power, all-optically power switching and all-optically tuneable power splitting can be achieved in a fixed-length fibre.

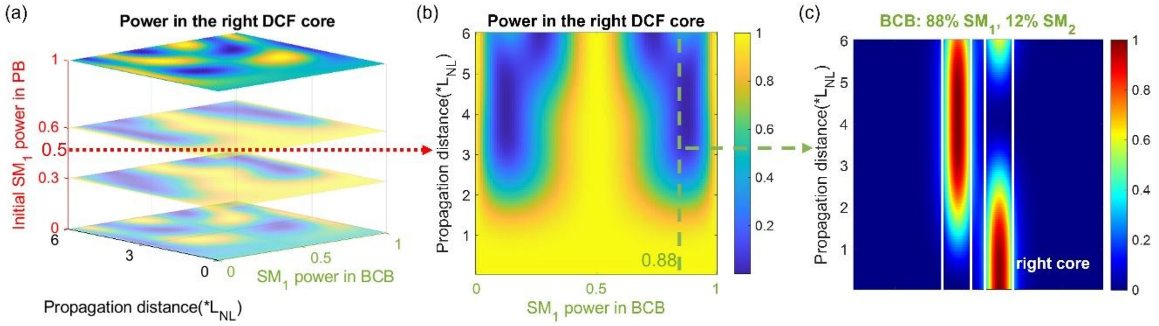

Figure 4.8 Theoretical power switching between the DCF cores in PB. (a) The PB power distributions in the right DCF core as a function of the SM$_1$ mode power in BCB (x-axis), the propagation distance (y-axis), and the initial SM$_1$ mode power in PB (z-axis). The slices are the results under the same initial SM$_1$ mode power in PB. (b) A slice of (a) when the initial SM$_1$ mode power in PB is set as 0.5. (c) The PB power distribution within the two DCF cores versus the propagation distance, with the initial SM$_1$ mode power of 0.5 in PB and the BCB coupled into 88% SM$_1$ mode and 12% SM$_2$ mode.

Subsequently, Figure 4.9 presents two examples showcasing complete power switching from one core to another core in the TCF. The fibre length is 1 m, with total powers of 10 kW and 0.1 kW for the BCB and PB, respectively. In Figure 4.9(a)-(c), the input PB consists of an in-phase combination of 50% SM$_1$ mode, 30% SM$_2$ mode, and 20% SM$_3$ mode, while the input BCB comprises an in-phase combination of 70% SM$_1$ mode, 10% SM$_2$ mode, and 20% SM$_3$ mode. Figure 4.9(a) illustrates the redistribution of PB power across the three cores as the propagation distance increases. The integrated power in the three cores is compared in the upper figure of Figure 4.9(c), indicating that most of the power focuses on core2 (as labelled in Figure 4.9(a)) at a propagation distance of 5.2*L_{NL}, then shifts to core1 at 11.4*L_{NL}, and finally to core3 at 17.4*L_{NL}. Additionally, as the BCB is coupled with a mixture of modes, although the relative mode content of each supermode remains constant, the varying phase differences between the modes could also lead to the BCB power variations among the cores, as depicted in Figure 4.9(b) and (c).

Similarly, Figure 4.9(d)-(f) shows the dynamics when the PB and the BCB are coupled into 2 of the 3 modes. The input PB is a combination of 50% SM$_1$ mode and 50% SM$_3$ mode, whereas the BCB is coupled with 80% SM$_1$ mode and 20% SM$_3$ mode. Under this condition, the TCF works as a 2-mode platform because the counter-propagating nonlinear grating is only composed of the SM$_1$ and SM$_3$ modes, resulting in mode switching between these two modes in the PB. Nevertheless, periodic power switching among the cores can still be observed. Starting from a condition with all the power located in the core1, Figure 4.9(d) and (f) demonstrate that most of the PB power returns to core1 after propagating a distance of 9.3*L_{NL}, while the power becomes evenly distributed in core2 and core3 at a distance ranging from 2.9*L_{NL} to 5.8*L_{NL}. The power redistribution among the cores for the BCB, as a result of varying phase differences between the SM_1 and SM_3 modes, is illustrated in Figure 4.9(e) and (f).

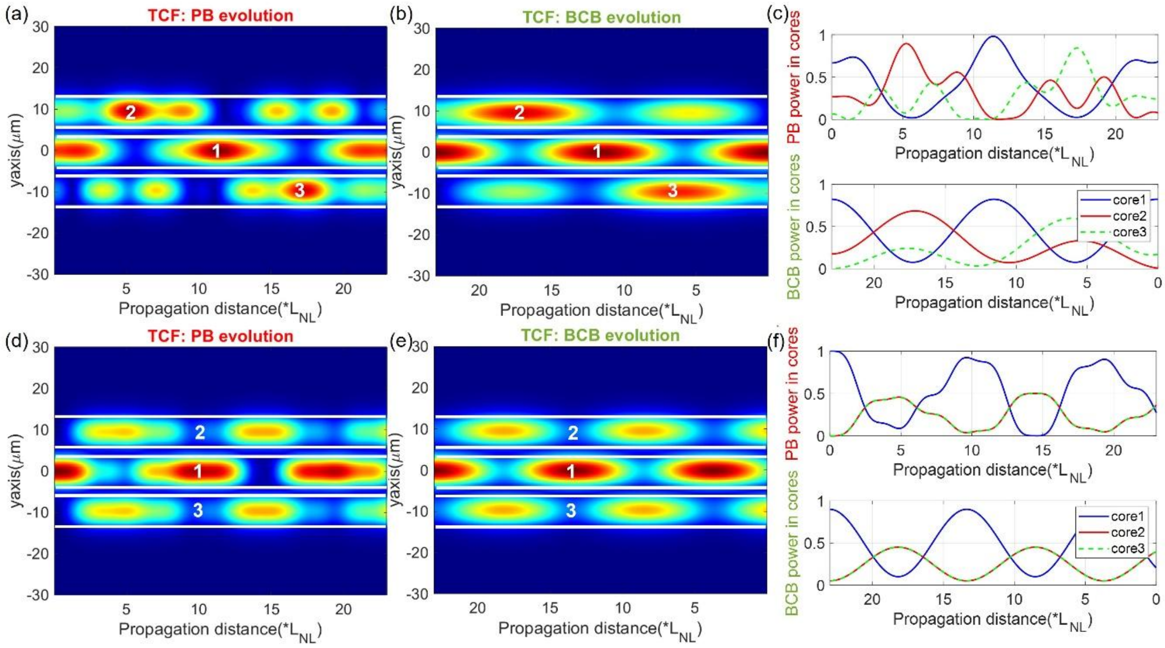

Figure 4.9 Theoretical power switching between the TCF cores, with the boundary conditions: (a)-(c) PB{50% SM_1, 30% SM_2, and 20% SM_3 modes}, CB{70% SM_1, 10% SM_2, and 20% SM_3 modes}; (d)-(f) PB{50% SM_1, 0% SM_2, and 50% SM_3 modes}, CB{80% SM_1, 0% SM_2, and 20% SM_3 modes}. The power distribution among the cores is depicted in (a) and (d) for the PB, and (b) and (e) for the BCB, with the integrated powers within individual cores plotted in (c) and (f).

Figure 4.8 and Figure 4.9 suggest that power switching among the MCF cores can be all-optically tuned via the total power and mode composition of the BCB, the fibre geometry and fibre length, as well as the polarization state of the BCB (though not shown in the figures, the power switching period will be stretched by 3 times if the BCB is converted from co-polarization to orthogonal polarization).

4.2.2.3 Comparison between linear and nonlinear probe beam regime

The dynamics of the counter-propagating system, as described in Eqs. (3.2.1) and (3.2.2) of Chapter 3, are significantly influenced by the degree of nonlinearity of both the forward probe beam and backward control beam.

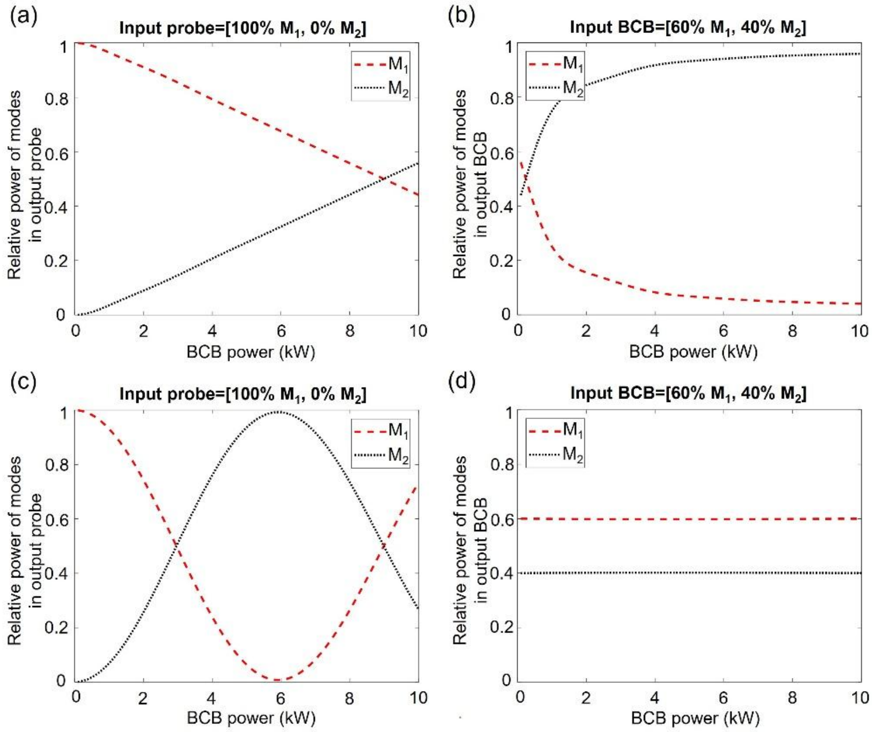

Figure 4.10 Comparison between high power probe (mode rejection) and low power probe in a bimodal fibre. (a)-(b) Mode distribution of the output probe (a) and output BCB (b) versus the BCB peak power when the probe is in a strong nonlinear regime (peak power fixed to 10 kW). The output probe is asymptotically organized to the mode state orthogonal to the input BCB, and vice versa. (c)-(d) Mode distribution of the output probe (c) and output BCB (d) versus the BCB peak power when the probe is in linear regime (peak power fixed to 0.01 kW). The output probe mode distribution oscillates sinusoidally as a function of the BCB power, whereas the BCB mode distribution is unchanged.

When both beams operate in a strongly nonlinear regime, the system exhibits asymptotic rejection of specific mode states, as introduced in Chapter 3. For instance, in the case of a bimodal fibre, the output probe beam is organized towards the mode state orthogonal to the input BCB, and vice versa. In the example shown in Figure 4.10 (a) and (b), a bimodal fibre with parameters L=1 m, γ_{11}= γ_{12}= γ_{22}= 1 W^{-1}km^{-1} is used for simulation. The input probe beam is entirely coupled to mode M$_1$, while the input BCB is distributed with 60% of its power in mode M$_1$ and 40% in mode M$_2$. The probe beam, with a total fixed peak power P_{PB} =10 kW, operates in a highly nonlinear regime (number of nonlinear lengths $L\gamma P_{\mathrm{PB}}$ =10, γ= 1 W^{-1}km^{-1} being the average Kerr coefficient). As the BCB power increases from 0 to 10 kW, entering itself a strongly nonlinear regime, the mode rejection process outlined above occurs. Indeed, the output probe (Figure 4.10(a)) tends to approach the mode state orthogonal to the input BCB, namely, ~40% in mode M$_1$ and ~60% in mode M$_2$. In turn, the output BCB (Figure 4.10(b)) tends to approach the mode state orthogonal to the input probe, namely, all power coupled to the mode M_2 (mode rejection of the mode M_1).

However, when the probe operates at a low peak power level, therefore remaining in a linear regime (which is the condition underlying the results in this chapter) the dynamics change drastically. The mode rejection process is not triggered. This is shown in Figure 4.10 (c) and (d) where the probe peak power is now arbitrarily low (here P_{PB} =0.01 kW, therefore the number of nonlinear lengths $L\gamma P_{PB}$ =0.01). In this case, the output BCB's mode distribution remains unchanged, mirroring the input (Figure 4.10(d)). Meanwhile, the output probe mode distribution exhibits a sinusoidal evolution as the BCB power increases (Figure 4.10(c)), in line with the predictions of the theoretical model (Eqs. (4.2.8) and (4.2.9)) and the simulations reported in this section.

To conclude, this section introduces and derives the nonlinear intermodal dynamics of a counter-propagating setup where the power difference between the mutually injected beams is substantially large. This gives rise to an effect, counter-propagating nonlinear grating, different from the mode rejection phenomenon discussed in Chapter 3. This nonlinear grating is generated by the backward control beam and can be all-optically tuned via various parameters including the total power, mode composition, and polarization state of the BCB, as well as the fibre geometry and nonlinearity. The counter-propagating nonlinear grating enables two intriguing effects in MMFs and MCFs: mode switching and power switching of a low-power forward-propagating PB. The developed theory is applicable to N-mode and N-core platforms. Theoretical prediction of mode switching between the LP modes (or the supermodes) are illustrated in several bimodal fibres (PM1550-xp, PMHN1, and DCF) and a 3-mode fibre (TCF). Furthermore, power switching, tuneable power splitting, and combining between the cores in DCF and TCF have been investigated. Based on the theory and simulations presented here, a series of experiments on mode and power switching will be demonstrated in the following sections.

4.3 All-optical switching of LP modes in multimode fibres

4.3.1 Experimental setup

To experimentally investigate the mode switching effect, FMFs are initially utilized to explore all-optical switching between the LP modes. The experimental setup is similar to Figure 3.3, with a simplified schematic depicted in Figure 4.11. The PB and BCB are split from the 1 μm MOPA system operating with ~0.5 ns pulse durations. The power ratio between the BCB and PB is adjusted to be larger than 20:1 by rotating HWP_1 to a proper angle. The PB and BCB are injected from opposite ends of the test fibres, such that the high-power BCB can generate counter-propagating nonlinear gratings to influence PB propagation. The BCB input end is cleaved at an angle of 8° to eliminate back reflection into the camera, thus the low-power output PB can be better observed. The PB input end is perpendicularly cleaved to ensure high quality mode excitation. The launched power of the BCB and PB can be controlled by appropriately rotating HWP_4 and HWP_2 in combination with PBSs. The polarization state of the BCB and PB can be adjusted by rotating HWP_5 and HWP_3. An SLM is used for BCB coupling, allowing for selectable coupling conditions by flexibly adjusting the phase pattern displayed on the SLM screen. The output PB is sampled using a wedge with an incident beam angle of ~10 deg, ensuring that the sampled laser beam maintains a similar polarization to the output PB. The near-field and far-field intensity profiles are measured with cameras, with PB output beam profiles corrected by subtracting BCB reflection at the flat-cleaved fibre end. Mode decomposition is then implemented based on the corrected profiles. A linear polarizer or a combination of PBS and HWP can be inserted before the BS to measure the output for different input polarization states. An identical setup is placed after the BCB output to measure the BCB output beam profile, which is used to analyse the BCB mode composition.

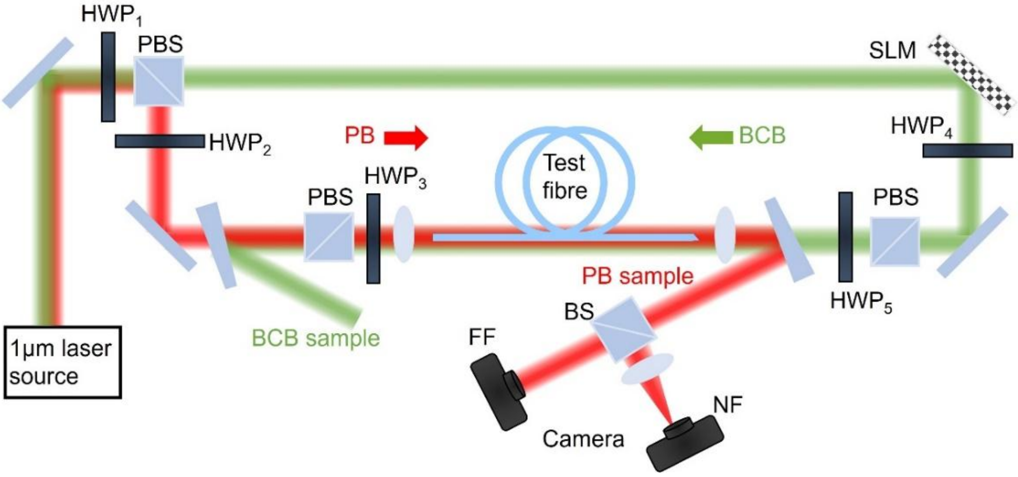

Figure 4.11 Experimental setup to investigate the mode switching dynamics in nonlinear optical fibres.

The experimental procedure for measuring mode switching comprises several steps: precisely coupling the BCB and PB to specific mode states, tuning the input beam properties, measuring the output PB and BCB intensity profiles, and post-processing the measured beam profiles. As the theory and simulation illustrate, an optimal mode switching requires specific mode compositions for the counter-propagating beams. Achieving all-optical switching of the PB involves tuning the input BCB from three perspectives - total power, polarization state, and mode composition – using waveplates, PBS, and SLM. The data post-processing involves mode decomposition based on numerical analysis of the measured beam profiles, a method that is discussed in Chapter 3. All-optical mode switching in the PB is measured as a function of BCB power by analysing a series of PB output beam profiles at different BCB powers.

4.3.2 Mode switching in PM1550-xp and PMHN1

Unlike the theoretical analysis developed in section 4.2, the laser beams used in the experiments are pulsed rather than CW, enabling the high peak power required for the experiments. The pulse width is ~0.5 ns, corresponding to a pulse length of 10 cm in the fibre. Consequently, the total interaction length of 10 cm is achieved in the fibre for the counter-propagating PB and BCB. The test fibre is ~0.4 m in length and placed in an optimized position to ensure synchronisation of the forward PB and backward BCB pulses.

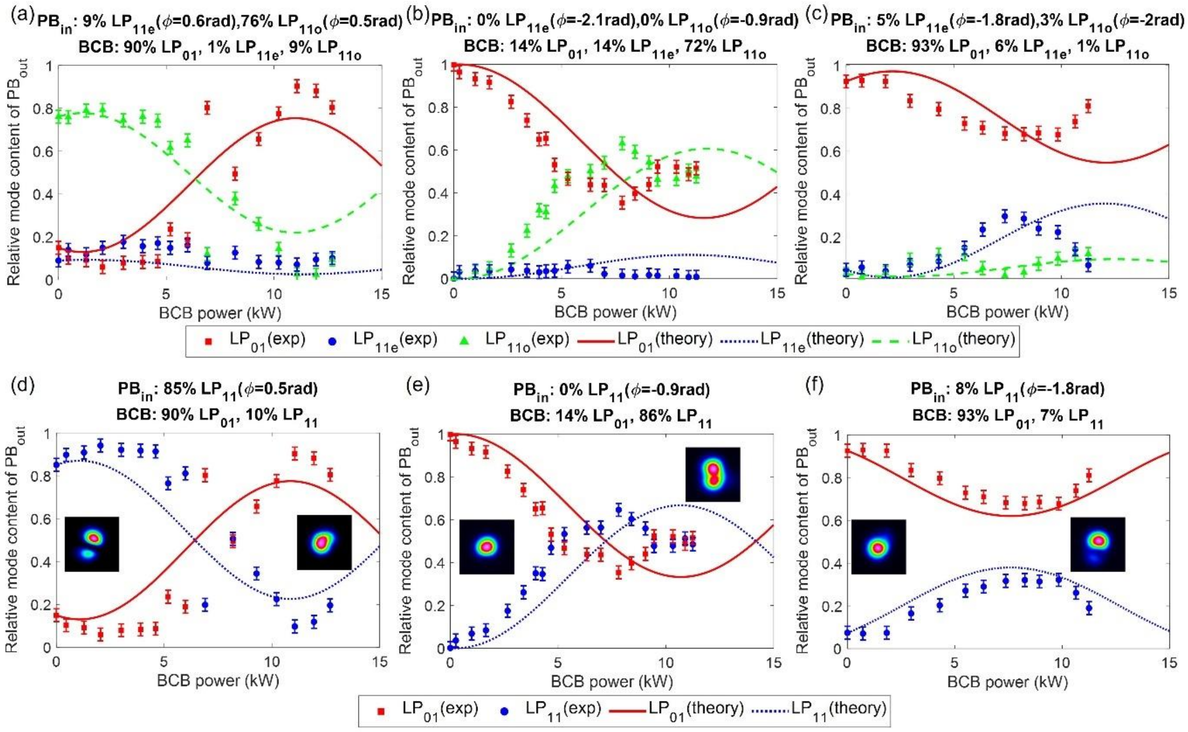

Figure 4.12 Observation of LP mode switching in the PM1550-xp fibre under various boundary conditions, as detailed at the top of each panel. The experimental results (dots with ±2% error bars) are compared with the theoretical calculations (lines). (a)-(c) Mode decomposition of the PB output PB_{out} over the LP_{01}, LP_{11e}, and LP_{11o} modes, as a function of BCB power. (d)-(f) Mode decomposition of PB_{out} over the LP_{01} and LP_{11} modes as a function of BCB power, with LP_{11} mode content as the content summation of the LP_{11e} and LP_{11o} modes.

The PM1550-xp fibre is placed in the experimental setup to explore LP mode switching in the PB. A series of preliminary optimizations has been conducted at a low BCB power prior to the mode switching experiments, including adjusting the rotation angles of waveplates and optimizing the phase patterns displayed on the SLM. The PB and BCB are set to the same linear polarization state aligned with either the fast or the slow axis of the fibre. The BCB is coupled with high peak powers with a tuneable range from 0 to ~12 kW, whereas the PB is coupled with a constant power of ~0.6 kW. There is no noticeable change in the PB output beam profiles when the BCB power is low and comparable to the PB power. However, as the BCB power increases, the mode distribution of the PB output gradually switches to another mode state. Figure 4.12 illustrates the power evolution of each LP mode in the PM1550-xp fibre under various boundary conditions, i.e., the input mode composition of PB and BCB.

Figure 4.12(a)-(c) present the PB output decomposed into the LP_{01}, LP_{11e}, and LP_{11o} modes, while Figure 4.12(d)-(f) display the summed relative powers of the LP_{11e} and LP_{11o} modes to illustrate mode switching between the LP_{01} and LP_{11} modes. Theoretical predictions (lines) are calculated based on Eq. (4.2.7) and are provided for comparison with the experimental results (dots). For instance, in Figure 4.12(a), the input PB is composed of 15% LP_{01} mode, 9% LP_{11e} mode, and 76% LP_{11o} mode with a relative modal phase of 0 rad, 0.6 rad, and 0.5 rad, respectively. Meanwhile, the BCB is coupled into a combination of 90% LP_{01} mode, 1% LP_{11e} mode, and 9% LP_{11o} mode. The relative modal phase for the BCB modes is not listed in Figure 4.12 because it does not affect mode switching between the PB modes, as illustrated by the $|B_m|$ and $|B_n|$ terms in Eq. (4.2.4). Under this boundary condition, as the BCB power increases, the relative LP_{01} mode power in the PB exhibits a variation from 0.2 down to 0.05, then increases from 0.05 to 0.9 before decreasing again. Correspondingly, Figure 4.12(d) illustrates the switching from the LP_{11} mode to the LP_{01} mode as the BCB power increases, achieved by summing the LP_{11e} and LP_{11o} mode powers in Figure 4.12(a). In this instance, the LP_{11o} mode content is higher than the LP_{11e} mode, both in the PB and BCB. Consequently, the LP_{11} mode content is approximated to be 85% in the PB_{in} and 10% in the BCB, with a relative LP_{11} mode phase of 0.5 rad in the PB_{in} retained from the phase of the LP_{11o} mode in Figure 4.12(a). Moreover, since the LP_{11o} mode predominates over the LP_{11e} mode in the BCB, mode switching primarily occurs between the LP_{11o} mode and the LP_{01} mode in the PB, resulting from a counter-propagating nonlinear grating primarily formed by these two modes. It is worth noting that the slight mismatch between experiment and theory in Figure 4.12 can be attributed to the mode decomposition error (discrepancy along y-axis) and variation in BCB power (discrepancy along x-axis, resulting from variation in coupling efficiency).

Figure 4.12(a) demonstrates an almost complete switching from the LP_{11} mode to the LP_{01} mode in the PB output (~85% power conversion between the modes) by using a co-polarized BCB power of ~11 kW. Note that further increasing the BCB power to ~22 kW would lead to a switching back to the LP_{11} mode. Additionally, partial switching between the LP_{01} and LP_{11} modes is illustrated in Figure 4.12(b) and (e), as well as (c) and (f). A tuneable mode switching ratio can be observed by adjusting the mode composition of the input PB and BCB, which can be estimated from the 3D plots provided in Figure 4.6(a). Notably, achieving a mode switching period for the PM1550-xp fibre requires a BCB power of ~10 kW and a propagation of $3*L_{NL}$ in the experiments, which aligns with the theoretical calculation in Figure 4.1(c). Given the pulse length of 10cm and a BCB power of 10 kW, the fibre supports propagation of $\sim 3*L_{NL}$ (L_{NL}=3.3 cm).

Subsequently, LP mode switching in the PMHN1 is investigated by using a 0.4m-long fibre and a BCB power of ~5 – 6 kW. The 10cm-long pulse length in the PMHN1 fibre supports propagation of ~6 – 8*L_{NL} at 5 – 6 kW BCB power. As shown with the theoretical calculation in Figure 4.2(c), the switching period is ~2.7*L_{NL} in the PMHN1 fibre. Therefore, periodic mode switching can be observed in the PB, with the modal distributions converting to another mode state as the BCB power increases, and then returning to the initial mode state when further increasing the BCB power. After preliminary optimizations of waveplate angles, SLM phase patterns, and coupling lenses at a low power level, the PB peak power is set constant at ~0.2 kW, while the BCB peak power is tuneable from 0 to 6 kW, ensuring that the BCB power is significantly higher than the PB power. The PB and BCB are set to the same linear polarization state aligned with either the fast or the slow axis of the fibre.

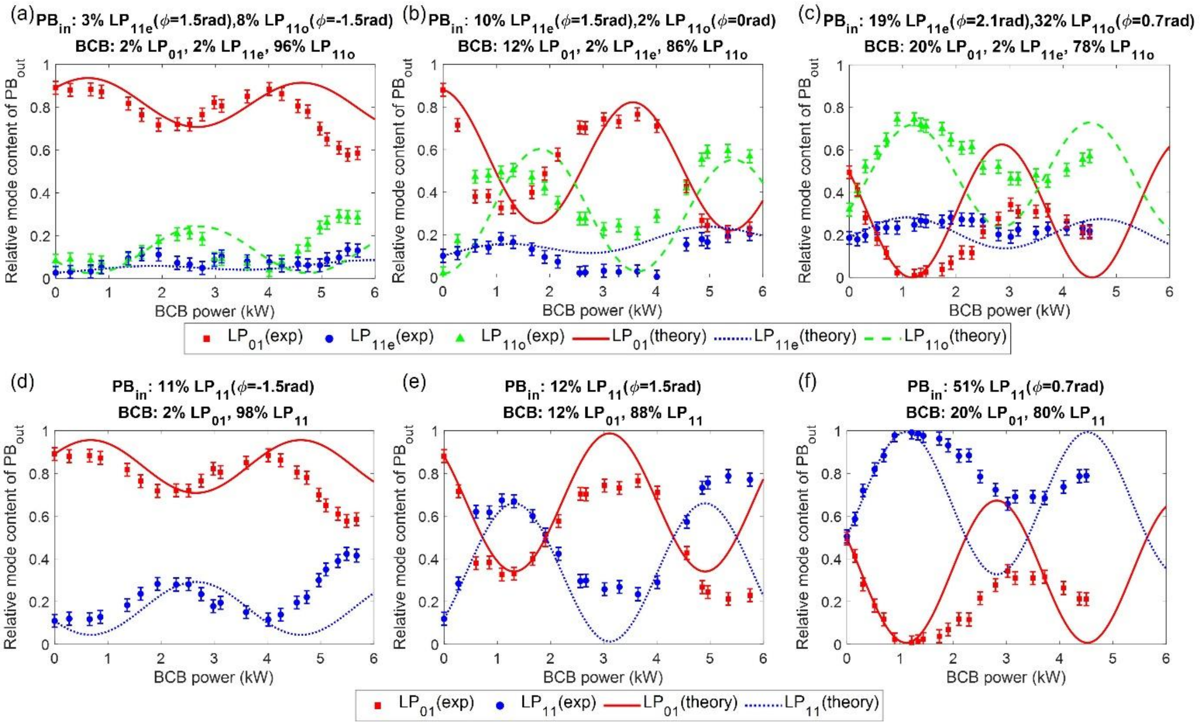

Figure 4.13 Observation of LP mode switching in the PMHN1 fibre under various boundary conditions, as detailed at the top of each panel. The experimental results (dots) are compared with the theoretical calculations (lines). (a)-(c) Mode decomposition of PB_{out} over the LP_{01}, LP_{11e}, and LP_{11o} modes, as a function of BCB power. (d)-(f) Mode decomposition of PB_{out} over the LP_{01} and LP_{11} modes as a function of BCB power, with LP_{11} mode content as the content summation of the LP_{11e} and LP_{11o} modes.

Similar to the observations in the PM1550-xp fibre, the PB output remains unchanged when the BCB power is low and comparable to the PB power. However, the mode distribution of the PB output gradually switches to another mode state as the BCB power increases. Figure 4.13 displays several mode switching results in the PMHN1 fibre under various boundary conditions and varying BCB powers. Figure 4.13(a)-(c) show the mode decomposition of the PB output into the LP_{01}, LP_{11e}, and LP_{11o} modes, while the relative powers of the LP_{11e} and LP_{11o} modes are summed in Figure 4.13(d)-(f) to illustrate the mode switching between the LP_{01} and LP_{11} modes. Figure 4.13(d)-(f) are derived from Figure 4.13(a)-(c) by assuming the LP_{11e} mode and LP_{11o} mode as degenerate modes and taking the phase of the dominant mode between them. Theoretical predictions (lines) are calculated based on Eq. (4.2.7) and are provided for comparison with the experimental results (dots).

For instance, in Figure 4.13(a) and (d), the input PB is composed of 89% LP_{01} mode, 3% LP_{11e} mode, and 8% LP_{11o} mode with a relative modal phase of 0 rad, 1.5 rad, and -1.5 rad, respectively, while the BCB is coupled with 2% LP_{01} mode, 2% LP_{11e} mode, and 96% LP_{11o} mode. By taking the approximation of a single LP_{11} mode propagation, the input PB consists of 89% LP_{01} mode and 11% LP_{11} mode with a phase difference of -1.5 rad between them, and the input BCB is a combination of 2% LP_{01} mode and 98% LP_{11} mode. Figure 4.13(a) shows a dominant mode switching between the LP_{01} mode and LP_{11o} mode, which results from the counter-propagating nonlinear grating generated primarily formed by these two modes. In this case, periodic switching between the LP_{01} and LP_{11o} mode can be obtained with intermodal power conversion of ~20%. Simultaneously, the LP_{11e} mode content exhibits minor fluctuations at different BCB powers. This is due to the low content of this mode in the BCB and the lower intermodal Kerr coefficient between the LP_{11e} and LP_{11o} modes. Consequently, Figure 4.13(d) illustrates periodic partial switching between the LP_{01} and LP_{11} modes in this fibre. Figure 4.13(b), (c), (e), and (f) illustrates other partial mode switching results in the PMHN1 fibre with intermodal power conversion of ~50 – 60%. Complete switching (100% conversion) from one mode to another mode is achievable if the BCB power and mode composition are further optimized, as indicated by the shift in the colour scale in Figure 4.6(b). It is worth mentioning that experimental results generally match the theoretical calculations when the BCB power is below 2 kW. However, as the BCB power increases further, the experimental results begin to diverge from the theoretical curves. This inconsistency is also observed during the mode rejection experiments using the PMHN1 fibre and is associated with significant spectral broadening of the BCB spectrum when the power exceeds 2 kW, as illustrated in Figure 3.14.

So far, LP mode switching has been demonstrated in both the PM1550-xp and PMHN1 fibres. To systematically illustrate this phenomenon, some of the results shown in Figure 4.12 and Figure 4.13 are directly compared in Figure 4.14. In the results of the PM1550-xp shown in Figure 4.14(a), the relative LP_{01} mode power in the PB varies differently as the BCB power increases, demonstrating tuneable maximum intermodal power conversion (the difference between the maxima and minima). The PB output beam profiles are illustrated in Figure 4.14(b) when the BCB is turned off ($P_{BCB}=0$) and on ($P_{BCB}=\sim 11$ kW), with the LP_{01} mode content in the BCB indicated. In comparison, Figure 4.14(c) and (d) summarise three mode switching results in the PMHN1 fibre with tuneable maximum intermodal power conversion. Given a higher nonlinearity in the PMHN1 fibre, lower BCB power is required for mode switching. A conversion from the peak(valley) to the valley(peak) in the LP$_{01}$ mode content of the PB requires a BCB power of ~2.05 kW in the PMHN1 fibre, corresponding to a propagation of ~2.7*L$_{NL}$ (pulse length=0.1m and nonlinear coefficient γ=13.2 W^{-1}km^{-1}). This periodic mode switching is also illustrated with the PB output beam profiles at four distinct BCB powers in Figure 4.14(d). In contrast, the PM1550-xp requires a BCB power of ~10 kW for a LP$_{01}$ mode content conversion from the peak(valley) to the valley(peak) (see Figure 4.14(a)), which corresponds to a propagation of 3*L$_{NL}$ (pulse length=0.1m and nonlinear coefficient γ=3 W^{-1}km^{-1}).

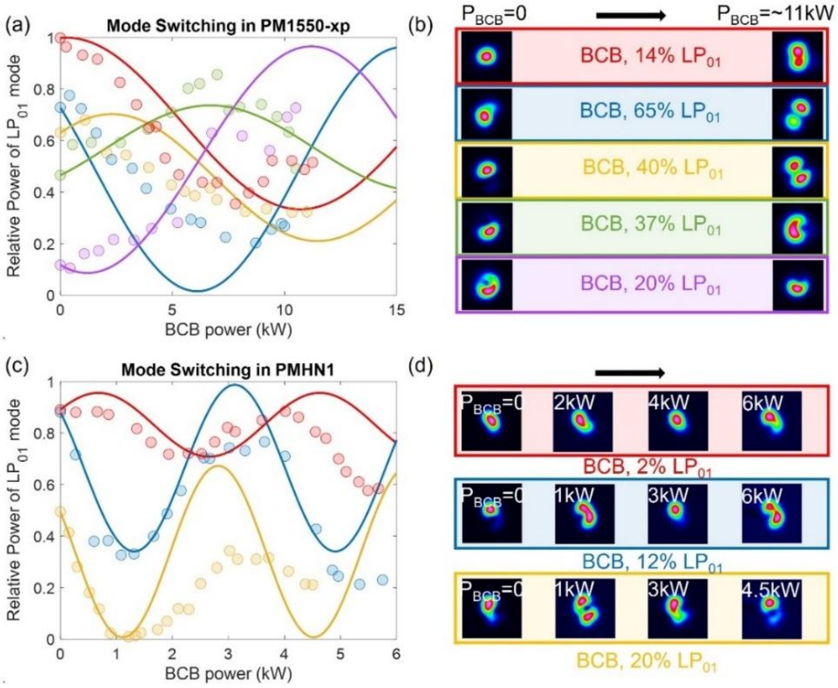

Figure 4.14 Comparisons of mode switching results using the PM1550-xp and the PMHN1 fibres. The evolution of the LP$_{01}$ mode power in the PB$_{out}$ is compared under varying PB$_{in}$ and BCB coupling conditions. The experimental results (dots) are compared with the theoretical calculations (lines). (a) Five different mode switching results of PM1550-xp, with the PB$_{out}$ beam profiles and BCB conditions illustrated in (b). (c) Three mode switching results of PMHN1, with the corresponding PB$_{out}$ beam profiles at various BCB powers displayed in (d), alongside the BCB conditions. P$_{BCB}$: BCB power.

In conclusion, mode switching in low-power PBs is experimentally observed in both the PM1550-xp and PMHN1 fibres by using ~0.4m-long fibres and a 0.5ns pulsed BCB with peak powers of 5 - 11 kW. Mode switching is driven by the counter-propagating nonlinear gratings generated by the high-power BCB, with the specific pairs of modes involved in the switching determined by the mode composition of the BCB. By using ~10 kW BCB power, a switching from the LP$_{01}$(LP$_{11}$) mode to the LP$_{11}$(LP$_{01}$) mode can be achieved in the PM1550-xp fibre. However, for the PMHN1 fibre, a BCB power of ~2.05 kW is sufficient to achieve a similar mode conversion result. The experimental results are consistent with the theoretical predictions, demonstrating successful tuneable mode switching.

4.4 Supermode switching and power switching in multicore fibres

4.4.1 Supermode switching in DCF and TCF

The DCF and TCF fibres are utilized to investigate the supermode switching effect, according to the theoretical predictions shown in Figure 4.6(c) and Figure 4.7. DCF and TCF fibres with a length of ~0.4m are used, and the experimental setup is the same as Figure 4.11. However, the BCB and PB are swapped with the SLM used for the PB coupling into the MCFs, while the BCB is coupled using an additional phase plate or by selectively coupling a single beam into one of the fibre cores. This allows for the PBs to be coupled with random mode compositions by varying the SLM phase patterns (see Section 3.4.1 for details of phase patterns used for MCF coupling), facilitating comprehensive mode switching experiments. Consequently, the fibre end at the BCB input is angle-cleaved to eliminate BCB reflections, whereas the PB input end is perpendicularly cleaved to ensure high-quality couplings. After preliminary optimizations of the waveplate angles, SLM phase patterns, and coupling lenses at low power levels, the PB is set as a random combination of supermodes with a constant peak power of ~0.25 kW, while the BCB is set as a specific combination of supermodes with a peak power tuneable from 0 to ~11 kW. Due to the polarization-maintaining capabilities of the DCF and TCF (introduced in Chapter 3), the polarization states of the PB and BCB can be set to either co-polarized or orthogonally polarized with a high polarization extinction ratio of ~10dB. The output beam profiles in the far field are then measured and analysed to illustrate the supermode switching in the MCFs.

The switching period for the DCF requires a propagation length ranging from 1.5*L_{NL} to 3*L_{NL}, as illustrated in Figure 4.6(c). The exact number of L_{NL} required depends on the mode compositions of the BCB and PB. Since the 0.1m-long pulse length in the fibre (0.5ns pulse width) supports a propagation of 3.3*L_{NL} at a BCB power of 11 kW, a complete switching between the SM_1 mode and SM_2 mode can be obtained at this power level. Figure 4.15(a) demonstrates a switching from a nearly SM_2 mode state to a pure SM_1 mode state as the BCB power (coupled with 65% SM_1 mode and 35% SM_2 mode) increases from 0 to ~8kW, corresponding to 2.4*L_{NL}. Due to the periodic nature of switching, the SM_1 mode content decreases when further increasing the BCB power. Conversely, Figure 4.15(b) illustrates a switching from a nearly SM_1 mode state to a nearly SM_2 mode with a BCB power of ~8 kW, using the same BCB configuration as in Figure 4.15(a). Similarly, Figure 4.15(c) and (f) illustrate the mode switching dynamics when the BCB remains unchanged, whereas the input PB is coupled with different relative modal phases. Both experimental results and theoretical calculations illustrate an opposite dynamic in the output PB, with complete conversion to the SM_1 (SM_2) mode obtained in Figure 4.15(c) (Figure 4.15(f)) at a BCB power of ~5 kW. Starting from varying input conditions, the PB output mode can be all-optically switched to a single supermode state by using a BCB power of ~5 – 8 kW, corresponding to a propagation of ~1.5 – 2.4*L_{NL} (pulse length=0.1m and nonlinear coefficient γ=3 $W^{-1}km^{-1}$).

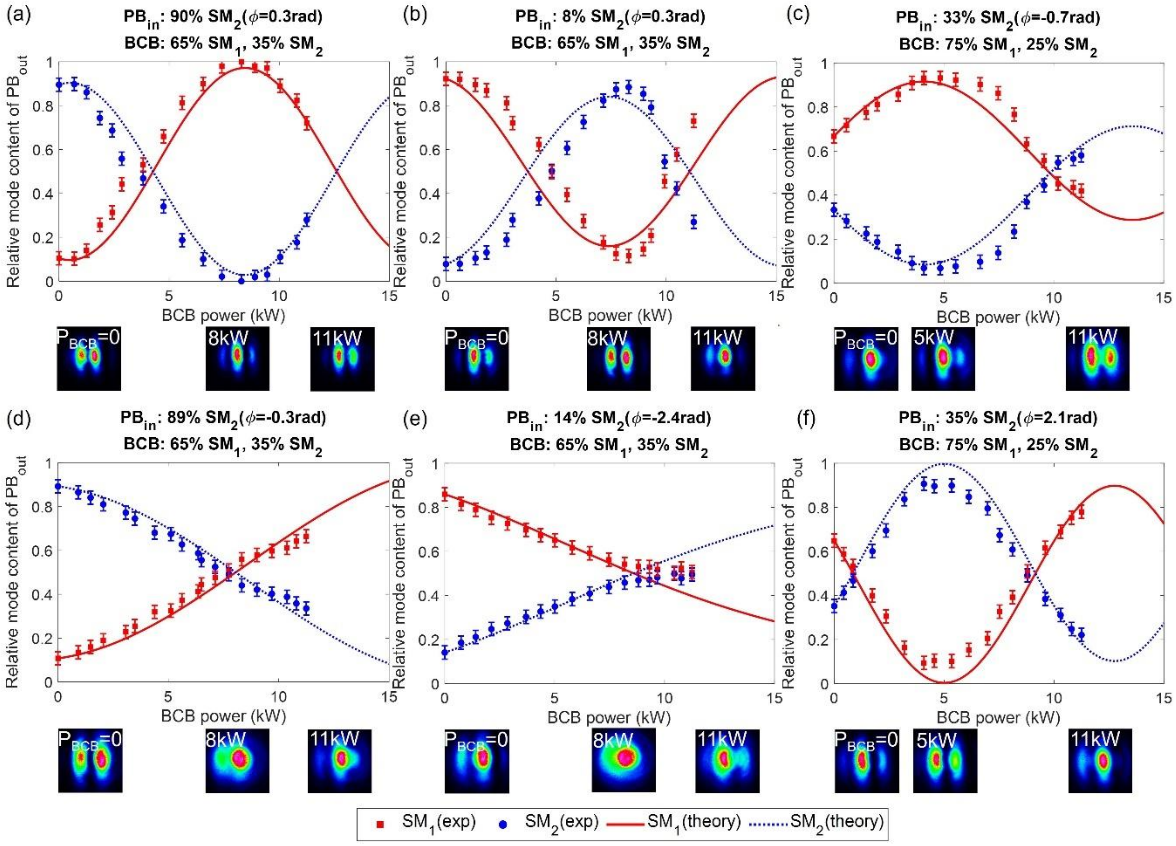

Figure 4.15 Observation of supermode switching in the DCF under various boundary conditions, as detailed at the top of each panel. The experimental results (dots) are compared with the theoretical calculations (lines). Mode decomposition of PB_{out} over the SM_1 and SM_2 modes, as a function of BCB power. PB and BCB are co-polarized in (a)-(c), and (f), whereas they are orthogonally polarized in (d) and (e).

Apart from tuning the mode switching dynamics through mode compositions, the relative polarization state of the PB and BCB is also investigated, as illustrated in Figure 4.15(d) and (e). Theoretical calculations suggest that the mode switching efficiency is ~3 times lower when the PB and BCB are orthogonally polarized compared to co-polarized cases (see Figure 4.4(c)). This implies that achieving the same mode switching results in orthogonally polarized cases requires either 3 times higher power or 3 times longer interaction length. This can be explained by comparing Figure 4.15(a) with (d) or Figure 4.15(b) with (e), where the input PB and BCB have identical mode compositions but different relative polarization states. For instance, in Figure 4.15(a) and (d), the input PB is coupled with ~10% SM_1 mode and ~90% SM_2 mode, and the BCB is coupled into a combination of 65% SM_1 mode and 35% SM_2 mode. In the co-polarized case

(Figure 4.15(a)), a BCB power of ~4 kW is required to achieve the SM_1 mode power conversion from 10% to 65%. On the contrary, it requires a BCB power of ~12 kW to obtain a similar amount of mode conversion in the orthogonally polarized case (Figure 4.15(d)).

Subsequently, supermode switching in a 0.4m-long TCF is measured by using a PB with a peak power of ~0.2 kW and a BCB with a peak power of 5 - 7 kW. Figure 4.16 illustrates the power evolution of the SM_1, SM_2, and SM_3 modes in the PB output as the BCB power increases, under various boundary conditions as denoted in the title of each panel. Experimental results (dots) are compared with theoretical calculations (lines), and the output PB beam profiles are shown in the inset pictures. In Figure 4.16(a) and (c), the three supermodes are switching their power mutually, whereas mode switching occurs only in the SM_1 mode and SM_2 mode in Figure 4.16(b) resulting from negligible power (just 1%) coupled to the SM_3 mode in the BCB. It is worth noting that the coupled BCB power is limited by the laser source and coupling efficiency in the experiments, but a complete switching to a specific mode state would be obtained if further increasing the BCB power.

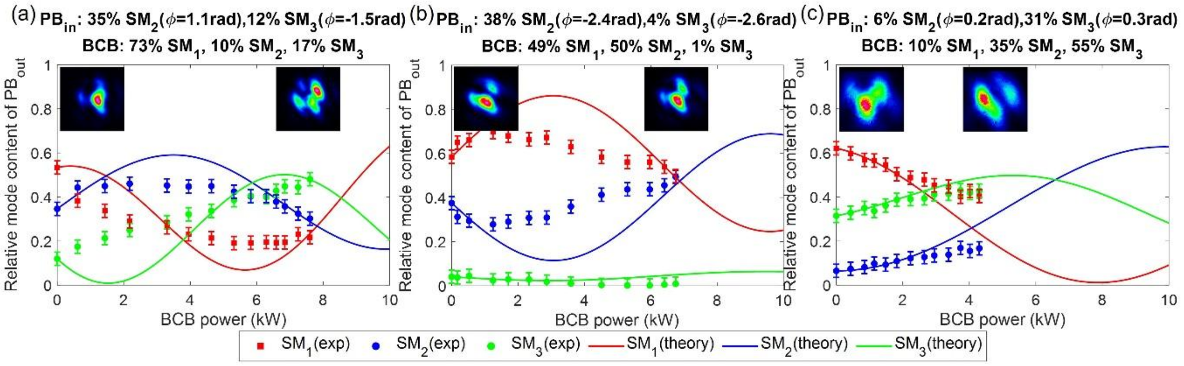

Figure 4.16 Observation of supermode switching in the TCF under various boundary conditions. Mode decomposition of PB_{out} over the SM_1, SM_2, and SM_3 modes, as a function of BCB power, with the boundary conditions detailed at the top of each panel. The experimental results (dots) are compared with the theoretical calculations (lines). The insets are PB_{out} beam profiles when the BCB is switched on or off.

In conclusion, mode switching in low-power PBs is experimentally observed in both the DCF and TCF fibres by using ~0.4m-long fibres and a 0.5ns pulsed BCB with peak powers of 5 - 11 kW. The mode switching dynamics are comprehensively explored in terms of the launched power, mode composition, and relative polarization state of the BCB, as well as various initial conditions of the PB. By using a 0.5ns pulsed BCB with ~8 kW peak power, one can achieve all-optical switching from the SM_1(SM_2) mode to the SM_2(SM_1) mode in the DCF when the BCB and PB are co-polarized. About 3 times higher BCB power is needed to achieve a similar conversion when the BCB is orthogonally polarized with respect to the PB. As for the TCF, mode switching can occur in two modes or among all the three supermodes, controlled by the counter-propagating gratings formed by the BCB.

4.4.2 Power switching between MCF cores

Due to the coherent combination of supermodes with varying relative powers and phases, supermode switching in the PB enables another intriguing effect: power switching between the MCF cores. As indicated by the theoretical calculations depicted in Figure 4.8 and Figure 4.9, exploring power switching among the MCF cores can be accomplished using the same experimental setup for the supermode switching experiments, with adjustments made to the input conditions of the PB and BCB.

Power switching between the two DCF cores in the PB is initially explored and observed in a 0.4m-long fibre. Experimental parameters are similar to the DCF mode switching experiments. The PB peak power is set constant at ~0.25 kW, while the BCB peak power is tuneable from 0 to 10 kW. Near-field beam profiles of the PB output are measured as the BCB power increases. The intensities in the pixels corresponding to the mode fields in the two cores are summed to represent the relative power in each core, with the total power normalized to 1.

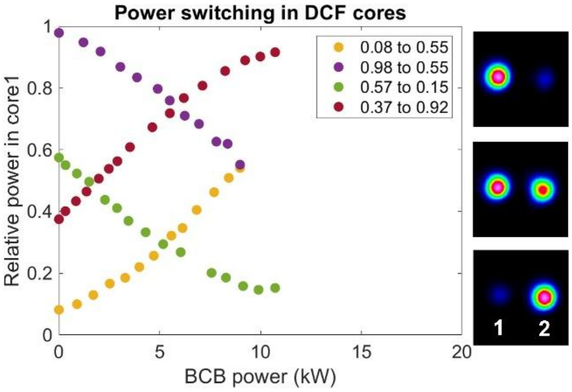

Figure 4.17 Experimental observation of power switching between the DCF cores with different initial states at a BCB power of ~10 kW. The relative power in the left core (labelled as core1) is plotted as a function of the BCB power, with the total power within the two cores normalized as 1.

Figure 4.17 illustrates four instances of power switching from different initial power distributions among the cores, where the BCB is coupled to a combination of 70% SM_1 mode and 30% SM_2 mode and is co-polarized with respect to the PB. Starting from 100% power distributed in core1, the PB power gradually switches from core1 to core2, with approximately 50% power conversion observed at a BCB power of ~10 kW, as illustrated by the purple dots. Subsequently, the green dots illustrate power decreasing in core1 from 60% to 15% as the BCB power increases from 0 to ~10 kW. Conversely, the yellow and red results demonstrate power switching from core2 to core1 with a BCB power of ~10 kW. The near-field beam profiles on the right depict three distinct states of power switching: predominantly in core1, evenly distributed between the two cores, and mainly in core2.

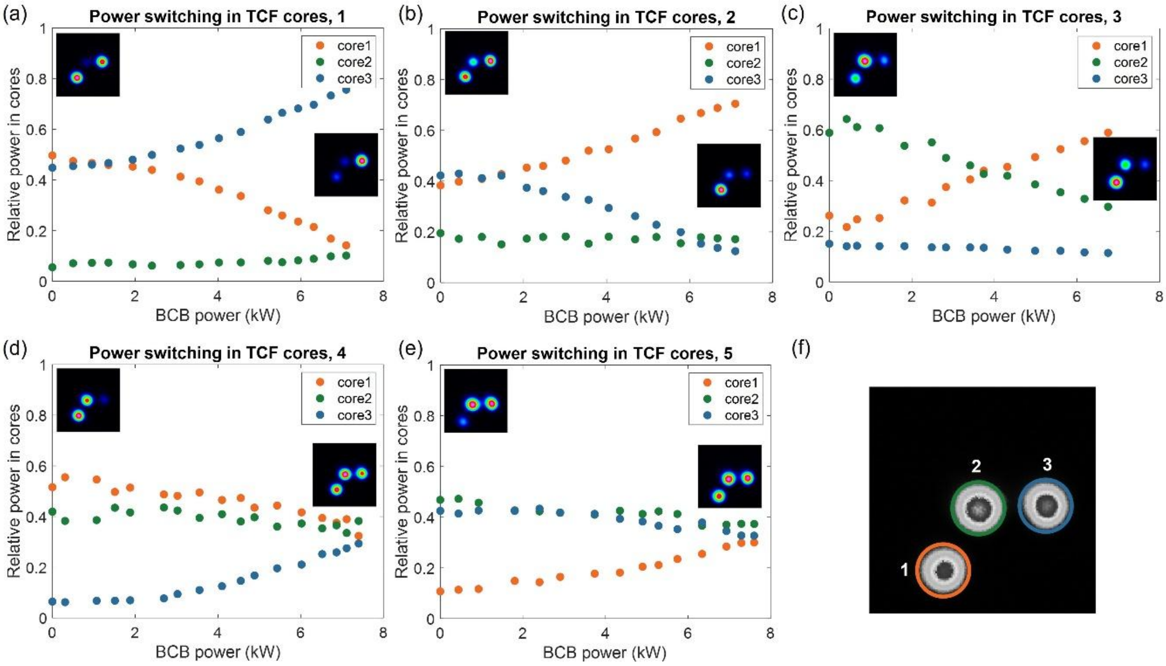

Figure 4.18 Observation of power switching between cores in the TCF under various boundary conditions. The relative power in each individual core is plotted as a function of BCB power, with the total power within all cores normalized to 1. Five experimental results are shown in (a)-(e), with the core labels indicated in (f).

Power switching between the three cores in the TCF is then explored by using a 0.4m-long fibre and ~7 kW BCB power. Figure 4.18 illustrates five instances of power switching in the PB with a constant power of ~0.2 kW and co-polarized with respect to the BCB. In these measurements, the BCB is selectively coupled into one of the three cores, which gives rise to the coupling to a combination of 9% SM_1 mode, 85% SM_2 mode, and 6% SM_3 mode for the results shown in Figure 4.18(a), (b), and (d), whereas a combination of 73% SM_1 mode, 10% SM_2 mode, and 17% SM_3 mode for the results shown in Figure 4.18(c) and (e). The forward PB is coupled to different combinations of cores using the SLM, as shown in the inset NF beam profiles when BCB power is 0. The core distribution of the output PB is displayed in Figure 4.18(f), and the PB output beam profiles are measured as the BCB power increases. The intensities in the pixels corresponding to the mode fields in the three cores are summed to represent the relative power in each core, with the total power normalized to 1. Figure 4.18 illustrates the complex power switching dynamics: the power switching may occur within two of the three cores or among all three cores. Specifically, Figure 4.18(a) shows the power switching from core1 to core3 as the BCB power increases from 0 to ~7 kW; Figure 4.18(b) displays the power focusing into core1 at a BCB power of ~7 kW; Figure 4.18(c) illustrates the power switching between core2 and core1; Figure 4.18(d) and (e) are the results where the PB evolves to a mode state with a uniform power distribution among the cores even if the input PB is randomly distributed.

To summarise, power switching in low-power PBs is experimentally observed in the DCF and TCF by using ~0.4m-long fibres and a 0.5ns pulsed BCB with peak powers of 7 – 10 kW. The exploration of power switching dynamics involves adjustments in BCB power and the mode compositions of the BCB and input PB. The experiments reveal that within DCF and TCF fibres, power can be mutually switched between cores by adjusting the BCB power.

It is worth noting that the power switching experiments presented here are limited by the available BCB peak power. A higher degree of power switching between cores can be achieved by further increasing the BCB power. The selection of a core for power transmission within an MCF, also termed core-switching, has been investigated using various techniques, including long period gratings[131], beam-steering mirror[132], multi-path interference, and phase modulation[133]. In uncoupled or weakly-coupled MCFs, an inter-core power extinction ratio of approximately 16-39 dB has been reported[133]. However, core switching in coupled MCFs remains an area of limited exploration. Femtosecond witching in nonlinear coupled waveguides has been demonstrated at a high peak power (>50 kW), achieving a power conversion efficiency of ~50% [134]. Additionally, an experiment using a triple-core photonics crystal fibre demonstrated SPM-induced inter-core combining at a power level of ~800 W[135]. The power switching results reported in this section, obtained at a BCB peak power of ~10 kW, are comparable to those reported in coupled MCFs. A higher power extinction ratio among the cores could be achieved by further increasing the BCB power or employing the materials with enhanced nonlinearity.

4.5 Applications: conceptual devices for all-optical light-by-light manipulation

The observations of mode switching and power switching in MMFs and MCFs suggest promising applications in several conceptual devices for light-by-light manipulation. These applications include the development of all-optically tuneable mode converters, ultrafast tuneable power splitters, combiners and switches, as well as all-optical phase detection at terminal ends.

4.5.1 0-100% All-optically tuneable mode converters

Based on the mode switching effect, an all-optically tuneable mode converter can be developed, offering a tuneable modal conversion ratio ranging from 0% to 100%. This converter operates by launching an intense counter-propagating BCB into the fibre. Given the mutual injection configuration, the BCB can be readily distinguished from the output PB signals. The desired modal conversion ratio can be achieved by precisely adjusting the power, mode composition, and polarization state of the BCB.

Taking the DCF as an example, Figure 4.19 presents three experimental outcomes: complete conversion (d), partial conversion (e), and negligible conversion (f) between the SM_1 mode and the SM_2 mode within the same piece of DCF. For a specific input PB (see the title in each panel), Figure 4.19(a)-(c) illustrate how mode conversion can be dynamically tuned by adjusting the BCB mode composition (y axis) and BCB power (x axis). The colour gradient reflects the relative SM_1 mode power in the output PB, demonstrating the mode conversion dynamics with a 0 – 100% tuning range. The dashed lines represent the evolution of SM_1 mode power in PB_{out} as BCB power increases, with the BCB coupled with a relative SM_1 mode power of 65% in Figure 4.19(a) and (b), and 99% in Figure 4.19(c). These dashed lines are replotted in Figure 4.19(d)-(f) for comparison with the experimental results, showing good agreement. PB output beam profiles at three distinct BCB powers are illustrated on the right for visualisation.

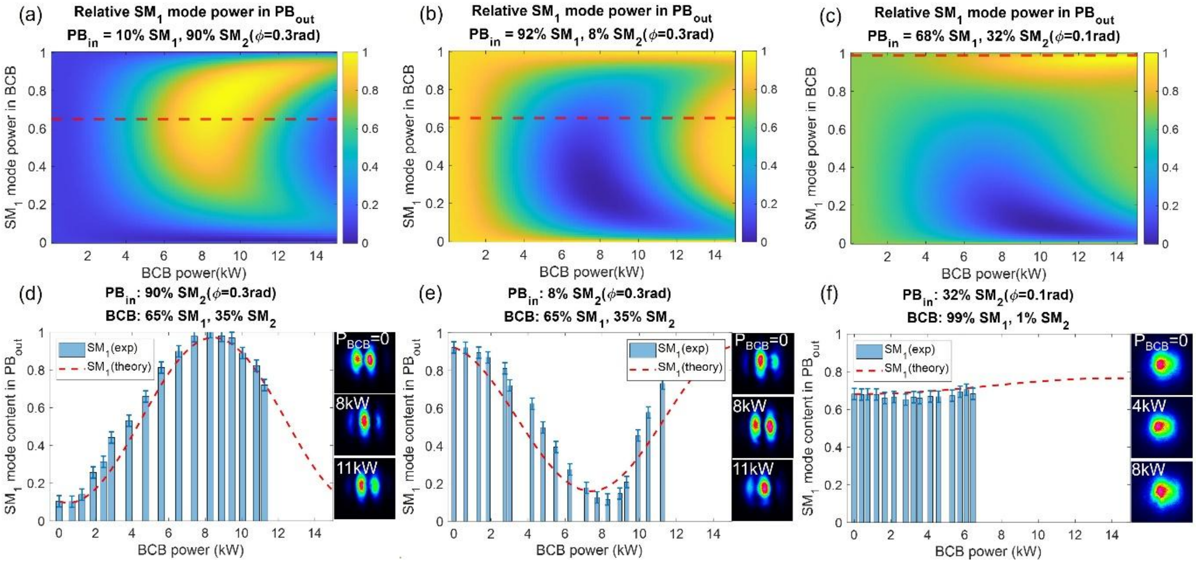

Figure 4.19 All-optically tuneable mode conversion in the DCF by adjusting BCB power and mode composition. (a)-(c) Theoretical mode conversion of PB_{out} as a function of the BCB power (x-axis) and the BCB mode composition (y-axis), with the input PB_{in} conditions indicated at the top of each panel. The colour scale represents the relative SM_1 mode power in PB_{out}. The red dashed lines denote the relative SM_1 mode content in PB_{out} when (a) 65%, (b) 65%, and (c) 99% of the BCB power is coupled to the SM_1 mode. The corresponding experimental results are illustrated in (d) a full conversion up to 100% SM_1 mode, (e) a partial conversion to the 88% SM_2 mode, and (f) a negligible conversion. Error bars of ±3% are added to the experimental results to represent the estimated uncertainty of the MD algorithm for MCFs. PB_{out} beam profiles at 3 distinct BCB powers are displayed on the right.

Furthermore, tuneable mode conversion can also be achieved by controlling the relative polarization state of the BCB with respect to the PB. Figure 4.20(a) and (b) present two comparative results when the relative BCB polarization state is adjusted from co-polarization to orthogonal polarization, while maintaining the mode compositions for the PB and BCB (as indicated in the panel titles). By using a BCB with a maximum power of ~11 kW, the relative SM_1 mode power in the output PB can be all-optically tuned in the range of 10 – 100% under the co-polarized condition, whereas the tuning range is constrained to 10 – 65% under the orthogonally polarized condition. PB output beam profiles at three distinct BCB powers are illustrated on the right for visualisation. Moreover, Figure 4.20(c) shows the PB output evolutions when the relative polarization state of the BCB is continually adjusted, with linear polarization direction differences ranging from 0 deg to 90 deg. In the absence of the BCB, the SM_1 mode content in the output PB remains around 100% (see the beam profiles on the right). However, with the BCB turned on, the SM_1 mode content can be converted to the range of ~36% - 70% under varying relative polarizations, demonstrating the tuneability of mode conversion.

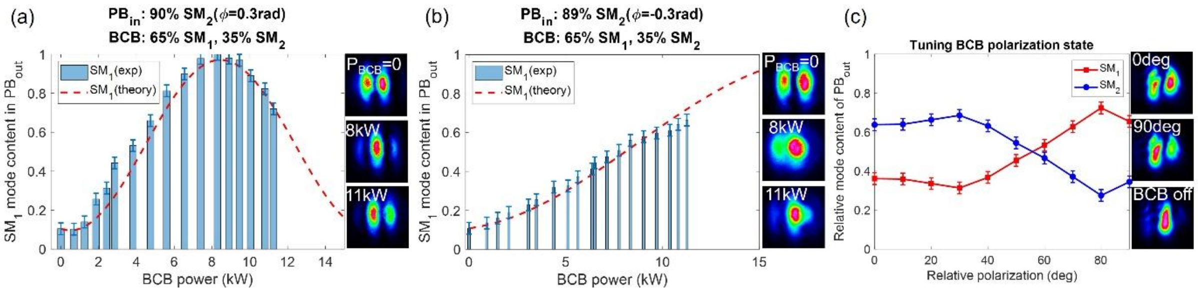

Figure 4.20 All-optically tuneable mode conversion in the DCF by adjusting the BCB polarization state. The SM_1 mode content in PB_{out} is plotted as a function of the BCB power when the BCB is (a) co-polarized or (b) orthogonally polarized with respect to the PB. The boundary conditions are detailed at the top of each panel, and the PB_{out} beam profiles at 3 distinct BCB powers are listed on the right. (c) Mode conversion in PB_{out} versus the relative polarization state of the BCB with respect to PB, starting from the SM_1 mode state when the BCB is turned off.

In a word, by launching a counter-propagating BCB with specific total power, mode composition, and polarization state into the fibre, the output of a PB with random mode compositions can be all-optically tuned to achieve a 0 – 100% conversion between the modes.

4.5.2 All-optically ultrafast tuneable power splitters, combiners, and switches

Based on the power switching effect, MCFs can be engineered as all-optically tuneable power splitters, power combiners, and power switches by launching a counter-propagating BCB into the fibre, as presented with the experimental tests in Figure 4.21 and Figure 4.22. Figure 4.21(a) showcases a tuneable power splitter implemented with a 0.4m-long DCF, where the power is all-optically split from a single core into the two cores with an arbitrary ratio of X/(1-X) at the PB output, achieved by adjusting the BCB power accordingly. The insets are side views of the spatial beam shape in the two cores, illustrating the power distributions between the two cores with an increasing BCB power from 0 to ~9 kW. Conversely, Figure 4.21(b) demonstrates a tuneable power combiner, where the power is all-optically combined from the two DCF cores into one of them. By using a BCB power of ~11 kW, the PB power can be effectively combined in either core1 or core2. The insets are side views of the spatial beam shape in the two cores with an increasing BCB power from 0 to ~11 kW. Moreover, Figure 4.21(c) introduces a tuneable power switch with the PB output power all-optically switched from core2 to core1 at a BCB power of ~10 kW. The insets are the side views of the spatial beam shape in the two cores with an increasing BCB power from 0 to ~10 kW. It is worth noting that proper adjustment of the BCB mode composition is essential for each case, and co-polarization of the BCB and PB is maintained throughout these experiments. In Figure 4.21(a) and (b), the BCB is coupled to a combination of 70% SM_1 mode and 30% SM_2 mode, whereas in Figure 4.21(c), it is coupled with 40% SM_1 mode and 60% SM_2 mode.

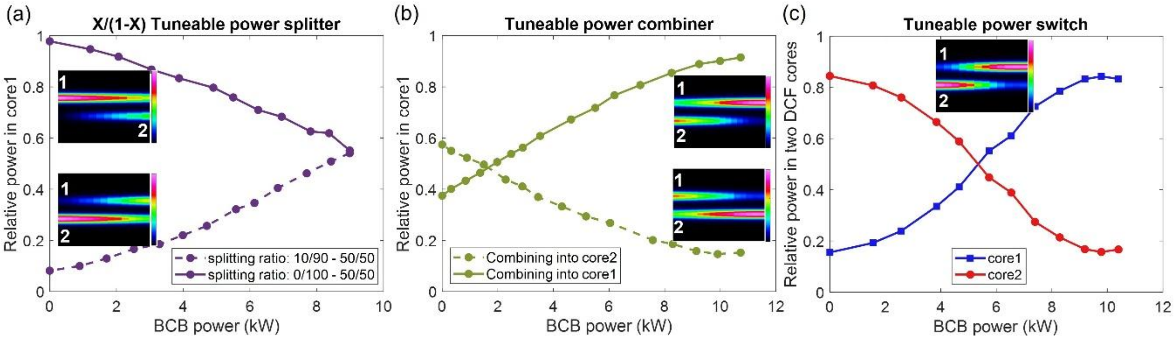

Figure 4.21 All-optically tuneable devices integrated with a 0.4m-long DCF. (a) Tuneable X/(1-X) power splitters by varying BCB power, with the measured relative powers illustrating power splitting from one core to two cores. The insets are side views of the spatial beam shape in the two cores. (b) Tuneable power combiner, with the measured relative powers and insets demonstrating power combining from two cores into one core. (c) Tuneable power switch, providing the power rerouting from one core to another core.

Similarly, TCF is also tested as a tuneable power splitter, combiner, and switch, as demonstrated in Figure 4.22(a)-(c). In these measurements, the BCB is selectively coupled into one of the fibre cores, with a composition of 9% SM_1 mode, 85% SM_2 mode, and 6% SM_3 mode for the results shown in Figure 4.22(a) and (b), whereas in Figure 4.22(c), the BCB is a combination of 73% SM_1 mode, 10% SM_2 mode, and 17% SM_3 mode. Using a BCB power of approximately 7 kW, the output PB from this 0.4m-long TCF can be all-optically split to an arbitrary ratio between the cores, combined to one single core, or switched from one core to another.

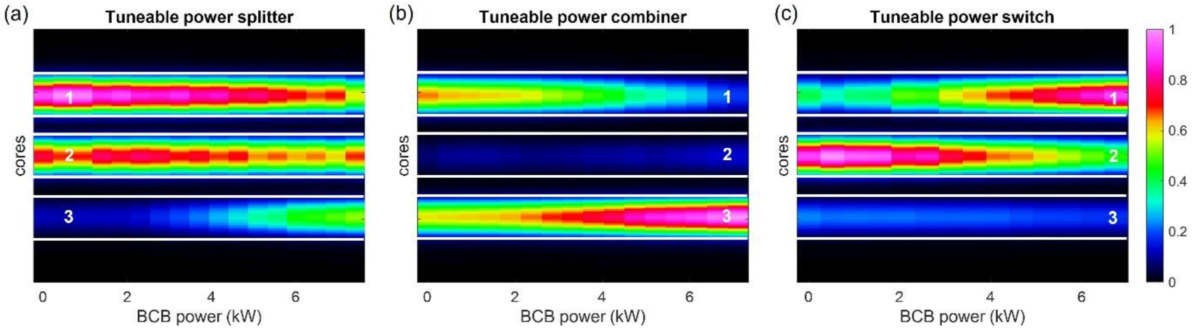

Figure 4.22 All-optically tuneable devices integrated with a 0.4m-long TCF. Side views of the spatial beam shape in the three cores illustrating power distribution among the cores. (a) Tuneable power splitters by varying BCB power, with measurement demonstrating even power splitting among three cores. (b) Tuneable power combiner, with measurement demonstrating power combining into one of the three cores. (c) Tuneable power switch, providing the power rerouting from one core to another core.

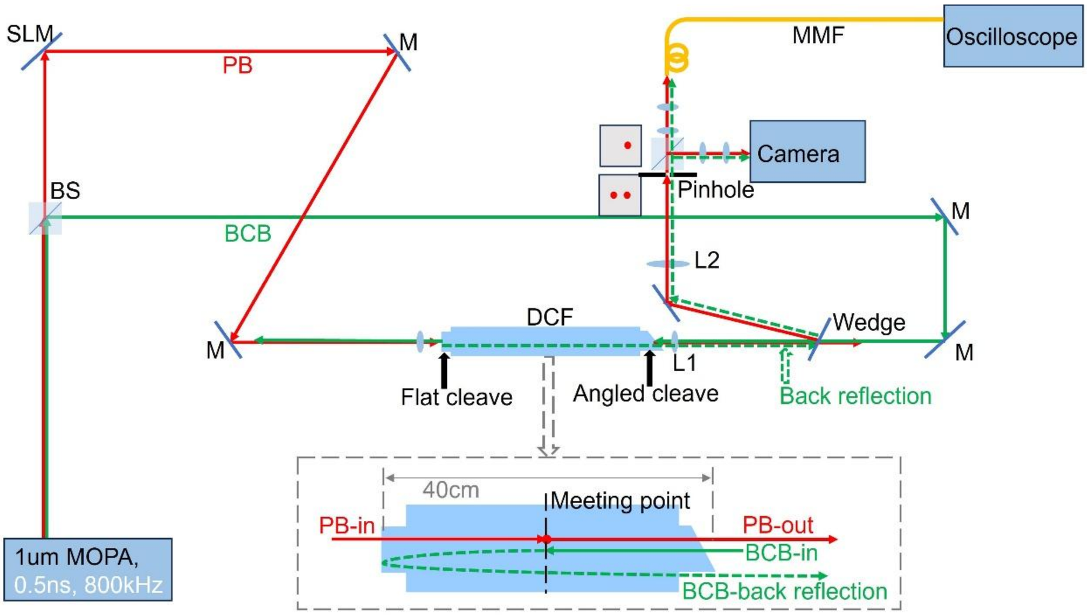

Figure 4.23 Experimental setup for investigating the temporal dynamics of power switching in the DCF, with an inset illustrating the counter-propagating PB and BCB, as well as the BCB reflection at the fibre end. M: mirror, L1(2): lens.

Given the promising performance of these all-optically tuneable devices, it is intriguing to investigate their switching speed. Figure 4.23 illustrates an experimental setup for measuring the temporal dynamics of power switching in the DCF. Although similar to the experimental setup in Figure 4.11, several adjustments are implemented: the SLM is used for the PB coupling to achieve a random power distribution between the cores; the PB output pulse from one of the two cores is selectively measured using a pinhole. The PB output is imaged at the pinhole position via a pair of lenses (L1 with a focal length of 13.86 mm and L2 with a focal length of 500 mm), providing a magnification of ~36x. With a diameter of ~200 μm, the pinhole can effectively filter out the beam from a single core, given that the magnified output beam diameter for each core is ~180 μm, and the centre-to-centre distance between the beams from two fibre cores is ~360 μm. The filtered PB output is then coupled through a telescope into a MMF connected to an oscilloscope to measure the temporal shape. A replica of the filtered output imaged onto the camera using another telescope to visualise the beam profile for the filtered PB output. Due to the flat cleave at the PB input end, some of the input BCB power could reflect backward from this flat-cleaved end. As depicted in the inset figure, the PB continues propagating forward after encountering the BCB in the middle of the fibre (as illustrated by the "Meeting point" in Figure 4.23). The back reflection of BCB at the flat-cleaved fibre end propagates in the same direction as PB. However, there is a delay length between the PB output and BCB back reflection. In this experiment where the "Meeting point" is in the middle of the fibre, the delay length equals to the fibre length (~40 cm), corresponding to a delay of ~2 ns in time for the BCB reflection.

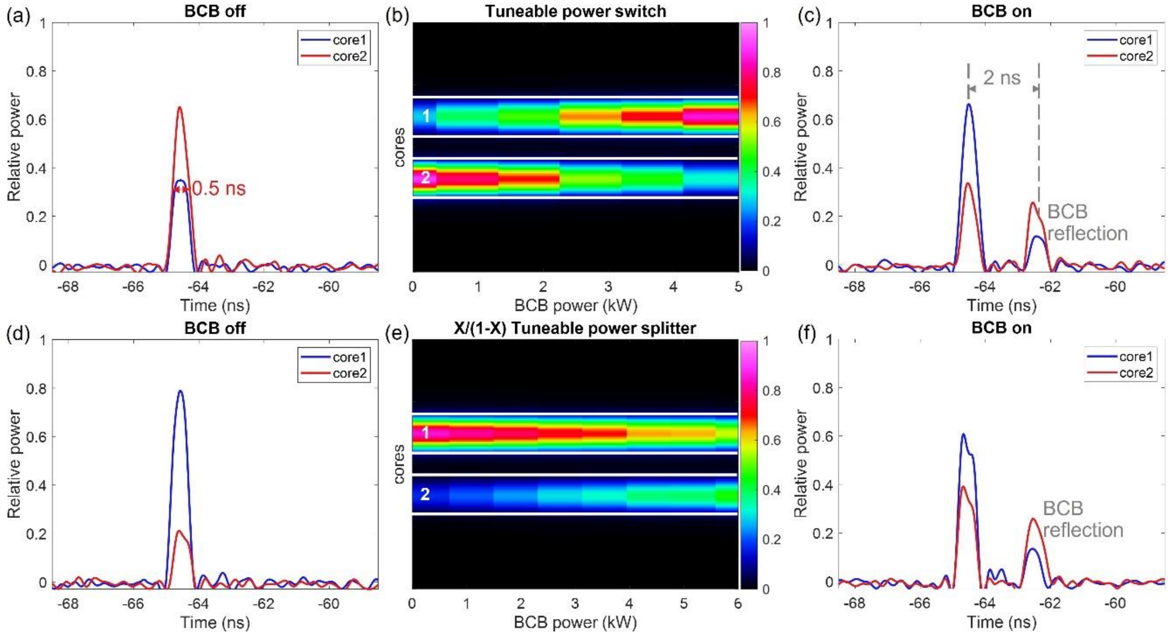

Figure 4.24 Measured temporal shapes for PB_{out} (0.5ns pulse width) in the two DCF cores, with the BCB either (a), (d) turned off or (c), (f) turned on. The relative powers in two cores are normalized such that their sum equals 1. (a)-(c) represent an example of power switch, with power distributions versus BCB power displayed in (b), whereas (d)-(f) illustrate an example of power splitter with power distributions shown in (e).

Figure 4.24 illustrates two measurements using the DCF as a power switch and a power splitter with a BCB power of 6 kW. In Figure 4.24(a)-(c), the PB output pulse in core2 has a relative power of 0.65 when the BCB is turned off, whereas it contains a relative power of 0.35 when the BCB is turned on. The power transfer from core2 to core1 occurs at a rapid speed of 2 GHz, corresponding to the 0.5 ns pulse width of the BCB in this measurement. Notably, this switching speed can be further enhanced by using shorter BCB pulses. Furthermore, Figure 4.24(d)-(f) illustrate the ultrafast switching speed in a tuneable power splitter, where the relative power of the PB output pulses splits to a ratio of 0.6:0.4. In these measurements, the PB pulses and the

BCB pulses have the same pulse duration, and they are synchronized to meet in the middle of the fibre, leading to the temporal shape of the output PB maintaining a similar shape as the input PB. However, the temporal dynamics may differ if the pulse duration of the PB is different or if the PB pulse is not synchronized with the BCB pulse.

4.5.3 All-optical phase detection at terminal ends

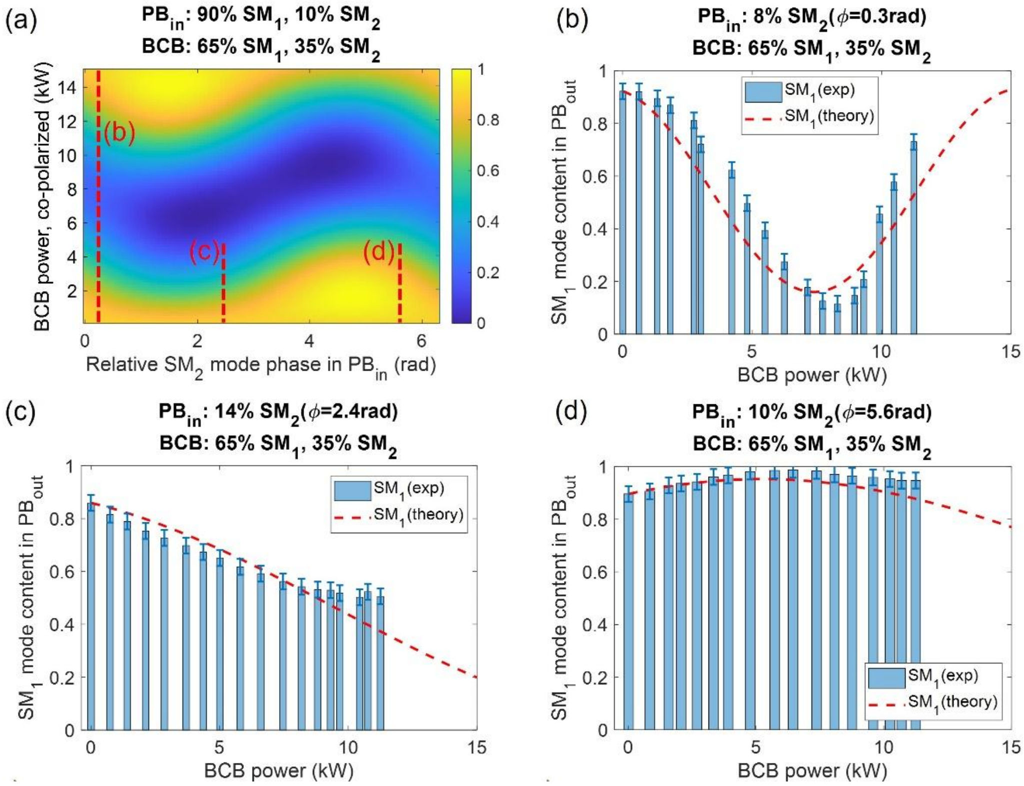

Figure 4.25 All-optical detection of input PB phase in the DCF by measuring the PB$_{out}$ evolution (at terminal ends). (a) Theoretical SM$_1$ mode power as a function of BCB power (y-axis) and the phase difference between the SM$_1$ and SM$_2$ modes in PB$_{in}$ (x-axis). Mode decomposition of the input PB and BCB is indicated at the top. The red dashed lines correspond to the experimental results in (b)-(d), where the BCB is coupled with 65% SM$_1$ mode and 35% SM$_2$ mode. The PB$_{in}$ is coupled with ~90% SM$_1$ mode and ~10% SM$_2$ mode, but with various SM$_2$ mode phases and various polarization states: (b) ϕ=0.3 rad, BCB and PB are co-polarized (parallel); (c) ϕ=2.4 rad, BCB and PB are orthogonally polarized; (d) ϕ=5.6 rad, BCB and PB are orthogonally polarized.

The PB mode conversion can vary depending on the initial mode composition of the PB, as demonstrated in Figure 4.6, Figure 4.14, and Figure 4.15. In a multimode system, maintaining a constant input BCB mode composition while randomly varying the input PB (in terms of mode contents or relative phases) enables the detection and estimation of the initial conditions of the PB by observing how the output PB mode composition evolves with changes in the launched BCB power. Figure 4.25 and Figure 4.26 present examples of phase detection for the input PB modes by measuring the output PB evolutions at the terminal end of a 0.4m-long DCF.

In Figure 4.25, the BCB maintains a consistent mode composition of 65% SM_1 mode and 35% SM_2 mode, while the input PB varies its mode composition by adjusting the coupling conditions, approximately comprising 90% SM_1 mode and 10% SM_2 mode with varying relative phases between them. Figure 4.25(a) illustrates the theoretical variation of SM_1 mode power in the output PB (colour-coded) versus the BCB power (y axis) and the relative phase of the SM_2 mode in the input PB (x axis), calculated using Eq. (4.2.7). Notably, the y-axis on the left indicates the required BCB power for co-polarized BCB and PB configurations, the required power would be 3x larger when the BCB and PB are orthogonally polarized.

For each specific relative phase of the SM_2 mode in the input PB, the evolution of SM_1 mode power in the output PB follows the direction of the y-axis, as shown by the dashed lines in Figure 4.25(a). By measuring the SM_1 mode power in the output PB at various BCB powers, as presented by the blue bars in Figure 4.25(b)-(d), the relative phase of the SM_2 mode in the input PB can be determined by aligning the experimental results with the theoretical plot in Figure 4.25(a). The red dashed lines are replotted in Figure 4.25(b)-(d), and they closely match the experimental results. Consequently, the relative phase of the SM_2 mode in the input PB can be detected: 0.3 rad (b), 2.4 rad (c), and 5.6 rad (d). In these measurements, Figure 4.25(b) corresponds to the co-polarized case, while Figure 4.25(c) and (d) are the orthogonally polarized cases.

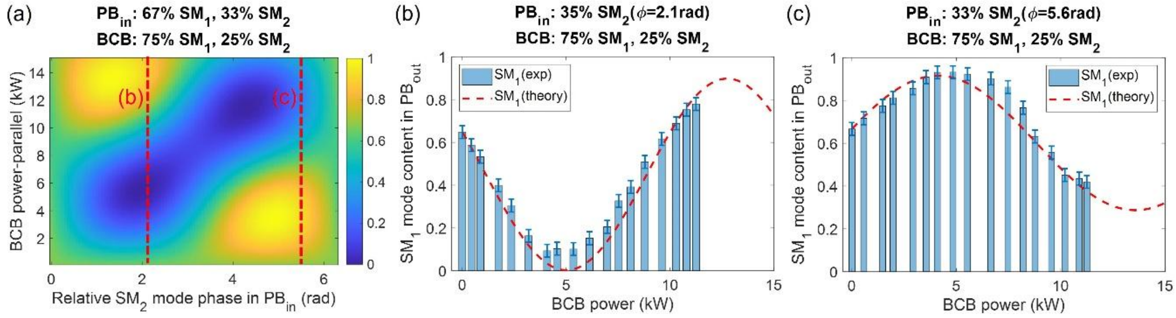

Figure 4.26 All-optical detection of input PB phase in the DCF by measuring the PB_{out} evolution at terminal ends. (a) Theoretical SM_1 mode power as a function of BCB power (y-axis) and the phase difference between the SM_1 and SM_2 modes in PB_{in} (x-axis). Mode decomposition of the input PB and BCB is indicated at the top. The red dashed lines correspond to the experimental results in (b)-(c), where the BCB is coupled with 75% SM_1 mode and 25% SM_2 mode. The PB_{in} is coupled with ~67% SM_1 mode and ~33% SM_2 mode, but with different SM_2 mode phases: (b) ϕ=2.1 rad; (c) ϕ=5.6 rad.

Similarly, Figure 4.26 presents another example where the BCB maintains a consistent mode composition of 75% SM_1 mode and 25% SM_2 mode, while the input PB varies its mode composition, approximately comprising 67% SM_1 mode and 33% SM_2 mode, with varying relative phases between them. Figure 4.26(a) illustrates the theoretical variation of SM_1 mode power in the output PB, which is completely different from the theoretical plot in Figure 4.25(a). However, the relative phase of the SM_2 mode in the input PB can still be determined by aligning the experimental results with the theoretical plot, as demonstrated in Figure 4.26(b) and (c). A relative phase of 2.1 rad (b) and 5.6 rad (c) for the SM_2 mode in the input PB can be precisely detected using this approach. These results highlight the feasibility of optically detecting phase variations in the input PB by monitoring the evolution of the output PB concerning the BCB power. This novel phase detection mechanism offers valuable insights, particularly for lengthy fibre setups, and presents an effective means of implementing phase detection at terminal ends.

4.6 Conclusions

In this chapter, the concept of counter-propagating nonlinear gratings is introduced in multimode systems. Unlike the mode rejection effect discussed in Chapter 3, this phenomenon occurs when there is a significant power difference between mutually injected beams. The theoretical framework underlying the multimodal interaction dynamics driven by this nonlinear grating is explored, along with experimentally investigations using various few mode fibres and multicore fibres. Through this exploration, two intriguing beam self-organization effects emerge: mode switching and power switching.

Mode switching involves the conversion between transverse modes within the low-power forward PB, a process that can be all-optically tuned by adjusting the total power, mode composition, and polarization state of the counter-propagating high-power BCB. Adjustments to fibre length, geometry, and nonlinearity can alter the required BCB power for specific mode switching outcomes. Table 4.1 provides a summary of mode switching results observed in PM1550-xp, PMHN1, DCF, and TCF fibres. By using 0.4m-long fibres and a total peak power of ~6 – 12 kW for the BCB (0.5 ns pulses), tuneable switching between LP modes or supermodes is achieved with a mode conversion efficiency ranging from 20% to 90%. Experimental results agree well with theoretical calculations, both illustrating that complete switching from one mode to another mode can be obtained by using a BCB power of 10 kW, 2.05 kW, and 5 -10 kW for the PM1550-xp fibre, PMHN1 fibre, and DCF, respectively. The maximum mode switching is obtained with a co-polarized PB and BCB configuration, and approximately 3 times higher BCB power is required for achieving similar mode switching result in orthogonally polarized configurations. In the fibres supporting more than two modes, such as the TCF, mode switching can occur among all supported modes or only between two modes, depending on the BCB mode composition.

Table 4.1 Summary of the mode switching results for MMFs and MCFs

Fibre	Theory		Experiments			
	Switching period (*L_{NL})	BCB power required for a switching period (kW)	Fibre Length (m)	Maximum BCB power (kW)	Participating modes	Mode conversion efficiency
PM1550-xp	3	10	0.4	12	LP_{01}, LP_{11}	30% - 90 %
PMHN1	2.7	2.05	0.4	6	LP_{01}, LP_{11}	20% - 60%
DCF	1.5 - 3	5 -10	0.4	11	SM_1, SM_2	40% - 90%
TCF	-	-	0.4	7	SM_1, SM_2, SM_3	20% - 50%

Core-to-core power switching in MCFs arises from the supermode switching effect, where combinations of supermodes with varying relative powers and phases lead to variations in power distribution among individual cores. This phenomenon is theoretically described in this chapter. Experimental observations of power switching in DCF and TCF fibres are demonstrated by using 0.4m-long fibres and a 0.5 ns pulsed BCB with peak powers of 7 – 10 kW. The dynamics of power switching are thoroughly investigated by adjusting the BCB power and the mode compositions of the BCB and input PB. The power within two cores of DCF and TCF can mutually switch when the BCB power is turned on. In an MCF containing more than two cores, power among the cores can be switched to focus to a single core or uniformly distributed among them.

These findings lead to the demonstration of several conceptual devices capable of all-optical light-by-light manipulations, leveraging the mode switching and power switching effects in MMFs and MCFs. These devices encompass a range of applications, including all-optically tuneable mode converters, ultrafast tuneable power splitters, combiners and switches, as well as all-optical phase detection at terminal ends.

Notes: The results reported in this chapter have been selectively published (see LoP2, LoP4, and LoP6 in the List of Publications). LoP2 includes the main results of mode switching and power switching in multimode and multicore fibres that were demonstrated in this chapter. This paper is currently under the first-round revision at Nature Communications Journal. The experiments, simulations, co-development of derivations and code were my work; the 3-core fibre was fabricated by Ian Davidson from the Optoelectronics Research Centre; the dual-core fibres used in the experiments were fabricated by Jayanta Sahu from the Optoelectronics Research Centre; this project was supervised by Massimiliano Guasoni and David J. Richardson from the Optoelectronics Research Centre. LoP4 and LoP6 are conference papers where we introduce the concept of counter-propagating nonlinear grating and reconfigurable all-optical mode switching.

Chapter 5 Four-wave mixing and wavelength conversion in multicore fibres

5.1 Introduction

Optical parametric amplification in optical fibres generates radiation with new wavelengths and different spatial modes based on the four-wave mixing effect. Researchers have investigated parametric amplification in multimode fibres from various perspectives, including the wavelength, mode composition, and polarization of the pump, as well as fibre nonlinearity, length, design, and material. For instance, pump wavelengths at 532nm[136, 137], 1μm[138, 139], and 1.55 μm[140-142] have been used to generate sidebands with different LP modes in few-mode fibres with lengths ranging from less than 1m to several kilometres. In parallel, intermodal four-wave mixing and parametric amplification have been investigated in a variety of fibre and waveguide types, including photonics crystal fibres[143], silicon core fibres[144], silicon waveguides[145], liquid-/gas-filled hollow core fibres[146], and multicore fibres[147, 148].

In the past decade, theoretical analyses of modulation instability and four-wave mixing in coupled MCFs have been presented by solving the couped NLSEs[149-152]. More recently, experimental demonstrations of four-wave mixing have been performed in a 2-core fibre[147, 148]. However, most studies have considered the FWM in the individual MCF cores. Due to the similarity between the MMFs and coupled MCFs, FWM in MCFs can be studied as FWM between multiple supermodes.

In this chapter, wavelength and supermode conversion based on intermodal four-wave mixing in coupled multicore fibres are demonstrated. Initially, the wave vector matching conditions involving different pairs of modes are described, which dictate the optimal circumstances under which FWM processes can effectively occur. Then, based on the analytical solutions to MMNLSEs (introduced in Chapter 2), theoretical estimations of FWM gain peaks and gain bandwidth is provided, considering various dispersion parameter conditions. The influence of various modes and frequencies, as well as of SRS, is investigated. Finally, FWM between the supermodes of several MCFs is explored both theoretically and experimentally. These MCFs include DCF, TCF, 4-core fibre (4CF), and 7-core fibre (7CF), with varying core diameters and core separations.

5.2 Mechanisms of four-wave mixing in optical fibres

5.2.1 Phase matching conditions

As introduced in Chapter 2, nonlinear interactions in multimode systems involve various mode pairs and frequencies. Specifically, by considering three waves (pump, signal, and idler), Eqs. (2.3.24) and (2.3.25) describe the interaction between the *m*-th and *k*-th modes at three frequencies (ω_p, ω_s, and ω_i). FWM requires specific phase matching conditions, including both frequency and wave vector matching. Effective FWM occurs when the phase mismatch is close to 0. Figure 5.1 illustrates the wave vector matching conditions for FWM between different mode pairs, corresponding to the different terms on the right-hand side of Eq. (2.3.24). The wave vector (propagation constant β) for different modes is plotted as a function of frequency, where the frequency matching condition is fulfilled (see Eq. (2.3.13)).

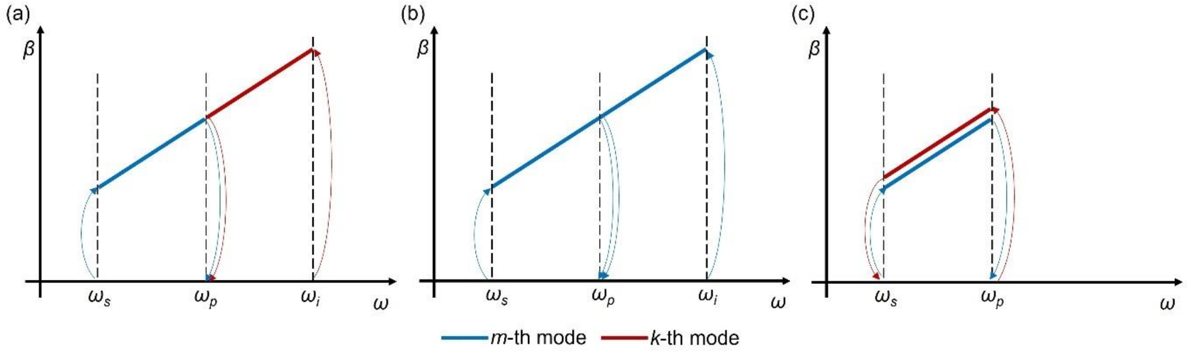

Figure 5.1 Wave vector matching conditions for FWM between different pairs of modes. (a) The *m*-th mode at frequencies ω_s and ω_p, and the *k*-th mode at frequencies ω_p and ω_i. (b) The *m*-th mode at frequencies ω_s, ω_p, and ω_i. (c) The *m*-th mode at frequencies ω_s and ω_p, and the *k*-th mode at frequencies ω_s and ω_p.

In Figure 5.1(a), with the annihilation of two pump photons in the *m*-th mode and the *k*-th mode, the *m*-th and *k*-th modes are generated at signal and idler frequencies, respectively. The wave vector mismatch can be expressed as (see the terms containing $Ap_m Ai_k^* Ap_k$ in Eq. (2.3.24)),

$$\Delta\beta_{\mathrm{I}} = \Delta\beta_m^{(s,p)} + \Delta\beta_k^{(i,p)} \tag{5.2.1}$$

Figure 5.1(b) represents the degenerate FWM process in single-mode fibres, where the signal and idler are generated in the same mode as the pump. The corresponding wave vector mismatch is,

$$\Delta\beta_{\mathrm{II}} = \Delta\beta_m^{(s,p)} + \Delta\beta_m^{(i,p)} \tag{5.2.2}$$

Lastly, in Figure 5.1(c), FWM involves only the pump and signal frequencies, with the *m*-th mode and *k*-th mode generated at the signal and pump frequencies, respectively. A similar process exists involving only the pump and idler frequencies, as described by the terms containing $A_{p_m} A_{p_k}^* A_{i_k}$ in Eq. (2.3.25). The wave vector mismatch for Figure 5.1(c) is,

$$\Delta\beta_{\mathrm{III}} = \Delta\beta_m^{(s,p)} - \Delta\beta_k^{(s,p)} \tag{5.2.3}$$

The phase matching conditions require that the wave vector mismatch is close to 0. By expanding the propagation constant in a Taylor series around the pump frequency (see Eq. (2.2.2)), Eqs. (5.2.1)-(5.2.3) can be rewritten as follows,

$$\begin{aligned}\Delta\beta_{\mathrm{I}} = \left[\beta_{1m}^{(\omega_p)} - \beta_{1k}^{(\omega_p)}\right](-\Delta\omega) + \frac{1}{2}\left[\beta_{2m}^{(\omega_p)} + \beta_{2k}^{(\omega_p)}\right](-\Delta\omega)^2 \\ + \frac{1}{6}\left[\beta_{3m}^{(\omega_p)} - \beta_{3k}^{(\omega_p)}\right](-\Delta\omega)^3 + \cdots\end{aligned} \tag{5.2.4}$$

$$\Delta\beta_{\mathrm{II}} = \beta_{2m}^{(\omega_p)}(\Delta\omega)^2 + \frac{1}{12}\beta_{4m}^{(\omega_p)}(\Delta\omega)^4 + \cdots \tag{5.2.5}$$

$$\begin{aligned}\Delta\beta_{\mathrm{III}} = \left[\beta_{1m}^{(\omega_p)} - \beta_{1k}^{(\omega_p)}\right](-\Delta\omega) + \frac{1}{2}\left[\beta_{2m}^{(\omega_p)} - \beta_{2k}^{(\omega_p)}\right](-\Delta\omega)^2 \\ + \frac{1}{6}\left[\beta_{3m}^{(\omega_p)} - \beta_{3k}^{(\omega_p)}\right](-\Delta\omega)^3 + \cdots\end{aligned} \tag{5.2.6}$$

where $\Delta\omega = \omega_p - \omega_s = \omega_i - \omega_p$, and $\beta_{Xm}^{(\omega p)}$ is the X-th order dispersion parameter for the m-th mode at the pump frequency ω_p.

Once the dispersion parameters at the pump frequency are determined, the phase-matching frequency separation of the signal or idler from the pump, $\Delta\omega$, can be estimated from Eqs. (5.2.4)-(5.2.6) (here by retaining only the first two terms of the expansions):

$$\Delta\omega_{\mathrm{I}} = \frac{2\left[\beta_{1m}^{(\omega_p)} - \beta_{1k}^{(\omega_p)}\right]}{\left[\beta_{2m}^{(\omega_p)} + \beta_{2k}^{(\omega_p)}\right]} \tag{5.2.7}$$

$$\Delta\omega_{\mathrm{II}} = \sqrt{\frac{-12\beta_{2m}^{(\omega_p)}}{\beta_{4m}^{(\omega_p)}}} \tag{5.2.8}$$

$$\Delta\omega_{\mathrm{III}} = \frac{2\left[\beta_{1m}^{(\omega_p)} - \beta_{1k}^{(\omega_p)}\right]}{\left[\beta_{2m}^{(\omega_p)} - \beta_{2k}^{(\omega_p)}\right]} \tag{5.2.9}$$

These frequencies can be shifted due to the contributions of self-phase and cross-phase modulations[68], which depend on the pump power distribution across multiple modes and the Kerr coefficients (see the first term in Eq. (2.3.24)). Considering higher order dispersion parameters can also contribute to changes in the value of $\Delta\omega$. Among the three types of FWM processes, the intermodal FWM process illustrated in Figure 5.1(a) is most attractive since the zero-dispersion requirement for intramodal FWM is relaxed by selecting different pairs of modes, allowing several distinct $\Delta\omega_{\mathrm{I}}$ values to be obtained using various modes in the same multimode fibre.

5.2.2 Theoretical estimation of FWM gain peak and bandwidth

Table 5.1 Theoretical gain peak and bandwidth of FWM

Intramodal FWM	Gain peak (Ω_{pk})	Gain bandwidth (Ω_B)	Gain (m^{-1})
$\beta_{2m}^{(\omega_p)} < 0$	$\sqrt{\frac{2\gamma_{mm}P}{\lvert\beta_{2m}^{(\omega_p)}\rvert}}$	$2\sqrt{\frac{\gamma_{mm}P}{\lvert\beta_{2m}^{(\omega_p)}\rvert}}$	$\sqrt{(\gamma_{mm}P_m)^2 - \frac{1}{4}\left(2\gamma_{mm}P_m + \beta_{2m}^{(\omega_p)}(-\Delta\omega)^2\right)^2}$
Intermodal FWM	Gain peak (Ω_{pk})	Gain bandwidth (Ω_B)	Gain (m^{-1})
D1 = 0, D2 < 0, D3 = 0	$\sqrt{\frac{-\begin{pmatrix}\gamma_{mm}P_m \\ +\gamma_{kk}P_k\end{pmatrix}}{D_2}}$	$\sqrt{\frac{-\begin{pmatrix}4\gamma_{mk}\sqrt{P_mP_k} + \\ \gamma_{mm}P_m + \gamma_{kk}P_k\end{pmatrix}}{D_2}}$	$\sqrt{4\gamma_{mk}^2P_mP_k - \frac{1}{4}\begin{pmatrix}\gamma_{mm}P_m + \gamma_{kk}P_k + \\ D_2(-\Delta\omega)^2\end{pmatrix}^2}$
D1 = 0, D2 > 0, D3 = 0	0	$\sqrt{\frac{-\begin{pmatrix}-4\gamma_{mk}\sqrt{P_mP_k} + \\ \gamma_{mm}P_m + \gamma_{kk}P_k\end{pmatrix}}{D_2}}$	$\sqrt{4\gamma_{mk}^2P_mP_k - \frac{1}{4}\begin{pmatrix}\gamma_{mm}P_m + \gamma_{kk}P_k + \\ D_2(-\Delta\omega)^2\end{pmatrix}^2}$
D1 ≠ 0, D2 ≠ 0, D3 = 0	$-\frac{D_1}{2D_2} \mp \sqrt{\frac{\frac{D_1^2}{4D_2^2} - \begin{pmatrix}\gamma_{mm}P_m \\ +\gamma_{kk}P_k\end{pmatrix}}{D_2}}$	$-\frac{D_1}{2D_2} \pm \sqrt{\frac{\frac{D_1^2}{4D_2^2} - \begin{pmatrix}\gamma_{mm}P_m \\ +\gamma_{kk}P_k \\ \pm 4\gamma_{mk}\sqrt{P_mP_k}\end{pmatrix}}{D_2}}$	$\sqrt{4\gamma_{mk}^2P_mP_k - \frac{1}{4}\begin{pmatrix}\gamma_{mm}P_m + \gamma_{kk}P_k + \\ D_2(-\Delta\omega)^2 + D_1(-\Delta\omega)\end{pmatrix}^2}$
D1 ≠ 0, D2 ≠ 0, D3 ≠ 0	$\mathit{\Omega}_{pk,L} = \frac{-D_2 \pm \sqrt{D_2^2 - 4D_1D_3}}{2D_3}$, $\mathit{\Omega}_{pk,NL} = \frac{-(\gamma_{mm}P_m + \gamma_{kk}P_k)}{3D_3\mathit{\Omega}_{pk,L}^2 + 2D_2\mathit{\Omega}_{pk,L} + D_1}$, $\mathit{\Omega}_{pk} = \mathit{\Omega}_{pk,L} + \mathit{\Omega}_{pk,NL}$	$\mathit{\Omega}_{pk} \pm \frac{4\gamma_{mk}\sqrt{P_mP_k}\mathit{\Omega}_{pk,NL}}{(\gamma_{mm}P_m + \gamma_{kk}P_k)}$	$\sqrt{4\gamma_{mk}^2P_mP_k - \frac{1}{4}\begin{pmatrix}\gamma_{mm}P_m + \gamma_{kk}P_k + \\ D_3(-\Delta\omega)^3 + D_2(-\Delta\omega)^2 \\ +D_1(-\Delta\omega)\end{pmatrix}^2}$

To comprehensively explore the intermodal FWM process and achieve a theoretical estimation of FWM gain peaks and gain bandwidths, the matrix formalisation of coupled-amplitude equations (Eq. (2.3.29)) can be employed. Here, the Raman contribution is omitted by setting f_R=0, and only the elements related to the *m*-th mode in the signal and the *k*-th mode in the idler are retained, leading to:

$$\partial_z \mathbf{v} = \mathbf{M}\mathbf{v}, \mathbf{v} = [\bar{A}s_m\ \bar{A}i_k^*]^T, \mathbf{M} = \begin{bmatrix} j\left[\Delta\beta_m^{(s,p)} + \gamma_{mm}P_m\right] & j2\gamma_{mk}\sqrt{P_mP_k} \\ -j2\gamma_{km}\sqrt{P_kP_m} & -j\left[\Delta\beta_k^{(i,p)} + \gamma_{kk}P_k\right] \end{bmatrix} \tag{5.2.10}$$

where $\gamma_{mk}=\gamma f_{mk}$ is applied to simplify the expression. As indicated in Eq. (2.3.31), the FWM gain depends on the eigenvalues of **M**. Specifically, it is proportional to the real part of the eigenvalues[78], which can be expressed as:

$$Gain \propto [4\gamma^2 f_{mk}^2 P_m P_k - \frac{1}{4}\left(\gamma f_{mm} P_m + \gamma f_{kk} P_k + \Delta\beta_m^{(s,p)} + \Delta\beta_k^{(i,p)}\right)^2] \tag{5.2.11}$$

This relationship indicates the condition for achieving gain peaks:

$$\left(\gamma_{mm} P_m + \gamma_{kk} P_k + \Delta\beta_m^{(s,p)} + \Delta\beta_k^{(i,p)}\right) = 0 \tag{5.2.12}$$

By substituting Eq.(5.2.4) into it, a solvable equation for $\Delta\omega$ can be obtained by considering up to the third order dispersion:

$$\mathrm{D}_3(-\Delta\omega)^3 + \mathrm{D}_2(-\Delta\omega)^2 + \mathrm{D}_1(-\Delta\omega) + \gamma_{mm} P_m + \gamma_{kk} P_k = 0 \tag{5.2.13}$$

where D1= $\beta_{1m}^{(\omega_p)} - \beta_{1k}^{(\omega_p)}$, D2= $\frac{1}{2}\left[\beta_{2m}^{(\omega_p)} + \beta_{2k}^{(\omega_p)}\right]$, and D3= $\frac{1}{6}\left[\beta_{3m}^{(\omega_p)} - \beta_{3k}^{(\omega_p)}\right]$. The frequency separation (Ω_{pk}) of the FWM gain peaks from the pump frequency can be obtain from Eq. (5.2.13), and the gain bandwidth (Ω_B) can be determined by finding $\Delta\omega$ that makes Eq.(5.2.11) equal to 0. This equation also illustrates the shift of the gain peak from $\Delta\omega_l$ (where $\Delta\omega_l$ makes the first three terms equal to 0) due to the contributions of $\gamma_{mm}P_m$ and $\gamma_{kk}P_k$. The estimations of gain peak and gain bandwidth[78] under different conditions for the signs of D1, D2, and D3 are provided in Table 5.1. To explain the shift of gain peaks due to the contribution of self- and cross-phase modulations, for example, the gain peak is modified from Eq. (5.2.7) due to the ($\gamma_{mm}P_m$+$\gamma_{kk}P_k$) term when D1≠0, D2≠0, and D3=0.

5.2.3 Influence of various modes and frequencies

Table 5.1 provides an overview of the predicted gain spectrum distribution when considering the *m*-th mode as the signal and the *k*-th mode as the idler. Variations in maximum gain and the corresponding frequencies can occur with changes in dispersion parameters, pump power, and Kerr coefficients. Moreover, the gain spectrum is influenced by the inclusion of additional modes and frequencies. For example, a bimodal fibre scenario is examined where $\beta_{1,m1}^{(\omega_p)}$=4.906 ps/mm, $\beta_{1,m2}^{(\omega_p)}$=4.907 ps/mm, $\beta_{2,m1}^{(\omega_p)}$=1 ps^2/km, $\beta_{2,m2}^{(\omega_p)}$=3 ps^2/km, $\beta_{3,m1}^{(\omega_p)}$=$\beta_{3,m2}^{(\omega_p)}$=0 ps^3/km, $\gamma_{m1,m1}$= $\gamma_{m2,m2}$= $\gamma_{m1,m2}$= 3 W^{-1}km^{-1}, and P_{m1}= P_{m2}= 1 kW, with *m*1 and *m*2 representing two modes. By considering only the *m*1 mode in the signal (As$_{m1}$) and the *m*2 mode in the idler (Ai$_{m2}$), the normalized gain spectrum derived from Table 5.1 is depicted in Figure 5.2(a), showing two gain peaks at frequencies separated from the pump by ±0.97 THz and ±78.6 THz. However, when including both modes in signal and idler (As$_{m1}$, As$_{m2}$, Ai$_{m1}$, and Ai$_{m2}$), the matrix **M** in Eq. (2.3.29) becomes a 4 x 4 matrix. Consequently, the eigenvalues of **M** differ from those in Eq.(5.2.10) at specific frequencies. For example, the gain peaks at the frequency of ±0.97 THz are absent, as illustrated in Figure 5.2(b). This variation in the FWM gain spectrum by incorporating additional modes and frequencies suggests that sufficient considerations should be taken when estimating output spectral distributions for multimode systems.

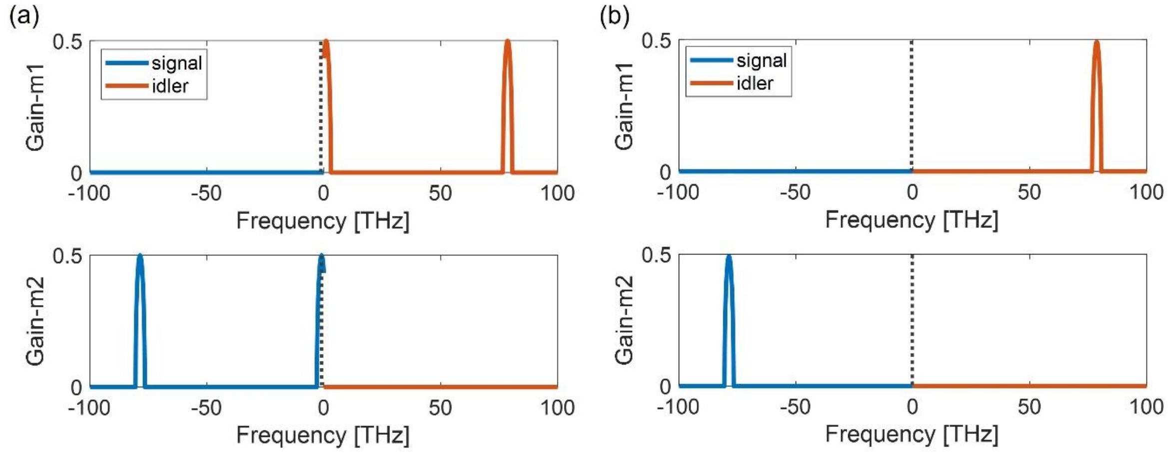

Figure 5.2 Variations in the gain spectrum (centred around the pump frequency) when additional modes and frequencies are taken into account. (a) Gain spectrum when considering only the *m*1 mode in signal and the *m*2 mode in idler (As$_{m1}$+Ai$_{m2}$). (b) Gain spectrum when considering both the *m*1 and *m*2 modes in signal and idler (As$_{m1}$+As$_{m2}$+Ai$_{m1}$+Ai$_{m2}$). Note that gain around zero frequency disappears.

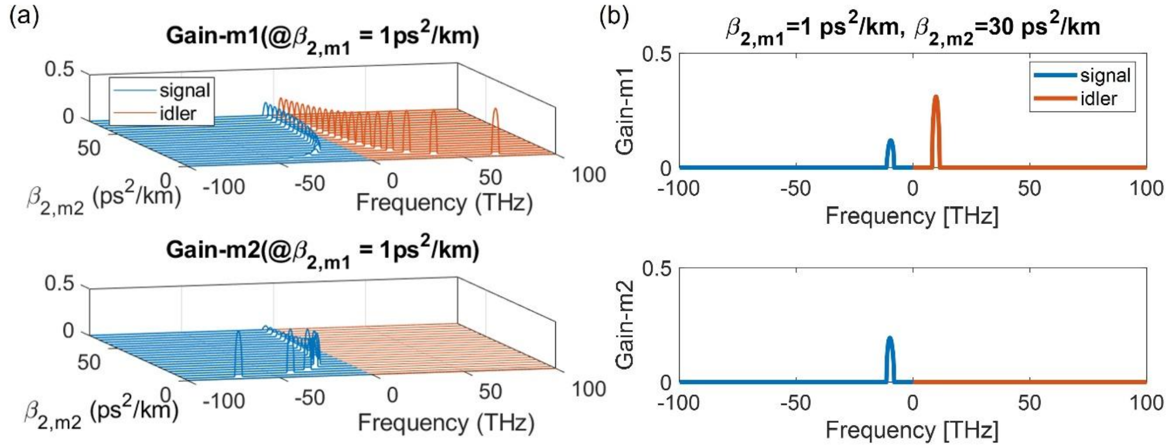

Figure 5.3 Variations in the gain spectrum with the adjustments in dispersion parameters. (a) Gain spectra under varying second order dispersion values for the *m*2 mode. (b) A specific instance of the gain spectrum with the second order dispersion of the *m*2 mode set to 30 ps^2/km.

The subsequent analysis investigates how the gain spectrum is affected by varying the dispersion parameters, specifically by adjusting the second-order dispersion for the *m*2 mode. Figure 5.3(a) illustrates how the gain spectrum changes as $\beta_{2,m2}$ varies from 0 ps^2/km to 70 ps^2/km, while keeping other parameters consistent with those in Figure 5.2(b). In this scenario, the idler has gain in the *m*1 mode and the signal has gain in the *m*2 mode. As $\beta_{2,m2}$ increases, the frequency corresponding to the gain peaks decreases, and simultaneously, the maximum gain at the gain peaks also decreases, as illustrated by the amplitude variations in Figure 5.3(a). Another noteworthy observation is that the signal in the *m*1 mode also obtains gain with increasing $\beta_{2,m2}$. For instance, Figure 5.3(b) demonstrates the gain spectrum when $\beta_{2,m1}$=1 ps^2/km and $\beta_{2,m2}$=30 ps^2/km, where the signal has gain in both modes, while the idler only has gain in the *m*1 mode. However, achieving such a significant difference in the second order dispersion parameters between spatial modes is challenging in conventional optical fibres. This limitation explains why intermodal FWM processes usually involve a one mode in the signal and another mode in the idler.

To validate the findings regarding variations in the FWM gain spectrum, numerical simulations of the MM-NLSEs are implemented using the parameters specified above and a fibre length of 1m. The gain spectra of two modes are compared between the numerical simulations and the analytical calculations, with different second order dispersion settings as described in the caption of Figure 5.4. The numerical results align with the analytical results in both cases. Methodology for obtaining these results is introduced in section 2.3.2, and discrepancy between numerical and analytical results around the pump frequency arises from the Lorentzian shape of the input spectra used in simulations. In Figure 5.4(a), with $\beta_{2,m1}$=1 ps^2/km and $\beta_{2,m2}$=3 ps^2/km, dominant gain occurs in the *m*1 mode for the idler and the *m*2 mode for the signal. In contrast, with $\beta_{2,m1}$=1 ps^2/km and $\beta_{2,m2}$=30 ps^2/km, the frequencies of idler and signal shift from ±78.6 THz to ±9.8 THz. Here, the *m*1 and *m*2 modes exhibit comparable gains in the signal, while the idler only obtains gain in the *m*1 mode, as shown in Figure 5.4(b). Additionally, the maximum gain is lower than that shown in Figure 5.4(a).

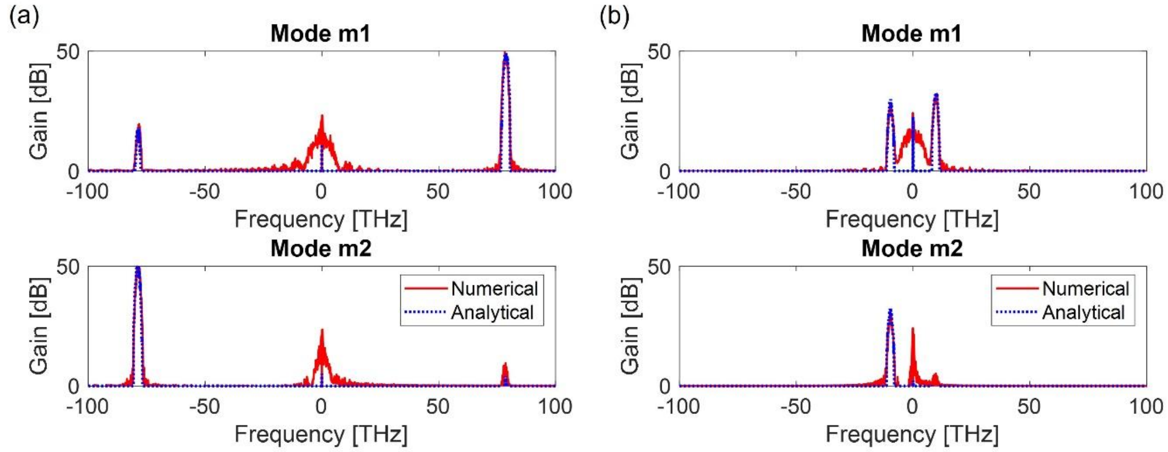

Figure 5.4 Comparison between the gain spectrum obtained by numerical (red lines) and analytical (blue dots) methods for a bimodal fibre with different second order dispersion parameters: (a) $\beta_{2,m1}$=1 ps^2/km and $\beta_{2,m2}$=3 ps^2/km; (b) $\beta_{2,m1}$=1 ps^2/km and $\beta_{2,m2}$=30 ps^2/km.

5.2.4 Influence of Raman effect

By adjusting parameters such as pump mode composition, pump power, Kerr coefficients, and dispersion parameters, the FWM gain spectrum can be modified in terms of gain peak frequency, maximum gain, and gain distributions among different modes. In the following analysis, the Raman effect is incorporated using the complete form of matrix **M** introduced in Eq. (2.3.30). Consequently, the eigenvalues of **M** are different due to the contribution of Raman effect, leading to variations in the FWM gain spectrum. Figure 5.5(a) illustrates the normalized gain spectrum when $\beta_{2,m2}$ varies from -50 ps^2/km to 50 ps^2/km, with all other parameters identical to those in Figure 5.3(a). Here, negative frequencies represent the signal, and positive frequencies represent the idler. By focusing on the gain at the Raman gain peak (-13.2 THz), as highlighted with white dashed lines, the gain variation as a function of $\beta_{2,m2}$ is depicted in Figure 5.5(b). Specifically, for the *m*1 mode, two local maxima at the Raman gain peak occur when $\beta_{2,m2}$=-26.8 ps^2/km and $\beta_{2,m2}$=21.9 ps^2/km, while for the *m*2 mode, local maxima are observed at $\beta_{2,m2}$=-1 ps^2/km and $\beta_{2,m2}$=21.2 ps^2/km.

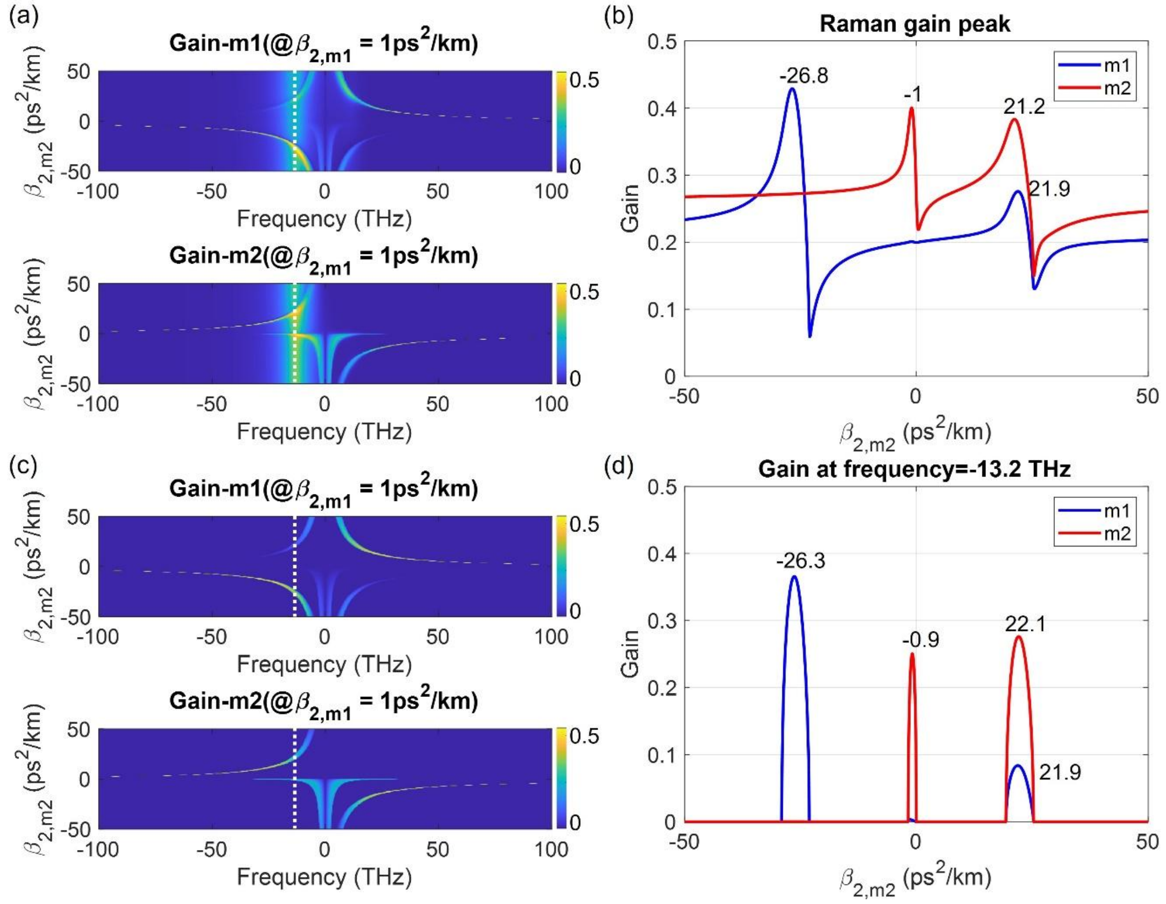

Figure 5.5 (a) Gain spectrum under varying second order dispersion values for the *m*2 mode when including Raman effect. (b) The gain at the Raman gain peak (frequency=-13.2 THz) for the *m*1 and *m*2 modes. (c), (d) Similar results to (a) and (b) when Raman effect is not considered.

Notably, these local maxima arise from the overlap of the Raman gain spectrum with the FWM gain spectrum. Figure 5.5(c) and (d) illustrate the FWM gain spectrum when the Raman effect is neglected. It is worth noting that the local maxima in FWM gain at the frequency of -13.2 THz occur at $\beta_{2,m2}$ values close to those depicted in Figure 5.5(b). However, there are slight differences in the $\beta_{2,m2}$ values corresponding to these gain maxima between Figure 5.5(b) and (d). This discrepancy arises because of the overlap between the narrow-bandwidth FWM gain spectrum and the broader-bandwidth Raman gain spectrum.

5.3 Estimations of four-wave mixing in multicore fibres

5.3.1 Fibre design and phase-matching conditions

The modification of the FWM gain spectrum can be achieved by adjusting the dispersion parameters and Kerr coefficients, and phase-matching conditions of modes within single-core fibres. Techniques involving the control of core diameter and core-cladding refractive index are pivotal in multimode fibres. However, MCFs offer enhanced degrees of freedom for manipulating the FWM gain spectrum. This versatility is achieved by varying factors such as the number of cores, core diameter, and spatial arrangement of cores. In this section, the phase-matching conditions between different supermodes for several multicore fibres are calculated, including DCF, TCF, 4CF, and 7CF. These fibre designs are characterized by distinct core diameters of 5 μm and 4 μm, along with core spacings of 10 μm and 8 μm, respectively. The design parameters are constrained by the etched preform, maintaining a fixed ratio of 2 between core spacing and core diameter. Nevertheless, variations in core arrangement can significantly influence the corresponding phase-matching conditions and FWM gain spectra.

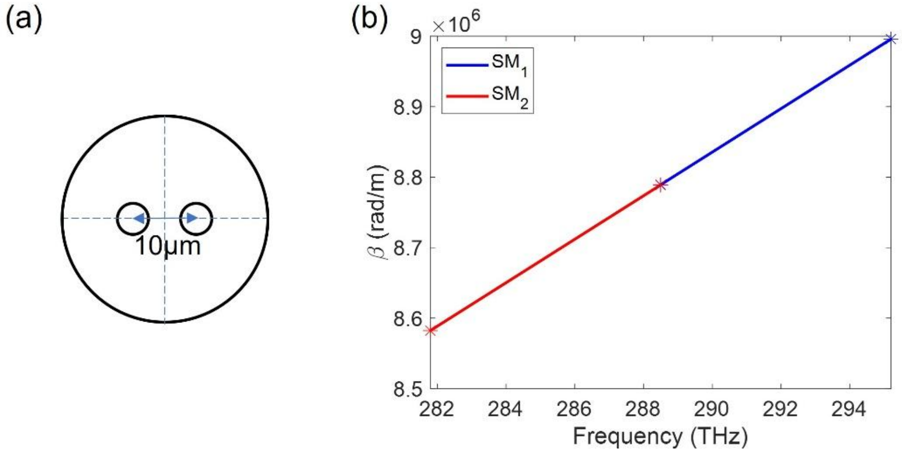

Figure 5.6 (a) Cross section of the DCF. (b) Phase matching condition for the supermodes in the DCF.

Figure 5.6 depicts the phase-matching condition for the SM_1 and SM_2 modes in the DCF that is used in Chapter 3 and 4. The fibre features core diameters of 5 µm and a core spacing of 10 µm, as illustrated in Figure 5.6(a). Using pumps centred at a frequency of 288.5 THz (corresponding to a wavelength of 1040 nm), the vector mismatch approaches 0 among the four waves: signal in the SM_2 mode, idler in the SM_1 mode, and the pump coupled into 2 modes, represented by stars in Figure 5.6(b). The frequency separation between the signal/idler and the pump is ±6.7 THz, corresponding to ±24 nm centred around the wavelength of 1040 nm.

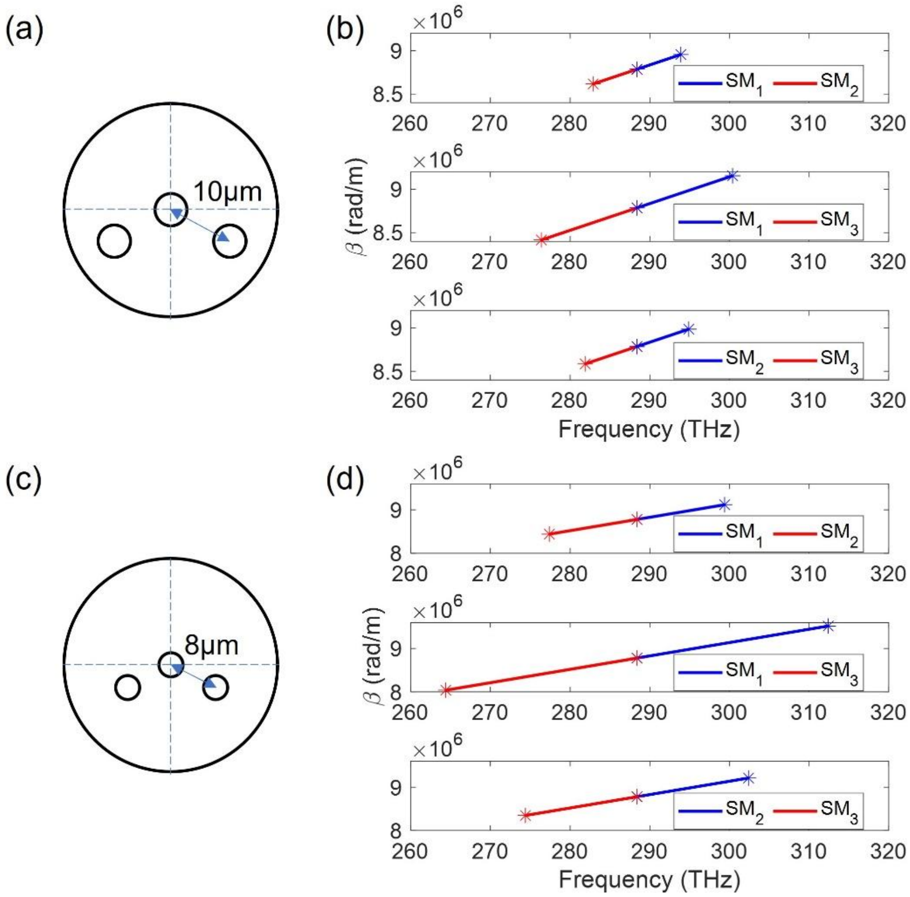

Figure 5.7 Phase matching conditions for different pairs of supermodes in the TCFs with varying geometries: (a), (b) core diameter is 5 µm and core-to-core distance is 10 µm; (c), (d) core diameter is 4 µm and core-to-core distance is 8 µm.

Similarly, phase-matching conditions for the supermodes in the TCF are calculated using a pump wavelength of 1040 nm. Figure 5.7 (b) presents the results when the core diameter is 5 µm and the core spacing equals 10 µm. Here the maximum frequency separation can be achieved using the SM_1 mode and the SM_3 mode for the FWM process. The idler in the SM_1 mode and the signal in the SM_3 mode can be obtained at a frequency separated from the pump by ±12 THz, leading to new wavelength generations at ~998 nm and ~1085 nm, respectively.

Subsequently, phase-matching conditions are recalculated using a modified TCF with reduced core diameter (4 µm) and core spacing (8 µm), as demonstrated in Figure 5.7(c) and (d). This adjustment in core geometry alters the propagation constants of supermodes, resulting in increased frequency separation for the signal/idler compared to the original TCF. For instance, the idler in the SM_1 mode and the signal in the SM_3 mode can be obtained at the frequencies separated from the pump by ±24 THz. This corresponds to new wavelength generations at ~960 nm and ~1134 nm, respectively.

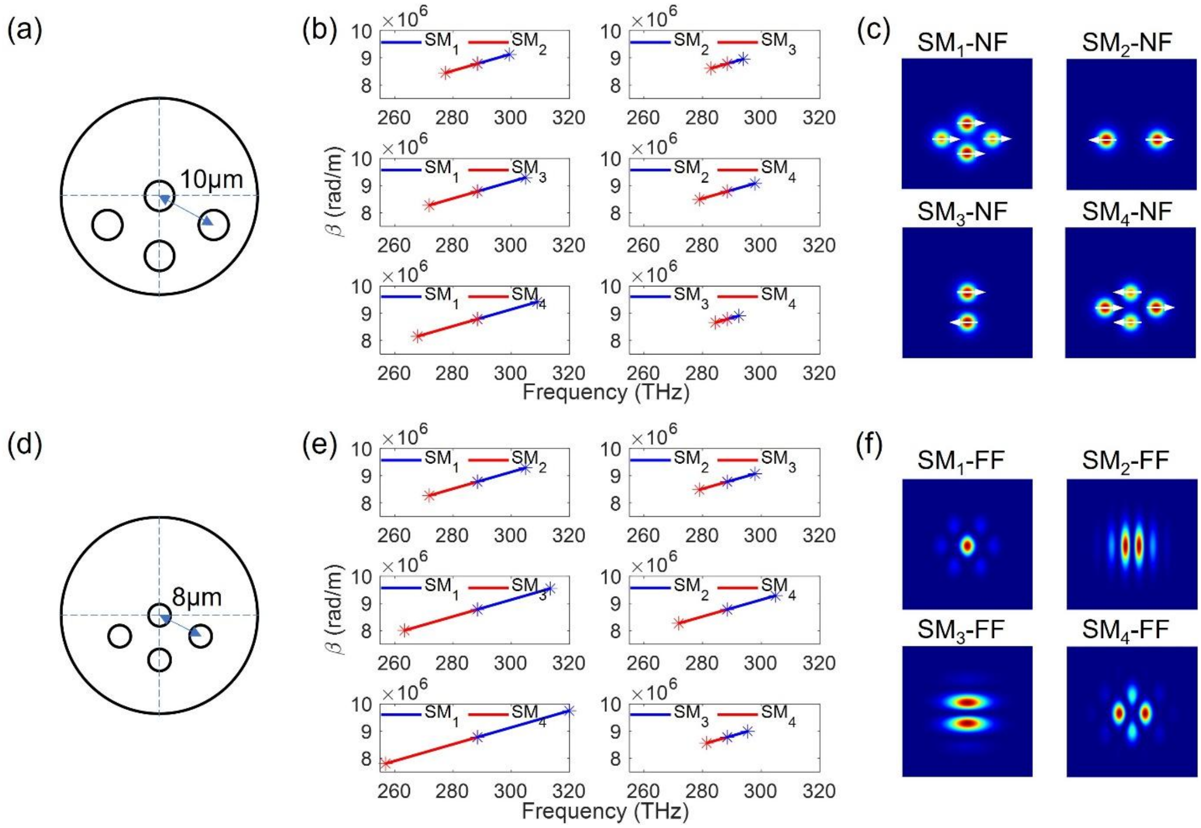

Figure 5.8 Phase matching conditions for different pairs of supermodes in the 4CFs with varying geometries: (a), (b) core diameter is 5 μm and core-to-core distance is 10 μm; (d), (e) core diameter is 4 μm and core-to-core distance is 8 μm. (c) Near-field distributions for the four supermodes in 4CF, with white arrows denoting the polarization directions in each core. (e) Corresponding far-field distributions.

Followingly, phase-matching conditions for 4CFs are investigated, as depicted in Figure 5.8. These 4CFs feature core diameters of 5 μm and 4 μm with core spacings of 10 μm and 8 μm, respectively, supporting the propagation of four distinct supermodes. The near-field and far-field intensity distributions of these four supermodes are provided in Figure 5.8(c) and (f), respectively. Figure 5.8(b) and (e) illustrate the phase-matching conditions between different pairs of supermodes with a pump wavelength of 1040 nm. The maximum frequency separation of the signal/idler from the pump is achieved by employing the SM_1 and SM_4 modes in the FWM process. In the 4CF with a core diameter of 5 μm and a core spacing of 10 μm, the signal in the SM_4 mode and the idler in the SM_1 mode can be generated at frequencies separated from the pump by ±20.5 THz, corresponding to new wavelength generations at ~971 nm and ~1119 nm, respectively.

Conversely, the minimum frequency separation for the signal/idler is achieved when the FWM process involves the SM_3 and SM_4 modes, with a separation of ±4 THz from the pump frequency. Furthermore, using a 4CF with a core diameter of 4 μm and a core spacing of 8 μm, the maximum frequency separation for the signal/idler can be extended to ±31.5 THz, resulting in new wavelength generations at ~937 nm and ~1167 nm, respectively. Figure 5.8(e) illustrates 6 pairs of gain peaks obtained in various supermodes, spanning frequencies from ±7 to ±31.5 THz relative to the pump frequency.

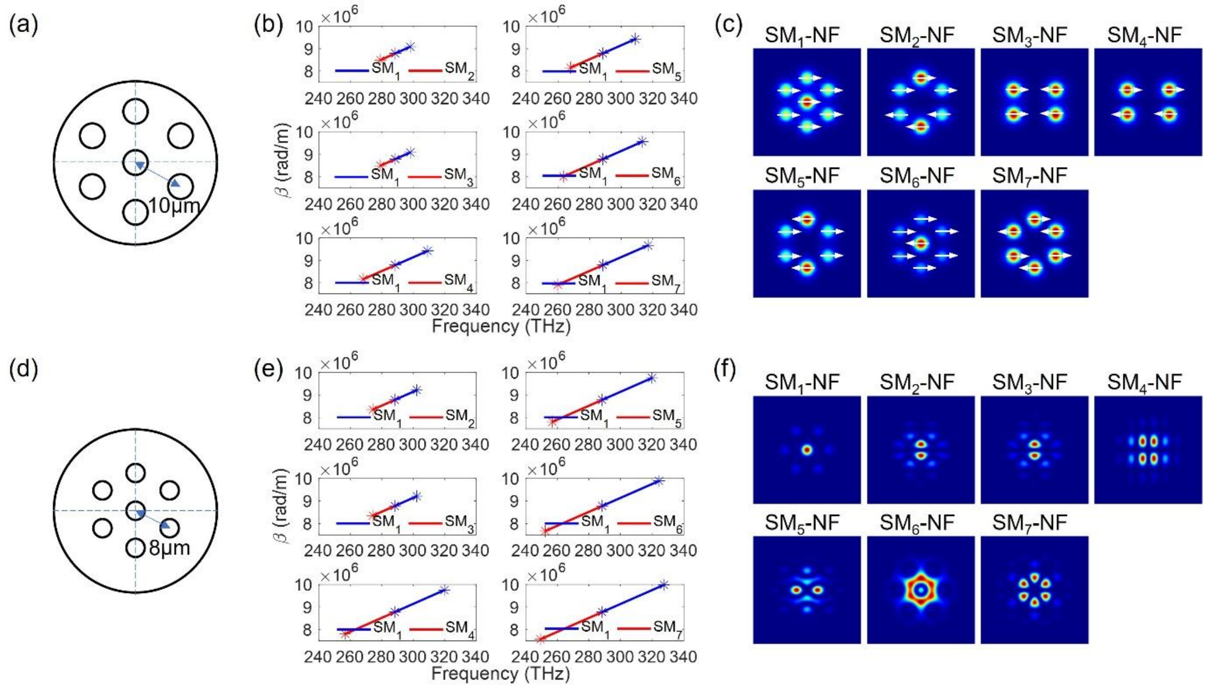

Figure 5.9 Phase matching conditions for different pairs of supermodes in the 7CFs with varying geometries: (a), (b) core diameter is 5 μm and core-to-core distance is 10 μm; (d), (e) core diameter is 4 μm and core-to-core distance is 8 μm. (c) Near-field distributions for the seven supermodes in 7CF, with white arrows denoting the polarization directions in each core. (e) Corresponding far-field distributions.

Finally, the phase-matching conditions for 7CFs are investigated, where seven cores arranged in a hexagonal pattern, with core diameters of 5 μm and 4 μm and core spacings of 10 μm and 8 μm, respectively, as shown in Figure 5.9(a) and (d). These fibres support the propagation of seven supermodes, with the corresponding near-field and far-field intensity distributions presented in Figure 5.9(c) and (f), respectively. Theoretically, there are 21 pairs of FWM peaks achievable by selecting any two of the seven supermodes involved in the FWM process. Figure 5.9(b) and (e) provide examples of phase-matching conditions between the SM_1 mode and other supermodes at a pump wavelength of 1040 nm. The maximum frequency separation between the signal/idler and the pump is achieved by using the SM_1 and SM_7 modes in the FWM process. In the 7CF with a core diameter of 5 μm and a core spacing of 10 μm, the signal in the SM_7 mode and the idler in the

SM_1 mode can be obtained at frequencies separated from the pump by ±28.5 THz, corresponding to new wavelength generations at ~946 nm and ~1154 nm, respectively.

In contrast, using a 7CF with core diameter of 4 μm and a core spacing of 8 μm, the maximum frequency separation for the signal/idler can be increased to ±39 THz, resulting in new wavelength generations at ~916 nm and ~1202 nm, respectively. The larger frequency separation for the FWM gain peaks in MCFs with smaller core spacing is due to the increased differences in the intermodal first-order dispersion parameters (D1). With a similar value of D2, the increase in D1 can shift the FWM gain peaks away from the pump frequency, as indicated in Table 5.1.

5.3.2 Simulations and the impact of Raman scattering

The analysis of phase-matching conditions discussed in section 5.3.1 indicates that four-wave mixing and wavelength conversion can effectively achieved in the MCFs. In this section, numerical simulations of the MM-NLSEs are conducted using the dispersion parameters and Kerr coefficients of supermodes in 1m-long MCFs. Here, the pump (wavelength 1040 nm) is evenly coupled into all supermodes with each mode containing a power of 2 kW. Background noise added to the input spectrum is amplified by FWM induced modulation instability. The gain spectra from numerical simulations and analytical results derived from Eq. (2.3.31) are compared. Detailed methodologies for obtaining the numerical and analytical gain are provided in section 2.3.2. Additionally, the impact of Raman scattering on FWM processes is investigated by comparing simulations that exclude and include the Raman contribution.

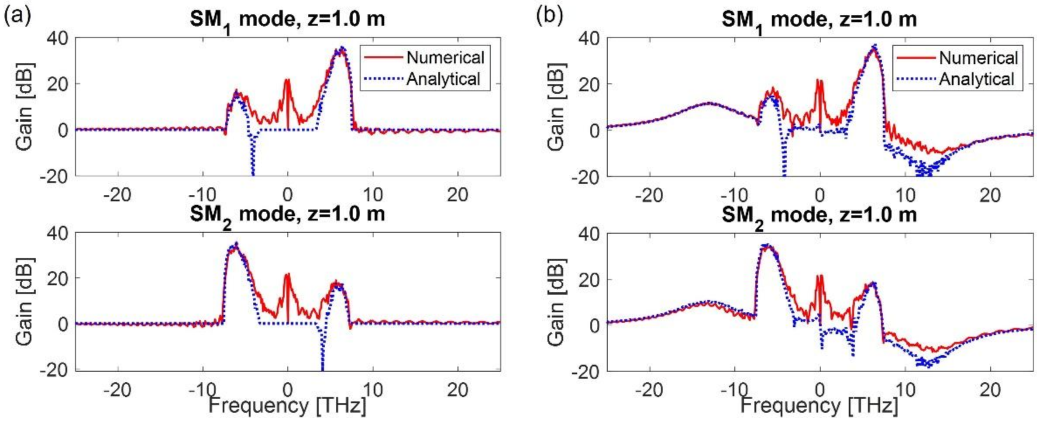

Figure 5.10 Comparison between the numerical and analytical gain spectra by solving the MM-NLSEs for a 1m-long DCF fibre, with Raman scattering neglected (a) and included (b).

Figure 5.10(a) compares the numerical and analytical gain spectra for the DCF. The gain peak is centred around 6.5 THz for the SM_1 mode and -6.5 THz for the SM_2 mode, closely matching the predicted ±6.7 THz from the phase-matching condition calculations in Figure 5.6(b). The slight shift in the FWM gain peaks results from the contributions of self-phase modulation and cross-phase modulation, as discussed in section 5.2.2. When the Raman contribution is included, as shown in Figure 5.10(b), the gain spectrum appears as a superposition of the FWM gain spectrum and a Raman gain spectrum. The maximum gain remains similar regardless of the inclusion of the Raman contribution, owing to the effective separation of the FWM gain peaks and the Raman gain peaks. It is worth noting that the numerical results align well with the analytical results.

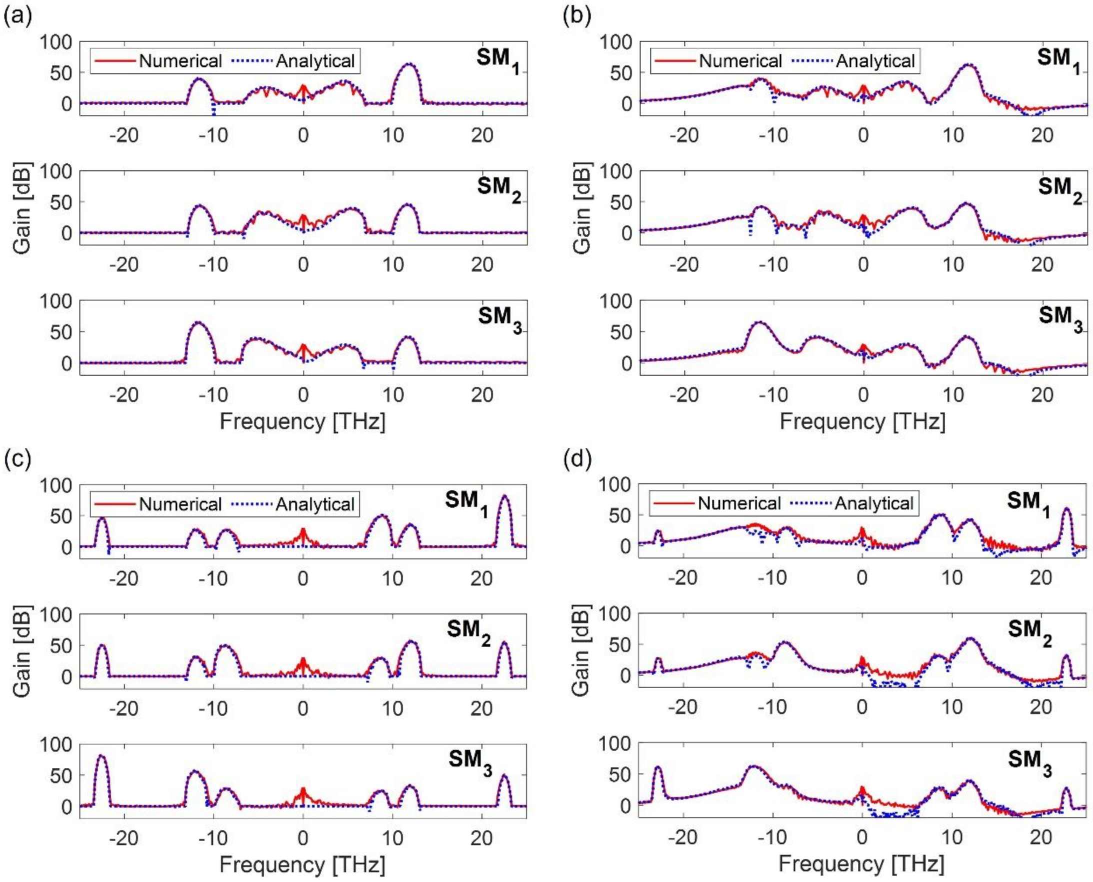

Figure 5.11 Comparison between the numerical and analytical gain spectra by solving the MM-NLSEs for 1m-long TCF fibres: (a),(b) core diameter is 5 μm and core spacing is 10 μm, and (c),(d) core diameter is 4 μm and core spacing is 8 μm, with Raman scattering neglected ((a),(c)) and included ((b),(d)).

Followingly, Figure 5.11 presents the comparison between the numerical and analytical gain spectra for two TCFs with different core diameters and core spacings, demonstrating a good alignment between the numerical and analytical results in each case. Figure 5.11(a) shows the FWM gain spectrum of each supermode in the TCF with a core diameter of 5 μm and a core spacing of 10 μm. The SM_1 mode shows four gain peaks at relative frequencies of ±12 THz and ±4.7 THz. The SM_2 mode has four gain peaks at relative frequencies of ±11.8 THz, 5.6 THz, and -4.5 THz. The SM_3 mode exhibits four gain peaks at relative frequencies of -12 THz, ±5.5 THz, and 11.8 THz. These FWM gain peaks are close to the predictions shown in Figure 5.7(b), with slight frequency shifts due to the contribution of phase modulations. Another notable difference between the gain spectrum and the predictions in Figure 5.7(b) is the number of gain peaks. For instance, the SM_1 mode has gain at higher relative frequencies of 5.6 THz (12 THz) when only considering its FWM with the SM_2 (SM_3) mode in Figure 5.7(b). However, the gain spectra in Figure 5.11(a) reveal that the SM_1 mode actually has four gain peaks at both lower (-12 THz and -4.7 THz) and higher frequencies (12 THz and 4.7 THz) when considering the FWM processes involving all the three modes. This discrepancy indicates that the interactions among all the frequencies and modes can modify the FWM gain spectra, resulting in an output that differs from what would be expected if only two modes were considered independently.

Similarly, using the TCF with a core diameter of 4 μm and a core spacing of 8 μm, six gain peaks are observed at frequencies of ±22.5 THz, ±12 THz, and ±9 THz for each supermode, as shown in Figure 5.11(c). These gain peaks closely align with the predictions in Figure 5.7(d) though with slight frequency shifts. The frequency separation in the gain spectrum is larger when using the fibre with a smaller core diameter and core spacing. When including Raman scattering, as shown in Figure 5.11(b) and (d), the gain spectrum exhibits noticeable changes, particularly at lower frequencies. The SM_3 mode shows dominant gain around -12 THz among the three supermodes, indicating that the Raman scattering benefits this mode when its FWM gain spectrum overlaps with the Raman gain spectrum. Specifically, the SM_3 mode exhibits FWM gain at the frequency of -12 THz due to interaction with the SM_1 mode in Figure 5.11(b) and has FWM gain at this frequency when interacting with the SM_2 mode in Figure 5.11(d).

The gain spectra for the supermodes in two 4CFs are displayed in Figure 5.12. Figure 5.12(a) shows the FWM gain spectrum for the fibre with a core diameter of 5 μm and a core spacing of 10 μm. Several gain peaks are obtained at relative frequencies of ±17 THz, ±13 THz, and ±7 THz across different modes, with the maximum frequency separation occurring in the SM_1 mode at 17 THz and the SM_4 mode at -17 THz. By adding the Raman contribution, Figure 5.12(b) illustrates that the SM_3 mode exhibits dominant gain among the four modes at the frequency around -13 THz. This dominance results from the overlap between the Raman gain spectrum and the FWM gain of the SM_3 mode when interacting with the SM_1 mode. Figure 5.12(c) displays the gain spectrum for the 4CF with a core diameter of 4 μm and a core spacing of 8 μm. The FWM gain peaks are more widely separated compared to Figure 5.12(a), with gain peaks located at relative frequencies of ±31 THz, ±24.7 THz, ±16 THz, and ±6.1 THz. The maximum frequency separation occurs in the SM_1 mode at 31 THz and the SM_4 mode at -31 THz. In addition, Figure 5.12(d) shows that the SM_4 mode has dominant gain among the four modes at the frequency around -16 THz, resulting from the overlap of the Raman gain spectrum and the FWM gain spectrum related to the interaction between the SM_2 and SM_4 modes. Consequently, the SM_2 mode exhibits dominant gain among the four modes at a frequency of ~16 THz.

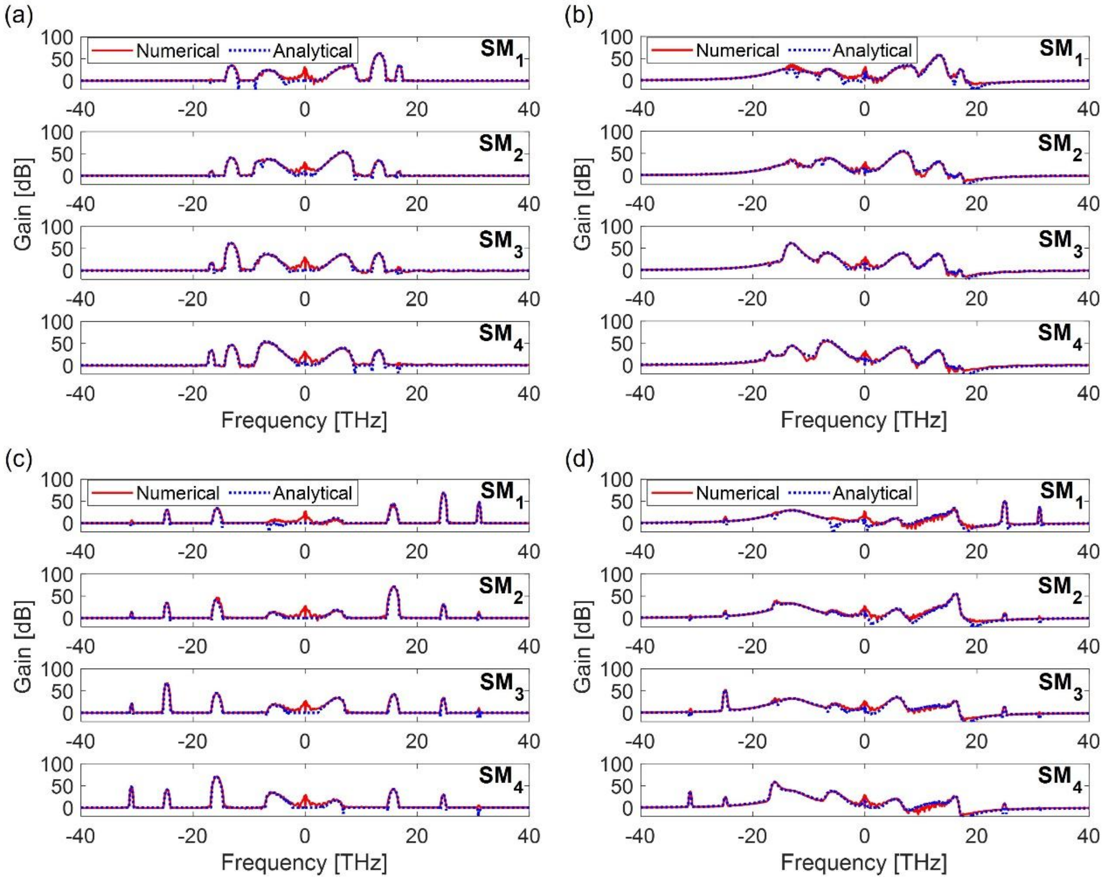

Figure 5.12 Comparison between the numerical and analytical gain spectra by solving the MM-NLSEs for 1m-long 4CF fibres: (a),(b) core diameter is 5 µm and core spacing is 10 µm, and (c),(d) core diameter is 4 µm and core spacing is 8 µm, with Raman scattering neglected ((a),(c)) and included ((b),(d)).

Lastly, the gain spectra for the supermodes in the 7CFs are compared in Figure 5.13. Figure 5.13(a) shows the FWM gain spectrum for the fibre with a core diameter of 5 µm and a core spacing of 10 µm. Several gain peaks are obtained at relative frequencies of ±22.8 THz, ±20.5 THz, ±17 THz, ±14 THz, ±7.6 THz, and ±4.7 THz across different modes. The maximum frequency separation occurs in the SM_1 mode at 28 THz and in the SM_7 mode at -28 THz. When the input pump power is equal across all supermodes, the output from the TCF shows maximum gain in the SM_2 mode and SM_3 mode at the frequency of 7.6 THz, and in the SM_5 and SM_4 modes at the frequency of -7.6 THz. By adding the Raman contribution, Figure 5.13(b) illustrates that the SM_7 mode exhibits dominant gain among the seven modes at the frequency around -14 THz. This dominance results from the overlap between the Raman gain spectrum and the FWM gain of the SM_7 mode during its interaction with the SM_2 and the SM_3 modes.

Figure 5.13(c) presents the gain spectrum for the 7CF with a core diameter of 4 µm and a core spacing of 8 µm. The FWM gain peaks are more widely separated compared to Figure 5.13(a), with gain peaks located at relative frequencies of ±39.1 THz, ±35.6 THz, ±31 THz, ±27 THz, ±17.8 THz, ±13.5 THz, ±9.5 THz, and ±3.8 THz. The maximum frequency separation is observed in the SM_1

mode at 39.1 THz and in the SM_7 mode at -39.1 THz. The maximum gain occurs at frequencies of ±17.8 THz in the SM_2, SM_3, SM_4, and SM_5 modes, where FWM interactions involve the SM_2 and the SM_5 modes as well as the SM_3 and SM_4 modes. Furthermore, Figure 5.13(d) indicates that the SM_4 and SM_5 modes maintain dominant gain among the seven modes at the frequency around -18 THz, even with the inclusion of Raman scattering.

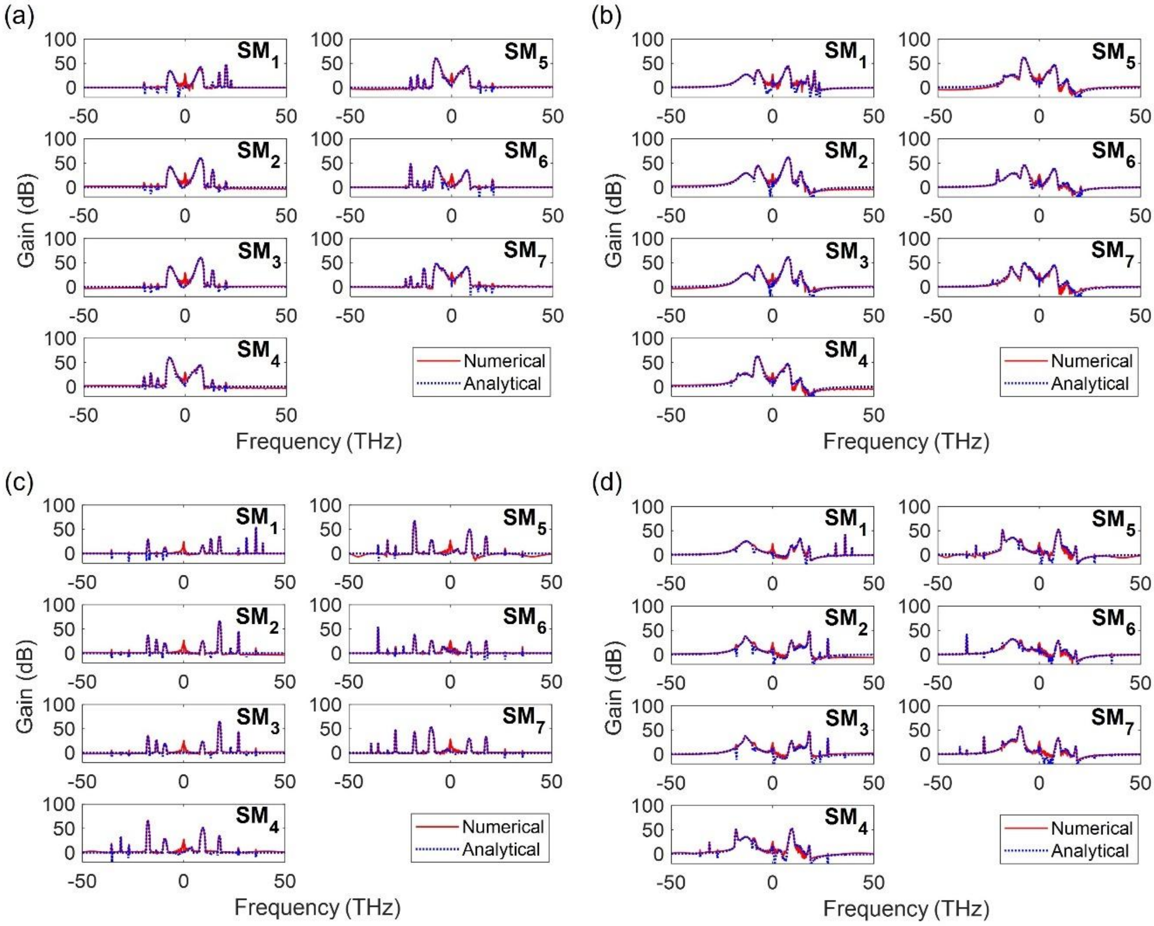

Figure 5.13 Comparison between the numerical and analytical gain spectra by solving the MM-NLSEs for 1m-long 7CF fibres: (a),(b) core diameter is 5 μm and core spacing is 10 μm, and (c),(d) core diameter is 4 μm and core spacing is 8 μm, with Raman scattering neglected ((a),(c)) and included ((b),(d)).

5.4 FWM and wavelength conversion in homemade multicore fibres

5.4.1 Experimental setup and homemade MCFs

An experimental investigation of four-wave mixing and wavelength conversion in multicore fibres was conducted using several homemade multicore fibres, designed as detailed in section 5.3.1. Figure 5.14(a) illustrates the experimental setup used to measure wavelength and supermode conversion in the MCFs, with the cross-sections of the homemade fibre presented in Figure 5.14(b). The pump source for the MCFs was the same MOPA system employed in Chapters 3 and

4, operating at a wavelength of 1040 nm with 500 ps pulses at an 800 kHz repetition rate. The input power, polarization state, and mode composition of the pump were controlled using HWPs and an SLM. Amplified spontaneous emission (ASE) and background noise beside the pump wavelength act as probes, which can be amplified by FWM or Raman gain during propagation through the MCFs. The output beam was directed to a power meter, and a sample was monitored with a camera and an optical spectrum analyser (OSA) to measure intensity profiles and spectra, respectively. A tuneable bandpass filter was used to filter the output at specific wavelengths. Mode decomposition over the supermodes was performed for the pump, signal, and idler based on the far-field intensity profiles.

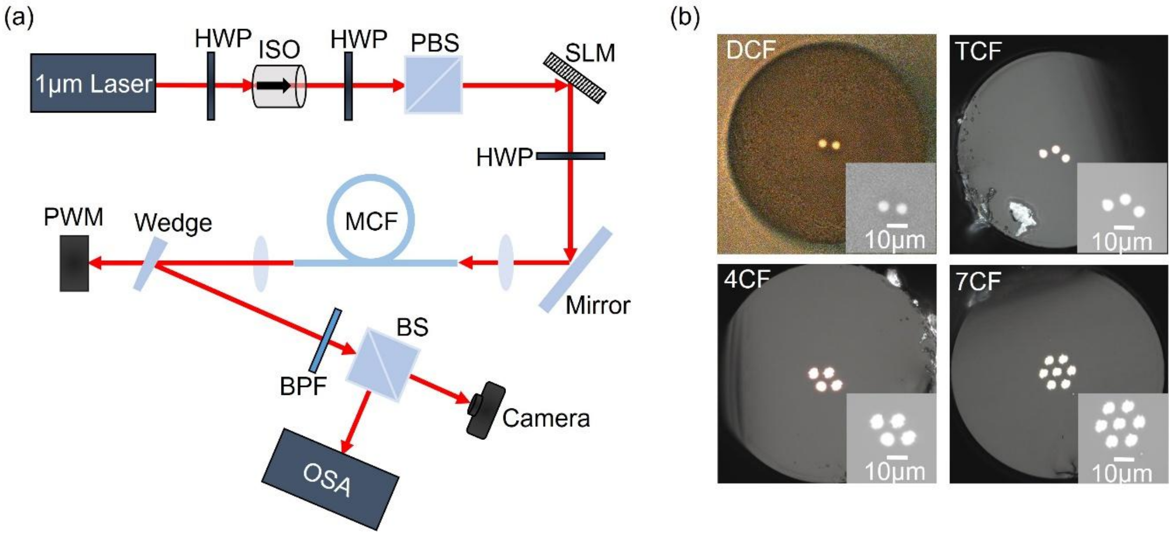

Figure 5.14 (a) Schematic of experimental setup to measure the four-wave mixing and wavelength conversion in MCFs. HWP: half-wave plate; ISO: isolator; PBS: polarization beam splitter; SLM: spatial light modulator; PM: power meter; BPF: bandpass filter; BS: beam splitter; OSA: optical spectrum analyser. (b) Cross-sections of homemade MCFs.

The homemade MCFs were fabricated from the same preform used for the DCF and TCF. Therefore, the MCFs have similar core-to-cladding refractive index difference. Table 5.2 provides details about these fibres, including the TCF, 4CF, and 7CF, which were fabricated with different core diameters and core spacings to explore variations in FWM as predicted by simulations. The core diameters and core spacings were measured by launching light from a white-light source (Bentham WLS100) into one end of the fibre and then imaging the other end with a microscope.

The coupled MCFs reported here have core arrangements and relative core separations (the ratio between core spacing and core diameter) similar to those reported in optical transmission experiments[153-155]. It is worth mentioning that the TCF, 4CF, and 7CF were fabricated from a single fibre preform using the stack and draw technique[156], as they have cores arranged in a similar pattern. The fibre preform consists of three segments, each containing 3, 4, and 7 core rods, respectively. Consequently, each 1/3rd portion of the preform results in fibre configurations with 3, 4, and 7 cores, respectively. The additional benefit to this fabrication approach is that all three fibre configurations are drawn from the same preform, the cores are naturally aligned and the fibre outside diameter will be consistent across the configurations, and hence inter-configuration splicing can be relatively easily achieved.

Table 5.2 Information of the homemade MCFs

		Core diameter (μm)	Core spacing (μm)	Cladding diameter (μm)
DCF	A1664	5.0±0.1	9.4	140.2
TCF	S01	5.0±0.15	9.4	137.9
	S1	4.6±0.14	7.4	110.5
4CF	S5	4.8±0.04	9.3	138.6
	S3	4.0±0.13	7.4	111.5
7CF	S7	4.7±0.05	9.4	137.9
	S9	4.4±0.1	7.4	111

5.4.2 Wavelength and supermode conversion in DCF

The wavelength and supermode conversion in the DCF were measured by using a 1m-long DCF at a pump power of ~6 kW. Figure 5.15(a) displays the input and output spectra when the pump is coupled only into the SM_2 mode. In this case, Raman scattering is the dominant nonlinear process compared to FWM, with the Raman peak (P_a at the wavelength of 1087 nm) exhibiting a similar mode composition to the pump, mainly in the SM_2 mode, as shown by the beam profiles. When the pump is coupled with a combination of modes, FWM becomes more prominent than Raman scattering. Figure 5.15(b) presents the input and output spectra when the pump is coupled with ~30% SM_1 mode and ~70% SM_2 mode, as determined by mode decomposition of the pump. Two peaks appear at wavelengths of 1016 nm (P_b) and 1064 nm (P_c), resulting from intermodal FWM between the SM_1 and SM_2 modes. By inserting a bandpass filter with a 3 dB bandwidth of ~2 nm, the beam profiles at P_b and P_c were measured. In agreement with the theoretical predictions, the SM_1(SM_2) mode turns out to be dominant at 1016 nm (1064 nm), as confirmed by the measured beam profiles. This demonstrates that different supermodes are amplified in the signal and idler, enabling wavelength-dependent supermode conversion. It is worth noting that the experiments fit well with the simulations of the MM-NLSEs using the experimental parameters, including pulse width, peak power, fibre length, and pump mode composition. Figure 5.15 (a) and (b) illustrate that the relative strength between intermodal FWM and Raman scattering can be adjusted by controlling the mode composition of the pump.

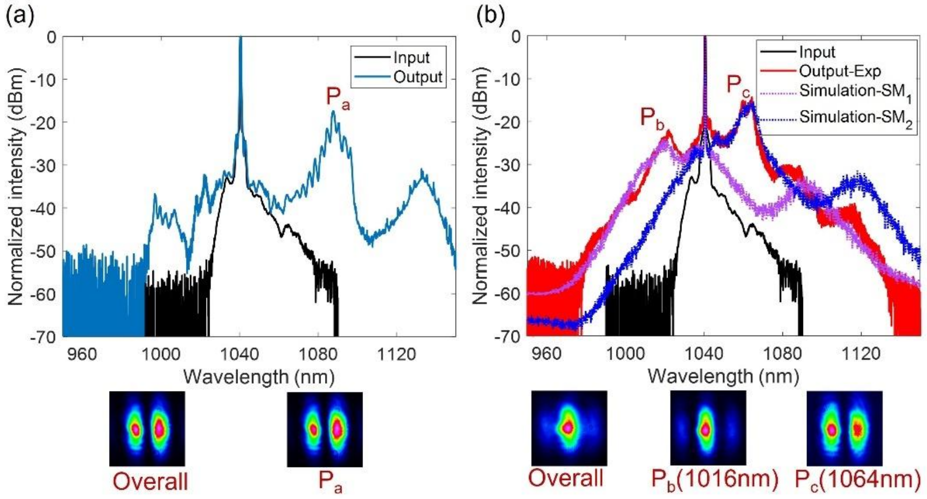

Figure 5.15 Raman and FWM processes measured in the DCF. (a) Raman scattering when pumping with a single supermode: the input and output spectra of a 1m-long DCF with the associated beam profiles. (b) FWM between two supermodes: the input and output spectra of a 1m-long DCF coupled with a combination of modes, in the comparison with the simulation. The below intensity profiles are the output of the overall spectrum and at two FWM peaks (P_b and P_c).

5.4.3 Wavelength and supermode conversion in TCF

The wavelength and supermode conversion in the TCF were investigated using a 3m-long TCF at a peak power of ~2 kW. The TCF used in the experiments is cut from S1 (see Table 5.2) and features a core spacing of ~8 μm. Figure 5.16 presents various output spectra and filtered beam profiles under different pump coupling conditions. In these experiments, the input beam is selectively coupled into one of the three cores of the TCF to excite a combination of supermodes in the pump. By moving or bending the fibre at different positions, the pump coupling conditions could be adjusted. In Figure 5.16(a), FWM peaks are observed at wavelengths of 1004 nm and 1077 nm, along with their cascaded peaks at 944 nm, 972 nm, 1119 nm, and 1158 nm. The beam profiles measured at 1004 nm and 1077 nm correspond to the SM$_1$ mode and the SM$_2$ mode of the TCF, respectively (see Figure 3.23). The frequency difference between the pump and the signal/idler is ±10 THz, which closely aligns with the estimated ±9 THz frequency separation for FWM between the SM$_1$ and SM$_2$ modes in Figure 5.11(c). The slight discrepancy between the experimental and simulation can be attributed to changes in the phase-matching conditions due to variations in fibre geometry or coiling of the fibre.

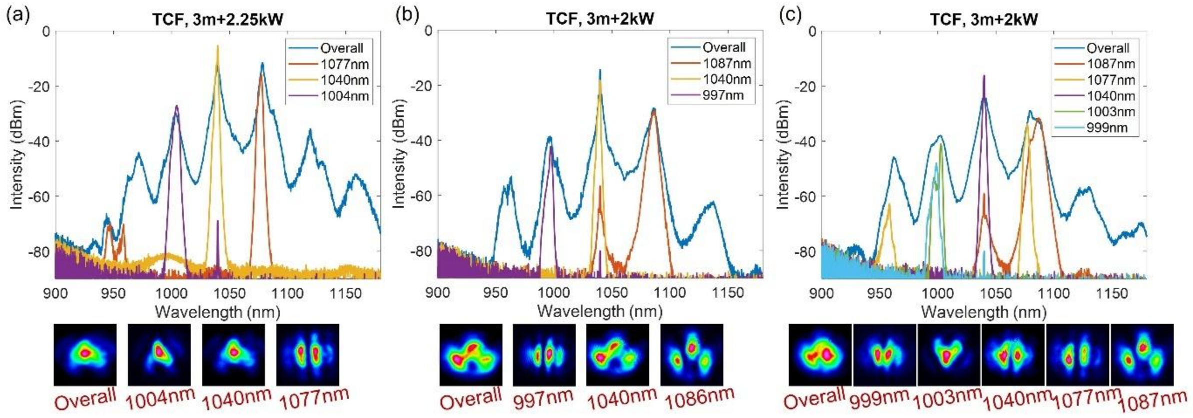

Figure 5.16 FWM and wavelength conversion in the TCF under different pump coupling conditions, along with the output beam profiles after a tuneable bandpass filter. (a) Output spectrum from a 3m-long TCF at a peak power of 2.25 kW, with two FWM peaks (filtered out using the BPF) centred at wavelengths of 1004 nm and 1077 nm. (b) Output spectrum from the same TCF at a peak power of 2 kW, with two FWM peaks centred at wavelengths of 997 nm and 1087 nm. (c) Output spectrum from the same TCF with four FWM peaks at wavelengths of 999 nm, 1003 nm, 1077 nm, and 1087 nm.

Figure 5.16(b) displays the results of another measurement where the pump mode composition was altered. FWM peaks are observed at wavelengths of 997 nm and 1087 nm, along with their cascaded peaks at 957 nm and 1138 nm. The beam profiles measured at 997 nm and 1077 nm correspond to the SM_2 mode and the SM_3 mode of the TCF, respectively. The frequency separation from the pump frequency is ±12.5 THz, closely aligning with the estimated ±12 THz for FWM between the SM_2 and SM_3 modes in Figure 5.11(c).

Subsequently, further adjustment of the pump coupling conditions demonstrates wavelength-dependent conversion to different supermodes from the same pump in the TCF, as shown in Figure 5.16(c). The SM_1 mode emerges at the wavelength of 1003 nm, the SM_2 mode is observed at 1077 nm and 999 nm, and the SM_3 mode appears at 1087 nm, as indicated by the filtered beam profiles. However, FWM between the SM_1 and SM_3 modes, which is estimated to have a relative frequency of ±22.5 THz, is not observed in the experiments. This could be attributed to ineffective pump coupling over these two modes.

5.4.4 Wavelength conversion in 4-core and 7-core fibres

With MCFs featuring more cores, the nonlinearity decreases due to increasing mode field effective areas. Consequently, longer fibres are used to measure wavelength and supermode conversion for the 4CF and 7CF. Figure 5.17 presents the measurements obtained using 4m- and 10m-long 4CFs with a core spacing of ~8 µm (cut from S3 in Table 5.2). Figure 5.17(a) summarizes the output spectra, displaying several FWM peaks under different pump coupling conditions.

Similar to the TCF experiments, the pump coupling conditions are modified by selectively coupling the input beam into one of the four cores of the 4CF or by manipulating the fibre's position or bending it. The observed FWM peaks are at wavelengths of 953 nm and 1145 nm (±26.3 THz frequency separation from the pump), 956 nm and 1139 nm (±25.2 THz), 996 nm and 1088 nm (±12.7 THz), 1016 nm and 1065 nm (±6.7 THz), and 985 nm and 1102 nm (±16.1 THz).

Specifically, Figure 5.17(b) shows the FWM peaks observed at wavelengths of 1016 nm and 1065 nm, along with their cascaded peaks at 995 nm and 1089 nm. The beam profiles measured at 1016 nm and 1065 nm resemble the SM$_3$ mode and the SM$_4$ mode of the 4CF, respectively, as inferred from the supermode distribution in Figure 5.8. The corresponding frequency separation from the pump, ±6.7 THz, closely matches the simulation result of ±6.1 THz for FWM between the SM$_3$ and SM$_4$ modes, as shown in Figure 5.12(c). Followingly, by adjusting the pump coupling condition, FWM peaks at 953 nm and 1145 nm are measured, with the beam profile at 1145 nm shown in Figure 5.17(c). The filtered output at 1145 nm resembles the SM$_4$ mode, aligning with the simulation in Figure 5.12(c), which indicates the largest frequency separation in the FWM process involving the SM$_1$ mode at a shorter wavelength and the SM$_4$ mode at a longer wavelength. The beam profile at 953 nm is not provided due to the limited tuning range of the BPF.

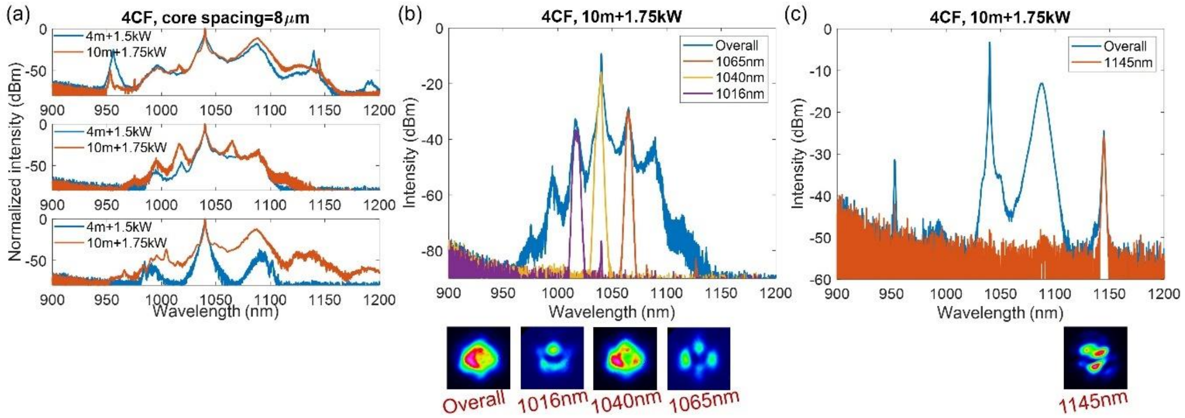

Figure 5.17 FWM and wavelength conversion in the 4CF with core spacing of ~8 μm. (a) Output spectra from a 4m-long and a 10m-long 4CF under different pump coupling conditions. (b) Output spectrum from the 4CF at a peak power of 1.75 kW, with two FWM peaks centred at wavelengths of 1016 nm and 1064 nm and the associated beam profiles after a tuneable bandpass filter. (c) Output spectrum from the 4CF and the filtered output beam profiles at the peak around 1145 nm.

In comparison, Figure 5.18 illustrates measurements conducted using a 5m-long 4CF with a core spacing of ~10 μm, cut from S5 as listed in Table 5.2. By adjusting the pump coupling conditions, several FWM peaks are observed at wavelengths of 995 nm, 1000 nm, 1012nm, and 1070 nm, corresponding to frequency separations from the pump by -13 THz, -11.5 THz, and ±8 THz. These values closely align with simulations depicted in Figure 5.12(a). The FWM peaks at relative frequencies of ±17 THz were not observed during the experiments, which could be attributed to challenges in effectively exciting specific combinations of supermode. Specifically, some supermodes may not have been sufficiently excited when coupling the pump light into individual fibre cores. Additionally, linear mode coupling, induced by fibre macro-bending, may have further influenced the supermode excitation process. However, due to the challenges in effectively exciting supermodes through pump coupling into individual fibre cores, FWM peaks with relative frequencies of ±17 THz are not observed during the experiments.

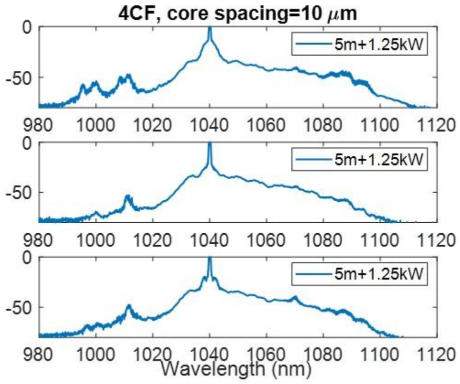

Figure 5.18 FWM and wavelength conversion in a 5m-long 4CF with a core spacing of ~10 μm under different pump coupling conditions at a peak power of 1.25 kW.

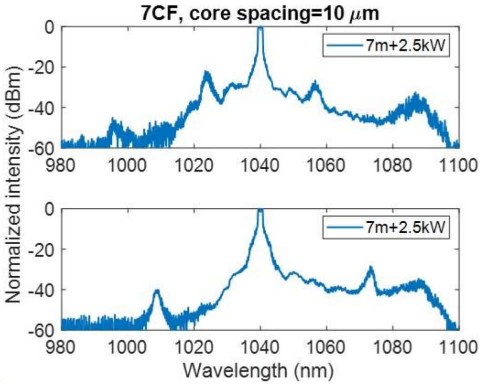

Figure 5.19 FWM and wavelength conversion in a 7m-long 7CF with a core spacing of ~10 μm under different pump coupling conditions at a peak power of 2.5 kW.

Followingly, FWM and wavelength conversion in 7CFs are investigated using 7m-long 7CFs with core spacings of ~10 μm (cut from S7 in Table 5.2) and ~8 μm (cut from S9 in Table 5.2). Figure 5.19 shows two results obtained under different pump coupling conditions at a peak power of 2.5 kW. FWM peaks are observed at wavelengths of 1009 nm, 1024 nm, 1057 nm, and 1073 nm, corresponding to frequency separations from the pump by ±4.6 THz and ±8.9 THz. Additionally, a Raman peak at 1088 nm and a peak at 996 nm generated by FWM between the pump and the Raman peak are also observed. It is worth noting that these experimental results are consistent with the simulations shown in Figure 5.13(a) and (b), where dominant FWM gains occur at relative frequencies of ±4.7 THz and ±7.6 THz for each supermode. In addition, the random excitation of supermodes when light is coupled into one of the seven cores may result in insufficient excitation of some supermodes, thereby hindering clear observation of FWM results. Achieving precise control over supermode excitation for the pump is crucial to reliably obtain desired FWM peaks.

Figure 5.20 demonstrates the output spectra from a 7CF with a core spacing of ~8 μm under various pump coupling conditions at a peak power of 4.5 kW. The pump is coupled with different mode compositions, as illustrated by the FF beam profiles for the overall spectra. However, throughout all instances, the dominant features are the Raman peak at 1089 nm and the peak at 995 nm resulting from FWM between the Raman peak and the pump. The filtered FF and NF beam profiles around 1089 nm indicate changes in mode composition at the Raman peak, aligning closely with one of the individual supermodes (as compared with the supermode distributions in Figure 5.9), denoted by "SM_X" next to the beam profiles in Figure 5.20. This observation suggests that in these measurements, the Raman gain exceeds the FWM gain. Notably, FWM peaks at other wavelengths or frequencies are not observed due to low FWM gains resulting from insufficient excitation of the corresponding supermodes in the pump. Additionally, advanced coupling techniques can be employed to improve efficient coupling into specific supermode combinations. For instance, a space-division multiplexer provided by Cailabs can offer high extinction-ratio (>20 dB) coupling into individual spatial modes[157].

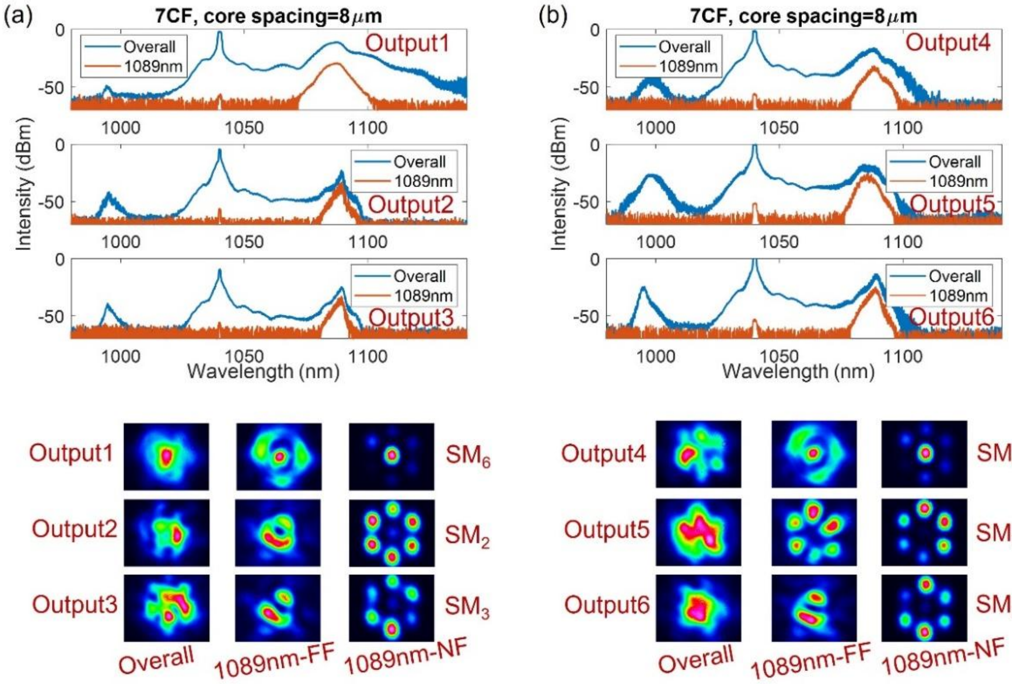

Figure 5.20 Wavelength and supermode conversion in the 7CF with a core spacing of ~8 μm under different pump coupling conditions at a peak power of 4.5 kW. Raman scattering and its FWM with the pump are dominant in each case, with below beam profiles showing the overall output and the filtered output around the Raman peak.

5.5 Conclusions

In this chapter, four-wave mixing and wavelength conversion in MCFs are investigated. Starting with a review of the mechanisms governing FWM in optical fibres, the phase-matching conditions and theoretical calculations are introduced to estimate key parameters such as FWM gain peaks and bandwidth, considering the diverse dispersion characteristics inherent to different fibres. An important focus of this study is the exploration of how the involvement of multiple modes and frequencies influences the dynamics of FWM processes. Both theoretical analyses and numerical simulations confirm that the FWM gain spectra can be significantly modified by the inclusion of additional modes and frequencies. By adjusting the pump mode composition, pump power, Kerr coefficients, and dispersion parameters, the FWM gain spectrum can be tailored in terms of gain peak frequency, maximum gain, and gain distributions across various modes. In addition, the impact of the Raman effect on FWM processes is explored, particularly when the Raman gain spectrum overlaps with the FWM spectrum.

Followingly, the theoretical estimation of FWM gain peaks in several MCFs is demonstrated by calculating the phase-matching conditions between supermodes in different fibre designs, including DCF, TCF, 4CF, and 7CF. Simulations of the FWM gain spectra in these MCFs are presented, along with comparisons when the Raman scattering effect is considered. Finally, these MCFs are fabricated with diverse core diameters and core spacings, enabling experimental investigation of FWM and wavelength conversion using a pump wavelength at 1040 nm. Table 5.3 summarizes the main results achieved, with comparisons between simulation predictions and experimental results across different fibres. Generally, the experiments are consistent with simulations in terms of the relative frequencies of FWM peaks and the corresponding involved modes. These outcomes indicate the feasibility of achieving specific wavelength conversions or wavelength-dependent mode conversions through tailored fibre designs. Indeed, control over phase-matching conditions among supermodes can be achieved by adjusting parameters such as the number of cores, core diameters, and core spacings in these fibres.

Table 5.3 Summary of the FWM results for MCFs

Fibre		Relative frequency (THz) and the corresponding modes for FWM peaks	With a pump wavelength of 1040 nm
		Simulation	Experiment
DCF	Core spacing=10μm	±6.5 (SM_1 and SM_2)	±6.5 (SM_1 and SM_2)
TCF	core spacing=8μm	±9 (SM_1 and SM_2), ±12 (SM_2 and SM_3),	±10 (SM_1 and SM_2), ±12.5 (SM_2 and SM_3),

		±22.5 (SM_1 and SM_3)	
4CF	Core spacing=10μm	±7 (SM_2 and SM_4), ±13 (SM_1 and SM_3), ±17 (SM_1 and SM_4)	±8, -11.5, -13
	Core spacing=8μm	±6.1 (SM_3 and SM_4), ±16 (SM_2 and SM_4), ±24.7 (SM_1 and SM_3), ±31 (SM_1 and SM_4)	±6.7 (SM_3 and SM_4), ±12.7, ±16.1, ±25.2, ±26.3
7CF	Core spacing=10μm	±4.7 (SM_4 and SM_7, SM_5 and SM_7), ±7.6 (SM_2 and SM_5, SM_3 and SM_4), ±14, ±17, ±20.5 (SM_1 and SM_6), ±22.8 (SM_1 and SM_7)	±4.6, ±8.9,
	Core spacing=8μm	±3.8 (SM_5 and SM_6), ±9.6, ±13.5, ±17.8 (SM_2 and SM_5, SM_3 and SM_4), ±27, ±30.9(SM_1 and SM_4, SM_1 and SM_5), ±35.5 (SM_1 and SM_6), ±39.1 (SM_1 and SM_7)	

Notes: The results reported in this chapter have been selectively published (see LoP3 and LoP10 in the List of Publications). These two paper are conference papers where we reported the wavelength conversion in coupled multicore fibres. The main results of this chapter have not been published yet, and we are working on the manuscript. For the content in this chapter, the experiments, simulations, development of derivations and code were my work; the 3-core, 4-core, and 7-core fibres were fabricated by Ian Davidson from the Optoelectronics Research Centre; the dual-core fibres used in the experiments were fabricated by Jayanta Sahu from the Optoelectronics Research Centre; this project was supervised by Massimiliano Guasoni and David J. Richardson from the Optoelectronics Research Centre.

Chapter 6 Reconfigurable spatial beam shaping from a multicore fibre amplifier

6.1 Introduction

Structured light[47], defined by spatially controlled distributions of amplitude, phase, and polarization, has become an attractive tool in a wide range of applications, including optical communications[158], optical trapping[159], environmental optics[160], and super-resolution microscopy[161, 162]. This is due to the additional degrees of freedom it offers in shaping the polarization state, phase, and amplitude. In particular, higher-order Poincaré sphere (HOPS) beams [163] with spatially variable polarization and orbital angular momentum (OAM) states are of great interest [47, 164]. The two poles of the HOPS represent the orthogonally circularly polarized vortex beams carrying OAM with opposite topological charges, while the other points on the HOPS can be represented as coherent superpositions of these, including cylindrical vector (CV) beams with spatially varying polarization states (e.g., radial and azimuthal polarization). Various methods have been developed to generate HOPS beams by incorporating appropriate spatial mode shapers either inside or outside of a laser cavity [165-168]. For instance, CV beams can be generated by using inhomogeneous birefringent optics[165] or by the controllable superposition of two orthogonally polarized beams[168]. OAM beams can usually be formed by conversion from fundamental Gaussian beams using an external beam-shaping element, such as a *q*-plate (QP)[166], geometric phase plate[167], meta surface device[169], or SLM[49].

Generating such beams directly from a laser cavity [170-173] allows achieving higher power scaling and efficiency. A few approaches have been implemented to generate HOPS beams with flexible mode selection and high mode purity in solid-state lasers; however, the power scalability is limited by the power-handling performance of the optical mode-selective elements used within the cavity[49]. Alternatively, adaptive spatial beam-shaping techniques have been demonstrated in multimode and multicore fibres [51, 52] based on the MOPA configuration. The adaptive beam-shaping elements are placed prior to the final power amplifier, allowing the amplified beam to be shaped into the desired beam intensity profile without exposing the beam-shaping elements to high power levels. In addition, the coherent combination of multiple parallel fibre lasers has been proposed as a promising way to achieve reconfigurable structured beams with high output powers and has been investigated both theoretically and experimentally[174-176]. Coherent beam combination (CBC) from an MCF amplifier has been demonstrated as an effective way to generate the structured beams[40, 46, 50, 177]. With all uncoupled cores embedded in a single fibre, the MCF amplifier offers many advantages with respect to an array of separate fibre amplifiers, e.g., the use of a common pump beam for all cores and reduced phase drift between cores due to the shared spatial/thermal environment, leading to more compact and stable systems. Nevertheless, the behaviour in the pulsed regime has not yet been properly investigated, where the coherence length of the light is much smaller.

In this chapter, spatial beam shaping is explored in a linear regime. A 6-core Yb-doped MCF is fabricated and employed as the gain medium in the final power amplifier stage in a picosecond pulsed MOPA system. A flexible beam shaper based on a reflective phase-only SLM is employed to adaptively adjust the wavefront and polarization states of the multiple beamlets incident on the individual MCF cores and to achieve the desired complex beam amplitude in the far-field of the MCF output by coherently combining the amplified multiple beamlets. The generation of ps-pulsed LP mode-like beams and HOPS beams (i.e., CV and OAM beams) are experimentally demonstrated with a high mode purity and a high peak power of ~10-14 kW.

6.2 Principle and system design

6.2.1 Coherent beam combination of multicore fibres

An uncoupled N-core MCF behaves as a bundle of single-core fibres where the cores are sufficiently separated to ensure negligible individual mode overlap, and the total electric field at the fibre output can be seen as the sum of the independent beams (under the single-mode approximation):

$$E(x,y,z) = \sum_{j=1}^{N} \boldsymbol{a}_j \, exp\left[-\frac{\left(x-x_j\right)^2+\left(y-y_j\right)^2}{w_0^2}\right] \tag{6.2.1}$$

where $\boldsymbol{a}_j = a_{xj}exp(i\varphi_{xj})\hat{\boldsymbol{x}} + a_{yj}exp(i\varphi_{yj})\hat{\boldsymbol{y}}$ is the complex amplitude of the fundamental Gaussian beam of the *j*-th core, in which $\hat{\boldsymbol{x}}$ and $\hat{\boldsymbol{y}}$ are unit vectors, $a_{x(y)j}$ and $\varphi_{x(y)j}$ are the amplitude and phase of the x(y) component in the *j*-th core, respectively. x_j and y_j are the centre position of the *j*-th core, and w_0 is the effective mode field radius of the individual cores. The electric field in the far-field of this MCF is determined by the interference between the individual beamlets. By properly tailoring the amplitude, phase and polarization of each beamlet from the MCF output, beams with various spatial modes can be shaped in the far-field in a tiled-aperture configuration. For instance, different scalar LP mode beams can be generated when the specific phase relationship is applied to each beamlet, and the most general case is a Gaussian-shape (LP_{01} mode) beam that arises from the in-phase coherent combination of all beamlets, as is shown in Figure 6.1(a). HOPS beams can be synthesized by controlling the relative polarization state and the relative phase of each beamlet. For example, an OAM beam (Figure 6.1(c)) with the topological charge of ℓ can be formed by the superposition of *N* beamlets when the relative phase of the j-th beamlet is set to be $2\pi\ell(1-j)/N$ under the same polarization state, and this beam has a helical phase structure (phase term $exp(i\ell\varphi)$, where φ is the azimuthal angle). In addition, a CV mode beam (Figure 6.1(d)) can be generated in the far-field when each beamlet has a linear polarization state which rotates by an angle of $2\pi(1-j)/N$ from a reference orientation.

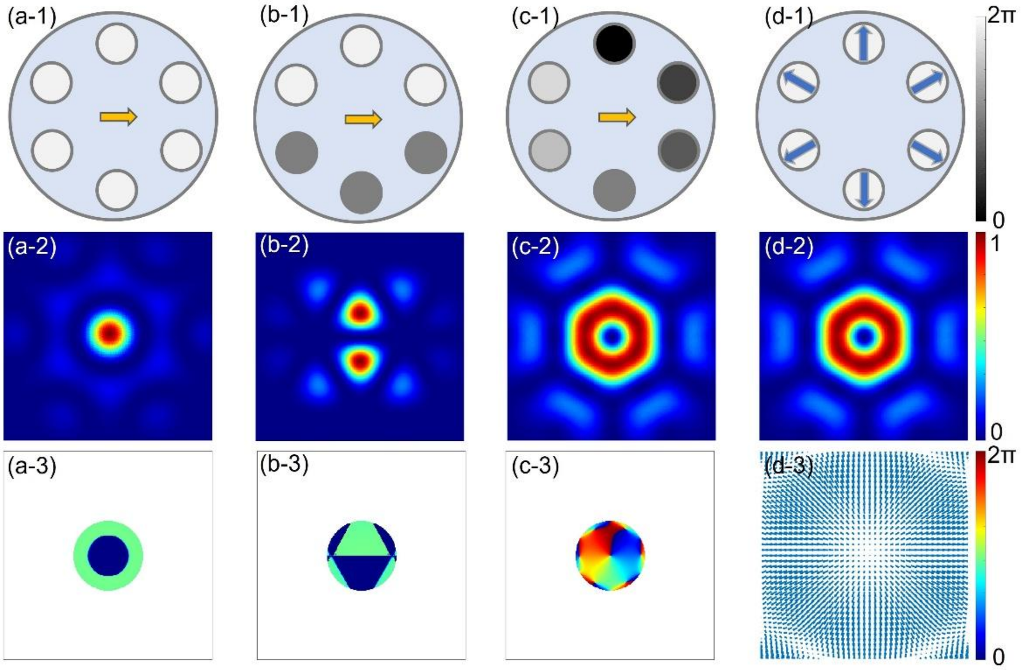

Figure 6.1 CBC from a 6-core fibre. The near-field phase and polarization distributions (a/b/c/d-1) with the corresponding combined intensity distributions (a/b/c/d-2) and phase/polarization distributions (a/b/c/d-3) in the far-field.

6.2.2 Yb-doped 6-core fibre

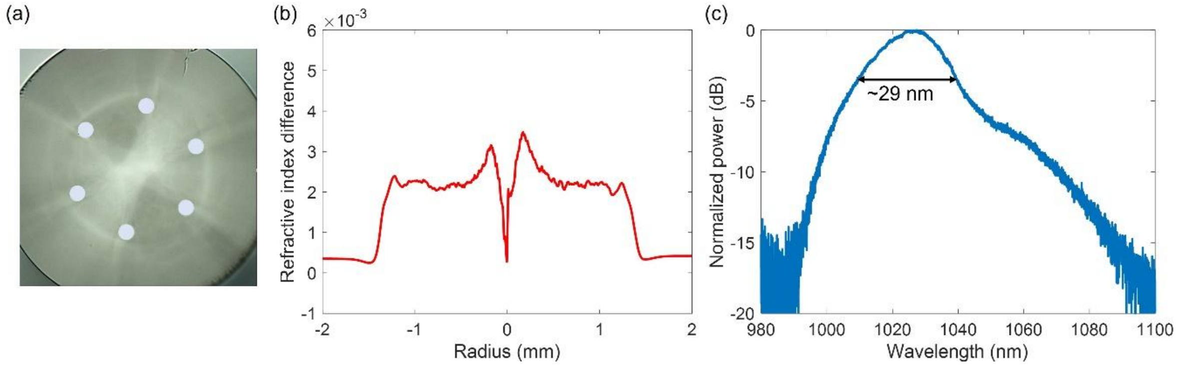

Figure 6.2 (a) Microscopic image of fibre cross-section. (b) Refractive index profile of the fabricated preform. (c) ASE spectrum of the MCF.

A cross-sectional microscope image of the Yb-doped 6-core MCF used in this work is shown in Figure 6.2(a). Starting from a flat-topped step-index Yb-doped fibre preform co-doped with aluminium (Al) and phosphorus (P), the MCF has been fabricated in-house by the stack-and-draw technique. By adding co-dopants such as Al and P, the absorption and emission properties of the

Yb ions can be efficiently controlled [178, 179]. The refractive index profile was measured with a preform analyser, and the refractive index difference between the core and the cladding was measured to be ~0.002, as shown in Figure 6.2(b). The MCF consists of six step-index circular cores in a hexagonal arrangement, and the core-to-core distance is ~50 μm. Each core has a diameter of 12.5 μm with a numerical aperture (NA) of ~0.076; the outer diameter of the fibre is ~220 μm. A low-index acrylate polymer coating was used to provide a double-clad fibre structure. The fibre absorption coefficient was measured to be ~19.7 dB/m at 975 nm, and the ASE spectrum was measured. The ASE spectrum of a 1.3m-long Yb-MCF had an emission peak around 1027 nm with a 3 dB bandwidth of ~29 nm, as shown in Figure 6.2(c).

6.2.3 Experimental setup

A schematic of the experimental setup is depicted in Figure 6.3. A gain-switched laser diode operating at a wavelength of 1035 nm and emitting ~90 ps pulses at a repetition rate of 2.95 MHz, is used as the seed, which is pre-amplified to an average power of ~600 mW. The pre-amplified Gaussian-shaped beam is then split into six beamlets, which are coupled into the individual cores of the Yb-MCF via a beam-shaper consisting of a reflective SLM (Holoeye PLUTO-2-NIR-149) and some polarization diversity optics, which enables independent control of the amplitude, phase, and polarization state of the seed light launched into the individual cores of the MCF. The input beam is collimated by a lens with a focal length of 40 mm and then is divided into two beams with orthogonal polarization states using a PBS. A half-wave plate placed in front of the PBS is used to control the relative power ratio between the two orthogonally linearly polarized beams, and a second half-wave plate is used to align the polarization orientations of the two beams to the SLM. The area of the SLM is divided into two halves to display the phase masks, which split each input beam into six independent Gaussian-shaped beamlets with controlled phase and amplitude. The phase mask represents a multiplex of six independent blazed gratings with the grating period determined by the relative position of the MCF cores. Another half-wave plate and a PBS are used to recombine these orthogonally polarized beams to form six individual Gaussian-shaped beamlets with user-defined polarization, amplitude, and phase in the Fourier plane of a focusing lens.

The shaped input beamlets are first demagnified by a factor of 2 with a pair of lenses (focal length of 1 m and 500 mm), and then passed through an in-house-made free-space polarization-independent isolator with a clear aperture of 8 mm, which prevents any backward-propagating light from damaging the SLM. The isolator consists of two birefringent beam displacers, a Faraday rotator, and a half-wave plate, which was carefully aligned to have a negligible displacement for beams with two orthogonal polarization components at the isolator output, thus ensuring a very low polarization-dependent coupling loss to the MCF. A lens with a focal length of 19 mm is used to couple the six individual beamlets into the individual cores of the Yb-MCF. This fibre is ~1.3 m long and was coiled with a diameter of ~7 cm on an aluminium cylinder to induce high excess losses for the higher-order modes so that each core could effectively act as a single-mode fibre (V number=2.89), ensuring that the output beam of each core maintains a Gaussian shape. Both ends of the Yb-MCF were spliced to silica coreless fibre endcaps with a length of ~1.4 mm and a diameter of ~400 μm to suppress potential parasitic lasing. The input end facet was perpendicularly cleaved for high-quality beam excitation, while the output end facet was polished with an angle of ~8° to suppress unwanted back-reflection. The multimode pump beam (wavelength=975 nm) was free space coupled into the MCF through a dichroic mirror. The insertion loss of the beam-shaper and of the isolator was characterized by means of a passive seven-core MCF having cores arranged in a hexagonal pattern with the same core-to-core distance (50 μm). The passive MCF features an extra core in the centre, and each core has a mode field diameter of ~10 μm with an NA of ~0.12, which is slightly different from the active fibre. Nevertheless, it can be used to assess the insertion loss of the devices. The total insertion loss of the beam-shaper and isolator (measured from the input PM-SMF to the output facet of the passive MCF) was measured to be ~7.6-11.6 dB with some variation between the cores, which is mainly due to imperfect coupling conditions. It is worth mentioning that the beam-shaper was constructed based on a specially designed compact architecture with most of the optical components glued to the mechanics in a Mach-Zehnder interferometer configuration. The coupling efficiency of the individual beamlets into the MCF is quite stable over periods of several hours.

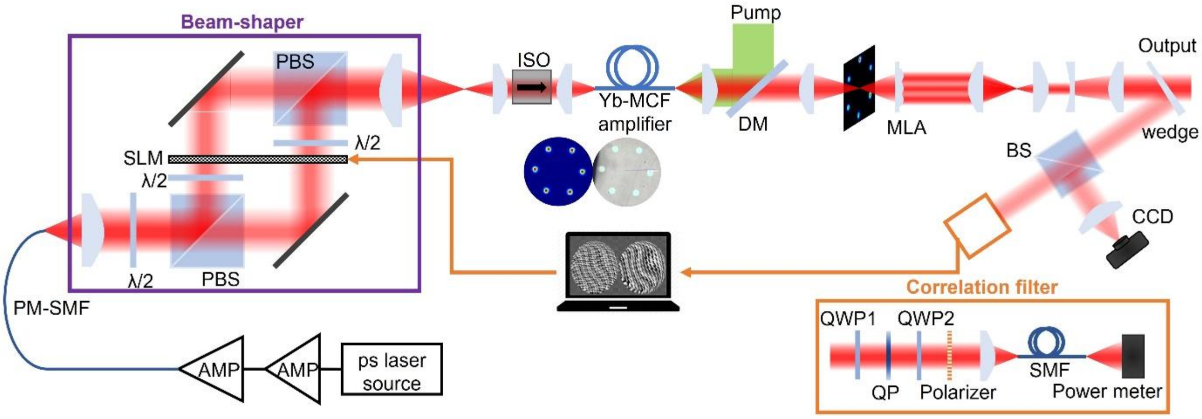

Figure 6.3 Schematic of the experimental setup. AMP: amplifier; PM: polarization-maintaining; SMF: single-mode fibre; PBS: polarization beam splitter; λ/2: half-wave plate; ISO: isolator; DM: dichroic mirror; MLA: microlens array; BS: beam splitter; CCD: charge-coupled device; QWP: quarter-wave plate; QP: *q*-plate.

The output beam from the Yb-MCF amplifier was first magnified by a factor of 10 to achieve a separation of ~500 μm between the neighbouring beamlets to match the lens pitch of the microlens array (MLA). The MLA has a hexagonal arrangement with a focal length of 50 mm, and it collimates the individual beamlets with a beam spot diameter of ~430 μm. Note that the use of MLA can increase the near-field filling factor of the output beamlets; hence, this significantly improves the beam combination efficiency in a tiled-aperture configuration [41, 50]. A spherical lens with a focal length of 200 mm was placed behind the MLA to achieve the CBC, thereby enabling the generation of different spatial beams in the far-field. Afterward, the coherently combined beam is collimated and magnified using a pair of lenses, with a fraction (~2%) imaged on a CCD camera, and a replica beam from the beam splitter passed through a mode correlation filter in order to characterize the quality of the combined beam. A q-plate in combination with two quarter-wave plates and a linear polarizer were used to form the correlation filter for the HOPS beam generation [46, 172]. When the collimated combined beam passes through the correlation filter, the on-axis intensity in the far-field is proportional to the power of the beam within the target mode. The resulting correlation signal is detected by coupling the light into an SMF and measuring the corresponding coupled power. This information is fed back to the computer, and an iterative optimization process (conjugate gradient algorithm [180]) is used to adjust the complex amplitude and polarization of the seed light injected into the individual cores of the MCF via the beam shaper (see Ref. [46] for a more detailed description). The bandwidth of the feedback loop is 4 Hz, determined by the time required to allow the SLM to update the phase mask, to measure the correlation signal, and to perform the associated software-based data processing.

It is worth mentioning that the coherently combined beams were stable and repeatable in the laboratory environment. The system typically took ~10 min to achieve the target beams in the experiments once the correlation filter is properly set and well aligned. Once the optimization process has completed, the generated beam could be well-preserved for at least 10 min with a fixed phase mask on the SLM. However, a certain degree of optical and mechanical drift over time was observed, requiring manual adjustments of specific mounts to optimal optical alignment every few tens of minutes.

6.2.4 Characterization of the MCF amplifier

In a preliminary experiment, the Yb-MCF amplifier was first characterized without implementing any adaptive beam shaping. Figure 6.4(a) shows the measured near-field beam intensity profile of the MCF output with a 10x magnification. The discrepancy in the amplification of each core results from the nonuniform pump absorption and unavoidable seed power variations, as mentioned in the previous section. The differential gain among individual cores is between 0.84 dB and 1.46 dB at different pump powers when sequentially launching light into each core. Figure 6.4(b) displays the average output power of the MCF amplifier (measured before the MLA) as a function of the launched pump power. A maximum output power of ~21.6 W was obtained with a launched pump power of ~35.1 W, corresponding to a slope efficiency of ~71.8% and a gain of

~25.6 dB. The measured spectra of the seed and the output beam at an output power of ~12.3 W (corresponding to a pump power of ~23.3 W) are provided in Figure 6.4(c), with a resolution of 0.5 nm and 0.02 nm, respectively. The output signal has an optical signal to noise ratio (OSNR) of ~26 dB. The 3 dB bandwidth was measured to be ~0.14 nm, and it contains ~70% of the total pulse energy, which is nearly equivalent to that of the seed laser. The FWHM pulse duration of the seed laser was measured to be ~92 ps, and the temporal shape was preserved in the output laser beam, as shown in Figure 6.4(d). It is worth noting that the coherent beam combination experiments were conducted at varying MCF output powers by gradually increasing the pump power. However, the system exhibited relatively high instability when the MCF output power exceeded ~12.3 W. Consequently, the controlled generation of different spatial modes was conducted at the MCF output power of ~12.3 W.

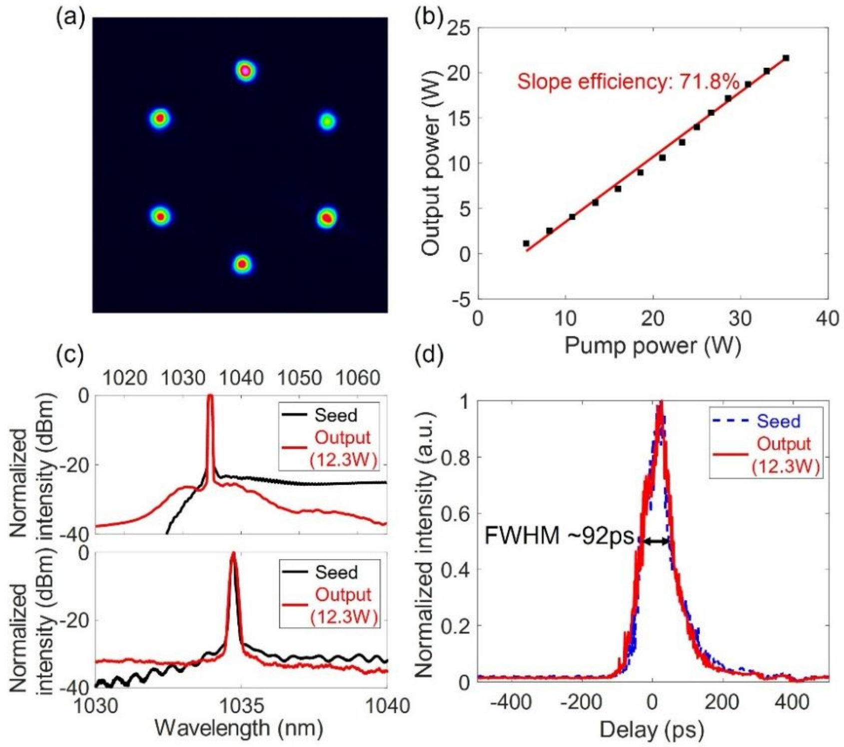

Figure 6.4 Yb-MCF amplifier characterization. (a) Measured near-field intensity distribution of the MCF output. (b) Average output power versus the launched pump power. (c) Measured spectra of the seed and the amplified output at an average output power of ~12.3 W, with a resolution of 0.5 nm (upper) and 0.02 nm (lower). (d) Temporal pulse shapes of the seed and the amplified output at ~12.3 W.

6.3 Controlled generation of linear-polarized modes

6.3.1 Polarization and phase control

When the phase control is not in place, the output beam of the MCF amplifier exhibits severe distortion in the far-field, as shown in Figure 6.5(a). A linear polarizer in combination with an SMF forms the spatial mode correlation filter that provides the correlation signal for the merit function. This finally results in a linearly polarized Gaussian-shaped beam within the main lobe via in-phase CBC, as illustrated in Figure 6.5(b).

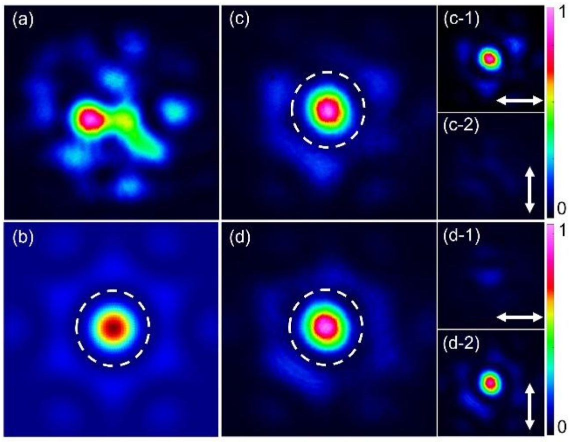

Figure 6.5 Generation of linearly polarized Gaussian beams. (a) Far-field beam profiles without beam shaping. (b) Simulated far-field intensity distribution when all cores are in-phase. (c), (d) Experimentally measured far-field Gaussian beam profiles at the peak power of ~8.14 kW with orthogonal polarization states.

Figure 6.5(c) and (d) demonstrate the corresponding measured beam intensity profiles with a seed signal of ~60 mW and a pump power of ~23.3 W. Figure 6.5(c-1), (c-2) and (d-1), (d-2) show the intensity distributions when the output beams pass through a rotatable linear polarizer, which clearly indicates the linear polarization state. The PER was measured to be ~10 dB. The 2D correlation coefficients [74] of the measured intensity profiles with respect to the theoretical intensity distributions (within the area marked with dashed white lines) are ~98.4% and ~98.1% in Figure 6.5(c) and (d), respectively. The measured beam combining efficiency was ~37.4 % (defined as the ratio of the power contained within the mode region marked with dashed white lines with respect to the total beam power), whereas the corresponding theoretical estimation is ~49%. The discrepancy results from the optical aberrations induced by the slight misalignment of the composite elements in the beam-combining system [46]. The average output power behind the wedge (see Figure 6.3) was ~5.9 W, resulting in an average output power of ~2.2 W, with a peak power of ~8.14 kW for the combined beams (marked region). The power loss from the MCF output to the wedge is mainly due to reflections from the uncoated MLA and wedge as well as the slight mismatch between the MCF output and the MLA.

6.3.2 Generation of the LP modes

The experimental Gaussian-shape beam profiles highly resemble the simulations, indicating that the complex amplitude and polarization of the individual beamlets can be optimized as expected. When a phase-plate is inserted in the correlation filter, different LP mode-like beams can be generated in the far-field. When three adjacent beamlets are in-phase and have a π phase difference with the other three beamlets, a LP_{11} mode-like beam can be obtained, as illustrated in Figure 6.6(a)-(c). In the case of LP_{21} mode generation, only four MCF cores are seeded with light and with specific relative phases, as shown in Figure 6.6(d). Consequently, the output beam profile in the far-field resembles the LP_{21} mode, as indicated by simulation and experimental results presented in Figure 6.6(e) and (f), respectively. The linear polarization of the generated LP modes was confirmed with a PER measurement of ~10 dB. The 2D correlation coefficients of the measured beam profiles in comparison with the simulated profiles are ~97.3% and ~92.0% for the LP_{11} and LP_{21} modes, respectively. The lower correlation of the LP_{21} mode is most likely due to unwanted ASE from the two unemployed cores of the MCF amplifier, which could distort the combined beams. The beam combining efficiencies for the LP_{11} and LP_{21} modes, defined as the ratio of the power contained within the squared region with respect to the total beam power, were ~42% and ~48%, respectively, compared to the theoretical values of ~59% and ~75%, respectively.

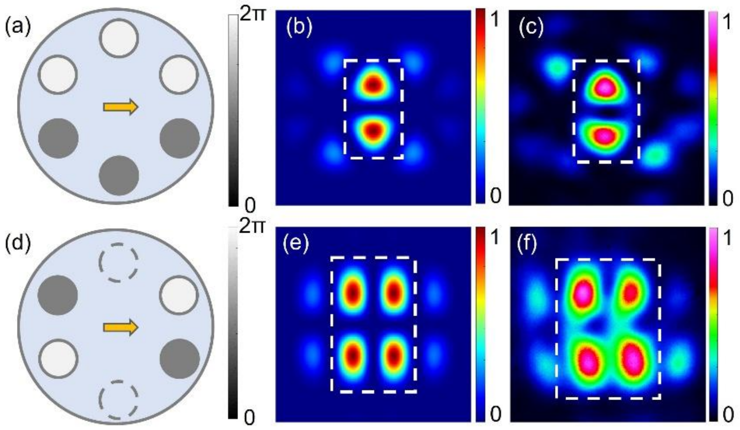

Figure 6.6 Generation of LP mode-like beams. (a) Relative phase distribution among the beamlets for the generation of LP_{11} mode, and the corresponding simulated far-field intensity distribution in (b). (d) Phase distribution among the beamlets for the generation of LP_{21} mode (the dashed circle indicating unused cores), and the corresponding simulated far-field intensity distribution in (e). (c), (f) Experimentally measured output beam profiles in the far-field.

6.4 Controlled generation of higher-order Poincaré sphere modes

The generation of HOPS beams was investigated with correlation filters formed by a pair of QWPs and a QP (charge q=1/2, 1), with specific orientations in combination with an SMF. The correlation filter is used to convert HOPS beams to a linearly polarized Gaussian beam, with an input-to-output relation described by [163, 172]:

$$E_{\mathrm{OUT}} = U_{\mathrm{QWP}}(\theta_\beta)U_{\mathrm{QP}}(\theta_\gamma, \ell)E_{\mathrm{HOPS}}(\theta_\gamma, \theta_\beta, \ell) = \cos 2\theta_\beta|\mathrm{H}\rangle + \sin 2\theta_\beta|V\rangle \tag{6.4.1}$$

$$\begin{aligned} E_{\mathrm{HOPS}} = \cos\left(\frac{\pi}{4} + \theta_\beta\right)\exp\left[-i(\theta_\gamma - \theta_\beta)\right]\exp(-i|\ell|\varphi|L\rangle) \\ + \sin\left(\frac{\pi}{4} + \theta_\beta\right)\exp\left[i(\theta_\gamma - \theta_\beta)\right]\exp(i|\ell|\varphi|R\rangle) \end{aligned} \tag{6.4.2}$$

where the circular polarization basis is applied and a global phase factor is discarded; E_{OUT} is the output state of the correlation filter; E_{HOPS} denotes the polarization state of the HOPS beam; U_{QWP} and U_{QP} represent the Jones matrix of QWP and QP[172], respectively; θ_β and θ_γ are the rotation angles of the QWP2 (see Figure 6.3) and of the q-plate with respect to the orientation of the linear polarizer, respectively; and ℓ is the topological charge ($|\ell| = 2q$) with $|L\rangle$, $|R\rangle$, $|H\rangle$, and $|V\rangle$ representing the left and right circular, horizontal and vertical polarization states. θ_β and θ_γ determine the position of the generated target beam on the Poincaré sphere, and any HOPS beam can be obtained by suitably adjusting the rotation of the QWP2 and the q-plate.

6.4.1 Generation of cylindrical vector modes

Cylindrical vector beams can be obtained when the fast axis of the QWP2 is aligned with the horizontal axis (θ_β=0°), including the radially polarized beam (θ_γ=0°) and the azimuthally polarized beam (θ_γ=90°). Figure 6.7(a) shows the calculated intensity distribution of coherently combined beams when the polarization state of each core is aligned with radial orientation (blue arrows) and azimuthal orientation (yellow arrows), as illustrated in Figure 6.7(b), resulting in a radially polarized beam and an azimuthally polarized beam, respectively. Figure 6.7(c) and (d) show the measured beam intensity profiles for the coherently combined radially polarized beam and azimuthally polarized beam, respectively, exhibiting a pronounced doughnut shape. The measured average output power within the white circle was ~3.1 W and ~2.7 W (measured with an iris diaphragm at a total output power of ~5.9 W for all lobes), corresponding to a beam combining efficiency of ~51.9% and ~46% and a peak power of ~11.4 kW and ~10 kW for the radial and azimuthal polarization, respectively. The theoretical combining efficiency of the CV beam is ~60%; note this is higher than that of the fundamental Gaussian beam, which can be attributed to a greater intensity overlap between the combined CV beams and the input beamlet array.

The polarization states of the combined beams were confirmed by passing the beams through a rotatable linear polarizer. As expected (see Figure 6.7), in the case of the radially (azimuthally) polarized beam, a two-lobe beam pattern parallel (orthogonal) to the transmission axis of the rotatable linear polarizer was systematically observed. The 2D correlation coefficients of the measured intensity profiles with respect to the theoretical intensity distribution (within the area of the doughnut-shaped beam) were ~96.1% and ~96.8% for the radially and azimuthally polarized beams, respectively. The slight beam distortion of the doughnut-shaped intensity profiles is most likely due to the nonuniform power distribution of the individual beamlets. The generated CV beams have high mode purity, and the mode extinction ratio was measured to be ~14.1 dB by the vector mode decomposition approach described in Refs. [181, 182].

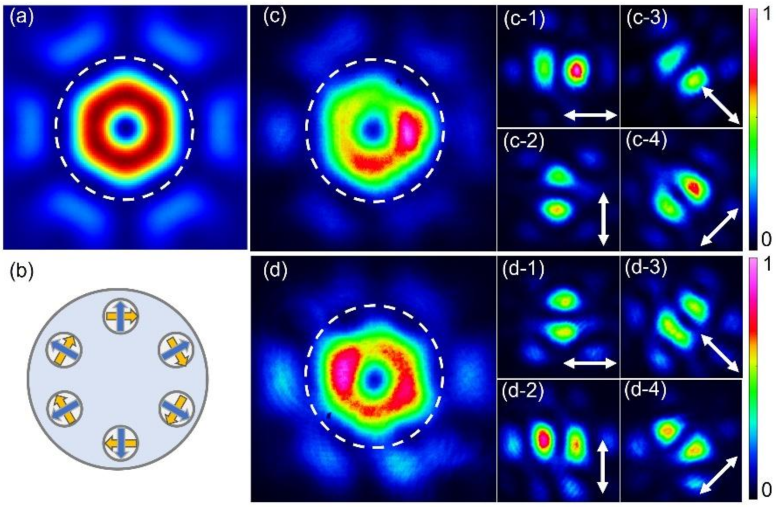

Figure 6.7 Generation of CV beams. (a) Simulated far-field intensity distribution when the polarization orientation of the six beamlets are set as per the arrow directions in (b). (c) Experimentally measured radially polarized output beam profile with a peak power of ~11.4 kW, and the two-lobe patterns when the beam is passed through a linear polarizer at different orientations (see white arrows in c-1 to c-4). (d) Experimentally measured azimuthally polarized beam profile (at ~10 kW) and the two-lobe patterns after passing through the linear polarizer (d-1 to d-4).

6.4.2 Generation of OAM beams

Subsequently, the OAM beams ($|\ell|$=1,2) with opposite handedness of helical phase front were successfully generated. Figure 6.8(a) and (d) show the generated first-order OAM beams ($|\ell|$=1). According to Eqs.(6.4.1) and (6.4.2), a left circularly polarized OAM beam with left handedness can be obtained when the fast axis of the QWP2 (see Figure 6.3) is rotated at -45° with respect to the horizontal axis. The QWP1 with the fast axis rotated at -45° was used to convert this beam to a horizontally polarized OAM beam. A right-handedness OAM beam in the vertical polarization state can be generated with the fast axes of the QWP1 and QWP2 both rotated at 45°. The polarization states of the OAM beams were confirmed by passing the beams through a rotatable linear polarizer, as shown in Figure 6.8(a-1), (a-2) and (d-1), (d-2), and the PER was measured to be ~7 dB and ~9 dB, respectively. The helicity was also analysed by interfering the beam with a reference spherical wavefront beam, and the characteristic spiral fringes with the opposite rotation directions, as shown in Figure 6.8(b) and (e), indicating beams with a topological charge of ±1, respectively. Figure 6.8(c) and (f) plot the 1D intensity profiles across the beam centre (marked with the red dashed lines in Figure 6.8(a) and (d)). The experimental 1D intensity profiles were fitted by an incoherent superposition of the LP$_{01}$ mode and the OAM mode. It turns out that the LP$_{01}$ mode accounts for only ~8% of the total power in these two beams, which proves the high modal purity of the generated OAM modes. In addition, the 2D correlation coefficients of the measured intensity profiles with respect to the theoretical intensity distribution (Figure 6.7(a)) were ~96%. The combining efficiency of the two OAM beams was ~46% (Figure 6.8(a)) and ~48% (Figure 6.8(d)), respectively, resulting in an output power of ~2.9 W with a peak power of ~10.7 kW for the combined OAM beams.

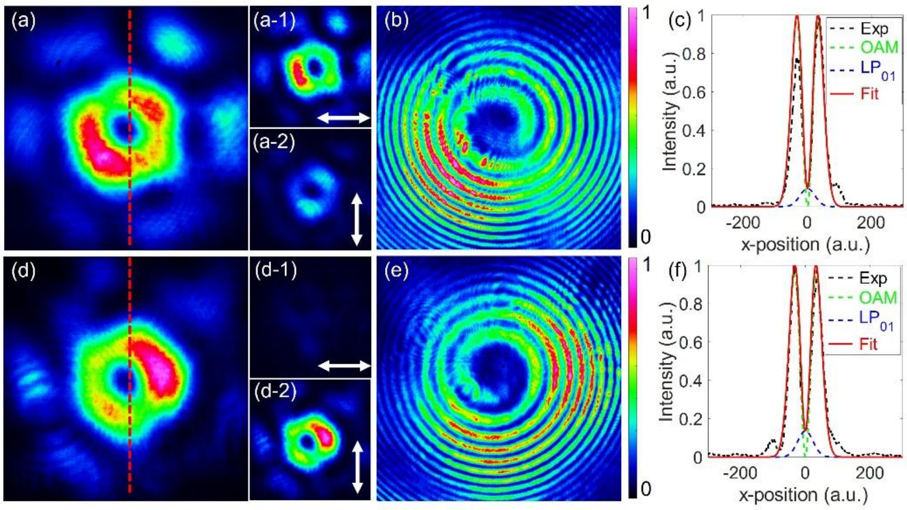

Figure 6.8 Generated OAM beams (first order). (a), (d) Experimentally measured output beam profiles with a peak power of ~10.7 kW and the topological charge of ±1, respectively, as well as the corresponding intensity distributions after the beam was passed through a rotatable linear polarizer (a-1,2 and d-1,2). (b), (e) Measured spiral interference fringes for the generated OAM beams shown in (a) and (d). (c), (f) 1D intensity profiles across the beam centre fitted with an incoherent superposition of the LP$_{01}$ mode and the OAM mode.

Finally, the second-order OAM beams ($|\ell|$=2) are generated by setting an appropriate correlation filter using a QP with a charge of q=1. In this case, the relative phase of the j-th beamlet is set to be $4\pi(j-1)/6$, as shown in Figure 6.9(b), which corresponds to a petal-like intensity distribution shown in Figure 6.9(a). It is worth noting that the petal-like intensity profile is due to the large relative phase (4π/6) among adjacent cores. By smoothing the relative phase with a large number

N of cores, a doughnut-shaped beam could be formed. Figure 6.9(c) and (d) present the measured intensity profiles for the orthogonally linearly polarized OAM beams generated in the far-field, which are close to the theoretical calculation, indicating that the phases and polarizations of the individual beamlets were well controlled. The PER was measured to be ~8 dB. Figure 6.9(e) and (f) demonstrate the interference patterns of the combined beams with a reference spherical wavefront beam, confirming that the beams have a helical phase front with a topological charge of ±2, respectively. The correlation coefficients of the measured intensity profiles with respect to the theoretical intensity distribution were ~95%. The discrepancy can be attributed to the slight power difference and residual phase shift between the individual beamlets. The average power of the combined beams within the white circle, as shown in Figure 6.9(c) and (d), was ~3.92 W with a peak power of ~14.4 kW, which corresponds to a combining efficiency of ~70% with respect to a theoretical value of 78%.

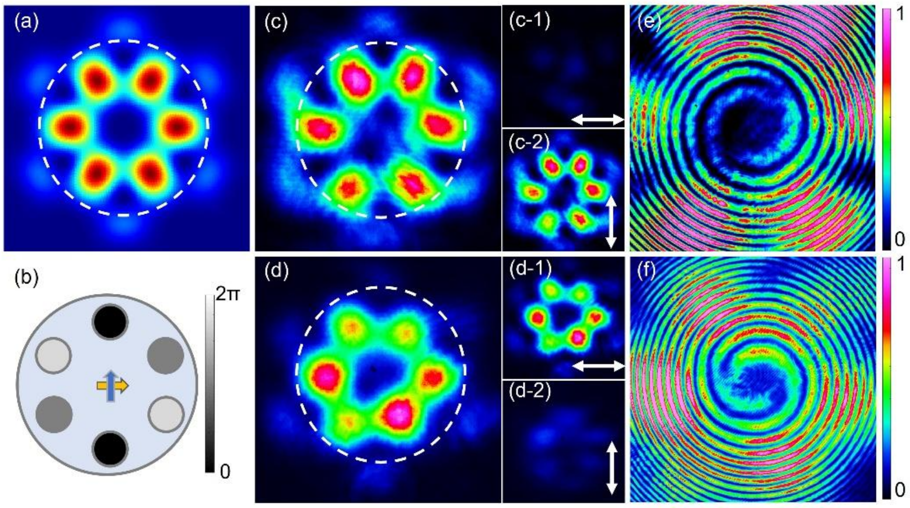

Figure 6.9 Generation of OAM beams (second order). (a) Simulated far-field distribution when the relative phase of the six beamlets is set to the value given in (b). (c), (d) Experimentally measured beam profiles with a peak power of ~14.4 kW and the topological charge of ±2, respectively, as well as the corresponding intensity distributions after passing through a rotatable linear polarizer. (e), (f) Measured spiral interference fringes for the generated OAM beams shown in (c) and (d).

6.4.3 Factors affecting coherent beam combination efficiency and beam shape

In order to understand the difference between the experimental results and theoretical calculations, various factors affecting the quality of the coherently combined beams are numerically analysed. First, the alignment and collimation condition in the CBC setup determine the beam-combining efficiency. Figure 6.10(a) shows the theoretical combining efficiency of the first-order OAM beams when each beamlet is composed of in-phase LP_{01} and LP_{11} modes with variable power weight *w*. The combining efficiency is plotted as a function of the defocus of the

MLA (*z*/*f*-1, where *z* is the distance between the MLA and the beam waist in the near-field of the MCF output, and *f* is the focal length of the MLA). The divergent ($z/f<1$) or convergent ($z/f>1$) beamlets in a tiled-aperture arrangement can result in increased electric field components having higher spatial frequencies in the far-field, leading to a reduced combining efficiency in the central target beams. The combining efficiency will decrease by ~10% when the defocus is ±0.25, and each beamlet is mainly in the LP_{01} mode ($w>0.64$). The optimal beam combination is achieved with a defocus of -0.05 to 0, resulting from the interaction of defocus and non-negligible diffraction loss when the beam diameter of each beamlet is close to the clear aperture of the microlens. Figure 6.10(b) illustrates the combining efficiency of the combined beams with different MLA shifts ($\delta x/D_{MLA}$, where δx is the shift of the MLA with respect to the optical axis, and D_{MLA} is the clear aperture of the MLA), showing that the efficiency decreases by ~10% with an MLA shift of 0.2.

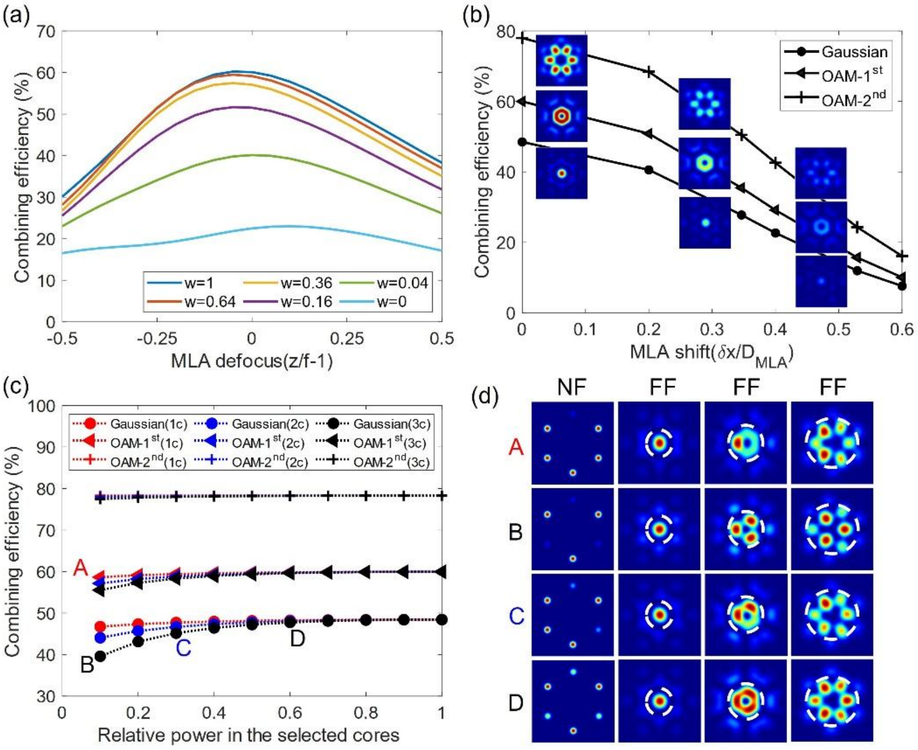

Figure 6.10 Numerical analysis on the factors affecting the combining efficiency and far-field beam shape. (a) Calculated combining efficiency of the first-order OAM as a function of MLA defocus with different mode composition (weight *w* of LP_{01} mode) of the MCF output. (b) Combining efficiency of the combined Gaussian and OAM beams with different MLA shifts in the CBC setup. (c) Combining efficiency of the combined beams with different power distributions of the MCF beamlets. (d) Near-field and far-field intensity profiles under different power distributions (A-D shown in (c)).

Second, the power distribution uniformity of the beamlets determines the spatial shape of the combined beams. When each beamlet has a different power distribution from the others, the OAM beams in the far-field will deviate from an ideal doughnut/petal shape, where the Gaussian-shaped beam can be relatively well preserved, as shown in Figure 6.10(d), respectively. The variation of the beam-combining efficiency (defined as the power ratio within the white dashed circle) was calculated when the relative power in the selected beamlets is different (1c: 1 beamlet has a different power from the other five beamlets; 2c: two nonadjacent beamlets have the same power but different from the other four beamlets; 3c: three nonadjacent beamlets have the same power but different from the residual beamlets), as shown in Figure 6.10(c). The beam-combining efficiency is quite stable even when the mode shape is fully distorted, and the variation in combining efficiency is less than 10%. 5%, and 1% for the Gaussian beam, the first- and second-order OAM beam, respectively. These analyses support the experimental observations that the slightly distorted OAM beam shape arises from the nonuniform power distribution in the MCF beamlets, whereas the lower combining efficiency is mainly related to the misalignment and collimating condition in the CBC setup.

6.5 Conclusions

In this chapter, the controllable generation of ps-pulsed HOPS beams from a coherently combined 6-core Yb-doped MCF amplifier is demonstrated. With the SLM offering adaptive wavefront shaping and polarization control on the seed light to the MCF amplifier, the complex amplitude of the amplified signal can be fully controlled, enabling various spatial modes to be obtained in the far-field. The linearly polarized Gaussian beams, LP mode-like beams, CV beams, and linearly polarized first- and second-order OAM beams were efficiently generated with a high mode purity. The generated HOPS beams exhibit an average output power of ~2.7-3.9 W with a peak power of ~10-14 kW and a pulse duration of ~92 ps. The MCF architecture offers a much simpler, more scalable, and more stable beam-shaping procedure compared with other CBC techniques based on multiple independent fibre amplifiers. Increasing the core count would allow for the generation of OAM beams with much higher-order topological charge. The capability to flexibly generate various spatial modes with high peak powers should provide advantages in many applications in optical communications, laser material processing, and biomedical imaging. It is worth noting that the approach for generating high-peak-power structured light can be applied to the generation of the control beam (or pump) introduced in previous chapters. The control beam (discussed in Chapters 3 and 4) and the pump (in Chapter 5) serve as key control parameters for achieving mode rejection, nonlinear gratings, and multiple wavelength conversion.

Notes: The results reported in this chapter have been selectively published (see LoP7 and LoP8 in the List of Publications). LoP7 includes the main results of controlled generated of high-peak-power structured light beams that were demonstrated in this chapter. This is a co-authored paper published in Photonics Research: the experiments, simulations, co-development of derivations and code were my work; the code used to control the feedback system connecting the power meter and SLM was developed by Joel Carpenter from The University of Queensland; the fibre preform was provided by Yoshimichi Amma from the Fujikura Ltd.; the 6-core active fibre was fabricated by Ian. Davidson and Siyi Wang from the Optoelectronics Research Centre; this project was supervised by Di Lin and David J. Richardson from the Optoelectronics Research Centre.

Chapter 7 Conclusions and future work

7.1 Conclusions

In summary, this thesis investigated mode control and beam shaping in multimode and multicore fibres by exploring multimode nonlinear dynamics in homemade coupled-core MCFs and commercial MMFs, as well as by coherently combining the output from an MCF amplifier with uncoupled cores.

Mode rejection and control in multimode counter-propagating systems were proposed and investigated using several FMFs and homemade DCF and TCF. Mode rejection of a specific LP mode (in FMFs) or supermode (in MCFs) was successfully observed in the output forward signal when the input BCB is coupled to the same mode with comparable intense power as the forward signal, using 0.4-1m long fibres with a total peak power of 4-16 kW for the counter-propagating beams with 0.5ns pulses at a wavelength of 1040 nm. The factors affecting the efficiency of mode rejection, such as launched power, fibre nonlinearity, and polarization state, were investigated. By adjusting the input BCB launch conditions, mode control was explored, showing that the output counter-propagating beams can be spatiotemporally controlled in an all-optical manner.

By introducing a substantial power difference between the counter-propagating beams in multimode systems, the concept of counter-propagating nonlinear gratings was introduced. Differently from the mode rejection effect, here, the input BCB power is significantly higher than the forward probe beam. The BCB generates a multimode nonlinear grating, which can be exploited to implement all-optical mode switching and core-to-core power switching. Mode switching in FMFs and MCFs was successfully observed using 0.4m-long fibres with a BCB power of 6-12 kW in 0.5 ns pulses at a wavelength of 1040 nm. Core-to-core power switching in DCF and TCF was measured using 0.4m-long fibres with a BCB power of 7-10 kW. Stemmed from these observations, several conceptual devices capable of all-optical light-by-light manipulations were demonstrated, including all-optically tuneable mode converters, ultrafast tuneable power splitters, combiners, and switches, as well as all-optical phase detection at terminal ends.

Wavelength and mode conversions in MCFs were investigated followingly by exploring FWM between supermodes in coupled MCFs. Efficient FWM and supermode conversion were successfully observed with a pump wavelength of 1040 nm in several homemade MCFs, including DCF, TCF, 4CF, and 7CF. By selectively exciting different intermodal FWM processes in MCFs, specific wavelength conversions and wavelength-dependent mode conversions were demonstrated, and the phase-matching conditions between supermodes were controlled by adjusting the fibre design in terms of core count, core diameters, and core spacings. These results highlight the potential of using MCFs for efficient wavelength conversion in a bespoke wavelength range.

Finally, spatial beam shaping in MCFs was investigated in a linear regime. Controllable generation of ps-pulsed structured beams was successfully demonstrated using a coherently combined 6-core Yb-doped MCF amplifier. With the SLM adaptively shaping the seed light to the MCF amplifier, the amplified output signal was fully controlled, enabling various spatial modes to be obtained in the far-field. The linearly polarized Gaussian beams, LP mode-like beams, CV beams, and linearly polarized OAM beams were efficiently generated with peak powers of ~10-14 kW and pulse durations of ~92 ps at the wavelength of 1035 nm.

By investigating mode control and beam shaping in terms of spatial, temporal, and spectral behaviours for MMFs and MCFs, this work could lead to all-optical light manipulations that is useful in many applications such as optical communications, data transmission, and laser material processing.

7.2 Future work

Although remarkable outcomes have been achieved in this thesis, there still exist many research opportunities related to topics and novel nonlinear phenomena raised here, described below:

1. Mode rejection and control based on feedback cavity or systems. The mode rejection and mode control experiments demonstrated in this thesis involve the coupling into the fibres at the opposite ends. However, the backward control beam can be replaced with a feedback cavity or system to provide spatiotemporal control over the forward signals. This would require specific cavity and system design, fibre couplers, or free-space coupling solutions. Exploring mode rejection and control with feedback systems would benefit many applications including intelligent beam shaping, efficient beam combination solutions, and beyond.
2. Core-to-core power switching in MCFs leveraging different wavelengths /temporal shapes /fibre lengths. The core-to-core power switching experiments demonstrated in Chapter 4 involve probe beam and backward control beam in the same wavelength and same pulse duration. It is worthy to explore the probe beam evolution when the counter-propagating beams are different, in terms of wavelength, pulse width, and repetition rate. Different fibre lengths can be used to obtain different temporal evolutions for the probe especially when the probe is in the CW state. These will contribute to the many applications requiring ultrafast mode or power switching.

3. Multiline, multimode optical parametric oscillator based on MCFs. The results reported in Chapter 5 shows that Four-wave mixing in MCFs provides solutions to generate wavelengths on demand by appropriate fibre designs with different core numbers, core size, and core arrangement. By using MCFs as the gain fibre, a multiline and multimode optical parametric oscillator can be built for new frequency laser generations with high efficiency.

Appendix A Mode decomposition in MCFs based on other methods

A.1 Mode decomposition in MCFs based on off-axis holography method

Mode decomposition in multimode fibres is a technique used to determine the relative power and phase of each eigenmode by analysing the output beam. Off-axis holography [183] is a wavefront measurement technique where the multimode beam interferes with a tilted reference beam. Figure A.1 illustrates the principle of off-axis holography method, using the example of analysing the SM_7 mode of 7CF.

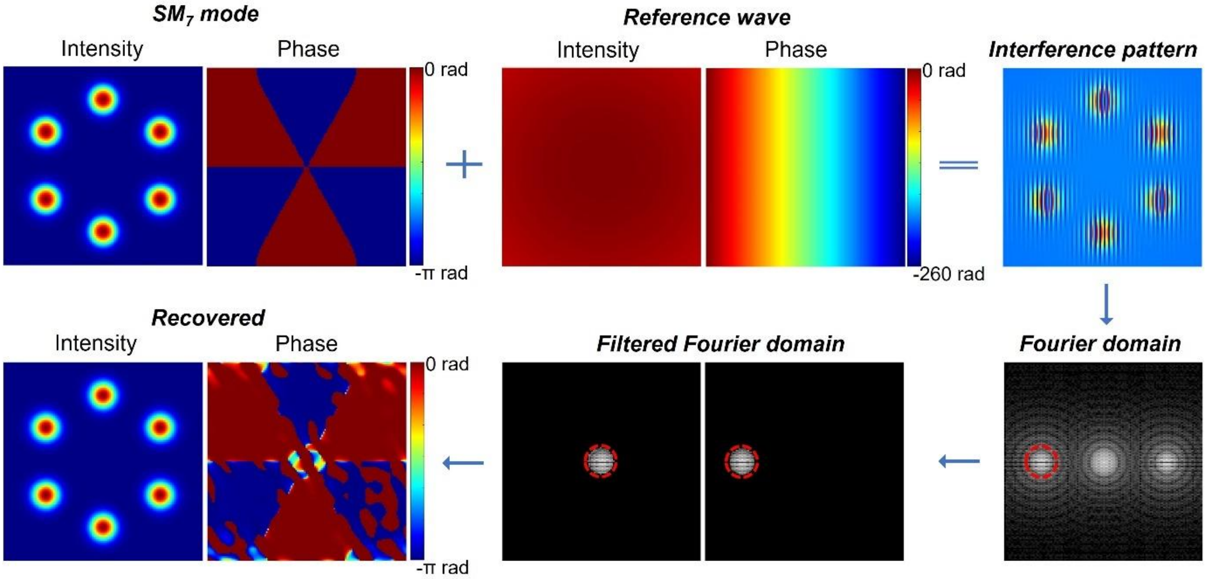

Figure A.1 Principle of off-axis holography method, with the SM_7 mode of 7CF demonstrated as an example.

The reference beam is a plane wave at the same wavelength with a highly tilted phase distribution, resulting in interference between the SM_7 mode (denoted as the target wave) and the reference beam. The interference pattern can be expressed as,

$$\begin{aligned} I_{int}(x,y) &= \left[E_{target}(x,y)+E_{ref}(x,y)\right]\left[E_{target}^{*}(x,y)+E_{ref}^{*}(x,y)\right] \\ &= \left|E_{target}(x,y)\right|^{2}+\left|E_{ref}(x,y)\right|^{2}+E_{ref}(x,y)E_{target}^{*}(x,y)+E_{target}(x,y)E_{ref}^{*}(x,y) \end{aligned} \tag{A.1.1}$$

where I_{int} is the intensity distribution of the interference pattern, and E_{target} and E_{ref} represent the electric fields of the target and reference waves, respectively. The first two terms in the last line of Eq. (A.1.1) are the zero-order terms, while the last two terms are the ±1-orders components, which carry the information of the target wave. The three orders can be separated in the Fourier domain when the reference beam is adjusted to suitable angles, as shown in Figure A.1. By using a bandpass filter in the Fourier domain (see the red circle in Figure A.1), one of the ±1-order terms can be isolated, such as the -1 order term shown in Figure A.1. Since the reference wave only contributes to shifting the target wave to different positions in the Fourier domain, the filtered -1 order term can be shifted to the centre of the Fourier domain to retrieve the information of E_{target}. Consequently, the intensity and phase of the target beam can be recovered by performing an inverse Fourier transform on the filtered Fourier spectrum.

Off-axis holography method can be used to obtain the phase distribution of an unknown electric field, which can be utilised for the mode decomposition of a multimode beam by projecting the recovered target electric fields onto the eigenmodes of MMFs[183]. Recently, the off-axis holography method has been demonstrated in MCFs[129], which can be used for mode decomposition of MCFs. In this appendix, an experimental demonstration of off-axis holography method using the TCF is provided. The experimental setup is illustrated in Figure A.2, where the signal and reference beam are split from the same laser source, ensuring coherence between them. The signal beam is selectively coupled into different supermodes of the TCF using a SLM, while the reference beam is collimated with a beam diameter of ~7 mm. The output signal is imaged onto the camera with a magnification of 36x using a pair of lenses with focal lengths of 13.86 mm and 500 mm. The reference beam is directed at an angle onto the camera to produce the interference pattern. The optical path difference between the signal and reference arms is precisely controlled by an optical delay line, ensuring clear interference fringes can be measured.

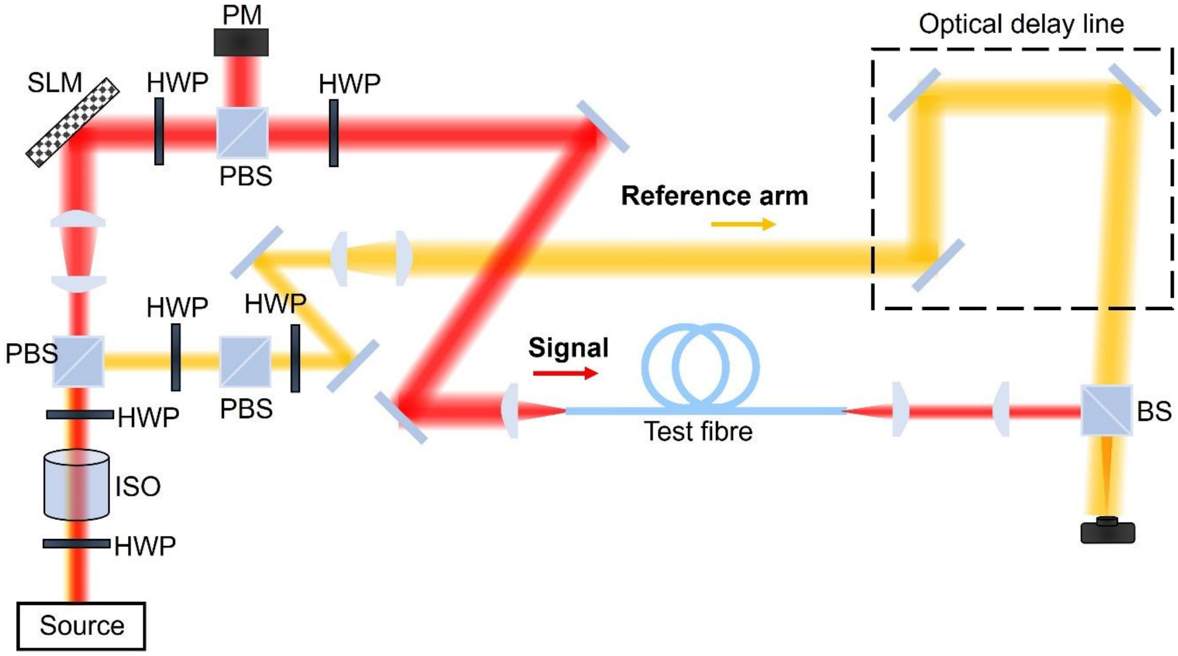

Figure A.2 Experimental setup implementing off-axis holography method for MCFs.

Figure A.3 displays the experimental results of the recovered electric fields of the TCF output based on the off-axis holography method. Following the procedures outlined in Figure A.1, the intensity and phase of three outputs, resembling the three theoretical supermodes in the near field (see Figure 3.23(b)), are recovered from the interference patterns. The results are shown in the last two columns of Figure A.3., denoted as "$SM_{3(2,1)}$ mode-like". The recovered phases in the three cores closely match the theoretical phases of supermodes in the near field. Specifically, for the SM_3 mode-like output, the relative phases are 3.1 rad, 0.33 rad, and 0 rad in core1, core2, and core3, respectively, corresponding to the theoretical values of π rad, 0 rad, and 0 rad, respectively. For the SM_2 mode-like output, the relative phases in core2 and core3 are 0 rad and 3.89 rad, respectively, closely matching the theoretical π rad phase difference between them. While for the SM_1 mode-like output, the relative phases in the three cores are 0 rad, 0.37 rad, and 0.75 rad, in line with the theoretical 0 rad phase differences among them.

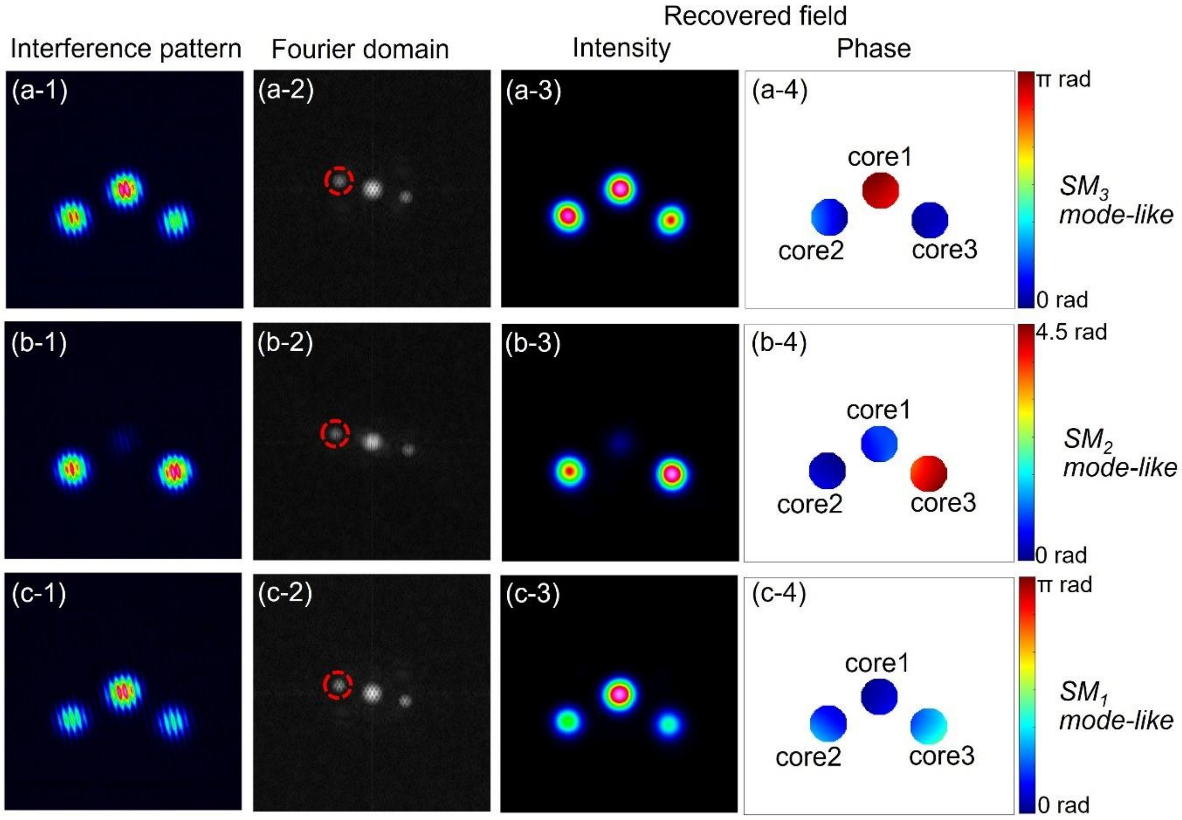

Figure A.3 Experimental results for measuring TCF outputs based on off-axis holography method. The near-field phase information within the individual cores is calculated from the interference pattern that is generated by the interference between a reference beam with the fibre output.

For a specific output, the recovered intensity and phase can be used for mode decomposition to determine the content and relative phase of different supermodes. The mode content and relative phase can be obtained using an equation similar to Eq.(3.3.1), where $E_{retrieved}$ and E_{LPmn} are replaced with E_{rec} and E_{SMx}, respectively. Here, E_{rec} represents the recovered electric field obtained from off-axis holography, and E_{SMx} represents the complex amplitude of the SM_x mode of MCFs in the near-field. Figure A.4 demonstrates two mode decomposition results using this method.

Figure A.4(a) shows the mode content and relative phase of the three supermodes in the TCF for the SM_3 mode-like output given in Figure A.3. The calculated SM_3 mode content is 92.2%, confirming the dominancy of this mode. By synthesizing the supermodes using the MD results, the synthesized intensity and phase distributions are compared with the recovered distributions obtained via off-axis holography. Both the high 2D correlation coefficients (97.6%) and the small differences between the synthesized and recovered distributions illustrate the validity of implementing mode decomposition for MCFs based on the off-axis holography method.

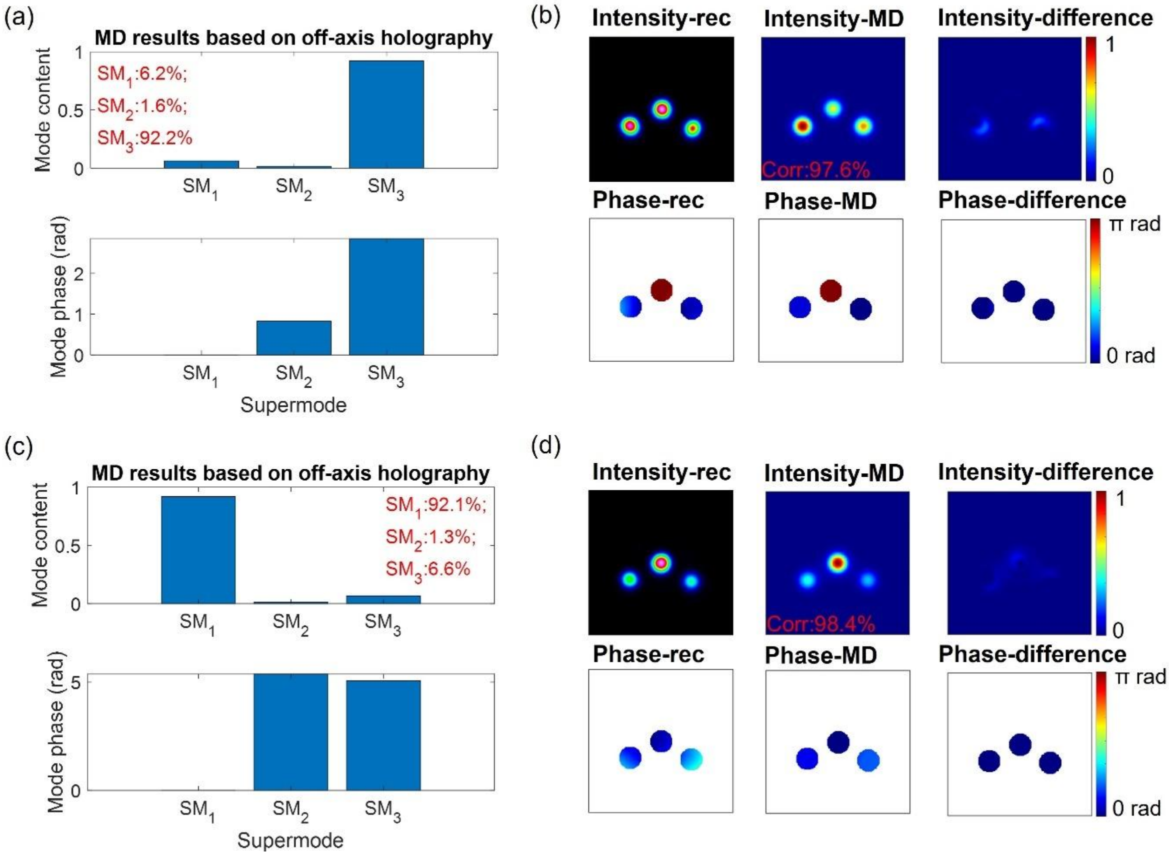

Figure A.4 Mode decomposition results of the TCF based on off-axis holography method. (a), (c) Mode content and relative phase of each supermode. (b), (d) The intensity and phase distributions synthesized by MD results (denoted as “Intensity-MD” and “Phase-MD”) are compared with the recovered distributions obtained by off-axis holography (denoted as “Intensity-rec” and “Phase-rec”). (a) and (b) are the results of the SM_3 mode-like output, and (c) and (d) are the results of the SM_1 mode-like output.

A.2 Mode decomposition of MCFs based on matrix formalism method

The matrix formalism mode decomposition method is a non-iterative algorithmic method based on intensity measurements without using reference beams. This method was initially proposed for few-mode fibres, offering high-performance mode decomposition with a processing time of tens of microseconds[67]. The key to this method is the creation of a transformation matrix *T*, which is used to determine the MD coefficients (mode content and relative phase) from a single intensity profile I. Considering an image consisting of M x M pixels, the 2D intensity profile can be written as an M^2 x 1 vector:

$$I^{(m)} = \sum_k \sum_j C_k C_j^* E_k^{(m)} E_j^{*(m)}, m = 1,2,\dots,M^2; k,j = 1,2,\dots,N. \tag{A.2.1}$$

where $C_{k(j)}$ are the complex modal coefficients for the $k(j)$-th mode, and N is the number of modes. The complex amplitude of the $k(j)$-th mode is also written in the form of an M^2 x 1 vector, and $E_{k(j)}^{(m)}$ is the complex amplitude at the m-th pixel. By defining an M^2 x $N(N+1)/2$ matrix T that only contains the $E_{k(j)}^{(m)}$ terms and a $N(N+1)/2$ x 1 vector V that only contains the $C_{k(j)}$ terms, Eq. (A.2.1) can be written in the matrix form as:

$$I = TV \tag{A.2.2}$$

$$T = \begin{bmatrix} E_1^{(1)}E_1^{(1)} \cdots E_N^{(1)}E_N^{(1)} & 2E_1^{(1)}E_2^{(1)} \cdots 2E_1^{(1)}E_N^{(1)} & \cdots & 2E_{N-1}^{(1)}E_N^{(1)} \\ E_1^{(2)}E_1^{(2)} \cdots E_N^{(2)}E_N^{(2)} & 2E_1^{(2)}E_2^{(2)} \cdots 2E_1^{(2)}E_N^{(2)} & & 2E_{N-1}^{(2)}E_N^{(2)} \\ \vdots & \vdots & \ddots & \vdots \\ E_1^{(M^2)}E_1^{(M^2)} \cdots E_N^{(M^2)}E_N^{(M^2)} & 2E_1^{(M^2)}E_2^{(M^2)} \cdots 2E_1^{(M^2)}E_N^{(M^2)} & \cdots & 2E_{N-1}^{(M^2)}E_N^{(M^2)} \end{bmatrix} \tag{A.2.3}$$

$$V = \left[C_1C_1^* \cdots C_NC_N^* \quad \frac{C_1C_2^* + C_2C_1^*}{2} \cdots \frac{C_1C_N^* + C_NC_1^*}{2} \quad \cdots \quad \frac{C_{N-1}C_N^* + C_NC_{N-1}^*}{2} \right]^T \tag{A.2.4}$$

The vector V can be solved from $V=T^{-1}I$ with T^{-1} as a pseudoinverse matrix of T, and the mode content (c_k) and relative phase (θ_k) of the k-th mode can be determined from Eq. (A.2.4):

$$c_k = \sqrt{V(k)}, k = 1,2,\dots,N \tag{A.2.5}$$

$$\theta_k = \mathrm{acos}\left[\frac{V(N+k-1)}{c_1 c_k}\right], k = 1,2,\dots,N \tag{A.2.6}$$

This method can be applied for mode decomposition of MCFs by substituting the complex amplitude of supermodes for specific MCFs into Eq. (A.2.3). It is worth noting that mode decomposition for MCFs based on intensity measurements is preferably implemented in the far-field, as illustrated in Figure 3.27. A simulation result for a multimode output from the 7CF is demonstrated in Figure A.5(b-1)-(b-4) using this method, labelled as "Ref[66]". However, the calculated mode content and phase exhibit significant deviations from the set values, and the reconstructed intensity and phase profiles differ from the target profiles, as shown in Figure A.5(a-1) and (a-2). This discrepancy arises because the terms $E_{k(j)}^{(m)}$ in Eq. (A.2.1) are complex numbers for the supermodes in the far-field. Consequently, $E_k^{(m)}E_j^{*(m)}$ differs from $E_j^{(m)}E_k^{*(m)}$, which is the approximation used in Eq. (A.2.3) when rewriting Eq. (A.2.1) into the form of Eq. (A.2.2). Therefore, Eqs. (A.2.3) and (A.2.4) need to be modified for mode decomposition of MCFs in the far-field. The new transformation matrix T_{new} is an M^2 x N^2 matrix and the new vector V_{new} is an N^2 x 1 vector:

$$T_{new} = \begin{bmatrix} E_1^{(1)}E_1^{*(1)} \cdots E_1^{(1)}E_N^{*(1)} & E_2^{(1)}E_1^{*(1)} \cdots E_2^{(1)}E_N^{*(1)} & \cdots & E_N^{(1)}E_1^{*(1)} \cdots E_N^{(1)}E_N^{*(1)} \\ E_1^{(2)}E_1^{*(2)} \cdots E_1^{(2)}E_N^{*(2)} & E_2^{(2)}E_1^{*(2)} \cdots E_2^{(2)}E_N^{*(2)} & & E_N^{(2)}E_1^{*(2)} \cdots E_N^{(2)}E_N^{*(2)} \\ \vdots & \vdots & \ddots & \vdots \\ E_1^{(M^2)}E_1^{*(M^2)} \cdots E_1^{(M^2)}E_N^{*(M^2)} & 2E_2^{(M^2)}E_1^{*(M^2)} \cdots 2E_2^{(M^2)}E_N^{*(M^2)} & \cdots & 2E_N^{(1)}E_1^{*(1)} \cdots 2E_N^{(1)}E_N^{*(1)} \end{bmatrix} \tag{A.2.7}$$

$$V_{new} = [C_1C_1^* \cdots C_1C_N^* \quad C_2C_1^* \cdots C_2C_N^* \quad \cdots \quad C_NC_1^* \cdots C_NC_N^*]^T \tag{A.2.8}$$

Similarly, the vector V_{new} can be solved from $V_{new}=T_{new}^{-1}I$ with T_{new}^{-1} as a pseudoinverse matrix of T_{new}, and the mode content (c_k) and relative phase (θ_k) of the k-th mode can be determined from Eq. (A.2.8):

$$c_k = \sqrt{V_{new}(N(k-1)+k)}, k = 1,2,\ldots,N \tag{A.2.9}$$

$$\theta_k = \text{acos}\left[\frac{V_{new}(k) + V_{new}(N(k-1)+1)}{2c_1c_k}\right], k = 1,2,\ldots,N \tag{A.2.10}$$

For the same target intensity profile, Eqs. (A.2.9) and (A.2.10) yield lossless mode decomposition results, as illustrated in Figure A.5(c-1) and (c-2).

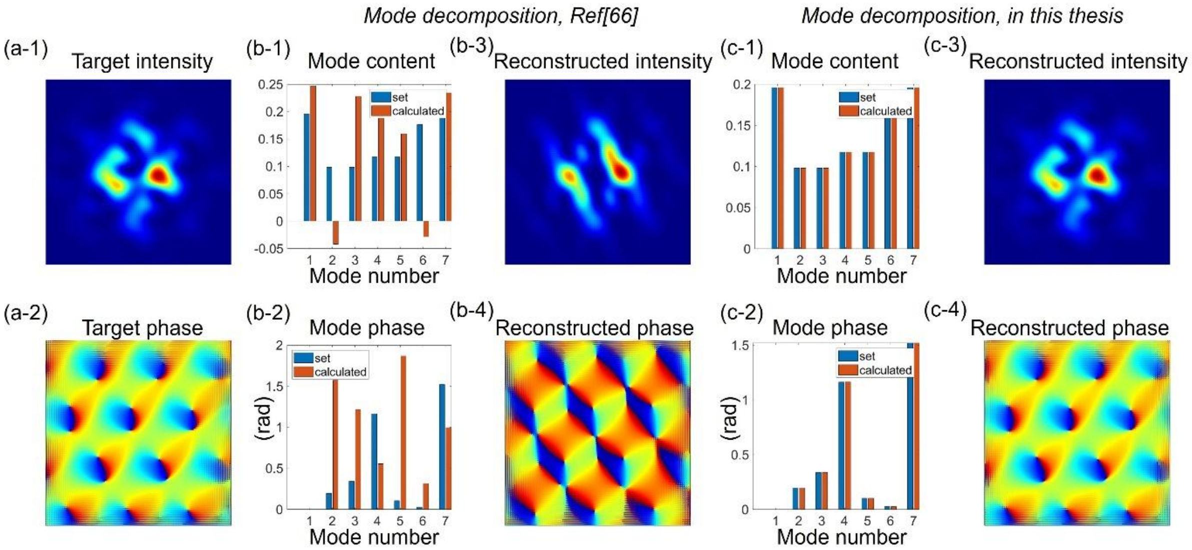

Figure A.5 Mode decomposition of MCFs based on the matrix formalism method, demonstrated with the simulation of 7CF. (a-1), (a-2) Target intensity and phase of the multimode state formed by the combination of seven supermodes with the mode content and phase illustrated with blue bars (see 'set') in (b-1) and (b-2). (b-3),(b-4) Reconstructed intensity and phase based on the method proposed in Ref[67], with the calculated mode content and phase plotted in red bars in (b-1) and (b-2). (c-1)-(c-4) Mode decomposition results and the reconstructed intensity and phase based the matrix formalism method introduced in this thesis.

This matrix formalism method can achieve high accuracy mode decomposition for MCFs. It is necessary to assess the impact of intensity noise on this method. Figure A.6 presents simulation results for mode decomposition of four different MCFs used in this thesis, including the DCF, TCF, 4CF, and 7CF. In each simulation depicted in Figure A.6, the target intensity profile is generated by combining all supermodes with random mode contents and relative phases specific to each MCF. Uniformly distributed random intensity noise, characterized by a signal-to-noise ratio (SNR) ranging from 10 dB to 30 dB, is added to the target intensity profile. Figure A.6 illustrates how varying levels of intensity noise affect the accuracy of mode decomposition of these MCFs.

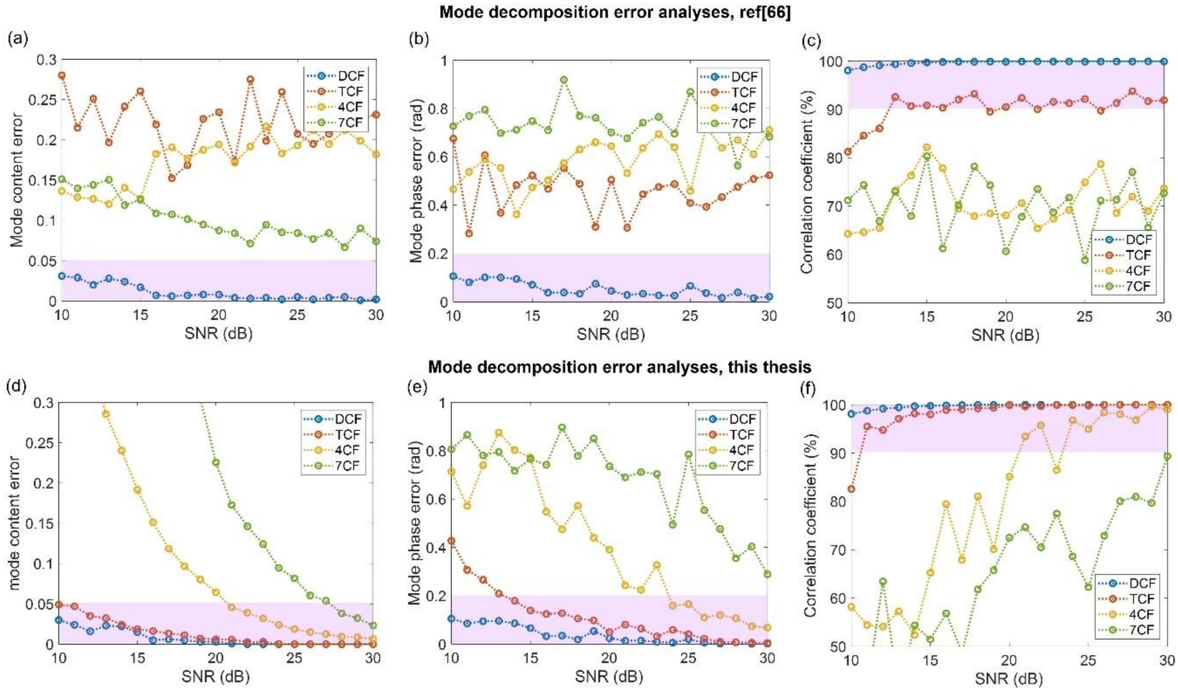

Figure A.6 Analyses of the impact of intensity noise on the mode decomposition accuracy for different MCFs, with comparisons between the method in Ref[67] and the method in this thesis. (a), (d) Mode content error versus SNR. (b), (e) Mode phase error versus SNR. (c), (f) Correlation coefficient versus SNR.

In Figure A.6(a) and (d), the mode content error at specific SNR values is determined by averaging the differences between the calculated mode contents and the set values across 10 simulation instances for different supermodes. Correspondingly, Figure A.6(b) and (e) shows the mode phase error at various SNR values, and Figure A.6(c) and (f) displays the correlation coefficients between the reconstructed intensity profile (using MD results) and the target intensity profile at different SNR values. Figure A.6(a)-(c) present results obtained using Eqs. (A.2.3)-(A.2.6) (Ref[67]), while Figure A.6(d)-(f) correspond to results obtained from Eqs. (A.2.7)-(A.2.10) (this thesis). The simulation results illustrate the following: by using the modified matrix formalism method, the mode content error is less than 0.05 for the DCF and TCF when the SNR of the measured intensity profile is higher than 10 dB; the mode content error can be controlled below 0.05 for the 4CF and 7CF when SNR is higher than 21 dB and 27 dB, respectively; the mode phase error can be controlled to less than 0.2 rad for the DCF, TCF, and 4CF when SNR is higher than 10 dB, 13 dB, and 24 dB, respectively; the correlation coefficients are higher than 90% for the DCF, TCF, and 4CF when SNR is higher than 10 dB, 11 dB, and 21 dB, respectively. These findings demonstrate that the modified matrix formalism method could provide robust mode decomposition results for various MCFs under different levels of intensity noise.

A.3 Details of Comsol simulations for the fibres used in this thesis

The fibres used in this thesis were simulated using Comsol Multiphysics software. The “Electromagnetic Waves, Frequency Domain (emw)” physics model and the “Mode Analysis” study were employed to model various fibres, including PM1550-xp, PMHN1, PM2000, SMF28, and MCFs with core numbers ranging from 2 to 7. The fibre geometry consists of core and cladding, with additional stress rods included for the panda type PM-fibres (PM1550-xp and PM2000). The refractive index of the cladding was defined from the Sellmeier equation (see Eq.(2.2.1)), while the refractive index of the stress rods was based on measured refractive index profiles (see Section 3.3.2 for details). For the fibre core, the refractive index of PM-fibres was determined through interpolation of measured index profiles around the core region, whereas MCFs were simulated using a step-index configuration.

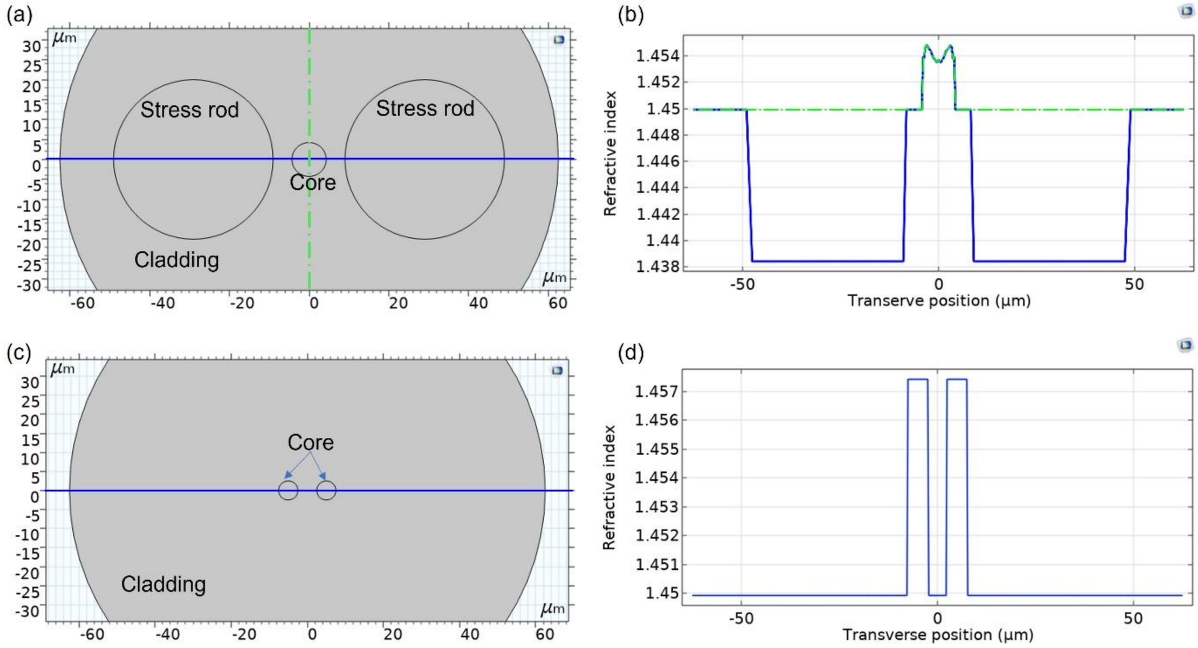

Figure A.7 Comsol modelling of PM1550-xp fibre and DCF. (a) Cross section of the PM1550-xp fibre showing core, stress rod, and cladding. (b) Refractive index of the PM1550 xp fibre along the fast (green dashed line) and slow (blue solid line) axes. (c) Cross section of the DCF. (d) Refractive index of the DCF along the slow axis.

The modelling details for these fibres are similar; thus, examples of the PM1550-xp fibre and DCF are provided for reference. Scattering Boundary Conditions were applied at the perimeter of the cladding, and free triangular meshes with a predefined extra fine size were used to ensure the accuracy and stability of the simulations. It is worth noting that, to account for fabrication errors, the shape of the fibre cores was defined as an ellipse with a diameter ratio of 1.01 along two orthogonal axes.

When calculating the dispersion coefficients for these fibres (see Table 3.1 for PM1550-xp, Table 3.2 for PMHN1, Table 3.3 for PM2000, Table 3.5 for SMF28, and Table 3.7 for DCF and TCF), the "Parametric Sweep" function was used to perform a frequency sweep. The sweep step was set to 0.1 THz, corresponding to a wavelength step of ~0.4 nm around a 1 μm wavelength. Followingly the frequency sweep, the propagation constants for all supported spatial modes at different frequencies were evaluated. The finite difference approximation was then applied to estimate the derivatives of the propagation constant for various spatial modes at consecutive frequency steps.

List of Publications

[LoP1]. K. Ji. "Mode decomposition for multicore fibers based on far-field intensity measurements." Optics Letters 50, 1045-1048 (2025).

[LoP2]. K. Ji, D. J. Richardson, S. Wabnitz, and M. Guasoni. "Sub-nanosecond all-optically reconfigurable photonics in optical fibres." arXiv preprint arXiv:2409.15929 (2024).

[LoP3]. **K. Ji**, M. I. M. Abdul Khudus, I. Davidson, L. Xu, and M. Guasoni, "Wavelength and Supermode Conversion based on Four-Wave Mixing in Coupled Multicore Fibres," in CLEO 2024, paper SF2Q.2 (2024).

[LoP4]. **K. Ji**, I. Davidson, J. Sahu, D. J. Richardson, S. Wabnitz, and M. Guasoni "Mode rejection and counter-propagating all-optical gratings in multimode waveguides", Proc. SPIE PC12871, Laser Resonators, Microresonators, and Beam Control XXVI, PC128710H (2024)

[LoP5]. **K. Ji**, I. Davidson, J. Sahu, D. J. Richardson, S. Wabnitz, and M. Guasoni “Mode attraction, rejection and control in nonlinear multimode optics”, Nat Commun 14, 7704 (2023).

[LoP6]. **K. Ji**, I. Davidson, J. Sahu, Y. Jung, D. J. Richardson, and M. Guasoni, "All-optical, reconfigurable mode switcher integrated in multicore fibers with a counter-propagating configuration," in CLEO 2023, paper SM4L.3 (2023).

[LoP7]. **K. Ji**, D. Lin, I. Davidson, S. Wang, J. Carpenter, Y. Amma, Y. Jung, M. Guasoni, and D. J. Richardson, "Controlled generation of picosecond-pulsed higher-order Poincaré sphere beams from an ytterbium-doped multicore fiber amplifier," Photon. Res. 11, 181-188 (2023)

[LoP8]. **K. Ji**, D. Lin, I. Davidson, S. Wang, J. Carpenter, Y. Amma, Y. Jung, and D. J. Richardson, "Generation of High-power Picosecond Optical Vortex beams from a Yb-doped Multicore Fiber Amplifier," in CLEO 2022, paper ATh2C.1 (2022).

[LoP9]. J. Haines, P. U. Naik, **K. Ji**, V. Vitali, Y. Franz, P. Petropoulos, and M. Guasoni, "Subwavelength and broadband on-chip mode splitting with shifted junctions," Opt. Express 32, 24072-24080 (2024)

[LoP10]. M. I. M. A. Khudus, **K. Ji**, L. Xu, A. Halder, and M. Guasoni, "Wavelength-Selectable Inter- and Intra-modal Four Wave Mixing in Elliptical Core Fibers," in CLEO 2024, paper JW2A.7 (2024).

[LoP11]. S. Jain, **K. Ji**, M. M. A. Núñez-Velázquez, I. Davidson, J. Sahu, J. Fatome, D. J. Richardson, S. Wabnitz, and M. Guasoni, "Observation of Light Self-Organization and Mode Attraction in a Multimode Optical Fiber," in CLEO 2022, paper STu4P.5 (2022).

[LoP12]. S. Jain, **K. Ji**, J. Sahu, David.J.Richardson, J. Fatome, S. Wabnitz, and M. Guasoni, "Multicore fibers: a novel platform for a robust and reconfigurable self-organization of light," in CLEO 2021, paper ef_4_6 (2021).

Bibliography

[1]. R. D. Maurer, P. C. Schultz. Fused silica optical waveguide. United States patent US 3,659,915., 1972.

[2]. D. Keck, P. Schultz. Method of producing optical waveguide fibers. United States patent US 3,711,262., 1973.

[3]. E. E. Basch, R. A. Beaudette, H. A. Carnes. Optical Transmission for Interoffice Trunks. *IEEE Transactions on Communications*. **26**(7):1007-1014, 1978.

[4]. D. J. Richardson, J. M. Fini, L. E. Nelson. Space-division multiplexing in optical fibres. *Nature Photonics*. **7**(5):354-362, 2013.

[5]. S. W. Harun, H. Arof. Current developments in optical fiber technology: *BoD–Books on Demand*. 2013.

[6]. I. Cristiani, C. Lacava, G. Rademacher, B. J. Puttnam, R. S. Luis, C. Antonelli, et al. Roadmap on multimode photonics. *Journal of Optics*. **24**(8), 2022.

[7]. S. Berdague, P. Facq. Mode Division Multiplexing in Optical Fibers. *Applied Optics*. **21**(11):1950-1955, 1982.

[8]. W. Chen, L. Yuan, B. Zhang, Q. Yu, Z. Lian, Y. Pi, et al., editors. Applications and Development of Multi-Core Optical Fibers. Photonics. **11**(3), 2024.

[9]. S. Inao, T. Sato, S. Sentsui, T. Kuroha, Y. Nishimura, editors. Multicore optical fiber. Optical Fiber Communication Conference. 1979.

[10]. B. J. Puttnam, G. Rademacher, R. S. Luís. Space-division multiplexing for optical fiber communications. *Optica*. **8**(9):1186-1203, 2021.

[11]. T. Mizuno, H. Takara, K. Shibahara, A. Sano, Y. Miyamoto. Dense Space Division Multiplexed Transmission Over Multicore and Multimode Fiber for Long-haul Transport Systems. *Journal of Lightwave Technology*. **34**(6):1484-1493, 2016.

[12]. T. Mizuno, Y. Miyamoto. High-capacity dense space division multiplexing transmission. *Optical Fiber Technology*. **35**:108-117, 2017.

[13]. A. Méndez, T. F. Morse. Specialty optical fibers handbook. Amsterdam ; Boston: *Academic Press*. 2007.

[14]. T. Sakamoto, K. Saitoh, S. Saitoh, Y. Abe, K. Takenaga, A. Urushibara, et al. 120 Spatial Channel Few-mode Multi-core Fibre with Relative Core Multiplicity Factor Exceeding 100. *2018 European Conference on Optical Communication (ECOC)*. 2018.

[15]. Q. Wang, Y. Liu. Review of optical fiber bending/curvature sensor. *Measurement*. **130**:161-176, 2018.

[16]. I. Ashry, Y. Mao, A. Trichili, B. W. Wang, T. K. Ng, M. S. Alouini, et al. A Review of Using Few-Mode Fibers for Optical Sensing. *Ieee Access*. **8**:179592-179605, 2020.

[17]. C. Caucheteur, J. Villatoro, F. Liu, M. Loyez, T. Guo, J. Albert. Mode-division and spatial-division optical fiber sensors. *Advances in Optics and Photonics*. **14**(1):1-86, 2022.

[18]. J. R. Guzman-Sepúlveda, R. Guzmán-Cabrera, A. A. Castillo-Guzmán. Optical Sensing Using Fiber-Optic Multimode Interference Devices: A Review of Nonconventional Sensing Schemes. *Sensors*. **21**(5), 2021.

[19]. K. Wang, X. C. Dong, M. H. Kohler, P. Kienle, Q. Bian, M. Jakobi, et al. Advances in Optical Fiber Sensors Based on Multimode Interference (MMI): A Review. *IEEE Sensors Journal*. **21**(1):132-142, 2021.

[20]. H. L. Zhang, Z. F. Wu, P. P. Shum, R. X. Wang, X. Q. Dinh, S. N. Fu, et al. Fiber Bragg gratings in heterogeneous multicore fiber for directional bending sensing. *Journal of Optics*. **18**(8), 2016.

[21]. S. Zhou, B. Huang, X. W. Shu. A multi-core fiber based interferometer for high temperature sensing. *Measurement Science and Technology*. **28**(4), 2017.

[22]. M. Plöschner, T. Tyc, T. Cizmár. Seeing through chaos in multimode fibres. *Nature Photonics*. **9**(8):529-535, 2015.

[23]. N. Borhani, E. Kakkava, C. Moser, D. Psaltis. Learning to see through multimode fibers. *Optica*. **5**(8):960-966, 2018.

[24]. A. M. Caravaca-Aguirre, R. Piestun. Single multimode fiber endoscope. *Optics Express*. **25**(3):1656-1665, 2017.

[25]. B. Rahmani, D. Loterie, G. Konstantinou, D. Psaltis, C. Moser. Multimode optical fiber transmission with a deep learning network. *Light-Science & Applications*. **7**, 2018.

[26]. L. Q. Wu, J. Zhao, M. H. Zhang, Y. Z. Zhang, X. Y. Wang, Z. Y. Chen, et al. Deep Learning: High-quality Imaging through Multicore Fiber. *Current Optics and Photonics*. **4**(4):286-292, 2020.

[27]. N. Stasio, C. Moser, D. Psaltis. Calibration-free imaging through a multicore fiber using speckle scanning microscopy. *Optics Letters*. **41**(13):3078-3081, 2016.

[28]. A. Porat, E. R. Andresen, H. Rigneault, D. Oron, S. Gigan, O. Katz. Widefield lensless imaging through a fiber bundle via speckle correlations. *Optics Express*. **24**(15):16835-16855, 2016.

[29]. D. J. Richardson, J. Nilsson, W. A. Clarkson. High power fiber lasers: current status and future perspectives. *Journal of the Optical Society of America B-Optical Physics*. **27**(11):B63-B92, 2010.

[30]. M. N. Zervas, C. A. Codemard. High Power Fiber Lasers: A Review. *IEEE Journal of Selected Topics in Quantum Electronics*. **20**(5), 2014.

[31]. K. S. Abedin, M. F. Yan, T. F. Taunay, B. Y. Zhu, E. M. Monberg, D. J. DiGiovanni. State-of-the-art multicore fiber amplifiers for space division multiplexing. *Optical Fiber Technology*. **35**:64-71, 2017.

[32]. S. Jain, C. Castro, Y. Jung, J. Hayes, R. Sandoghchi, T. Mizuno, et al. 32-core erbium/ytterbium-doped multicore fiber amplifier for next generation space-division multiplexed transmission system. *Optics Express*. **25**(26):32887-32896, 2017.

[33]. W. Fu, L. G. Wright, P. Sidorenko, S. Backus, F. W. Wise. Several new directions for ultrafast fiber lasers [Invited]. *Optics Express*. **26**(8):9432-9463, 2018.

[34]. Y. M. Jung, S. U. Alam, D. J. Richardson, S. Ramachandran, K. S. Abedin. Multicore and multimode optical amplifiers for space division multiplexing. *Optical Fiber Telecommunications Vii*.301-333, 2020.

[35]. L. Sirleto, M. A. Ferrara. Fiber Amplifiers and Fiber Lasers Based on Stimulated Raman Scattering: A Review. *Micromachines*. **11**(3), 2020.

[36]. G. Nemova. Brief Review of Recent Developments in Fiber Lasers. *Applied Sciences-Basel*. **14**(6), 2024.

[37]. B. Fu, C. Shang, H. Y. Liu, S. Z. Fan, K. J. Zhao, Y. L. Zhang, et al. Recent advances and future outlook in mode-locked lasers with multimode fibers. *Applied Physics Reviews*. **10**(4), 2023.

[38]. A. Klenke, C. Jauregui, A. Steinkopff, C. Aleshire, J. Limpert. High-power multicore fiber laser systems. *Progress in Quantum Electronics*. **84**, 2022.

[39]. B. M. Shalaby, V. Kermene, D. Pagnoux, A. Desfarges-Berthelemot, A. Barthelemy, A. Popp, et al. 19-cores Yb-fiber laser with mode selection for improved beam brightness. *Applied Physics B-Lasers and Optics*. **100**(4):859-864, 2010.

[40]. A. Klenke, M. Muller, H. Stark, F. Stutzki, C. Hupel, T. Schreiber, et al. Coherently combined 16-channel multicore fiber laser system. *Optics Letters*. **43**(7):1519-1522, 2018.

[41]. V. E. Leshchenko. Coherent combining efficiency in tiled and filled aperture approaches. *Optics Express*. **23**(12):15944-15970, 2015.

[42]. F. Prevost, L. Lombard, J. Primot, L. P. Ramirez, L. Bigot, G. Bouwmans, et al. Coherent beam combining of a narrow-linewidth long-pulse Er3+-doped multicore fiber amplifier. *Optics Express*. **25**(9):9528-9534, 2017.

[43]. K. H. Ji, T. R. Hou, J. B. Li, L. Q. Meng, Z. G. Han, R. H. Zhu. Fast measurement of the laser beam quality factor based on phase retrieval with a liquid lens. *Applied Optics*. **58**(11):2765-2772, 2019.

[44]. K. H. Ji, D. Lin, I. A. Davidson, S. Y. Wang, J. Carpenter, Y. Amma, et al. Controlled generation of picosecond-pulsed higher-order Poincare sphere beams from an ytterbium-doped multicore fiber amplifier. *Photonics Research*. **11**(2):181-188, 2023.

[45]. I. Fsaifes, L. Daniault, S. Bellanger, M. Veinhard, J. Bourderionnet, C. Larat, et al. Coherent beam combining of 61 femtosecond fiber amplifiers. *Optics Express*. **28**(14):20152-20161, 2020.

[46]. D. Lin, J. Carpenter, Y. Feng, S. Jain, Y. Jung, Y. Feng, et al. Reconfigurable structured light generation in a multicore fibre amplifier. *Nature Communications*. **11**(1):3986, 2020.

[47]. A. Forbes. Structured Light from Lasers. *Laser & Photonics Reviews*. **13**(11), 2019.

[48]. M. Piccardo, V. Ginis, A. Forbes, S. Mahler, A. A. Friesem, N. Davidson, et al. Roadmap on multimode light shaping. *Journal of Optics*. **24**(1), 2022.

[49]. S. Ngcobo, I. Litvin, L. Burger, A. Forbes. A digital laser for on-demand laser modes. *Nature communications*. **4**, 2013.

[50]. L. P. Ramirez, M. Hanna, G. Bouwmans, H. El Hamzaoui, M. Bouazaoui, D. Labat, et al. Coherent beam combining with an ultrafast multicore Yb-doped fiber amplifier. *Optics Express*. **23**(5):5406-5416, 2015.

[51]. R. Florentin, V. Kermene, J. Benoist, A. Desfarges-Berthelemot, D. Pagnoux, A. Barthelemy, et al. Shaping the light amplified in a multimode fiber. *Light-Science & Applications*. **6**, 2017.

[52]. D. Lin, J. Carpenter, Y. T. Feng, Y. M. Jung, S. U. Alam, D. J. Richardson. High-power, electronically controlled source of user-defined vortex and vector light beams based on a few-mode fiber amplifier. *Photonics Research*. **9**(5):856-864, 2021.

[53]. J. W. Sun, J. C. Wu, N. Koukourakis, L. C. Cao, R. Kuschmierz, J. Czarske. Real-time complex light field generation through a multi-core fiber with deep learning. *Scientific Reports*. **12**(1), 2022.

[54]. O. Tzang, A. M. Caravaca-Aguirre, K. Wagner, R. Piestun. Adaptive wavefront shaping for controlling nonlinear multimode interactions in optical fibres. *Nature Photonics*. **12**(6):368-374, 2018.

[55]. T. Sylvestre, E. Genier, A. N. Ghosh, P. Bowen, G. Genty, J. Troles, et al. Recent advances in supercontinuum generation in specialty optical fibers [Invited]. *Journal of the Optical Society of America B-Optical Physics*. **38**(12):F90-F103, 2021.

[56]. L. Chang, S. T. Liu, J. E. Bowers. Integrated optical frequency comb technologies. *Nature Photonics*. **16**(2):95-108, 2022.

[57]. A. Zadok, H. H. Diamandi, Y. London, G. Bashan. Forward Brillouin scattering in standard optical fibers: single-mode, polarization-maintaining, and multi-core: *Springer Serious in Optical Sciences*. 2022.

[58]. A. Picozzi, G. Millot, S. Wabnitz. NONLINEAR OPTICS Nonlinear virtues of multimode fibre. *Nature Photonics*. **9**(5):289-291, 2015.

[59]. R. Guenard, K. Krupa, R. Dupiol, M. Fabert, A. Bendahmane, V. Kermene, et al. Kerr self-cleaning of pulsed beam in an ytterbium doped multimode fiber. *Optics Express*. **25**(5):4783-4792, 2017.

[60]. K. Krupa, A. Tonello, B. M. Shalaby, M. Fabert, A. Barthelemy, G. Millot, et al. Spatial beam self-cleaning in multimode fibres. *Nature Photonics*. **11**(4):237-241, 2017.

[61]. F. O. Wu, A. U. Hassan, D. N. Christodoulides. Thermodynamic theory of highly multimoded nonlinear optical systems. *Nature Photonics*. **13**(11):776-782, 2019.

[62]. L. G. Wright, F. O. Wu, D. N. Christodoulides, F. W. Wise. Physics of highly multimode nonlinear optical systems. *Nature Physics*. **18**(9):1018-1030, 2022.

[63]. M. Ferraro, F. Mangini, Y. Leventoux, A. Tonello, M. Zitelli, T. Mansuryan, et al. Multimode Optical Fiber Beam-By-Beam Cleanup. *Journal of Lightwave Technology*. **41**(10):3164-3174, 2023.

[64]. C. Antonelli, A. Mecozzi, M. Shtaif. Raman amplification in multimode fibers with random mode coupling. *Optics Letters*. **38**(8):1188-1190, 2013.

[65]. E. N. Christensen, J. G. Koefoed, S. M. M. Friis, M. A. U. Castaneda, K. Rottwitt. Experimental characterization of Raman overlaps between mode-groups. *Scientific Reports*. **6**, 2016.

[66]. N. Andermahr, C. Fallnich. Optically induced long-period fiber gratings for guided mode conversion in few-mode fibers. *Optics Express*. **18**(5):4411-4416, 2010.

[67]. E. S. Manuylovich, V. V. Dvoyrin, S. K. Turitsyn. Fast mode decomposition in few-mode fibers. *Nature communications*. **11**(1), 2020.

[68]. G. P. Agrawal. Nonlinear Fiber Optics (Sixth Edition): *Academic Press*. 2019.

[69]. H. Sakr, Y. Chen, G. T. Jasion, T. D. Bradley, J. R. Hayes, H. C. H. Mulvad, et al. Hollow core optical fibres with comparable attenuation to silica fibres between 600 and 1100 nm. *Nature communications*. **11**(1):1-10, 2020.

[70]. R. W. Boyd, A. L. Gaeta, E. Giese. Nonlinear optics: *Springer Handbook of Atomic, Molecular, and Optical Physics*. 2008.

[71]. C. Jauregui, C. Stihler, J. Limpert. Transverse mode instability. *Advances in Optics and Photonics*. **12**(2):429-484, 2020.

[72]. M. Paurisse, L. Leveque, M. Hanna, F. Druon, P. Georges. Complete measurement of fiber modal content by wavefront analysis. *Optics Express*. **20**(4):4074-4084, 2012.

[73]. D. Flamm, D. Naidoo, C. Schulze, A. Forbes, M. Duparre. Mode analysis with a spatial light modulator as a correlation filter. *Optics Letters*. **37**(13):2478-2480, 2012.

[74]. R. Bruning, P. Gelszinnis, C. Schulze, D. Flamm, M. Duparre. Comparative analysis of numerical methods for the mode analysis of laser beams. *Applied Optics*. **52**(32):7769-7777, 2013.

[75]. L. J. Huang, S. F. Guo, J. Y. Leng, H. B. Lu, P. Zhou, X. Cheng. Real-time mode decomposition for few-mode fiber based on numerical method. *Optics Express*. **23**(4):4620-4629, 2015.

[76]. Y. An, L. J. Huang, J. Li, J. Y. Leng, L. J. Yang, P. Zhou. Deep Learning-Based Real-Time Mode Decomposition for Multimode Fibers. *Ieee Journal of Selected Topics in Quantum Electronics*. **26**(4):1-6, 2020.

[77]. F. Poletti, P. Horak. Description of ultrashort pulse propagation in multimode optical fibers. *Journal of the Optical Society of America B-Optical Physics*. **25**(10):1645-1654, 2008.

[78]. M. Guasoni. Generalized modulational instability in multimode fibers: Wideband multimode parametric amplification. *Physical Review A*. **92**(3), 2015.

[79]. L. Lombard, A. Brignon, J. P. Huignard, E. Lallier. Beam cleanup in a self-aligned gradient-index Brillouin cavity for high-power multimode fiber amplifiers. *Optics Letters*. **31**(2):158-160, 2006.

[80]. B. Steinhausser, A. Brignon, E. Lallier, J. P. Huignard, P. Georges. High energy, single-mode, narrow-linewidth fiber laser source using stimulated Brillouin scattering beam cleanup. *Optics Express*. **15**(10):6464-6469, 2007.

[81]. N. B. Terry, T. G. Alley, T. H. Russell. An explanation of SRS beam cleanup in graded-index fibers and the absence of SRS beam cleanup in step-index fibers. *Optics Express*. **15**(26):17509-17519, 2007.

[82]. Q. L. Gao, Z. W. Lu, C. Y. Zhu, J. H. Zhang. Mechanism of beam cleanup by stimulated Brillouin scattering in multimode fibers. *Applied Physics Express*. **8**(5), 2015.

[83]. K. Krupa, A. Tonello, A. Barthelemy, T. Mansuryan, V. Couderc, G. Millot, et al. Multimode nonlinear fiber optics, a spatiotemporal avenue. *APL Photonics*. **4**(11), 2019.

[84]. A. G. Kuznetsov, S. I. Kablukov, E. V. Podivilov, S. A. Babin. Brightness enhancement and beam profiles in an LD-pumped graded-index fiber Raman laser. *OSA Continuum*. **4**(3):1034-1040, 2021.

[85]. C. C. Fan, Y. An, T. F. Yao, H. Xiao, L. J. Huang, J. M. Xu, et al. Seeing the beam cleanup effect in a high-power graded-index-fiber Raman amplifier based on mode decomposition. *Optics Letters*. **46**(17):4220-4223, 2021.

[86]. Y. Z. Chen, T. F. Yao, L. J. Huang, H. Xiao, J. Y. Leng, P. Zhou. 2 kW high-efficiency Raman fiber amplifier based on passive fiber with dynamic analysis on beam cleanup and fluctuation. *Optics Express*. **28**(3):3495-3504, 2020.

[87]. L. G. Wright, Z. W. Liu, D. A. Nolan, M. J. Li, D. N. Christodoulides, F. W. Wise. Self-organized instability in graded-index multimode fibres. *Nature Photonics*. **10**(12):771-776, 2016.

[88]. E. Deliancourt, M. Fabert, A. Tonello, K. Krupa, A. Desfarges-Berthelemot, V. Kermene, et al. Kerr beam self-cleaning on the LP11 mode in graded-index multimode fibers. *Osa Continuum*. **2**(4):1089-1096, 2019.

[89]. E. Deliancourt, M. Fabert, A. Tonello, K. Krupa, A. Desfarges-Berthelemot, V. Kermene, et al. Wavefront shaping for optimized many-mode Kerr beam self-cleaning in graded-index multimode fiber. *Optics Express*. **27**(12):17311-17321, 2019.

[90]. W. T. He, S. X. Peng, F. L. Hu, Z. H. Wang, Q. B. Zhang, P. X. Lu. Cascaded Kerr beam self-cleaning in graded-index multimode fibers. *Optics and Laser Technology*. **171**, 2024.

[91]. K. Krupa, A. Tonello, A. Barthélémy, V. Couderc, B. M. Shalaby, A. Bendahmane, et al. Observation of Geometric Parametric Instability Induced by the Periodic Spatial Self-Imaging of Multimode Waves. *Physical Review Letters*. **116**(18), 2016.

[92]. Z. W. Liu, L. G. Wright, D. N. Christodoulides, F. W. Wise. Kerr self-cleaning of femtosecond-pulsed beams in graded-index multimode fiber. *Optics Letters*. **41**(16):3675-3678, 2016.

[93]. M. F. E. Deliancourt, A. Tonello, K. Krupa, A. Desfarges-Berthelemot, V. Kermene, A. Barthelemy, D. Modotto, G. Millot, S. Wabnitz, and V. Couderc. Modal attraction on low order modes by Kerr effect in a graded refractive index multimode fiber. Advanced Photonics Congress, 2018.

[94]. A. Niang, T. Mansuryan, K. Krupa, A. Tonello, M. Fabert, P. Leproux, et al. Spatial beam self-cleaning and supercontinuum generation with Yb-doped multimode graded-index fiber taper based on accelerating self-imaging and dissipative landscape. *Optics Express*. **27**(17):24018-24028, 2019.

[95]. M. Fabert, M. Sapantan, K. Krupa, A. Tonello, Y. Leventoux, S. Fevrier, et al. Coherent combining of self-cleaned multimode beams. *Scientific Reports*. **10**(1), 2020.

[96]. F. Mangini, M. Gervaziev, M. Ferraro, D. S. Kharenko, M. Zitelli, Y. Sun, et al. Statistical mechanics of beam self-cleaning in GRIN multimode optical fibers. *Optics Express*. **30**(7):10850-10865, 2022.

[97]. J. Laegsgaard. Spatial beam cleanup by pure Kerr processes in multimode fibers. *Optics Letters*. **43**(11):2700-2703, 2018.

[98]. M. Ferraro, F. Mangini, M. Zitelli, S. Wabnitz. On spatial beam self-cleaning from the perspective of optical wave thermalization in multimode graded-index fibers. *Advances in Physics-X*. **8**(1), 2023.

[99]. Z. L. Chen, J. Hou, P. Zhou, Z. F. Jiang. Mutual injection-locking and coherent combining of two individual fiber lasers. *IEEE Journal of Quantum Electronics*. **44**(5-6):515-519, 2008.

[100]. J. Q. Cao, Q. S. Lu, J. Hou, X. J. Xu. Self-organization of arrays of two mutually-injected fiber lasers: theoretical investigation. *Optics Express*. **17**(9):7694-7701, 2009.

[101]. J. Q. Cao, Q. S. Lu, J. Hou, X. J. Xu. Dynamical model for self-organized fiber laser arrays. *Optics Express*. **17**(7):5402-5413, 2009.

[102]. P. L. Cheo, A. Liu, G. G. King. A high-brightness laser beam from a phase-locked multicore Yb-doped fiber laser array. *Ieee Photonics Technology Letters*. **13**(5):439-441, 2001.

[103]. E. J. Bochove, P. K. Cheo, G. G. King. Self-organization in a multicore fiber laser array. *Optics Letters*. **28**(14):1200-1202, 2003.

[104]. Y. M. Huo, P. K. Cheo, G. G. King. Fundamental mode operation of a 19-core phase-locked Yb-doped fiber amplifier. *Optics Express*. **12**(25):6230-6239, 2004.

[105]. I. S. Chekhovskoy, M. A. Sorokina, A. M. Rubenchik, M. P. Fedoruk, S. K. Turitsyn. On Demand Spatial Beam Self-Focusing in Hexagonal Multicore Fiber. *IEEE Photonics Journal*. **10**(1), 2018.

[106]. A. V. Andrianov, N. A. Kalinin, M. Y. Koptev, O. N. Egorova, A. V. Kim, A. G. Litvak. High-energy femtosecond pulse shaping, compression, and contrast enhancement using multicore fiber. *Optics Letters*. **44**(2):303-306, 2019.

[107]. H. Tunnermann, A. Shirakawa. Self-focusing in multicore fibers. *Optics Express*. **23**(3):2436-2445, 2015.

[108]. A. M. Rubenchik, I. S. Chekhovskoy, M. P. Fedoruk, O. V. Shtyrina, S. K. Turitsyn. Nonlinear pulse combining and pulse compression in multi-core fibers. *Optics Letters*. **40**(5):721-724, 2015.

[109]. S. Pitois, A. Picozzi, G. Millot, H. R. Jauslin, M. Haelterman. Polarization and modal attractors in conservative counterpropagating four-wave interaction. *Europhysics Letters*. **70**(1):88-94, 2005.

[110]. S. Pitois, G. Millot, S. Wabnitz. Nonlinear polarization dynamics of counterpropagating waves in an isotropic optical fiber: theory and experiments. *Journal of the Optical Society of America B-Optical Physics*. **18**(4):432-443, 2001.

[111]. P. Y. Bony, M. Guasoni, P. Morin, D. Sugny, A. Picozzi, H. R. Jauslin, et al. Temporal spying and concealing process in fibre-optic data transmission systems through polarization bypass. *Nature communications*. **5**, 2014.

[112]. G. Millot, S. Wabnitz. Nonlinear polarization effects in optical fibers: polarization attraction and modulation instability [Invited]. *Journal of the Optical Society of America B-Optical Physics*. **31**(11):2754-2768, 2014.

[113]. S. Pitois, J. Fatome, G. Millot. Polarization attraction using counterpropagating waves in optical fiber at telecommunication wavelengths. *Optics Express*. **16**(9):6646-6651, 2008.

[114]. J. Fatome, S. Pitois, P. Morin, G. Millot. Observation of light-by-light polarization control and stabilization in optical fibre for telecommunication applications. *Optics Express*. **18**(15):15311-15317, 2010.

[115]. V. V. Kozlov, J. Nuno, S. Wabnitz. Theory of lossless polarization attraction in telecommunication fibers. *Journal of the Optical Society of America B-Optical Physics*. **28**(1):100-108, 2011.

[116]. J. Fatome, P. Morin, S. Pitois, G. Millot. Light-by-Light Polarization Control of 10-Gb/s RZ and NRZ Telecommunication Signals. *IEEE Journal of Selected Topics in Quantum Electronics*. **18**(2):621-628, 2012.

[117]. J. Fatome, S. Pitois, P. Morin, E. Assemat, D. Sugny, A. Picozzi, et al. A universal optical all-fiber Omnipolarizer. *Scientific Reports*. **2**:938, 2012.

[118]. M. Guasoni, P. Morin, P. Y. Bony, S. Wabnitz, J. Fatome. [INVITED] Self-induced polarization tracking, tunneling effect and modal attraction in optical fiber. *Optics and Laser Technology*. **80**:247-259, 2016.

[119]. M. Guasoni, V. V. Kozlov, S. Wabnitz. Theory of polarization attraction in parametric amplifiers based on telecommunication fibers. *Journal of the Optical Society of America B-Optical Physics*. **29**(10):2710-2720, 2012.

[120]. M. Guasoni, V. V. Kozlov, S. Wabnitz. Theory of modal attraction in bimodal birefringent optical fibers. *Optics Letters*. **38**(12):2029-2031, 2013.

[121]. T. Hellwig, K. Sparenberg, C. Fallnich. Analytical model for transverse mode conversion at all-optically induced, transient long-period gratings: from continuous-wave to ultrafast. *Applied Physics B-Lasers and Optics*. **122**(9), 2016.

[122]. T. Hellwig, T. Walbaum, C. Fallnich. Optically induced mode conversion in graded-index fibers using ultra-short laser pulses. *Applied Physics B-Lasers and Optics*. **112**(4):499-505, 2013.

[123]. T. Hellwig, M. Schnack, T. Walbaum, S. Dobner, C. Fallnich. Experimental realization of femtosecond transverse mode conversion using optically induced transient long-period gratings. *Optics Express*. **22**(21):24951-24958, 2014.

[124]. T. Walbaum, C. Fallnich. Theoretical analysis of transverse mode conversion using transient long-period gratings induced by ultrashort pulses in optical fibers. *Applied Physics B-Lasers and Optics*. **115**(2):225-235, 2014.

[125]. M. Schnack, T. Hellwig, M. Brinkmann, C. Fallnich. Ultrafast two-color all-optical transverse mode conversion in a graded-index fiber. *Optics Letters*. **40**(20):4675-4678, 2015.

[126]. G. M. Fernandes, A. M. Rocha, M. Facao. Mode switching using optically induced long-period gratings: a theoretical analysis. *Optics Express*. **29**(10):14601-14614, 2021.

[127]. G. M. Fernandes, A. M. Rocha, M. Facao. Core Switch Using Optically Induced Long-Period Gratings. *Photonics*. **9**(11), 2022.

[128]. A. Hofstrand, P. Jakobsen, J. V. Moloney. Bidirectional shooting method for extreme nonlinear optics. *Physical Review A*. **100**(5), 2019.

[129]. N. A. Kalinin, E. A. Anashkina, O. N. Egorova, S. G. Zhuravlev, S. L. Semjonov, A. V. Kim, et al. Controlled Excitation of Supermodes in a Multicore Fiber with a 5 x 5 Square Array of Strongly Coupled Cores. *Photonics*. **8**(8), 2021.

[130]. K. H. Ji, I. Davidson, J. Sahu, D. J. Richardson, S. Wabnitz, M. Guasoni. Mode attraction, rejection and control in nonlinear multimode optics. *Nature Communications*. **14**(1), 2023.

[131]. L. Huo, R. X. Wang, M. Tang, Q. Wu, S. N. Fu, D. M. Liu. Reconfigurable Inter-Core Signal Switching Within Multicore Fibers Based on Long-Period Gratings. *Journal of Lightwave Technology*. **37**(24):6025-6032, 2019.

[132]. C. Deakin, M. Enrico, N. Parsons, G. Zervas. Design and Analysis of Beam Steering Multicore Fiber Optical Switches. *Journal of Lightwave Technology*. **37**(9):1954-1963, 2019.

[133]. C. Melo, D. Arroyo, E. S. Gómez, S. P. Walborn, G. Lima, M. Figueroa, et al. A new architecture for high speed core-selective switch for multicore fibers. *arXiv preprint arXiv:2411.17641*. 2024.

[134]. S. R. Friberg, A. M. Weiner, Y. Silberberg, B. G. Sfez, P. S. Smith. Femtosecond Switching in a Dual-Core-Fiber Nonlinear Coupler. *Optics Letters*. **13**(10):904-906, 1988.

[135]. Y. Yan, J. Toulouse. Nonlinear inter-core coupling in triple-core photonic crystal fibers. *Optics Express*. **17**(22):20272-20281, 2009.

[136]. H. Pourbeyram, E. Nazemosadat, A. Mafi. Detailed investigation of intermodal four-wave mixing in SMF-28: blue-red generation from green. *Optics Express*. **23**(11):14487-14500, 2015.

[137]. M. Kwasny, P. Mergo, M. Napierala, K. Markiewicz, U. A. Laudyn. An Efficient Method for the Intermodal Four-Wave Mixing Process. *Materials*. **15**(13), 2022.

[138]. J. Demas, G. Prabhakar, T. He, S. Ramachandran. Broadband Wideband Parametric Gain via Intermodal Four-Wave Mixing in Optical Fiber. *2017 Conference on Lasers and Electro-Optics (CLEO)*. 2017.

[139]. S. Perret, G. Fanjoux, L. Bigot, J. Fatome, G. Millot, J. M. Dudley, et al. Supercontinuum generation by intermodal four-wave mixing in a step-index few-mode fibre. *APL Photonics*. **4**(2), 2019.

[140]. R. J. Essiambre, M. A. Mestre, R. Ryf, A. H. Gnauck, R. W. Tkach, A. R. Chraplyvy, et al. Experimental Investigation of Inter-Modal Four-Wave Mixing in Few-Mode Fibers. *Ieee Photonics Technology Letters*. **25**(6):539-542, 2013.

[141]. S. M. M. Friis, I. Begleris, Y. Jung, K. Rottwitt, P. Petropoulos, D. J. Richardson, et al. Inter-modal four-wave mixing study in a two-mode fiber. *Optics Express*. **24**(26):30338-30349, 2016.

[142]. O. F. Anjum, M. Guasoni, P. Horak, Y. M. Jung, P. Petropoulos, D. J. Richardson, et al. Polarization-Insensitive Four-Wave-Mixing-Based Wavelength Conversion in Few-Mode Optical Fibers. *Journal of Lightwave Technology*. **36**(17):3678-3683, 2018.

[143]. J. H. Yuan, Z. Kang, F. Li, G. Y. Zhou, X. Z. Sang, Q. Wu, et al. Polarization-dependent intermodal four-wave mixing in a birefringent multimode photonic crystal fiber. *Optics Letters*. **42**(9):1644-1647, 2017.

[144]. D. Wu, L. Shen, H. N. Ren, M. Huang, C. Lacava, J. Campling, et al. Four-Wave Mixing-Based Wavelength Conversion and Parametric Amplification in Submicron Silicon Core Fibers. *Ieee Journal of Selected Topics in Quantum Electronics*. **27**(2), 2021.

[145]. S. Signorini, M. Mancinelli, M. Borghi, M. Bernard, M. Ghulinyan, G. Pucker, et al. Intermodal four-wave mixing in silicon waveguides. *Photonics Research*. **6**(8):805-814, 2018.

[146]. T. L. Courtney, C. Chester, C. Keyser. Optical parametric generation in liquid- and gas-filled hollow core fibers. *Optical Waveguide and Laser Sensors*. **11405**, 2020.

[147]. A. D. Szabó, V. Ribeiro, C. B. Gaur, A. A. I. Ali, A. Mussot, Y. Quiquempois, et al. Dual-Polarization C plus L-Band Wavelength Conversion in a Twin-Core Highly Nonlinear Fibre. *2021 Optical Fiber Communications Conference and Exposition (OFC)*. 2021.

[148]. V. Ribeiro, A. D. Szabo, A. M. Rocha, C. B. Gaur, A. A. I. Ali, Y. Quiquempois, et al. Parametric Amplification and Wavelength Conversion in Dual-Core Highly Nonlinear Fibers. *Journal of Lightwave Technology*. **40**(17):6013-6020, 2022.

[149]. J. H. Li, K. S. Chiang, K. W. Chow. Modulation instabilities in two-core optical fibers. *Journal of the Optical Society of America B-Optical Physics*. **28**(7):1693-1701, 2011.

[150]. V. Ribeiro, M. Karlsson, P. Andrekson. Parametric amplification with a dual-core fiber. *Optics Express*. **25**(6):6234-6243, 2017.

[151]. J. H. Li, T. T. Sun, Y. Q. Ma, Y. Y. Chen, Z. L. Cao, F. L. Xian. The effects of fourth-order dispersion on modulation instabilities in two-core optical fibers with asymmetric CW state. *Physica Scripta*. **95**(11), 2020.

[152]. M. J. Shi, V. Ribeiro, A. M. Perego. Parametric amplification based on intermodal four-wave mixing between different supermodes in coupled-core fibers. *Optics Express*. **31**(6):9760-9768, 2023.

[153]. T. Sakamoto, T. Mori, M. Wada, T. Yamamoto, F. Yamamoto, K. Nakajima. Fiber Twisting- and Bending-Induced Adiabatic/Nonadiabatic Super-Mode Transition in Coupled Multicore Fiber. *Journal of Lightwave Technology*. **34**(4):1228-1237, 2016.

[154]. T. Sakamoto, T. Mori, M. Wada, T. Yamamoto, F. Yamamoto, K. Nakajima. Strongly-coupled multi-core fiber and its optical characteristics for MIMO transmission systems. *Optical Fiber Technology*. **35**:8-18, 2017.

[155]. T. Hayashi, T. Sakamoto, Y. Yamada, R. Ryf, R. J. Essiambre, N. Fontaine, et al. Randomly-Coupled Multi-Core Fiber Technology. *Proceedings of the IEEE*. **110**(11):1786-1803, 2022.

[156]. P. Russell. Photonic crystal fibers. *Science*. **299**(5605):358-362, 2003.

[157]. CAILABS. https://www.cailabs.com/en/products/proteus. 2021.

[158]. J. Wang, J. Y. Yang, I. M. Fazal, N. Ahmed, Y. Yan, H. Huang, et al. Terabit free-space data transmission employing orbital angular momentum multiplexing. *Nature Photonics*. **6**(7):488-496, 2012.

[159]. M. Padgett, R. Bowman. Tweezers with a twist. *Nature Photonics*. **5**(6):343-348, 2011.

[160]. Y. Li, L. Yu, Y. X. Zhang. Influence of anisotropic turbulence on the orbital angular momentum modes of Hermite-Gaussian vortex beam in the ocean. *Optics Express*. **25**(11):12203-12215, 2017.

[161]. R. Chen, K. Agarwal, C. J. R. Sheppard, X. D. Chen. Imaging using cylindrical vector beams in a high-numerical-aperture microscopy system. *Optics Letters*. **38**(16):3111-3114, 2013.

[162]. G. Bautista, J. P. Kakko, V. Dhaka, X. R. Zang, L. Karvonen, H. Jiang, et al. Nonlinear microscopy using cylindrical vector beams: applications to three-dimensional imaging of nanostructures. *Optics Express*. **25**(11):12463-12468, 2017.

[163]. G. Milione, H. I. Sztul, D. A. Nolan, R. R. Alfano. Higher-Order Poincare Sphere, Stokes Parameters, and the Angular Momentum of Light. *Physical Review Letters*. **107**(5), 2011.

[164]. Y. J. Shen, X. J. Wang, Z. W. Xie, C. J. Min, X. Fu, Q. Liu, et al. Optical vortices 30 years on: OAM manipulation from topological charge to multiple singularities. *Light-Science & Applications*. **8**, 2019.

[165]. G. Machavariani, Y. Lumer, I. Moshe, A. Meir, S. Jacket. Efficient extracavity generation of radially and azimuthally polarized beams. *Optics Letters*. **32**(11):1468-1470, 2007.

[166]. B. Piccirillo, V. D'Ambrosio, S. Slussarenko, L. Marrucci, E. Santamato. Photon spin-to-orbital angular momentum conversion via an electrically tunable q-plate. *Applied Physics Letters*. **97**(24), 2010.

[167]. M. Beresna, M. Gecevicius, P. G. Kazansky, T. Gertus. Radially polarized optical vortex converter created by femtosecond laser nanostructuring of glass. *Applied Physics Letters*. **98**(20), 2011.

[168]. S. Z. Chen, X. X. Zhou, Y. C. Liu, X. H. Ling, H. L. Luo, S. C. Wen. Generation of arbitrary cylindrical vector beams on the higher order Poincare sphere. *Optics Letters*. **39**(18):5274-5276, 2014.

[169]. H. Sroor, Y. W. Huang, B. Sephton, D. Naidoo, A. Valles, V. Ginis, et al. Generation of arbitrary Higher-Order Poincare beams from a visible metasurface laser. *Laser Resonators, Microresonators, and Beam Control Xxii*. **11266**, 2020.

[170]. I. A. Litvin, S. Ngcobo, D. Naidoo, K. Ait-Ameur, A. Forbes. Doughnut laser beam as an incoherent superposition of two petal beams. *Optics Letters*. **39**(3):704-707, 2014.

[171]. H. L. Li, D. B. Phillips, X. Y. Wang, Y. L. D. Ho, L. F. Chen, X. Q. Zhou, et al. Orbital angular momentum vertical-cavity surface-emitting lasers. *Optica*. **2**(6):547-552, 2015.

[172]. D. Naidoo, F. S. Roux, A. Dudley, I. Litvin, B. Piccirillo, L. Marrucci, et al. Controlled generation of higher-order Poincare sphere beams from a laser. *Nature Photonics*. **10**(5):327-+, 2016.

[173]. D. Lin, N. Baktash, S. U. Alam, D. J. Richardson. 106 W, picosecond Yb-doped fiber MOPA system with a radially polarized output beam. *Optics Letters*. **43**(20):4957-4960, 2018.

[174]. D. Zhi, T. Y. Hou, P. F. Ma, Y. X. Ma, P. Zhou, R. M. Tao, et al. Comprehensive investigation on producing high-power orbital angular momentum beams by coherent combining technology. *High Power Laser Science and Engineering*. **7**, 2019.

[175]. H. X. Chang, Q. Chang, J. C. Xi, T. Y. Hou, R. T. Su, P. F. Ma, et al. First experimental demonstration of coherent beam combining of more than 100 beams. *Photonics Research*. **8**(12):1943-1948, 2020.

[176]. T. Y. Hou, Y. An, Q. Chang, P. F. Ma, J. Li, L. J. Huang, et al. Deep-learning-assisted, two-stage phase control method for high-power mode-programmable orbital angular momentum beam generation. *Photonics Research*. **8**(5):715-722, 2020.

[177]. J. Lhermite, E. Suran, V. Kermene, F. Louradour, A. Desfarges-Berthelemot, A. Barthelemy. Coherent combining of 49 laser beams from a multiple core optical fiber by a spatial light modulator. *Optics Express*. **18**(5):4783-4789, 2010.

[178]. A. El Sayed, S. Pilz, J. Scheuner, H. Najafi, T. Feurer, V. Romano. Properties of Yb doped silica fibers with different Al and P co-dopants concentrations produced by the Sol-Gel based granulated silica method. *Micro-Structured and Specialty Optical Fibres V*. **10681**, 2018.

[179]. S. Unger, A. Schwuchow, J. Dellith, J. Kirchhof. Optical properties of ytterbium/aluminium doped silica glasses. *Optical Materials Express*. **10**(4):907-925, 2020.

[180]. ALGLIB. https://www.alglib.net/.

[181]. B. Ndagano, R. Bruning, M. McLaren, M. Duparre, A. Forbes. Fiber propagation of vector modes. *Optics Express*. **23**(13):17330-17336, 2015.

[182]. D. Lin, N. Baktash, M. Berendt, M. Beresna, P. G. Kazansky, W. A. Clarkson, et al. Radially and azimuthally polarized nanosecond Yb-doped fiber MOPA system incorporating temporal shaping. *Optics Letters*. **42**(9):1740-1743, 2017.

[183]. M. Lyu, Z. Q. Lin, G. W. Li, G. H. Situ. Fast modal decomposition for optical fibers using digital holography. *Scientific Reports*. **7**, 2017.